MULTISCALE POLYMER AND NANOPARTICLE DYNAMICS IN POLYMER NANOCOMPOSITES

Eric Joseph Bailey

A DISSERTATION

in

Materials Science and Engineering

Presented to the Faculties of the University of Pennsylvania

in

Partial Fulfillment of the Requirements for the

Degree of Doctor of Philosophy

2020

Supervisor of Dissertation

_____

Karen I. Winey, Professor, Materials Science and Engineering

Graduate Group Chairperson

_____

I-Wei Chen, Professor, Materials Science and Engineering

Dissertation Committee

Russell J. Composto, Professor, Materials Science and Engineering

Robert A. Riggleman, Associate Professor, Chemical and Biomolecular Engineering

Daeyeon Lee, Professor, Chemical and Biomolecular Engineering

MULTISCALE POLYMER AND NANOPARTICLE DYNAMICS IN POLYMER NANOCOMPOSITES

DEDICATION

The culmination of this work is dedicated to my family: Mom, Dad, Olivia, Zach, Alana, and Jackie. I would also like to dedicate this thesis to those affected most by the ongoing COVID-19 (novel coronavirus) pandemic that is changing current life throughout the world.

ACKNOWLEDGMENTS

Those who know me know that I'm much more practical than emotional, but when it comes to acknowledging those who helped me both in and out of lab, it's impossible to separate the two. This work would literally not have been possible without the motivational, emotional, and intellectual support of everybody in my life. And for that, I am eternally grateful to more people than I can list.

First and foremost, I would like to thank my advisor, Karen Winey, for teaching me how to develop research questions, solve problems, and think critically. She provided me the ideal amount of support: she allowed me to try new things, fail, learn from my failures, and pursue new ideas, but she also provided suggestions and guidance when I was stuck and needed it. I really appreciated her open mindedness, attention to scientific detail, and meticulous edits to sentence structure and grammar. I am also grateful for her support in attending conferences and traveling for experiments, her nominations for different honors/awards, and her continued support in and out of lab for the past almost 5 years. It was a pleasure to work with her and I'm deeply grateful for her mentorship.

I'd also like to thank my committee both holistically and individually. Professor Russell Composto not only blindly donated to my cross-country bicycle trip before we even met, but his excitement to talk about science, insight into polymer dynamics and ion scattering, and encouragement when I needed it most was immensely helpful. I also would like to thank Professor Rob Riggleman for his guidance into the simulation world and for his part in me developing into a multifaceted researcher. Also, I would like to thank him for letting me join his group for a few months when the ion beam was down, and more importantly, for taking a group picture during those months that lasted three years. Last but not least, I'd like to thank Professor Daeyeon Lee for helping me think outside of my bubble of nanocomposites, and often providing his unique perspective to our discussions.

My research has taken me to several different labs and given me the pleasure of working closely with some wonderful people. For QENS at NIST, I would like to thank Madhu Tyagi for his assistance and guidance, even in the middle of the night. At Argonne National Lab, I am grateful to Suresh

Narayanan for the introduction to XPCS and assistance with measurements. I am also thankful for the collaborations with Derek Demaree (Army Research Lab), Barney Doyle (Sandia National Lab), Ronald Jones (NIST), and Bharath Natarajan and Adam Burns (ExxonMobil). I am also immensely grateful for the people at Penn that have made my research technically possible: Doug Yates, Jamie Ford, Matt Brukman, and Steve Szewczyk. Doug was instrumental in reviving and maintaining the ion beam to make several of these experiments possible. His time, effort, and frustration is very much appreciated. Steve was essential for countless measurements I have made in LRSM, and can always be counted on to help with a new or uncooperating experiment. Thank you to the LRSM facilities personnel (Mario, Craig, Tim, and Enrique) and staff (Vicky, Abby, Irene, and Pat), as well.

I want to also extend a sincere thank you to the past and present Winey group including those that I was fortunate enough to work closely with (Philip Griffin, Francisco Buitrago, James Pressly, Jinseok Park, Kait Wang, Nicky Han, Dakota Wallach, and Tia Denby) and those that I was fortunate enough to work adjacent to (Robert Middleton, Ted Trigg, Lu Yan, Ben Paren, Lizhu Zhang, Drew Wang, Junwei Xiang, Miko Stulajter, Clark Shurtleff, Demi Moed, Lauren Hoang, Anita Yang, and Arjun Kanthawar). In particular, I'd like to thank Phil for helping me get started in polymer physics research, and James for chatting with me when I had some tough research problems to work through. Thanks to Ben, Jinseok, and Lu for the countless fun conversations about science and not, and thanks to Rob and Ted for all of the advice that you've given me over the years, setting great examples for me, and for the various out-of-lab activities which I cherished. Finally, I'd like to thank Tia, Dakota, and Nicky for working with me, bringing energy, and for contributing to various aspects of this research.

I'd like to extend a thank you to the broader Penn community, even though there are too many to name. Thank you to Ana Alverez, Charles Stovall, Nadia Krook, Boris Rasin, Katie Rose, Shawn Maguire, Mike Boyle, Emily Lin, Tiaren Zhang, Ben Lindsay, members of the MSE community, members of the tennis league, the Friday morning pick-up basketball guys, and all of my intramural sports friends. You all have been instrumental in getting my mind off research and helping me have fun outside of lab. I want to emphasize my appreciation to the intramural sports folks: together my rein at

Penn culminated in a remarkably average record of 35-35-1 accompanied by four gold, two silver, and three bronze finishes, but more importantly, countless memories.

Outside of Philly, I have the most wonderful and supportive family, both immediate and extended, and for that I am immensely thankful. Not only do they endure my failure to reply to texts and calls, but they go out of their way to be there for me when I don't even tell them I need it, and they help keep me motivated. My parents, Jane and Steve, are always willing to help me talk through my problems, forget about them, or help solve them, even from 120 miles away. I'm also lucky to have my siblings Olivia, Zach, and Alana, who always know how to make me laugh and keep me grounded.

For maybe the easiest acknowledgement of all, with more love than I know how to express, I want to thank Jackie: my ex-girlfriend, soon to be ex-fiancé, future wife, and forever best friend. I am lucky to even know someone as kind and caring as her, let alone get to see her every day. I can count on Jackie to let me complain, to celebrate with me, and to always offer to help, even if only to let me know she's there. I can also count on her for finding my typos, including deptartment, probabaileyty, Avagodro, doctor balding, MDF, and she only knows how many others. I can't wait to spend the rest of my life with her and I am excited to match her unwavering support for the many years to come.

Finally, in an effort to give thanks where thanks are due, there are a few more people that I would like to acknowledge for contributions I am confident they don't know they had. I want to thank Daniel Ek, Martin Lorentzon, Jack Dorsey, Noah Glass, Evan Williams, Biz Stone, Jawed Karim, Steve Chen, and Chad Hurley for their contribution to my mental well-being. I'd also like to thank Raffaele Esposito, David Der Hairabedian, Walter Diemer, Adolph Coors, Jacob Schueler, Walter Wingfield, and James Naismith for their contribution to my physical well-being. And, on a more serious note, I acknowledge funding and resource support from XSEDE, the Department of Energy, the Department of Commerce, the National Science Foundation, and the University of Pennsylvania.

ABSTRACT

MULTISCALE POLYMER AND NANOPARTICLE DYNAMICS IN POLYMER NANOCOMPOSITES

Eric J. Bailey

Karen I. Winey

The addition of nanoparticles (NPs) to a polymer matrix, forming a polymer nanocomposite (PNC), can extend and control macroscopic material properties. Many macroscopic properties (e.g. mechanical strength and small molecule transport) are dictated by microscopic dynamic processes, including dynamics of the polymer segments, chains, and NPs. Because the NPs and polymers have overlapping characteristic length, time, and energy scales, the interactions within these materials are complex, the dynamics are interrelated, and both remain poorly understood. Developing a fundamental and mechanistic understanding of polymer and NP dynamics in PNCs will lead to new opportunities, new innovations, and improved manufacturability, all of which may accelerate their universal introduction to society.

This dissertation aims to navigate the hierarchy of dynamics in model PNCs. At the smallest length scale, we show that polymer segmental dynamics are slowed by the addition of highly-attractive, immobile NPs, particularly at the NP-polymer interface, and depend only weakly on temperature and matrix molecular weight. Despite measurable reductions in the timescale of motion, we show that the segmental diffusion process is mechanistically similar in PNCs and bulk. At longer length and timescales, we use molecular dynamics simulations to study chain-scale conformations and diffusion near confining athermal NPs. We show polymer diffusion is perturbed at longer length-scales than conformations and identify slow diffusion through confining NPs but bulk-like diffusion away from them. Using model attractive PNCs, we develop and demonstrate

ion scattering measurements to extract the fraction of chains bound to the immobile NPs. These measurements show that the slow segmental relaxations at the interface persist to the chain-scale and reveal slow bound polymer desorption that occurs more readily at higher temperatures, lower polymer molecular weight, and longer times. Finally, we sample multiple length and timescales in mixtures of entangled polymer and very small, attractive NPs. We present experimental support of vehicular diffusion of NPs, which produces anomalously fast NP motion and commensurate slowing of polymer segments and polymer chain diffusion. Finally, we present X-ray photon correlation spectroscopy measurements of NP dynamics, small-angle neutron scattering measurements of the bound polymer layer in solution, and protocols for NP surface functionalization.

TABLE OF CONTENTS

LIST OF TABLES

LIST OF FIGURES

CHAPTER 1: Dynamics of Polymer Segments, Polymer Chains, and Nanoparticles in Polymer Nanocomposites: A Review

Content in this chapter was accepted for publication in *Progress in Polymer Science* (DOI: 10.1016/j.progpolymsci.2020.101242) in a modified version and the authors are Eric J. Bailey and Karen I. Winey.

1.1 Introduction

Polymer nanocomposites (PNCs), or materials comprised of nano-sized fillers imbedded in a polymer matrix, have generated substantial academic and industrial attention in recent decades. Compared to composites with micron-sized fillers, the use of nanoparticles (NPs) drastically increases the NP-polymer interfacial area and decreases NP-NP separations at the same concentration of filler.[1,2] As such, a resulting PNC can have drastically different properties as compared to the host matrix or traditional composites. In fact, these different properties can be varied, controlled, and tuned using the broad set of parameters that these hybrid materials offer. These parameters include those associated with the NP (size, shape, and surface), polymer (molecular weight, chemistry, and architecture), and PNC (concentration, NP-polymer interaction, and NP dispersion state). In addition, inclusion of the NP can add functionality including electrical, plasmonic, barrier, or stimuli-responsive properties to a polymer matrix otherwise devoid of those properties. Importantly, many PNCs still maintain the favorable properties of the polymer such as processability and low mass density.

Polymer nanocomposites are exciting candidates for a variety of applications and industries, as reviewed by others.[3–12] Early interest in nanoparticle-filled polymers was for car tires, where NPs are added to rubber to increase strength, wear resistance, and traction while maintaining

low cost and weight.[4] Similar properties make PNCs desirable for different applications, including various parts in ground and air transportation and sports equipment. In addition, PNCs have desirable barrier, permeability, and selectivity properties making them ideal candidates for membrane and separation technologies such as gas separation, water filtration, and food packaging.[7,13] For example, the addition of fumed silica NPs with poly(4-methyl-2-pentyne) (PMP) resulting in substantial increases in both n-butane permeability and n-butane/methane selectivity, two parameters that often compete with each other.[14] As a final example, the addition of NPs can add functional properties, especially optic and electronic, to the polymer matrices. The most common example is adding electrical conductivity to an otherwise insulating polymer matrix through the inclusion of a percolated network of silver nanowires, carbon nanotubes, or other conductive fillers.[15–18] Similarly, adding plasmonic or upconverting NPs to a polymer matrix has optoelectronic applications and can enhance the efficiency of solar cells.[10,12,19]

Despite the appealing properties that have been observed, much remains unknown, especially regarding PNCs more fundamentally. In this vein, this review will broadly survey and discuss recent studies of multiscale polymer dynamics and NP dynamics in polymer nanocomposites, as depicted in Figure 1.1. As discussed in Section 1.2, PNCs exhibit several different dynamic processes that are interrelated and dictate or influence meaningful properties and performance. In subsequent sections, we will discuss and review selected theoretical, simulation, and experimental approaches and studies as they pertain to the different dynamic processes. Beginning at the shortest length and timescales, Section 1.3 will explore polymer segmental dynamics in PNCs, followed by non-diffusive polymer chain relaxations (intermediate dynamics, Section 1.4), center-of-mass polymer diffusion through PNCs (Section 1.5), and NP dynamics in polymer and PNC melts (Section 1.6).

This review will generally focus on model PNCs systems of linear thermoplastics filled with hard nanoparticles in the melt state, although in some cases, other relevant systems will be

discussed. Although many different polymers and fillers will be discussed, the majority will be inorganic metallic and ceramic nanoparticles. PNCs with silicates and carbon-materials (CNTs, C60, graphene, carbon black) have been reviewed elsewhere[16,20–24] and will receive very cursory mention in this review. More focused reviews regarding various classes of PNCs or aspects of dynamics may also be of interest.[25–34]

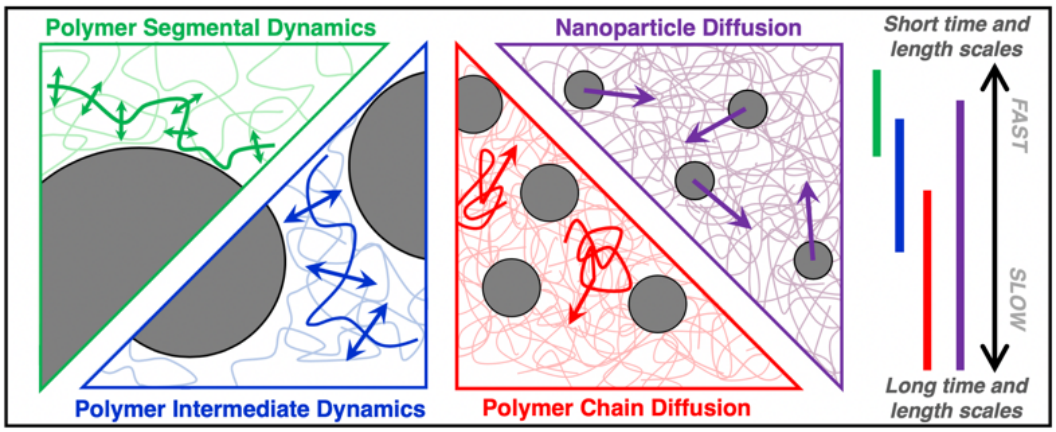

Figure 1.1: Schematic to highlight the time- and length-scales of various dynamic processes in polymer nanocomposites.

1.2 The Importance of Dynamics in Polymer Nanocomposites

1.2.1 Overview of dynamics processes in polymer nanocomposites

Polymer melts have a rich hierarchy of time- and length-scale dependent dynamic processes.[35] At the smallest timescales and sub-angstrom length-scales, atoms in a solid undergo thermal vibrations at finite temperature. These fast dynamics are often on the pico-second time scale and are characterized by particles rattling in cages formed by the local packing of nearby atoms. Generally, these fast dynamics are unaffected by the connectivity of monomers that form polymer chains, except when the molecular weight (M_w) affects the local packing. Unlike longer

length-scale dynamics, these local relaxations may be active even when the temperature (T) is less than the glass transition temperature (T_g). This review will not discuss these local, fast dynamics.

Segmental dynamics occur at various timescales and at length-scales at or below those associated with a Kuhn segment. Broadly, segmental dynamics can be defined as the non-diffusive relaxations of a group of bonded atoms within a polymer chain. The α-process is the primary structural relaxation that refers to the cooperative reorientation and conformational fluctuations of a set of adjacent monomers along the polymer backbone. The glass transition temperature of a polymer can be defined dynamically through the arrest of this α-process or thermodynamically through changes in thermodynamic properties (such as density, thermal expansion coefficient, or heat capacity).[36] At smaller length scales within a Kuhn segment and generally faster timescales, secondary relaxations (β, γ, etc.) occur in some polymers. These relaxations are often associated with motions of side groups as opposed to the backbone, especially for bulky, flexible, or complex repeat units. For example, several secondary relaxations have been identified in polystyrene (PS) melts both above and below T_g.[37] In general, this review will focus on the α-process when discussing segmental dynamics in PNCs.

The dynamics at time- and length-scales beyond segmental dynamics are the dynamics associated with the polymer chains, which include non-diffusive relaxations or translational diffusion, and are therefore on the order of or less than the radius of gyration (R_g) of the chain. The Rouse model is used to describe the dynamics of chain sections (modes) of arbitrary length in the melt, while the Zimm model is the analogous theory for polymers in solution.[35] For sufficiently short polymers, the Rouse model extends to describe the translational diffusion coefficient of the entire chain. However, as the degree of polymerization increases, chains in the melt eventually interpenetrate and form topological constraints known as entanglements. For entangled polymer melts, Rouse dynamics describe the relaxation of Rouse modes between entanglements, but no

longer apply to chain-level dynamics when the relaxations are restricted by the entanglement network. For an entangled chain to fully relax and diffuse, it must either diffuse through the entanglement network through a process called reptation or the entanglement network must relax to no longer impede the chain motion through a process called constraint release.[35] Reptation refers to the process by which segmental relaxations and friction within the confining tube (following Edwards tube theory) lead to chain translocation along it's contour length through the entanglement nodes. Whether the an unentangled chain diffuses via Rouse motion or an entangled chain diffuses via reptation, the dynamics are characterized by the center-of-mass diffusion coefficient (D).

When considering polymer nanocomposites, it is important to note that the sizes of NPs are similar to or smaller than the characteristic size of polymers (R_g). As such, the relaxational and motional processes of NPs and polymers often have overlapping time-, energy-, and length-scales. To be specific, NP motion is considered a competition between thermally-driven kinetic forces that promote NP diffusion and viscous drag forces from the polymer medium that slow the NP diffusion, qualitatively similar to Stokes-Einstein.[38] However, as will be discussed in Section 1.6, the molecular origin of these forces depends on the time-, energy-, and length-scales of the NPs and polymer medium. In addition, at small length scales, NPs can exhibit non-diffusive relaxation dynamics, including rattling in the local environment, ballistic motion, and in the case of anisotropic NPs, reorientation fluctuations.

1.2.2 Polymer nanocomposites properties dictated by dynamics

The microscopic dynamics of polymers and NPs are critically important to understand, design, develop, and fabricate new PNCs. The dynamic processes discussed in Section 1.2.1 often influence or even dictate various macroscopic properties and the processability of PNCs. Thus, fundamental studies of dynamics, like those discussed herein, in these materials are essential to realize next generation technologies and to mass produce PNCs cost effectively. This is not to say

dynamic properties are the only barrier to widespread PNC development and application. In fact, other recent reviews have highlighted other critical aspects of PNC research[2,4,9,12,25,33], but many others have noted the importance of dynamics.[25–29]

Polymer dynamics in melts and nanocomposites are critical for various macroscopic PNC properties, so understanding and documenting the polymer dynamics can help predict, control, and understand the final PNC performance. For example, mechanical properties including stiffness, strength, and stress relaxation are known to be influenced by segmental dynamics. Slow secondary segmental relaxations in the glassy state lead to enhanced mechanical stiffness and slower dynamics in the melt can increase the melt viscosity. In fact, the addition of NPs can controllably alter segmental dynamics and therefore control various mechanical properties.[39–41] In addition, segmental mobility often dictates transport properties, including ion transport for energy applications[42] and small molecule transport for membrane and separation technology.[7,14,43–45] For example, enhanced permeability of CO_2 was observed at an intermediate grafting molecular weight in matrix-free PNCs comprised of silica (SiO_2)-grafted poly(methylacrylate) (PMA),[43] and this behavior was correlated to increased local free volume and faster segmental dynamics.[46]

Dynamics in PNCs can also lead directly to unique and functional properties, including stimuli-responsive and self-healing properties.[47–49] For example, multilayer films comprised of flexible polymer and brittle oxides are common in electronic components for various industries, but suffer from crack formation and propagation. However, if the polymer is replaced with a PNC, the NPs can be engineered to diffuse into cracks to provide self-healing properties and achieve improved durability.[48] Similar responsive properties can be used to make advanced sensors and other responsive materials.

The appealing properties that have been reported for small batches of PNCs, cannot be ubiquitously deployed until the PNCs can be manufactured cost-effectively in mass quantities. Importantly, the dynamic processes in PNC materials can inform or guide processing routes and

parameters necessary for mass production. For example, melt processing and molding requires flow of the PNC material, which is related to the chain-scale dynamics. After processing, the NP morphology is often metastable, so understanding how rapidly a PNC evolves is necessary to maintain the metastable condition, if desirable, or achieve equilibrium. When a random NP dispersion is desired in the glassy state and NPs tend to aggregate in the melt state, then precise knowledge of polymer chain and NP dynamics allows engineers to properly design the process protocols. Furthermore, NPs can be added to enhance the manufacturability of materials by either enhancing dynamics and rheology (i.e. a plasticizer or diluent) or slowing dynamics (i.e. an anti-plasticizer).

Polymer nanocomposites are also model systems to understand multicomponent systems with related physics. For example, the large surface area to volume ratio of NPs increases the amount of interfacial polymer. Thus, systematic studies of well-defined PNCs can probe the structure and dynamics of polymers near interfaces.[31,50] Similar effects can be studied at solid and flat interfaces, but these thin films suffer from weak signal, because comparatively fewer polymer chains are at the interface. In addition, PNCs (especially those with entangled polymers) are a model system that can be used for understanding diffusion of NPs and molecules in complex media, such as biological tissue and other organic matter.[26,51–53] As such, understanding the dynamics in PNCs can provide insights into other, more complicated systems.

1.3 The Polymer Segmental Dynamics

1.3.1 Experimental and simulation methods

For $T > T_g$, polymer segments cooperatively relax and reorient in the melt and their relaxation times follow Vogel-Fulcher-Tammann (VFT) behavior:

$$\tau_\alpha(T) = \tau_\infty \exp\left(\frac{B}{T-T_0}\right) \qquad (1.1)$$

where τ_∞, B, and T_0 are fitting parameters related to high temperature relaxation time, fragility, and Vogel temperature, respectively.[35] As shown in Figure 1.2, the segmental relaxation time (α-process) can be probed with a variety of experimental techniques, each of which has a unique temporal range and corresponding temperature for a given polymer.[36,54,55] Furthermore, as will be discussed in subsequent sections, each technique samples the material and population of dynamics differently.

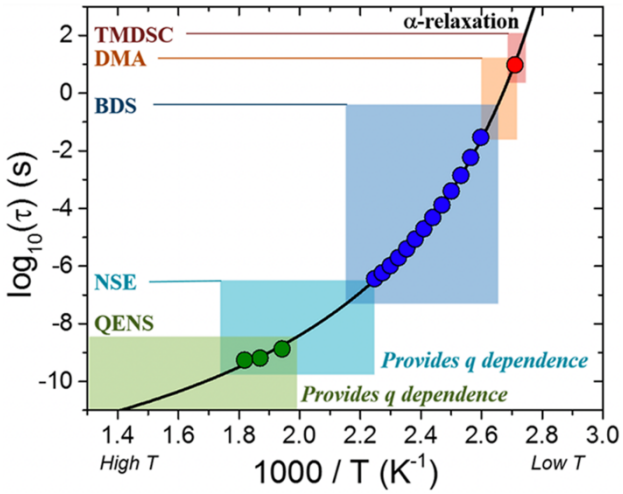

Figure 1.2: Primary segmental relaxation times (α-process) of bulk 40 kg/mol P2VP as a function of inverse temperature. Shaded regions depict the approximate time scales and their corresponding temperature scale for five techniques: temperature-modulated differential scanning calorimetry (TMDSC), dynamic mechanical analysis (DMA), broadband dielectric spectroscopy (BDS), neutron spin echo (NSE), and quasi-elastic neutron scattering (QENS). Black line represents a VFT fit for TMDSC (red circle), BDS (blue circles), and QENS (green circles) measurements of neat P2VP. Reprinted with permission from Ref 55. Copyright 2019, American Chemical Society.

When the relaxation time is slow (τ > ~1 s) at T~T_g, temperature modulated differential scanning calorimetry (TMDSC) can be used to measure segmental dynamics, as described elsewhere[54,56]. Differential scanning calorimetry (DSC) characterizes the glass transition temperature by monitoring the change in heat capacity, which reflects changes in polymer configurational degrees of freedom upon heating or cooling a polymer sample.[36] Similarly, TMDSC monitors heat capacity upon heating or cooling with a superimposed sinusoidal function to separate the reversible and non-reversible heat flows to improve sensitivity, resolution, and isolation of

overlapping transitions.[56] Although T_g is dynamically defined as the temperature at which the α-process becomes infinitely slow, it is often used as a proxy for segmental dynamics whereby an increase in T_g is attributed to slowing of the α-relaxation process.[36]

For faster dynamics ($\tau \sim 10^{-7} - 10^{0}$ s) at $T > T_g$, broadband dielectric spectroscopy (BDS) offers a broad dynamic window over which to probe molecular dynamics. As detailed elsewhere[57], BDS applies a sinusoidal electric field to the sample and precisely measures complex impedance, which is converted to dielectric permittivity, as a function of frequency of the oscillating field. Encoded in the BDS spectra are the timescales associated with reorientations of unpolarized dipole moments along or pendent to the chain as well as the movement of free ions in the sample.[57] Limitations of BDS include an insensitivity to length-scales, the requirement for a permanent dipole on the polymer, and somewhat complicated fitting[58]. Conversely, the benefits to BDS include a broad frequency range, high accuracy and precision, and a measurement of the fraction of relaxing dipoles through the integrated amplitude.

For fast segmental dynamics ($\tau \sim 10^{-11} - 10^{-6}$ s) at $T >> T_g$, inelastic neutron scattering such as neutron spin echo spectroscopy (NSE) and quasi-elastic neutron scattering (QENS) can characterize polymer segmental relaxations and, importantly, simultaneously provide length-scale information. In both measurements, the distribution of neutron energies is measured after scattering from the sample as a function of the wave vector, q. Since neutrons and molecular motions are on the μeV range, scattered neutrons gain or lose energy during a scattering event with mobile species and elastically scatter with atoms immobile on the experimental timescale.[59,60] NSE is commonly used for intermediate dynamics (Rouse) so it will be more thoroughly discussed in Section 1.4.1. For QENS, time-of-flight and backscattering approaches precisely measure the broadening of the elastic scattering peak. This dynamic structure factor, $S(q,\omega)$, is often dominated by hydrogen atoms in the sample due to their large neutron scattering cross-section and can be fit to reveal the

molecular relaxation times as a function of q. Although instrument access and data analysis can be challenging, QENS is unique in that it simultaneously probes the length- and time-scales to thoroughly study motions and allows H/D labelling to delineate inter- or intrachain dynamics.

Additional experimental techniques exist for characterizing the segmental dynamics in PNCs. Dynamic mechanical analysis (DMA) and rheology are mechanical measurements that can probe the dynamics of segments, and like NSE, can address intermediate polymer dynamics (see Section 1.4.1). Nuclear magnetic resonance (NMR) is not pictured in Figure 1.2 but can measure segmental dynamics over various timescales with various techniques.[54,61,62] Most relevant to PNC segmental dynamics are measurements of proton spin-spin relaxation times (T_2) from spin echoes pulse sequences. The proton relaxation curves are usually fit to a function comprised of several contributions for different phases of segmental mobility. Most commonly, fits are comprised of three phases: an apparently immobile glassy phase attributed to segments adjacent to the NP, a phase of reduced mobility attributed to relaxations in proximity to the NP, and a bulk-like phase attributed to free polymer segments.

Computer simulations, namely molecular dynamics (MD) simulations, are often used to probe segmental dynamics as well. In many cases, the dynamics of segments can be observed in fully atomistic MD simulations. Due to computational expense, atomistic MD simulations are often restricted to low M_w, small NPs, and short (fast) dynamics. Coarse-graining atoms into segments (or beads) and accordingly altering atomic potentials is often done to reduce simulation time and access slower dynamics and longer length-scales. A common model used to study fundamental polymer physics is the Kremer-Grest model wherein non-bonded beads interact through a pairwise Leonard Jones (LJ) potential and bonded beads interact via a harmonic spring.[63] The NP-polymer interaction in PNCs is also often modelled with an LJ potential. Generally, each bead in these simulations represents at least a few monomers and less than a Kuhn segment when compared to experiments. With a record of atom or bead coordinates as a function of time, several different

analysis routes (including bond correlations, intermediate scattering function (ISF), and mean-squared-displacement (MSD)) lead to insights regarding the timescales and mechanisms of segmental motion in atomistic and coarse-grained polymer melts.

1.3.2 Heterogenous segmental dynamics in attractive PNCs

Segmental dynamics occur over small length scales (within a few nanometers), are sensitive to the local polymeric environment, and are affected by cooperativity and local free volume. Thus, polymer melts exhibit a distribution of relaxation times in the melt state. PNCs exhibit an even broader distribution of segmental relaxation times, because spatial heterogeneities exist and dynamics near NP surfaces differ from those far from NPs. With this in mind, there are three general models used to describe dynamics in PNCs, Figure 1.3. The simplest model is the homogeneous model, where the average relaxation time measured is assumed to be the relaxation time for all segments in a PNC. The core-shell model simply has two populations of relaxations, namely those near and far from NP surfaces, the latter of which normally relax at timescales similar to bulk. Finally, the interfacial layer model is similar to the core shell model, but the transition from interfacial relaxations to bulk-like relaxations is smooth rather than stepwise, and therefore assumes some functional form. Naturally, details of the PNCs system, such as the NP-polymer interactions, NP size (R_{NP}), and NP volume fraction (ϕ_{NP}), influence which model is most appropriate to describe the population of segmental dynamics. Similarly, some measurement methods permit the use of different models whereas other methods restrict the analysis to a single model. For example, it is possible to use any model in Figure 1.3 to interpret BDS measurements of well-dispersed NPs because the broad frequency range surveys the full distribution of relaxation times. Conversely, for measurements with less precision and a smaller temporal window, the homogeneous model may be the only option due to the difficulties associated with separating multiple relaxations. We also note that heterogeneities displayed in Figure 1.3 can be observed in the form of a distribution of

relaxation times through stretching or shape parameters, most commonly in BDS and QENS using Havriliak−Negami (HN) and Kohlrausch–Williams–Watts (KWW) functions.

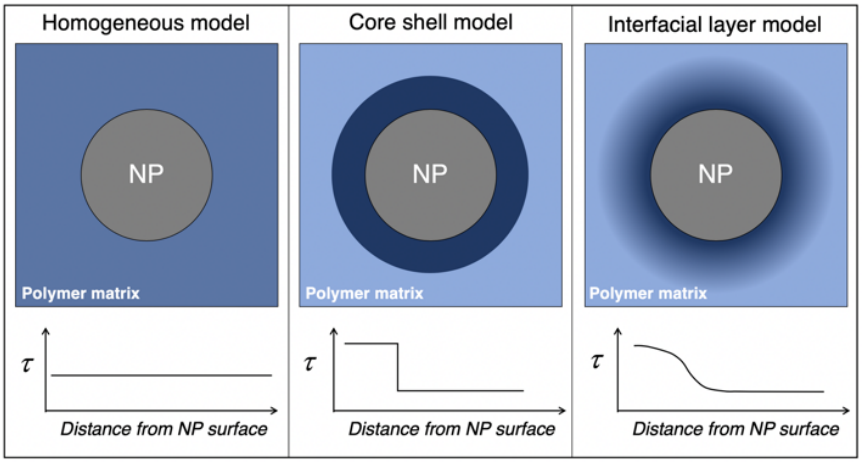

Figure 1.3: Schematic showing polymer segmental dynamics as a function of distance from a single NP. The homogeneous model (left) assumes an average relaxation time throughout the polymer matrix. The core-shell model (center) spatially separates the polymer relaxations into a slower population adjacent to the NP and another bulk-like population away from the NP surface. The interfacial layer model (right) assumes a distribution of relaxation times that decreases smoothly from the NP surface into the matrix.

At this point, it is well-established that the addition of well-dispersed attractive NPs to a polymer melt (for $R_g \sim R_{NP}$) slows segmental dynamics as a function of NP loading (i.e. NP-polymer interfacial area). To demonstrate and understand this effect, several authors have studied the model system of poly(2-vinylpyridine) (P2VP) mixed with colloidal silica (SiO_2) and measured segmental relaxations with TMDSC[64,65], BDS[65–67], and QENS[55]. In this system, hydrogen bonding between pyridine in P2VP and hydroxyls on the surface of SiO_2 NPs leads to a strong NP-polymer interaction (on the order of ~10 k_BT).[64,68,69]

Using the core-shell model and combining TMDSC, BDS, and small-angle X-ray scattering (SAXS), Sokolov and coworkers revealed a shell of slow P2VP segmental dynamics at the P2VP/SiO_2 interface.[65] A single Havriliak−Negami (HN) function[57] was unable to capture the broad distribution of α-relaxations in the PNC, so two HN functions were used and attributed to

bulk-like relaxations far from the NP surface (α_1) and slower relaxations near the NP-polymer interface (α_2). The extracted relaxation times reveal three important observations (Figure 1.4): (i) α_1 relaxations far from the NP interface are approximately bulk-like, (ii) α_2 relaxations near the NP interface are ~100 times slower than bulk, and (iii) the temperature dependence of α_1, α_2, and neat P2VP are comparable although α_2 relaxations have a slightly weaker temperature dependence.[65] Using the dielectric strength of each process as a measurement of the amount of relaxing polymer, the authors estimate a shell thickness on the order of ~4 nm, which is between the Kuhn size and R_g of P2VP and matches structural measurements from SAXS. In addition the authors observe that all segments are mobile, albeit many are slow, which is in contrast to other reports that discuss and immobile polymer layer[68,70,71]. It is worth noting that simpler and more sophisticated models have been used to describe BDS data from various PNC systems[58,66,72,73], and they all result in observations of slow interfacial relaxations within a few nanometers of the NPs. Fitting the same BDS data with a core shell model (two HN functions) results in a thinner apparent bound layer and apparently slower interfacial relaxations as compared to fitting with the interfacial layer model, but both qualitatively show slow interfacial dynamics.[73]

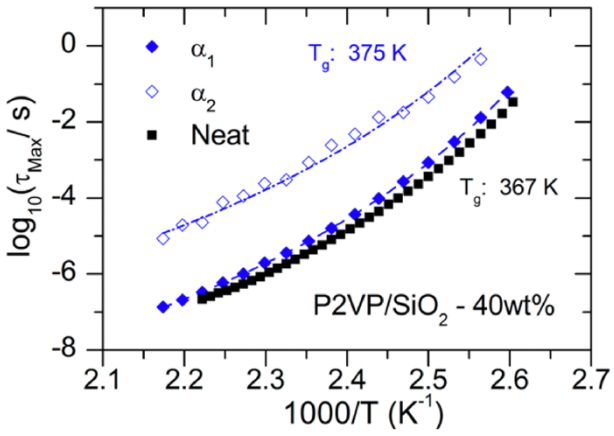

Figure 1.4: Mean molecular relaxation time (τ_{Max}) as a function of inverse temperature for neat poly(2-vinylpyridine) (black) and P2VP segments in P2VP/SiO_2 PNCs (ϕ_{NP} = ~26 vol%, blue).

Relaxation times in the PNC are separated and plotted as interfacial relaxations (blue open symbols) and bulk-like relaxations (blue filled symbols). Reprinted with permission from Ref 65. Copyright 2014, American Chemical Society.

Similarly slow dynamics have been measured in P2VP/SiO_2 nanocomposites using TMDSC[64,65,74] and QENS[55]. The simplest analysis of TMDSC assumes a single glass transition like the homogeneous model[64], but more detailed analysis reveals high temperature broadening (i.e. slower dynamics)[65] and even can lead to extraction of an interfacial layer thickness commensurate with BDS[73,74]. QENS measurements on neat P2VP showed diffusive motions ($\tau \sim q^{-2}$) for length- and time- scales of ~1 nm and ~1 ns, which agreed with extrapolations of the α-process from TMDSC and BDS in neat P2VP (Figure 1.2).[55] In P2VP/SiO_2 PNCs these relaxations occurred with a similar q-dependence but at slower timescales than bulk and timescales monotonically decreased with NP loading (i.e. NP-polymer interfacial area).[55] This result implies, at least preliminarily, that segments are perturbed temporally more than spatially.

This case study of segmental dynamics in P2VP/SiO_2 PNCs demonstrates the sensitivity of experimental observations to the measurement technique, data interpretation, and measurement conditions, although this is not specific to the P2VP system. Each experimental technique has different sensitivities, dynamic ranges, and probes the population of relaxation times differently, all of which may lead to distinct experimental observations. For example, TMDSC fundamentally measures the freezing out of modes of motion near T_g, and samples all segments evenly.[29,56,75] In contrast, QENS is measured at $T>>T_g$, fundamentally measures the incoherent dynamic structure factor, and it's sampling is nontrivial.[55,76,77] In general, extreme care should be used when comparing different PNC systems and measurement techniques. Nevertheless, subsequent sections aim to compare the effect of different PNC parameters using a combination of experimental methods, material systems, and simulations.

Finally, it is worth noting that several reports have suggested analogies between polymer nanocomposites and thin film confinement[50,68,78–80], polymer confined to nanopores[26,31,81–83], and

intercalated systems[23,24,84]. In thin polymer films for example, T_g can change drastically as a function of film thickness (up to ~100 nm) depending on the substrate-polymer interaction and the presence of a free surface.[85–87] The most realistic comparison here is between PNCs with strong confinement, i.e. where the interparticle distance (ID) is smaller than the chain size ($2R_g$), and thin films capped on both ends by a rigid substrate.[31,36] However, the role of NP curvature and the subsequent heterogenous levels of confinement between spherical NPs in PNCs cannot be ignored.[80] Nevertheless, several concepts demonstrated and learned in thin films, as well as infiltrated nanopores and PNC systems with silicates, can be extended this discussion and vice versa.

1.3.3 Effect of polymer attributes

Several inherent parameters to the polymer can affect the dynamics in PNCs and the perturbation imposed by the NPs, including but not limited to molecular weight, polymer stiffness, and polymer architecture. This section reviews how changes to these properties affect the segmental dynamics in PNCs.

Although segmental dynamics in neat polymer are nearly independent of M_w for $M_w >> M_0$, the substantial presence of interfaces in PNCs and the relative size of the NPs leads to different perturbations based on matrix molecular weight. Detailed BDS and TMDSC measurements on poly(vinyl acetate) (PVAc)/SiO_2 and P2VP/SiO_2 PNCs found the magnitude that segmental dynamics were slowed relative to neat polymer and the length-scale over which they were perturbed increased with decreasing M_w.[73] In other words, the perturbation imposed by the NPs was stronger with low M_w polymer as compared to large M_w. These authors describe this behavior in terms of interfacial packing and bound layer density, as supported by SAXS, spectroscopy, and mass density measurements[69,73], Figure 1.5. Specifically, low molecular weight polymers are proposed to adsorb more densely (forming more trains than loops or tails) as compared to higher molecular weight.

This difference in polymer conformations leads to more adsorbed segments and more suppressed dynamics in PNCs with lower molecular weight. In addition, the dynamic interfacial layer (DIL) defined by slow interfacial dynamics and bound loop layer (BLL) as defined by structural measurements are similar for low M_w, while the BLL is thicker than the DIL for high M_w. A similar molecular weight effect was observed in other experiments as well.[39,55,88] In contrast, NMR studies on segmental dynamics in polyethylene glycol and SiO_2 PNCs observed a weak M_w-dependence where the fraction of slow segments increased with M_w[89] or remained the same[70]. These differences could be attributed to weaker polymer-NP interactions or other experimental system-specific parameters.

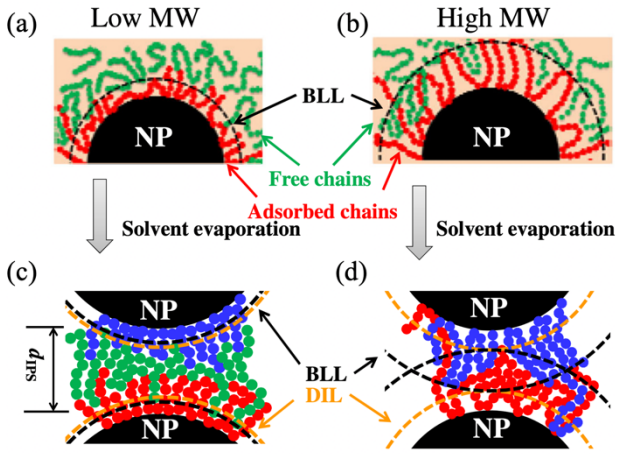

Figure 1.5: Schematic representation of the MW effect in PNCs with attractive NP-polymer interactions. (a) and (c) Nanoparticles in polymer solutions with free (green) and adsorbed (red) chains. (b) and (d) polymer nanocomposites formed by solvent evaporation with free (green) and adsorbed (blue and red) polymers. For PNCs with low M_w, the bound chains are compact resulting in a similar BLL (bound loop layer) and DIL (dynamic interfacial layer) and overall slower segmental dynamics as compared to PNCs with higher M_w which exhibit larger BLL than DIL. Adapted with permission from Ref 73. Copyright 2016, American Physical Society.

It remains unclear if the structure and polymer conformations proposed in Figure 1.5 are at equilibrium or kinetically trapped and therefore depend on PNC processing. In fact, the bound layer thickness and fraction of immobilized segments were recently measured via NMR in

PEO/SiO_2 PNCs fabricated from different solvents.[70] PNCs fabricated from a poor solvent (ethanol) produced more adsorbed segments and a thicker bound layer than those fabricated from a good solvent (water) and this effect was observed at two molecular weights.[70] These measurements show that the bound layer structure and dynamics depend on the processing conditions, indicating the polymer chains and PNCs in general are not at a global equilibrium state in the melt. Interestingly, the M_w-effect captured in Figure 1.5 persisted after annealing for ~10^{14} τ_α, meaning the effect (if not at equilibrium) is long-lasting and thermally stable.[73] However, in another study of P2VP/SiO_2 PNCs, a similar M_w-dependence was observed in TMDSC ($T \sim T_g$), while only a modest M_w-dependence was found in QENS ($T >> T_g$).[55] More measurements are needed to determine if these differences are the result of relaxations toward equilibrium at sufficiently high temperatures, differences in the bound layer as a function of temperature, or simply differences in precision and uncertainty in the different techniques.

Next, we consider matrix-free PNCs comprised of only polymer grafted NPs and specifically consider the molecular weight dependence.[46,88,90–92] One may expect grafted polymer chains to have reduced mobility compared to neat polymer because one end of the chain is covalently bonded to the NP surface and therefore immobile. In fact, grafted PS[90] and P2VP[88] chains have higher T_g (slower dynamics) than neat polymer of the same M_w. Shorter grafts exhibit larger differences relative to neat PS in the breadth of the glass transition, the step in heat capacity (ΔC_p), and fragility because a larger fraction of the chain is near the surface.[90] However, the NP concentration in matrix-free PNCs (and NP-NP separation distance) depends on the M_w of the grafted polymer, the surface grafting density (σ_{graft}), and the NP size, thus complicating comparisons. As such, it is important to consider the conformations of the grafted chains that lead to non-monotonic behavior with M_w.[5,46,88] For example in P2VP/SiO_2 matrix-free PNCs measured by BDS, segments from low M_w P2VP grafts are slower than bulk because each segment resides

near a NP and chain stretching impedes relaxations but high M_w grafted P2VP exhibit bulk-like relaxations because most segments are far from the NP surface and interfacial effects are less significant.[88] In PMA/SiO_2 matrix free PNCs measured by QENS and assuming a jump diffusion model, segmental diffusion is faster than bulk for all M_w, consistent with increased free volume.[46] Interestingly, the fastest relaxations are measured at intermediate M_w, which are long enough for chains to begin to interdigitate with neighboring NPs and short enough so that the majority of segments are still near NP cores.[46] In matrix-free PNCs of grafted NPs more generally, it is important to consider the brush conformations as a function of M_w, σ_{graft}, and R_{NP} because different dynamics are expected for different conditions. Systematic studies showing these complicated effects are necessary but remain synthetically and experimentally challenging.

Another polymer characteristic that has a profound effect on segmental dynamics in PNCs is the chain stiffness, likely because it strongly affects interfacial packing. In coarse-grained MD simulations, the polymer chain stiffness was controlled by adjusting bending potential (without changing other polymer or PNC parameters) and the dynamics were measured near a flat attractive substrate which simulates an infinitely large NP.[93] The segmental dynamics of chains near the interface were slower than bulk but the degree of slowing and length scale over which chains were perturbed both increased for stiffer chains.[93] Isolating the chain stiffness experimentally is challenging because changing the polymer chemistry also changes the NP-polymer interaction, a variable discussed in Section 1.3.5. Nevertheless, Sokolov and coworkers probed the DIL in SiO_2 PNCs with polypropylene glycol (PPG), PVAc, P2VP, and literature data to reveal qualitatively similar dependencies as simulations.[74] This result suggests that the structure and dynamics of the interfacial polymer layer are impacted by the persistence length and cooperativity of the polymer. More simulations and experiments could further develop the understanding of this relationship.

1.3.4 Effect of filler attributes

A common parameter to study in PNCs is the relative amount of polymer and filler, which effectively increases the NP-polymer interfacial area. In addition, in certain PNC systems especially at sufficiently high NP concentrations, NP-NP aggregation and polymer bridging between adjacent NPs produce non-trivial effects on segmental dynamics. The case of NP aggregation can often be considered in terms of the matrix-accessible NP-polymer interfacial area because aggregated NPs have considerably less accessible surface area (per unit volume NP) than individually dispersed NPs. As a result, segmental dynamics are generally less perturbed in aggregated PNCs compared to those with the same volume fraction of individually dispersed NPs.[71,94,95]

In PNCs with spherical NPs that are individually and randomly well-dispersed in a polymer melt, the interparticle separation distance (ID)[96] can be expressed as:

$$ID = d_{NP}\left[\left({}^{2}/_{(\pi\phi_{NP})}\right)^{1/3} - 1\right] \qquad (1.2)$$

When ID approaches the chain size (~$2R_g$) polymer bridging between adjacent NPs is observed in simulations and experiments, mainly through mechanical measurements.[39,40,97–101] Although isolating the segmental dynamics in bridging chains is difficult, the segmental dynamics are expected to be more perturbed than non-bridging chains.[39,99] When ID is further reduced toward the Kuhn length of the polymer segments (b), all of the polymers in the PNC are effectively interfacial. For NPs on the order of or larger than 10 nm, this level of confinement (ID~$2R_g$) is difficult to achieve except through unique processing routes[18,102–105], grafted and matrix-free PNCs[106], underfilling[72], layered NP systems, or solvent washing[88,107]. Large changes in T_g measured via ellipsometry[104,105] and segmental dynamics measured via BDS[72,88] have been reported in highly loaded PNCs, but these measurements are challenging due to low signal-noise-ratios.

Another critical parameter of the filler that affects segmental dynamics is the NP size. Note that decreasing the NP size at a fixed NP concentration and random dispersion state increases the NP-polymer interfacial area and decreases ID. Since segmental dynamics are often perturbed at the NP-polymer interface, this implies that smaller NPs will affect more segments in the PNC. Profound differences in segmental dynamics were observed by comparing P2VP filled with SiO_2 NPs ($2R_{NP} \sim 2R_g$) to P2VP filled with octaaminophenyl polyhedral oligomeric silsesquioxane (OAPS, $2R_{NP} \sim b$), both of which exhibit favorable NP-polymer interactions, Figure 1.6.[108] In PNCs with small NPs, increasing ϕ_{NP} increased T_g considerably (reaching ~35 K higher than bulk), while ΔC_p remained unchanged and the fragility of τ_α increased.[108,109] In contrast, PNCs with larger NPs exhibited only weak increases in T_g and fragility and exhibited a linear drop in heat capacity with increased ϕ_{NP}.[108] These results, supported by corresponding simulation and theory, suggests that small NPs slow segmental relaxations more uniformly, participate in the relaxation process, and perturb segmental dynamics more strongly than larger NPs. However, it should be noted that comparing SiO_2 NPs ($2R_{NP} \sim 25$ nm) and OAPS ($2R_{NP} \sim 1.8$ nm) is extreme. As will be discussed in future sections (including Section 1.6.4), the OAPS NPs are mobile on the timescale of polymer relaxations so the contrast between P2VP/SiO_2 and P2VP/OAPS likely reflects the mobility of the NPs rather than the effect of only NP size and curvature.[109]

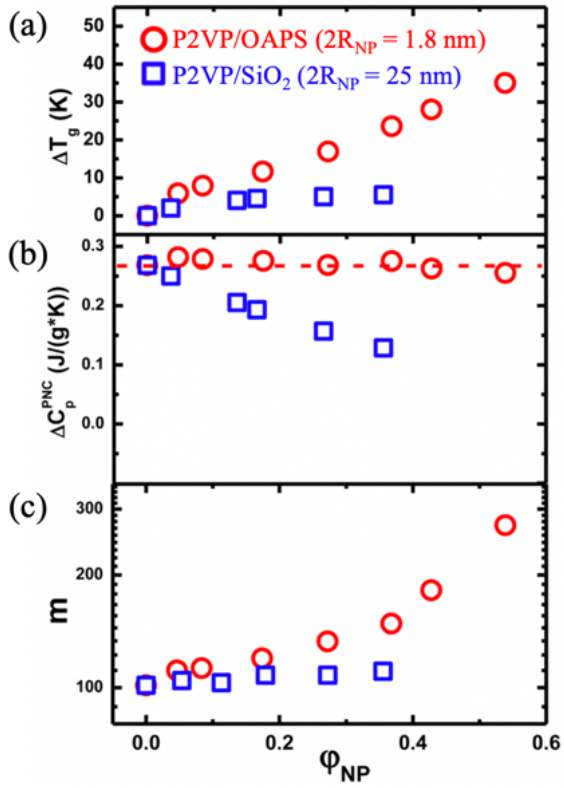

Figure 1.6: Effect of NP size in P2VP PNCs with SiO_2 NPs (blue, $2R_{NP}$ = 25 nm) and octaaminophenyl polyhedral oligomeric silsesquioxane (OAPS) (red, $2R_{NP}$ = 1.8 nm) as a function of NP volume fraction. (a) Changes in glass transition temperature, $\Delta T_g = T_{g,PNC} - T_{g,bulk}$, (b) magnitude of the step in heat capacity from TMDSC, and (c) fragility. Adapted with permission from Ref 108. Copyright 2017, American Chemical Society.

Few studies have isolated the role of NP curvature on segmental dynamics, i.e. systematically changing NP size within the regime of $2R_{NP} > b$. In a study of P2VP/SiO_2 PNCs with NP diameters ranging from 7 to 50 nm, the bound layer thickness extracted from BDS measurements only slightly increased from 1 to 4 nm.[66] Unfortunately, relaxation dynamics were not reported. Starr and coworkers performed coarse-grained MD simulations of a single facetted icosahedron NP in a melt of low molecular weight polymer to also probe the role of NP size. Here, the segmental relaxations at the interface of a larger NP are slower than near a small NP.[80,99] These authors argue that the relevant parameter to describe changes in T_g is ID relative to

R_g, because this captures the convoluted influence of ϕ_{NP} and R_{NP} and defines the amount of interfacial polymer in the PNC.[99] The infinite limit of NP size is a flat substrate and these comparisons have been provided.[50,78–80] Still, a universal understanding of how NP size and NP curvature impacts the glass transition and segmental dynamics in PNCs remains elusive, especially experimentally. A combined study that systematically varies NP size (R_{NP}), chain size (R_g), and NP concentration (ϕ_{NP}) may help characterize the roles NP size relative to ID.

In regard to the shape of the nanoparticle filler, experimental efforts are scarce with the notable exception of carbon-based NPs and clays. Complications include limited availability of non-spherical NPs and changes in NP-polymer interaction with changes in shape. However, we anticipate NP shape to impact segmental dynamics primarily through changes in the local interfacial packing, local radius of curvature, and amount of polymer-accessible interface. Isolating and deconvoluting these effects remains an experimental challenge.

1.3.5 Role of NP-polymer interaction on interfacial dynamics

When a polymer is adjacent to a solid interface, such as a NP, the segmental dynamics are affected by several interrelated factors including the differences in density[69,73,80], perturbed polymer conformations[79,110], and the energetics at the interface. Regarding the energetics of a polymer at a NP surface, there is an enthalpic component that characterizes the NP-polymer affinity and an entropic one which characterizes the conformation of free chains near the NP surface. Modulating the NP-polymer interaction enthalpy (through chemical modifications or material selection) or entropy (through interfacial softness or grafting polymer chains to the NP) typically changes other important parameters and therefore complicates experimental comparisons. For example, it is known that the NP-polymer dispersion state depends intimately on the NP-polymer interaction[9,12,97] so it is difficult to deconvolute changes in segmental dynamics from changes in NP-polymer interfacial area. In addition, changing the NP-polymer interaction through materials selection is

often accompanied by changes in other important parameters including solvent quality during preparation, chain stiffness, and NP dispersion state.

While many experiments have tried to explore the role of the NP-polymer interaction through altering the NP[84,111–116] or the polymer[64,117], the resulting PNCs frequently have different NP dispersion states and consequently different accessible interfacial area at fixed ϕ_{NP}. In a thorough study of NP dispersion and glass transition using an array of surface-modified silica and different polymers, Schadler and coworkers argued that NP-polymer energetics and work of adhesion can predict dispersion state of NPs in the melt, as well as the direction and magnitude of T_g changes.[118] Reasonable NP dispersion is achieved when the polymer-NP interaction exceeds the NP-NP interaction and the relative work of adhesion is minimized. In systems with similar dispersion states (characterized by TEM), stronger NP-polymer interactions result in a larger increase in T_g.[118] Measurements of segmental dynamics (rather than the vitrification process) or other characteristics of the bound layer are mostly unreported and present a worthwhile future direction. One way to access interfacial dynamics at repulsive interfaces while circumventing aggregation in PNCs is using infiltrated polymer in nanopores with well-characterized surfaces. For hydrophobic poly(ethylene-alt-propylene) (PEP) infiltrated into hydrophilic anodic aluminum oxide (AAO) nanopores, bulk-like segmental dynamics were measured using neutron scattering.[83] In comparison, hydrophilic polydimethylsiloxane (PDMS) in hydrophilic AAO nanopores (an attractive interaction) displays segmental dynamics slower than bulk.[82]

MD simulations of an isolated NP in a polymer melt offer the unique ability to tune NP-polymer interaction without changing other parameters or causing NP-NP aggregation. For example, by extracting the segmental relaxation time as a function of distance from the NP surface for a variety of NP-polymer interactions, Starr and coworkers (Figure 1.7) showed slower interfacial relaxations for attractive NPs ($\varepsilon>1$) and faster interfacial relaxations for repulsive NPs

(ε<0.5).[119] The surface relaxation (inset of Figure 1.7) reveals surface dynamics between 10^2 times faster and 10^4 times slower than bulk depending on the NP-polymer interaction, with the crossover for bulk-like being slightly more repulsive than athermal. This crossover may indicate an unfavorable entropic effect or an effect of local ordering.[119] This profound effect of NP-polymer interaction on local dynamics is consistent with other simulation results[120–124] but mostly undocumented in experimental PNCs. Interestingly, bulk-like segmental relaxations are recovered after ~3σ, or ~ 3 nm in experimental units, from the NP surface regardless of NP-polymer interaction parameter.[119] Other simulations have shown similar effects.[29,79,121]

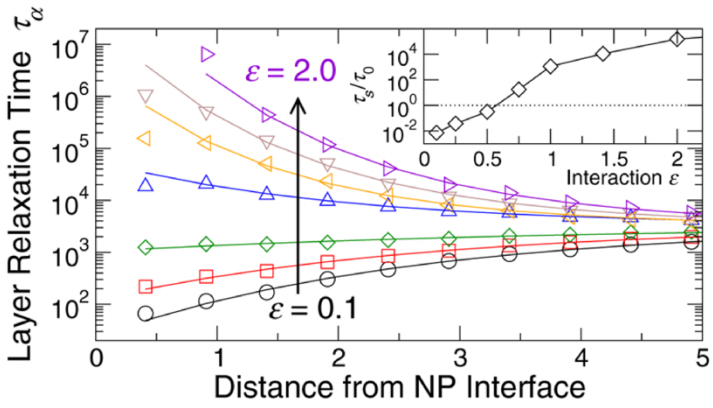

Figure 1.7: Segmental relaxation time for ε = 0.1, 0.25, 0.5, 0,75, 1.0, 1.4, and 2.0 as a function of distance from the NP surface. Inset shows surface segmental relaxation time (normalized to that of bulk) as a function of interaction strength. Reprinted with permission from Ref 119. Copyright 2016, American Chemical Society.

For systems that exhibit hydrogen bonding, such as PNCs comprised of any hydrophilic polymers and SiO_2 NPs, temperature may impact the NP-polymer interaction. Specifically, the relaxation time of adsorbed segments is likely related to the activation energy of the hydrogen bond (relative to kT) and the attempt frequency (related to the bulk relaxation time), both of which are temperature dependent. NMR measurements as a function of temperature showed the measured bound layer thickness in various PNCs decreased with increasing temperatures; unfortunately, measurements of the relaxation time in that bound (glassy) layer were inaccessible.[125,126] Thinner

dynamic bound layers were also observed with BDS as temperature increases in a variety of materials.[74,123] As discussed in regards to Figure 1.4 and Figure 1.6, BDS measurements observe only a weak change in fragility upon the addition of NPs with $2R_{NP} > b$.[65,108] This result may indicate that the NP-polymer interaction is not significantly changed over this temperature range. For $2R_{NP} \sim b$, differences in fragility as T approaches T_g may reflect the frustrated packing during the vitrification process rather than segmental relaxation at higher temperatures[108], meaning the dependence on NP-polymer interaction remains unclear. To access a broader range of temperatures, multiple experimental methods with overlapping temperature ranges is optimal, Figure 1.2.[54,55,76,77]

Finally, the role of NP-polymer interaction has also been studied by comparing the segmental dynamics of physically adsorbed chains to those that are covalently grafted to the surface.[62,88,91,92,125,127] For example, Sokolov et al. compared P2VP/SiO_2 PNCs of the same ϕ_{NP} and molecular weight wherein the P2VP was grafted to the NP (a matrix-free PNC) or physically adsorbed to the NPs (a traditional PNC).[88] Using BDS along with other techniques, they measured the α-relaxation[88] and β-relaxation[127] as a function of M_w. One of their main conclusions is that the degree of chain stretching in the interfacial layer critically affected the segmental dynamics. For low molecular weight systems, P2VP matrix-free and traditional PNCs exhibit similar interfacial dynamics while for intermediate M_w, where grafting induces chain stretching, the primary segmental relaxation dynamics in matrix free PNCs are slower than in traditional PNCs.[88] Other studies using BDS and NMR have also revealed slower α-relaxation dynamics for covalently bonded polymers to NPs as compared to physically adsorbed chains.[91,125] Note that secondary segmental relaxations (β-process) in the glassy state sometimes behave differently. For example, in the aforementioned P2VP/SiO_2 matrix-free PNCs, secondary relaxations are faster relative to bulk while adsorbed chains in traditional PNCs are more bulk-like[127]. This observation and others[92,128] highlight the decoupling between α and β processes and the many parameters, such as

chain stretching and local free volume, that affect the two differently. The use of polymer-grafted NPs adds variables to the already expansive parameter space for PNCs and more research investigating different regimes of R_{NP}, σ_{graft}, and graft M_w will help develop a thorough understanding of relaxations within the polymer brush in PNCs.

1.4 Intermediate Polymer Dynamics

1.4.1 Experimental and simulations methods

Intermediate polymer dynamics, also called Rouse dynamics in the melt[35], involve relaxations associated with chains of segments and are therefore slower than segmental dynamics (Section 1.3) and faster than the center-of-mass polymer diffusion (Section 1.5). The exact delineation between segmental dynamics and intermediate dynamics can sometimes be unclear, but we consider intermediate dynamics to be the collective motion of several segments. Experimentally, these intermediate dynamics are primarily measured using neutron scattering and rheology. MD simulations are insightful as well. Due to the limited experimental techniques and because these cooperative motions are often complicated to analyze, progress on understanding intermediate dynamics is comparatively slow, especially with respect to the dense parameter space presented by PNCs.

In unentangled polymer melts, the Rouse model describes the relaxation dynamics of chains with p-sized chains and can be extended to the full chain ($p \leq N$).[35] When the degree of polymerization (N) exceeds the degree of polymerization between entanglements (N_e), the Rouse model describes relaxations within entanglement strands. However, larger scale dynamics ($p>N_e$) are considered confined to a tube formed by entanglement nodes, according to the Edwards tube model.[35] Clearly, intermediate dynamics are intimately tied to the entanglement network. In PNCs,

the polymer entanglements are perturbed by the presence of NPs, so measurements of these intermediate dynamics can provide insight into entanglements as well as the dynamics.

Rheology is a dynamic mechanical measurement that measures the complex modulus (often shear, G' and G") as a function of frequency, usually with a polymer melt placed between parallel plates. For a neat polymer melt at shearing frequencies longer than the slowest characteristic relaxation of the polymer, the terminal flow regime is reached where $G' \sim \omega$ and $G'' \sim \omega^2$. At faster shearing frequencies, the frequency-dependent moduli changes with the dynamics in the sample, thus giving insight into intermediate dynamics. The addition of NPs often stiffens the polymer melt and usually introduces additional dynamic processes, such that extracting polymeric relaxation times from linear viscoelastic measurements of PNCs is difficult, especially at high NP concentrations[40] and for poorly dispersed systems[129]. In many cases, the rheological spectra can reflect NP-polymer interactions, dynamics of the NPs, and heterogeneous dynamics of free polymers, and deconvoluting these contributions is arduous.[130]

Inelastic neutron scattering methods, QENS and NSE, can access intermediate polymer dynamics more directly. For sufficiently flexible polymers with small Kuhn segments measured at $T >> T_g$, QENS can measure Rouse dynamics. For example, QENS of polyethylene oxide (PEO, b = 0.6 nm) shows $\langle r^2 \rangle \sim t^{1/2}$, characteristic of Rouse dynamics.[131] However, QENS experiments on PS[37] and P2VP[55] (both with b ~ 2 nm) reveal various geometries of motion, but are generally incapable of accessing Rouse length- and time-scales. In NSE, the change in velocity of incident and scattered neutrons, which is related to the transfer of energy of the scattering event, can be precisely measured for a variety of q by monitoring neutron spin before and after the scattering event through Larmor precession.[60] NSE offers a wave vector range of $\sim 10^{-3}$ – 1 $Å^{-1}$ (length scales of ~0.6 – 600 nm) and energy range of $\sim 10^{-1}$ – 10^{-6} meV (timescales of $\sim 10^{-11}$ – 10^{-6} s) and, thus, NSE is a powerful tool for probing intermediate polymer dynamics in PNCs. The normalized

intermediate scattering functions, ISF or I(q,t), are directly obtained in NSE, and can be readily fit to system-specific functions including the Rouse model and reptation model. NSE requires specialized instrumental access available at global user facilities, necessitates collection times on the order of days per sample, and samples are often comprised of majority deuterated polymer.

Due to the complexity of dynamics of chains and chain segments, MD simulations are also useful to probe intermediate dynamics. In simulations, Rouse analysis can comprehensively extract the timescales associated with various sections of the chain (Rouse mode analysis) to further understand the relaxation mechanism. In addition, simulations access various parameters associated with the entanglement network via primitive path calculations that provide entanglement densities and visualizations of the Edwards tube in melts and PNCs.[132–134] Although the average tube diameter can be measured in NSE and the molecular weight between entanglements can be estimated from rheology, simulations provide unique insights about spatial heterogeneities and locations of the entanglements in PNCs.

1.4.2 Intermediate dynamics in PNCs

Measurements of the full rheological spectrum in PNCs usually explore up to three key relaxations: the relaxation time of a Rouse monomer (τ_0, on the order of b), the relaxation of the entanglement strand (τ_e for $N/N_e > 1$), and the terminal relaxation time (τ_t, on the order of R_g). The Rouse monomer relaxations, also called the elementary relaxations, measured by rheology are similar to measurements from BDS, while τ_e and τ_t relaxations are usually inaccessible to techniques discussed in Section 1.3.1. Several authors have made thorough rheological measurements to probe microscopic dynamic processes, but most suffer from gel-like PNC responses at high NP concentration[67,117,131,135–138], with a few exceptions.[108,139] For example, by forming rheological master curves referenced to the T_g of PNCs comprised of PEG-grafted SiO_2

and PMMA, measurements of τ_0, τ_e, and τ_t revealed a monotonic increase in each relaxation time with the addition of NPs, indicating slowing across these length-scales.[139]

Rheology also provides measurements of viscosity that characterize how PNCs flow and provide insight related to intermediate and chain dynamics. The literature about viscosity in nanoparticle-filled polymers is expansive. Several parameters are known to affect the viscosity of PNCs, including NP-polymer interaction, polymer M_w, ϕ_{NP}, and NP size. Both increases[67,138,140–144] and decreases[139,140,145] in viscosity have been observed in PNCs, indicating complex and often competing effects of different variables. For large NPs in short polymers, the Einstein-Batchelor law[146] describes the increase in viscosity as a function of ϕ_{NP}:

$$(\eta_{PNC}/\eta_{bulk} = 1 + 2.5\phi_{NP} + 6.2\phi_{NP}^2) \qquad (1.3)$$

The viscosity increases above the prediction in Equation 1.3 with strong NP-polymer attractions.[142–144] Decreased viscosity relative to bulk has been observed particularly in high M_w polymer filled with athermal or small NPs.[139,140,145] Kumar and coworkers proposed a "universal" behavior for viscosity in athermal and attractive PNCs by considering only polymer M_w and NP size.[147] While this treatment captures many experimental studies and serves as a zeroth-order description of viscosity deviations from bulk, it fails to capture some experimental results and remains to be fully tested with a more expansive set of materials and parameters. These results (and other rheological measurements) imply that mechanical measurements and viscosity are complex functions of several variables and dynamic processes that synergistically affect stress relaxation behavior.

We next discuss more direct measurements of intermediate dynamics through neutron scattering. For example, PEO-based PNCs with different NP-polymer interactions were probed using QENS and NSE. The PNCs contained either bare SiO_2 NPs or SiO_2 NPs coated with polymethyl methacrylate (PMMA) and dispersed in PEO.[141] Interestingly, the QENS broadening

for PEO-SiO_2/PMMA matches bulk PEO, while the QENS broadening is narrower for PEO-SiO_2/bare systems, indicating slower PEO intermediate dynamics (Figure 1.8).[141] In both sets of PNCs, after the Fourier transformation of S(Q,ω) and using the relation $S(q,t) = \exp\left[-{q^2}/{6}\langle r^2(t)\rangle\right]$, Rouse scaling is observed where $\langle r^2(t)\rangle \sim t^{1/2}$.[141] The authors attribute the decreased $\langle r^2(t)\rangle$ and reduced Rouse parameter (Wl^4) to PEO adsorption to SiO_2, because this analysis inherently assumes a homogeneous model (Figure 1.3). Complimentary NSE measurements on these PNCs revealed similar dynamics at short times. At long times, disentanglement was observed in the PEO-based PNCs with glassy PMMA-coated SiO_2, while the entanglement network was largely unperturbed in the other PNCs studied.[141] These neutron measurements provided a microscopic view of segmental and intermediate dynamics in PNCs with different interactions, although the PMMA-mediated NPs introduce additional interfacial complexities that remain largely unknown.

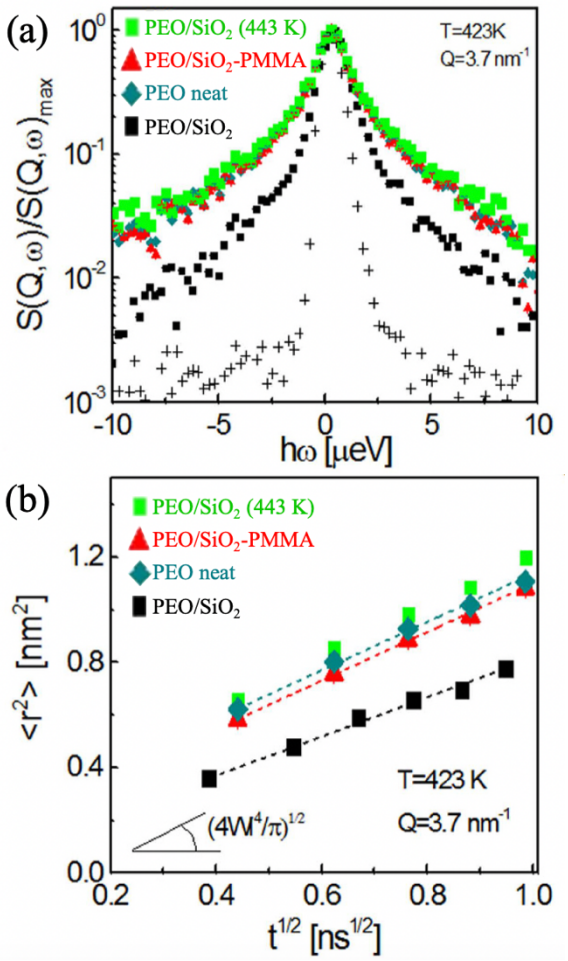

Figure 1.8: Incoherent dynamic structure factor (top) and mean square displacement (bottom) of PEO in neat PEO (teal) and PEO-based PNCs composed of PMMA-coated SiO_2 (red) and bare SiO_2 (black) at T=423 K and bare SiO_2 in PEO at T=443 K (green). All PNCs were filled with ϕ_{NP} = 17.6% (core only). Adapted from Ref 141.

In another set of measurements on low M_w PEO/SiO_2 PNCs, the interfacial interactions were altered by the polymer end group.[77] Although Rouse dynamics were slowed in these PNCs relative to neat polymer, OH-terminated chains exhibited a larger perturbation than CH_3-terminated chains, showing that attractive interactions even at the chain ends slow Rouse dynamics in PNCs.[77] In a largely non-attractive set of PNCs, Richter and coworkers studied dynamics of PEP segments and chains in PNCs with SiO_2 NPs.[148,149] In these PNCs, the Rouse dynamics were unperturbed relative to bulk, even at high ϕ_{NP} (~60 vol%) and the population of dynamics within the PNCs

remained bulk-like. Using these cases as examples, the NP-polymer interactions certainly affect intermediate dynamics and in many cases, insights from segmental dynamics can be extended to Rouse dynamics for $p < N_e$.

The intermediate dynamics of polymers grafted to NPs has also been measured in a few contributions and much remains unknown.[92,128,150] In general, confined dynamics are observed as the grafted-chains restrict Rouse motion of adjacent chains and the presences and magnitude of this effect depends strongly on grafted M_w, σ_{graft}, and R_{NP}.[27,33] In matrix-free PNCs, polyisoprene segmental dynamics were found to be relatively unperturbed until large enough Rouse length-scales where grafted chains interacted with adjacent grafts and were slowed relative to bulk.[92] Upon the addition of matrix chains forming a traditional PNC, the topological constraint was reduced.[92] In solutions of SiO_2 NPs with selective isotopically labelled polymer grafts studied by NSE, slow Zimm dynamics (akin to Rouse dynamics in the melt) were observed near the polymer interface but faster dynamics were observed far from the NP surface.[150] Understanding the heterogenous dynamics within the polymer brush on NPs in the melt and documenting the dependence on various PNC and NP variables is critical to understanding PNCs with grafted NPs.

The effect of NP size has also been measured on Rouse-like time scales. Using NSE to study PEO-based PNCs with PEG-functionalized 3-nm and 20-nm gold NPs (an athermal system), Faraone and coworkers showed Rouse dynamics were comparable to neat PEO and largely unaffected by NP size.[131] Whether this NP size-independent observation holds for attractive interactions or higher NP concentrations remains to be explored. In a combined QENS and NSE study, poly(vinyl methyl ether) (PVME) was filled with glassy polystyrene-based NPs of different M_w.[151] The Rouse dynamics of PVME in these PNCs were slower than bulk and the slowing was independent of PS architecture (linear or star) or M_w according to QENS.[151] NSE measurements also showed slower collective PVME dynamics in the PNCs and, interestingly, revealed a

difference between the PS NPs from linear and star polymers. The authors attribute this effect to geometric confinement that was only apparent at the longer length-scales accessible to NSE.[151]

Using MD simulations, the effect of NP concentration[152], NP size[153–155], and NP-polymer interaction[153,156] on Rouse dynamics was probed. At low ϕ_{NP}, coarse-grained MD simulations show the local Rouse dynamics are largely unperturbed although the disentanglement time gets faster.[152] At high ϕ_{NP} (at least 31 vol%), NPs become confining to the Rouse motion and disentanglement time and local relaxations begin to slow down.[152] In a thorough study of Rouse relaxation in athermal PNCs, Rouse relaxations were faster in PNCs with small NPs ($R_{NP} < d_{tube}$) and largely unaffected in PNCs with larger NPs.[155] In general, it is reported that Rouse dynamics over different length-scales are more perturbed in PNCs with favorable NP-polymer interactions.[153,156]

1.4.3 Entanglement network in PNCs

Entangled polymers at intermediate timescales are confined by the entanglement network in the polymer melt. As a result, at timescales beyond Rouse relaxations, a long-time plateau is observed in S(Q,t) from NSE and an entanglement plateau is observed in rheology as segments cannot relax beyond topological entanglements. This entanglement network is described by a confining tube in the Edwards model. Given enough time, polymer chains will escape their confining tube or the entanglement network will relax, leading to chain diffusion discussed in Section 1.5. However, measurements of intermediate dynamics in polymer melts gives insights into the entanglement network.

To understand how spherical NPs perturb the entanglement network, Richter and coworkers measured NSE on poly(ethylene-alt-propylene) (PEP) based PNCs as a function of hydrophobic-SiO_2 NP concentration and fit S(Q,t) at long times to extract the tube diameter, Figure 1.9.[149,157]. As ϕ_{NP} increases from bulk (black) to 60% (purple), polymer chains become more confined and the apparent tube diameter, d_{app}, decreases.[149] Importantly, this PNC system exhibits

reasonable NP dispersion, unperturbed local segmental dynamics and Gaussian polymer conformations as measured by TEM, NSE, and small angle neutron scattering (SANS), respectively.[149,157] To understand the decrease in the d_{app}, the authors define "particle entanglements" to describe the impact of geometric confinement imposed by the NPs (d_{geo}) by estimating the void distribution function. With knowledge of d_{app} and d_{geo}, the tube diameter associated with only the polymer matrix (d_{tube}) can be evaluated by assuming Gaussian statistics and is found to increase significantly with ϕ_{NP}, Figure 1.9.[149] This result, that the addition of NPs effectively decrease the tube diameter (adding effective entanglements) through geometric constraints and increase the tube diameter (removing polymer entanglements) of the polymer network, is also observed in MD simulations[152] and first-principles theory[158]. In MD simulations, below a critical volume fraction (ϕ_c = 31 v%) the chain dynamics are controlled by polymer entanglements, while above ϕ_c the geometric confinement or NP entanglements dominate the intermediate polymer dynamics.[152] A reduction in d_{app} was reproduced theoretically using mixtures of rods and spheres and the magnitude of the reduction was found to depend on only the volume fraction of NPs and the dimensions of the rods and spheres.[158] The convergence of this theory, simulations, and experiments establishes how spherical NPs perturb the entanglement network in model PNCs.

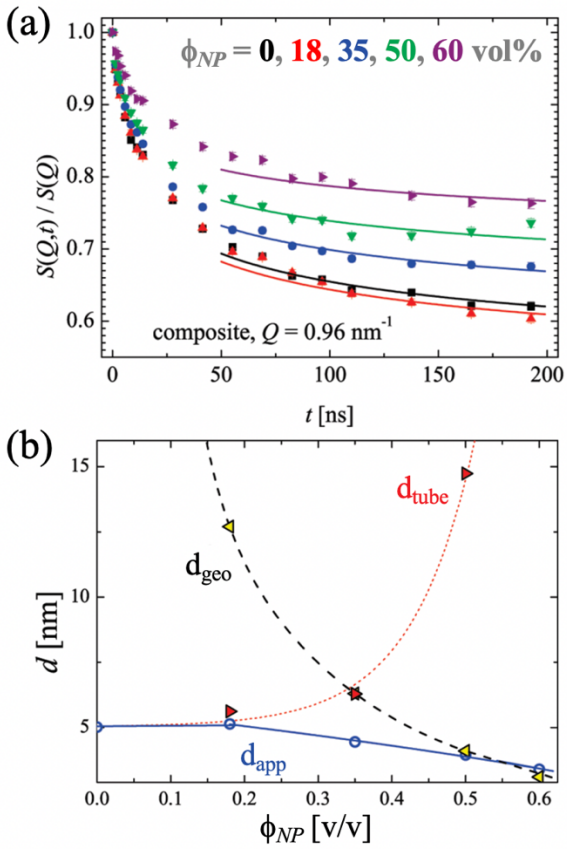

Figure 1.9: (a) Normalized dynamic structure factor from NSE of PEP for a variety of NP concentrations (ϕ_{NP} = 0, 0.18, 0.35, 0.5, and 0.6 from black to purple and $2R_{NP}$ = 17 nm). (b) Separation of apparent tube diameter, d_{app}, measured in (top) and contributions of polymer entanglements (d_{tube}) and geometric NP-induced entanglements (d_{geo}). Adapted with permission from Ref 149. Copyright 2011, American Chemical Society.

It is well known that small molecules (such as a solvent) or a low-M_w polymer disentangle high M_w polymer (increase d_{tube}), so it is reasonable to expect small NPs may have similar effects. Faraone and coworkers show exactly this effect: the addition of 20-nm diameter athermal Au NPs at ϕ_{NP} = 20 vol% to PEO does not measurably perturb the apparent tube diameter (as measured by NSE), but 3-nm diameter athermal Au NPs increase the tube diameter by ~25% at the same ϕ_{NP}.[131] This concept of tube dilation has been observed and discussed in other PNC systems as well.[109,145,159]

MD simulations also provide valuable information about the entanglement network in PNCs.[152,153,160–165] For example, PNCs with athermal NPs and $R_g >> R_{NP}$ exhibit disentanglement ($N_{e,PNC} > N_{e,bulk}$) and more specifically, a depletion of entanglements near the NP.[165] Moreover, the NPs often contribute to the primitive path indicating that NPs can act as topological constraints akin to entanglements.[165] This result agrees with the aforementioned NSE observations. In another simulation, the entanglement tube diameter increased as a function of NP concentration, demonstrating disentanglement, and this increase was larger for smaller NPs and stronger NP-polymer attractions.[162,166] It is important to note that in simulations, the entanglement network is defined by the primitive network but in experiments, it is usually defined by polymer dynamics or stress relaxation, so NPs may contribute differently.

1.5 The Polymer Chain Diffusion

1.5.1 Experimental and simulation methods

As described in Section 1.4.1, rheology and NSE provide insights to chain-scale diffusion in certain systems and experimental conditions. For example, without NP percolation or significant mechanical stiffening, the terminal relaxation behavior in rheological spectra provides a measurement of the largest relaxation time (τ_t) associated with the chain, which can be used to estimate the polymer diffusion coefficient. In addition, the diffusion of unentangled chains can be measured by NSE and BDS at $T>>T_g$. While NSE measurements of ISF usually plateau at long times due to the confined relaxations in the entanglement mesh, full decorrelation can be observed in unentangled polymer chains.[148] In addition, for polymers with a permanent dipole along the backbone (such as PPG), BDS can measure the so-called normal mode relaxation time, which represents full chain relaxation.[167] Specialized NMR techniques can also be used to measure the diffusion coefficient in PNCs, but this measurement is generally less common.[168]

The most common way to measure chain-scale center-of-mass diffusion in PNCs is through depth profiling, Figure 1.10. Typically, a bilayer film of deuterated and protonated polymer is assembled and annealed at $T>T_g$. While the interface is initially sharp, as chains diffuse they interpenetrate and the interface broadens. By measuring the depth profile of the deuterated chains in the protonated matrix and knowing the annealing time, the interdiffusion rate or diffusion coefficient can be determined. Deuterium depth profiles are most commonly measured by elastic recoil detection (ERD), secondary ion mass spectroscopy (SIMS) or neutron reflectivity (NR).

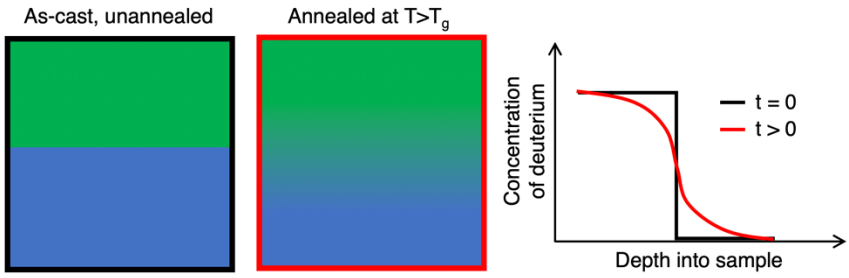

Figure 1.10: General schematic of diffusion experiment using a mutual diffusion sample configuration.

Elastic recoil detection (ERD) offers a relatively large penetration depth and can characterize the depth profile up to nearly 800 nm with approximately or less than 80 nm resolution.[169] In ERD, ^{4}He ions of known energy are accelerated towards the sample at a glancing angle and light elements such as ^{1}H and ^{2}D are forward recoiled toward the detector where their energy is measured. With knowledge of the beam parameters and atomic composition of the sample, the difference in measured and incident energy can be related to the depth of the collision event. These samples typically consist of a thin deuterated polymer film (< 50 nm) on a protonated polymer film (>10 μm), namely a tracer configuration. Following Figure 1.10 (but where the green tracer polymer is much thinner than the blue matrix) these diffusion couples are annealed at $T>T_g$ for a variety of annealing times, then cooled below T_g. The depth profile of the deuterated species

is measured ex situ and a diffusion coefficient is extracted by fitting the deuterated depth profile with a solution to Fick's second law assuming a finite source in a semi-infinite medium.[169,170]

In SIMS, an incident ion beam rasters over the sample surface to sputter ions and atoms from the sample. To measure the concentration of different elements, the charged species are detected by a mass spectrometer tuned to the appropriate elemental mass.[171] Typical samples are nearly symmetric bilayer films as depicted in Figure 1.10 with total thicknesses on the order of 300 nm. The penetration depth in SIMS is defined by the raster duration, intensities, and geometries and the maximum practical depth is on the order of several hundred nanometers. The depth resolution of dynamics SIMS and time-of-flight SIMS is typically on the order of 10 nm.[172]

Neutron reflectivity (NR) is a depth profiling technique for thin films where highly collimated neutrons are incident on the sample surface and the reflected intensity is measured as a function of incident angle.[173] Since neutrons are sensitive to differences in atomic nuclei, especially isotopes ^{1}H and ^{2}D, the reflectivity profile can be fit to reveal the concentration depth profile. NR offers a depth resolution and depth penetration on the order of ~1 nm and ~200 nm, respectively.[173] Samples for NR are usually comprised of a bilayer of deuterated and protonated films, each usually ~100 nm or less. Unlike ERD or SIMS that rely on ex situ annealing, NR experiments can be either ex situ or in situ. To fit NR data for interdiffusion, the diffusion profile is often assumed to follow an error function between pure ^{1}H and ^{2}D phases and the interfacial width is extracted as a function of time. An observed increase in interfacial width with $t^{1/2}$ is indicative of polymer diffusion, although sometimes NR length scales are too small to reach this regime.

Diffusive dynamics can also be studied through molecular dynamics, Monte Carlo, and various other methods, as recently summarized for melts and PNCs.[32] Molecular dynamics simulations are most common using coarse-graining methods to alleviate the computational expense of long simulation times. The Kremer-Grest model introduced in Section 1.3.1 is often used, but imposes a practical limit of lightly entangled chains ($N/N_e < 10$). Monte Carlo simulations

are commonly used to for polymer diffusion of entangled chains.[136,154,174–176] Other models including dissipative particle dynamics and slip-spring simulations[32] and force-based theoretical predictions[177] are less common but have been applied.

1.5.2 Polymer diffusion in the presence of spherical nanoparticles

The inclusion of NPs in a polymer matrix often impedes chain-scale polymer center-of-mass diffusion. This effect can be anticipated because polymer chains need to diffuse around impenetrable NPs, thus causing a longer diffusion trajectory. One may expect this to be confounded by other influences including altered polymer conformations, unique interactions, and changes to smaller-scale dynamics or the entanglement network, all of which may have non-trivial influences on polymer diffusion.

We start this discussion with the simple case of entangled polymer diffusion in the presence of athermal NPs. Composto and coworkers used ERD to measure dPS tracer diffusion (M_w = 49 – 530 kg/mol) into PS-based PNCs[178] with well-dispersed phenyl-functionalized 28-nm SiO_2 NPs at ϕ_{NP} = 0 – 50 vol%.[170] Polymer tracer diffusion was slowed as a function of ϕ_{NP} to a degree larger than expected from excluded volume and tortuosity, as predicted by the Maxwell model [179]. These results were in line with the entropic barrier model[174,175]. Furthermore, a master curve was developed by plotting the diffusion coefficient relative to the diffusion coefficient of neat polymer (D/D_0) as a function of $ID/2R_g$, or interparticle separation distance (ID) relative to the size of the deuterated polymer ($2R_g$).[170]

In later publications, a similar collapse was observed for ERD measurements of tracer diffusion in various PNCs to probe the influence of NP size[180,181], NP polydispersity[181], interfacial interactions[180], and interface softness using grafted NPs[182,183]. The effective interparticle distance (ID_{eff}) is used to account for the polydispersity of NPs and the volume accessible to the tracer molecule in the presence of densely grafted NPs, Figure 1.11.[181,182] At the limits, D is reduced

nearly an order of magnitude in strongly confined PNCs ($ID_{eff}/2R_g < 1$) and the reduction in tracer diffusion extends to weakly confining PNCs, where bulk diffusion is only recovered at $ID_{eff}/2R_g \sim 20$. To compare with these experiments, Meth et al. developed an analytical method that treats polymers diffusing through nanocomposites as spheres diffusing through cylinders (mimicking the network of free space in the PNC).[184] This model quantitatively agrees with data in Figure 1.11 at $ID/2R_g > 5$ and underestimates D/D_0 at $ID/2Rg < 5$, likely because the model does not account for perturbed conformations and entropic penalties.

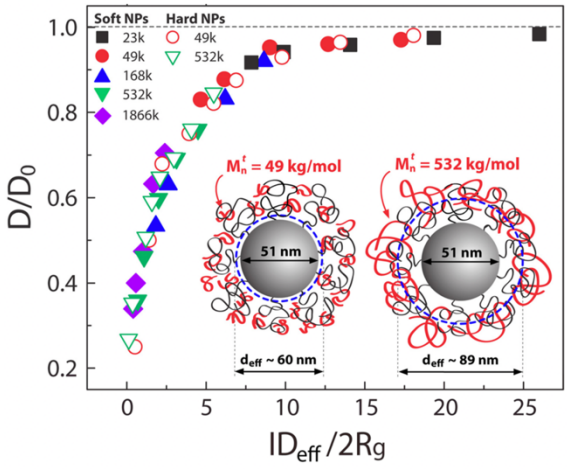

Figure 1.11: Master curve developed for a variety of PS-based PNC systems showing collapse of the tracer diffusion coefficient normalized to bulk as a function of the effective interparticle distance relative to the tracer polymer chain size. Filled and open symbols refer to grafted and bare NPs, respectively. Reprinted with permission from Ref 182. Copyright 2013, American Chemical Society.

Measurements of chain diffusion from an attractive interface[185–187] and segmental dynamics near attractive NPs imply that attractive interactions may impact chain-scale dynamics. Composto and coworkers compared PS/SiO_2-Ph (athermal interactions) and PMMA/SiO_2 (attractive interactions) and observed that tracer diffusion through these PNCs are independent of interfacial interactions.[180] This result suggests that tracer polymer molecules can diffuse within the bound layer in PMMA/SiO_2 and the increased friction at the NP-polymer interface is either similar to PS/SiO_2-Ph or insignificant.

The collapse presented in Figure 1.11, as measured by ERD, is at a fixed T-T_g with large M_w polymer for the protonated matrix. Although a qualitatively similar dependence on ID/2R_g exists over a range of temperatures, the normalized tracer diffusion is more perturbed from bulk at higher temperatures (Figure 1.12).[188] This difference was reconciled by entropic arguments, where the entropic barrier extracted from temperature-dependent measurements scaled with $ID^{-0.5}$, consistent with an entropic perturbation imposed by the NPs. This result highlights that the

convenient and successful scaling of $ID/2R_g$ omits the temperature dependence of the physics governing tracer diffusion through PNCs. Also note that Figure 1.11 applies to PNCs wherein the spherical NPs are immobile on the timescale of polymer diffusion. ERD studies of very small, attractive NPs (~2 nm OAPS) in P2VP found polymer diffusion to be more dependent on ϕ_{NP} than measurements in PS/SiO_2 PNCs at the same temperature.[109] By comparing D/D_0 with $\tau_\alpha/\tau_{\alpha,0}$ and measuring NP diffusion, a friction-dominated mechanism was proposed for the P2VP/OAPS system with mobile NPs[109]. In summary, the master curve in Figure 1.11 is appropriate for tracer diffusion in PNCs with immobile spherical NPs under isothermal conditions.

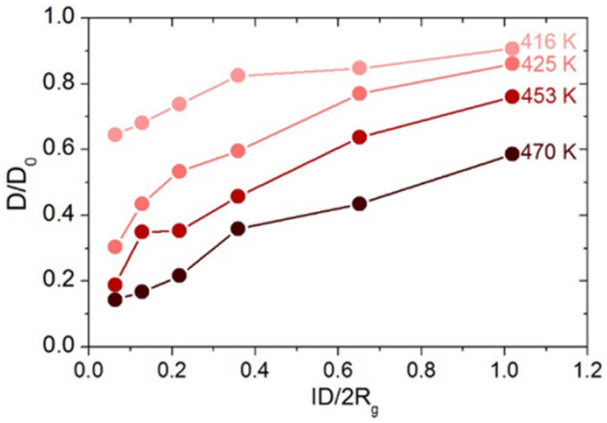

Figure 1.12: Temperature dependence of polymer diffusion showing more perturbed diffusion at higher temperatures. Measurements are for 532 kg/mol dPS diffusion into PS/SiO_2 PNCs (ϕ_{NP} = 0 – 50 vol%, $2R_{NP}$ = 28.5 nm, T_g^{PS} ~ 375 K). Adapted with permission from Ref 188. Copyright 2016, American Chemical Society.

In addition to the ERD measurements of tracer diffusion, other techniques have been applied to the problem of polymer diffusion in PNCs. Early measurements of pulsed-gradient spin-echo NMR on entangled PE diffusion in PE/ZnO PNCs (non-attractive) showed bulk-like diffusion in PNCs of varying M_w, NP concentration, and NP size.[189] This observation may result from low ϕ_{NP} and poor NP dispersion, among other factors. In a study using in-situ neutron reflectivity, entangled PS diffusion in all-polymer athermal PNCs comprised of PS and soft crosslinked-PS NPs

were measured.[190,191] In these measurements, the relative size of NPs and polymers lead to enhanced or suppressed diffusion resulting from the competing effects of constraint release or disentanglement and added topological barriers, respectively.[191] To be specific, for small PS NPs in large M_w PS, $D/D_0 > 1$ was observed and attributed to increased constraint release akin to a diluent. Conversely, for large NPs in low M_w polymer, polymer diffusion was slowed apparently by the presence of barriers, qualitatively similar to ERD measurements with immobile NPs, although NP softness may contribute[190,191]. In another contribution, the segmental dynamics and translational diffusion of unentangled PEP chains in the presence of SiO_2 NPs was measured via NSE which showed slow chain diffusion beyond expected solely from geometric confinement, which is consistent with increased friction or entropic effects associated with confined diffusion.[148]

As recently reviewed[32], computer simulations have been broadly applied to polymer diffusion in PNCs to investigate the extensive parameter space such as NP-polymer interactions[124,153,163,192], NP size[136,193,194], polymer M_w[195], and other factors[176,194]. Early MD simulations by Kumar et al. showed polymer diffusion in the presence of attractive NPs slowed monotonically with increasing ϕ_{NP}.[192] In contrast, PNCs with repulsive NPs exhibited diffusion faster than bulk ($D/D_0 > 1$) at ϕ_{NP}<8 vol% and slower at higher ϕ_{NP}, implying that diffusion at low ϕ_{NP} results from interfacial perturbations.[192] Other simulations have observed $D/D_0 < 1$ in repulsive and attractive PNC systems, and observed deviations from experimental results presented in Figure 1.11.[194,195] For example, while a qualitatively similar trend with $ID/2R_g$ was recently observed using a dynamic Monte Carlo technique, larger NPs perturb diffusion more strongly than smaller NPs, even at the same ID.[194]

1.5.3 Polymer diffusion in the presence of non-spherical nanoparticles

Understanding the impact of anisotropic NPs on the polymer translational diffusion requires consideration of the multiple length-scales associated with the non-spherical NPs. For

example, whereas spherical NPs have one characteristic size (R_{NP}), cylindrically-shaped NPs have two relevant length scales (R_{NP} and L). Figure 1.13 shows that geometric considerations of the NP length (L) and diameter ($d=2R_{NP}$) relative to R_g distinguish monotonic (open symbols) and nonmonotonic (closed symbols) dependencies of polymer normalized tracer diffusion coefficient as a function of ϕ_{NP}. For highly anisotropic NPs with $2R_{NP} < 2R_g < L$ (red region in Figure 1.13), polymer diffusion slows relative to bulk at small ϕ_{NP} and slowly recovers at ϕ_{NP} larger than the critical concentration ($\phi_{NP,crit}$).[196–201] For PNCs with spherical NPs in Section 1.5.2 or less anisotropic NPs, the polymer diffusion coefficient decreases monotonically with ϕ_{NP}.[170,180,182,197,200,201] These different dependencies of D/D_0 vs ϕ_{NP} are shown schematically in the inset of Figure 1.13. This comparison highlights that the perturbation to polymer dynamics changes considerably when only one dimension of the NP is smaller than the chain size.

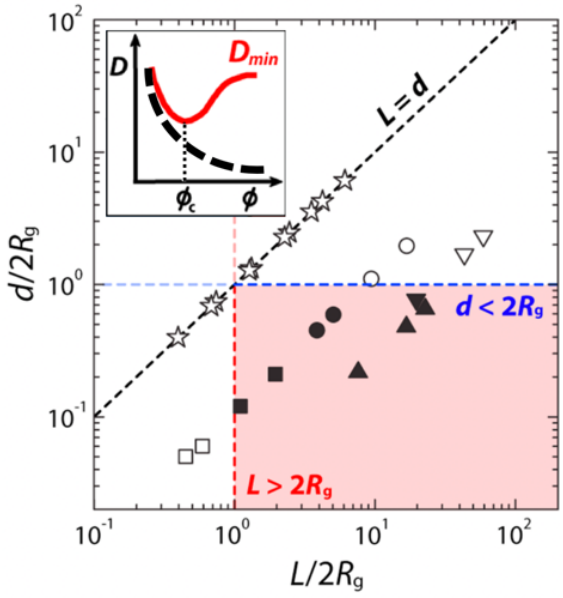

Figure 1.13: Diagram representing the effect of NP diameter and length relative to polymer R_g on observations of monotonic (open symbols) or non-monotonic (closed symbols) dependence of normalized tracer diffusion coefficient as a function of NP concentration, as schematically shown in the inset. Data is compiled from PNCs containing spherical SiO_2 (star symbols), CNTs (triangle symbols), and nanorods (square and circle symbols) Adapted with permission from Ref 201. Copyright 2014, American Chemical Society.

The non-monotonic decrease in D with ϕ_{NP} was first observed in PS-based PNCs comprised of highly anisotropic single-walled carbon nanotube (CNT) bundles using ERD.[196–198]. The D/D_0 reaches a minimum value at $\phi_{NP,crit}$, which correlates with the mechanical percolation threshold as determined by DMA. Furthermore, $\phi_{NP,crit}$ was found to depend on the PS matrix M_w and not dPS tracer M_w[196] or temperature [198], while both M_w and T affected the minimum value of D/D_0. A trap model was simultaneously developed to test the hypothesis that diffusion along CNTs is faster than diffusion perpendicular to CNTs.[196] This model qualitatively captures the decrease in $\phi_{NP,crit}$ with increasing matrix M_w and decrease in the minimum value of D/D_0 with decreasing tracer M_w, suggesting that anisotropic diffusion could be the origin of a minimum in D/D_0 as a function of ϕ_{NP}.[196] Other simulations further developed these results.[161,163,202] Using a variety of tracer M_w with multi-walled CNTs[197,198], long and short TiO_2 NRs[200,201], and spherical NPs in chain-like aggregates[199], it was determined that when $D_{NP} << D_{polymer}$, the general criteria for observation of a minimum D/D_0 (i.e. anisotropic diffusion) is $2R_{NP} < 2R_g < L$, Figure 1.13.

When NPs are small relative to the entanglement network ($2R_{NP} < d_{tube}$), NP diffusion can be fast compared to the polymer diffusion and therefore can be considered mobile during polymer relaxations.[203] By using ϕ_{NP} and matrix M_w to control the nanorod mobility, the dPS tracer diffusion coefficient into PS/TiO_2 ($2R_{NP} < L < 2R_g$) nanorod-based PNCs with mobile ($D_{NP} > D_{chain}$) and immobile ($D_{NP} < D_{chain}$) NPs was measured.[200] While polymer diffusion in the PNC was consistently slower than bulk diffusion ($D/D_0 < 1$), faster polymer diffusion was observed in PNCs with mobile NPs than immobile NPs at the same ϕ_{NP}.[200] This enhanced polymer diffusion in the presence of mobile anisotropic NPs was captured by a numerical slip-spring model representing fixed topological constraints from the PS matrix and immobile NRs with additional constraints with a finite release time representing mobile NPs.[200] These results, along with those with mobile spherical

NPs[109], clearly demonstrate the importance of NP mobility in understanding the polymer diffusion dynamics.

Experiments probing polymer diffusion through PNCs with NPs of other geometries, including plates/platelets, non-linear NRs, and self-assembled structures, are quite limited. In one study, polymer diffusion was measured using SIMS in dPMMA and dPS into PNCs containing 5 vol% montmorillonite clay platelets.[22] The diffusion of dPMMA in these clay PNCs was 3x slower than bulk while the diffusion of dPS was unperturbed from bulk, a difference that was attributed to preferential adsorption of PMMA chains but these results may be confounded by poor dispersion and surface aggregation. Future studies of polymer diffusion in PNCs with well-dispersed planar NPs would further develop Figure 1.13.

1.5.4 Exchange dynamics from the NP interface

Analogous to the separation of segmental dynamics in the bound layer from those of free chains (Section 1.3.2 and Figure 1.3), a recent experimental direction that has emerged is measuring the desorption, or exchange dynamics of bound chains in the melt state. Exchange dynamics from a flat substrate have been studied by depth profiling techniques such as SIMS, ERD, and NR.[185–187,204,205] Generally, these studies reveal polymer diffusion slows near a solid interface[204,205], depends on the polymer-substrate interaction[187,205], and the effect is spatially long-lasting (in that slow polymer diffusion is observed at distances well beyond R_g from the interface)[186]. However, exploring polymer exchange dynamics in PNCs is considerably more challenging because experimentally distinguishing bound polymer and free polymer is difficult. Unfortunately, MD simulations are typically too slow to study polymer desorption.

Recently, polymer exchange has been probed in P2VP/SiO_2 PNCs using two different experimental approaches: SANS[206] and ERD[207]. For SANS, dP2VP/SiO_2 PNCs were successively solvent washed to remove free polymer and the dP2VP-coated SiO_2 NPs were redispersed in

protonated P2VP. These PNCs with deuterated bound layers were then annealed at two temperatures for various times, measured using SANS, and analyzed by assuming a core-shell model where the shell is the dP2VP bound layer.[206] The dP2VP shell thickness decreased from ~3 nm to ~0.6 nm when annealing at T_g+75ºC, but remained largely unchanged after annealing at T_g+50ºC, indicating a strong temperature-dependent process.[206] Using ERD measurements on P2VP/SiO_2 PNCs, the fraction of bound chains was measured in the melt state after conventional PNC fabrication procedures by spatially separating free polymer from bound polymer as a function of annealing time, annealing temperature, and M_w. First, measurements at relatively short annealing conditions isolate NP-bound polymer from free polymer, and a bound layer of ~R_g was observed, as expected from other measurements[208–210]. Upon further annealing, polymer desorption was observed as the fraction of chains originally bound to the NPs decreased, and some polymer remained adsorbed after all annealing conditions studied.[206] In fact, the kinetics of desorption were slower for lower temperatures and higher M_w, and this effect correlates with the polymer chain relaxation time, albeit over a relatively narrow window of M_w and temperature in this study. Despite differences in sample preparation and measurements, these two studies are in qualitative agreement in that polymer desorption is much slower than bulk polymer dynamics, some chains remain bound for experimentally inaccessible timescales (>10^6 τ_t), and the desorption kinetics depend strongly on temperature.

Much remains unknown about the desorption and exchange process of bound polymers in PNCs. First and foremost, the dense parameter space in PNCs remains largely untested, particularly NP size and NP-polymer interactions. In addition, ERD and SANS studies of P2VP/SiO_2 showed that some chains remained adsorbed for experimentally accessible timescales.[206,207] It remains unclear how this observation and others depends on the material system or if PNCs with weaker interactions will also show “permanently” bound polymer. In addition, the interfacial conformations and evolution of conformations during annealing are unexplored and but this will

require the development of techniques beyond those mentioned here. Finally, a mechanistic description of the desorption and exchange of different populations of chains (tightly bound vs lightly bound) remains elusive and may require considerable experimental and simulation efforts. This is a fruitful direction of research, even though the desorption process is expected to be very complicated and depend strongly on various experimental and PNC parameters.

1.6 The Nanoparticle Diffusion in Polymer Melts

1.6.1 Theoretical background

The Stokes-Einstein (SE) relationship describes the diffusion of spherical particles (D_{SE}) through a continuous medium as a competition between driving forces from thermal fluctuations and viscous drag forces of the medium:

$$D_{SE} = \frac{kT}{f\pi\eta R_p} \qquad (1.4)$$

where η is the viscosity of the medium, R_p is the particle radius, kT is the thermal energy term, and f is either 4 or 6 for slip or non-slip conditions at the interface, respectively.[38] Equation 1.4 assumes the characteristic particle size exceeds the largest characteristic length scale of the medium, i.e. R_g in a polymer melt. To apply The SE model to nanoparticle diffusion in polymer melts, the zero-shear viscosity (η_0) and core NP size (R_{NP}) are often used for η and R_p, respectively.

In PNCs, deviations from SE behavior are be expected.[38] Several theories have been developed to describe the diffusion of dilute nanoparticles in polymer melts, including by De Gennes[38], Rubinstein[211,212], Schweizer[177,213–217], and others[218,219]. Early work by De Gennes an coworkers qualitatively predicted that small NPs diffuse faster than $D_{SE}(\eta_0, R_{NP})$, because NPs sample a length-scale dependent friction dictated by Rouse relaxations when $2R_{NP} \sim d_{tube}$ or by monomeric relaxations when $2R_{NP} \sim b$, both of which decrease the drag forces.[38] This concept was

further developed quantitatively for repulsive NPs of various sizes in entangled and unentangled polymer melts.[211–213,215,216,218] More recently, theory was developed that begins to tackle the case of attractive NPs in Section 1.6.4.[214]

1.6.2 Experimental and simulation methods

Rutherford Backscattering spectrometry (RBS) is an ion beam method analogous to ERD, which was introduced in Section 1.5.1 and can be used for measure NP diffusion. RBS is used to measure the depth profile of elements heavier than H or D. In RBS, He ions are incident to the sample, typically in normal geometry, and are backscattered to a detector to measure the particle energy. The loss in energy is related to the incident energy, the kinematic factor of the collision (which depends on colliding particles), and the energy loss through the sample, and can provide a direct measure of the composition as a function of depth. RBS offers a depth resolution of <100 nm and a depth penetration of ~1 μm.[169] To measure NP diffusion using RBS bilayer samples typically comprise a ~150 nm layer of PNCs with low NP concentration on a bulk matrix of the same polymer. As samples are annealed at $T>T_g$, the NP depth profile is monitored by tracking the relevant elements (e.g. Si for SiO_2 NPs). Similar to ERD, the measured depth profiles are fit with a solution to Fick's second law and a diffusion coefficient is extracted. RBS requires access to an ion beam facility and data reduction and interpretation can be difficult, but it can survey a wide array of R_{NP}, η, M_w, annealing conditions, and can be applied to many different material systems.

Dynamic scattering measurements can also be used to measure the diffusion of NPs in a polymer melt, including X-ray photon correlation spectroscopy (XPCS) and dynamics light scattering (DLS). Fundamentally, both techniques are similar in that they measure the temporal fluctuations of the speckle patterns produced by coherent light scattering from dilute NPs in a polymer medium. They differ however, in the specifics of the measurement, details of the

instrumentation, and the length and time scales that they probe. XPCS uses a high-brilliance coherent X-ray source to measure the decorrelation in the spatial distribution of electron density in the sample as a function of q. Generally, XPCS offers a q range of $0.002\ Å^{-1} < q < 0.07\ Å^{-1}$ (spanning length scales of ~5 – 250 nm) and a dynamic range of ~500 μs to $\sim 10^3$ s. Analysis of the intensity time-autocorrelation functions, which are related to the ISF, uses a stretched exponential to reveal the relaxation time of the system. Plotting the extracted relaxation time vs q reveals the geometry of the motion where $\tau \sim q^{-2}$ is purely diffusive motion. In contrast, DLS uses a longer wavelength light, the scattering comes from differences in index of refraction, and typically only one q value is measured. Both methods can probe NP motion in PNCs with dilute NP concentrations ($\phi_{NP} < \sim 1$ vol%) and provide access to unique length- and timescales. As with RBS, these provide an ensemble average of the NP dynamics and may be difficult to interpret or separate different dynamic processes in PNC systems.

More specialized measurements of NP dynamics exist as well. For example, a modified fluctuation correlation spectroscopy (FCS) method has been applied to melts and solutions.[220,221] Here, a laser is rastered over the polymer melt with a dilute NP concentration until an increase in the photon count was observed as indication of the presence of a NP. After the NP is placed in the focal volume of the laser beam, the photon counts are continuously recorded until the value reaches the background count, indicating that the NP diffused out of the focal volume. The diffusion coefficient is obtained by the decay time of the photon counts (extracted with a stretched exponential) and the size of the focused laser beam. Single particle tracking (SPT) has been applied to polymer solutions and gels[222–224] and, more recently, to polymer melts with NPs[225]. SPT uses either florescent or photon-emitting NPs (such as quantum dots) to precisely measure the center-of-mass position of individual NPs as a function of time.[224] From this measurement, van Hove distributions and mean-squared displacement (MSD) curves are constructed to analyze the

distribution of dynamics, isolate different populations, and calculate the ensemble average. Although the requirements on the PNC system are somewhat stringent in that the NPs must emit light and the polymeric matrix must have a low T_g (since it is difficult to heat the sample), SPT can uniquely sample the motion of each individual NP and provide unique insight into the population of dynamics.

Finally, coarse-grained MD simulations can also probe NP motion in polymer melts. The NPs can either be constructed as a single bead with larger size and mass or a collection of smaller beads. The latter option reduces artificial crystallization and dense packing at the NP-polymer interface but produces a non-uniform potential at the NP-surface that may be unrealistic. Unlike many of the simulations discussed in previous sections to isolate polymer dynamics, the NPs in these simulations are free to diffuse and their MSD can be directly measured. The NPs in these simulations tend to aggregate if there are more than one in the simulation and weak NP-polymer interactions, and single NP simulation suffer from poor statistics for NP dynamics, especially at long times. So, to access the diffusive regime, the NPs are typically smaller than the chain size ($R_{NP} < R_g$) or the M_w is small.

1.6.3 Diffusion in athermal and weakly interacting PNCs

PNCs without NP-polymer enthalpic attractions and with dilute NP concentrations are the simplest PNCs for theoretical predictions.[211–213,215,216,218] At short length scales (~$2R_{NP}$) and fast time scales, scaling descriptions[212] and force-level statistical dynamical theory[213] propose NP caging in the correlation mesh on the order of b or d_{tube} in entangled melts.[211,216] In this regime, relaxations of the surrounding polymer environment lead to random Brownian NP diffusion at longer length-scales (>$2R_{NP}$). This type of motion has been observed in NP-polymer solutions through non-Gaussian dynamics[226] and in the melt through subdiffusion at short length and times scales[227]. Specifically in entangled polymer melts when $R_{NP} \sim d_{tube}$, NPs are predicted to hop

between the entanglement network.[212,213] For larger NPs ($R_{NP} >> R_g$), NPs are unable to escape the entanglement network until it fully relaxes, which decreases the likelihood of this mechanism and leads to slower SE diffusion.

For small NPs ($R_{NP} < R_g$) regardless of the chain length, NP diffusion does not require full chain relaxation, so diffusion is fast relative to $D_{SE}(\eta_0,R_{NP})$. To further understand NP diffusion in entangled polymers, Schweizer and coworkers developed a microscopic, force-level, self-consistent generalized Langevin equation (SCGLE) approach to quantitatively predict the diffusion of repulsive or athermal NPs as a function of NP size and molecular weight.[216] Importantly, this theory does not consider hopping but predicts that particle motion is coupled to the entanglement network dynamics, even if the R_{NP} exceeds the entanglement mesh size. As shown in Figure 1.14, for $2R_{NP} \geq \sim 10d_{tube}$, D_{SE} from Equation 1.4 approximately captures the diffusion of repulsive NPs in a polymer melt. For smaller NPs, especially $2R_{NP} < d_{tube}$, NPs diffuse faster than the SE prediction, particularly for smaller NPs in more entangled polymers, because they are influenced by smaller length scale polymer relaxations.

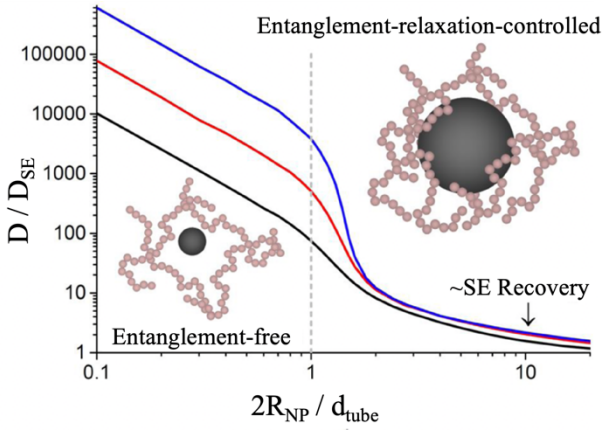

Figure 1.14: Self-consistent generalized Langevin equation (SCGLE) predictions for repulsive NP diffusion relative to SE behavior in entangled polymer melts as a function of NP size, R_{NP}, relative to the tube diameter, d_{tube}, for $N/N_e = 4$ (black), 8 (red), and 16 (blue). Adapted with permission from Ref 216. Copyright 2015, American Chemical Society.

The SCGLE theoretical predictions[216] in Figure 1.14 are in reasonable quantitative agreement with coarse-grained MD simulations[228] in unentangled and lightly entangled polymers for $0.1 < 2R_{NP}/d_{tube} < 2$. In this comparison, the authors establish that athermal NP motion is controlled by polymer constraint release wherein NPs are trapped until the polymer environment on the order of $2R_{NP}$ relaxes. Although the hopping mechanism was not observed in these simulations[228], it is expected in highly entangled systems with small NPs ($2R_{NP} \sim d_{tube}$ and $N >> N_e$). MD simulations have also been used to systematically study repulsive or weakly interacting NP diffusion in the dilute limit as a function of NP size[124,166,195,228–232], polymer M_w[195,228–230,232], NP concentration[124,195,229], surface structure[231], and NP shape[233]. In general, the MD results are consistent with theoretical calculations, in that the diffusion of small NPs or NPs in well-entangled polymers exhibit faster diffusion than the SE prediction. As NP concentration increases, NPs begin to interact and the viscosity of the melt increases, leading to a diffusion coefficient that is reduced relative to the dilute limit.[195,229]

Stokes-Einstein enhancements (as predicted in Figure 1.14) have been experimentally realized in a variety of weakly interacting PNC systems, especially for small NPs in well-entangled polymers. For example, early XPCS measurements of quantum dots ($2R_{NP}/d_{tube} \sim 0.7$) in PS ($N/N_e \sim 12$) revealed SE enhancements of ~200 with only a subtle dependence on temperature; this is ~100 times slower than predicted in Figure 1.14.[234] In a systematic study of NP size using a modified fluctuation correlation spectroscopy technique, SE enhancements of ~10 – 2000 were measured for gold NPs with $2R_{NP}/d_{tube} \sim 0.8 – 3.3$ in well-entangled poly(butyl methacrylate) (PBMA).[221,235] While these results qualitatively agreed with SCGLE predictions, they did not quantitatively capture the transition around $2R_{NP} \sim d_{tube}$. More recently, using SPT of non-attractive quantum dots in PPG ($2R_{NP}/d_{tube} \sim 2.6$), Gaussian dynamics were observed at all timescales studied and SE diffusion was observed ($D \sim D_{SE}$) in unentangled and lightly entangled melts (up to $N/N_e \sim 2.8$).[225] To date, the theoretical curves in Figure 1.14 remain largely unverified experimentally, in

part due to the difficulty of dispersing athermal or repulsive NPs in a polymer melts and the challenge of systematically accessing a broad range and relevant values of $2R_{NP}/d_{tube}$ and N/N_e.

One way to improve the dispersion of athermal NPs in a polymer melt is to use grafted NPs, which also alters the NP diffusion coefficient. For example, using athermal grafted NPs with $2R_{NP}<d_{tube}$, the diffusion coefficient measured by RBS was found to be slower than predicted by Equation 1.4 and in stark contrast to Figure 1.14.[236] By comparing to field theory calculations, this slowing was attributed to the larger hydrodynamic radius caused by interpenetration of matrix chains and grafted polymer. Interestingly, SE behavior was recovered by using an effective radius, $R_{eff} > R_{NP}$, to account for the presence of grafted chains.[236] This effect was also observed in MD simulations.[231]

The dynamics of non-spherical NPs in entangled and unentangled polymer melts has received less attention.[177,203,233,237,238] The center of mass diffusion coefficient (D_{CM}) of a nanorod with dimensions L and R_{NP} is often described as a combination of diffusion coefficients perpendicular ($D_\perp$) and parallel ($D_\parallel$) to the long axis, both of which follow the form of Equation 1.4[239]:

$$D_{CM} = \frac{D_\parallel}{3} + \frac{2D_\perp}{3} = \left(\frac{kT}{6\pi\eta L}\ln\left[\frac{L}{2R_{NP}}\right]\right) + \left(\frac{kT}{6\pi\eta L}\ln\left[\frac{L}{2R_{NP}}\right]\right) = \frac{kT}{3\pi\eta L}\ln\left[\frac{L}{2R_{NP}}\right] \qquad (1.5)$$

This equation is known to describe the diffusion of nanorods in a simple liquid when L and R_{NP} are larger than the characteristic length scale of the liquid[240], and much like Equation 1.4 for spherical NPs, it is expected to breakdown for small NRs in an entangled polymer melt. Using RBS measurements to study TiO_2 NR diffusion in well-entangled PS ($2R_{NP}< d_{tube}$), the measured NR diffusion coefficient was faster than expected from Equation 1.5, reaching enhancements of ~1000 at $M/M_e \sim 100$.[203] The observed scaling of $D_{CM} \sim M_w^{-1.4}$ implies that NR diffusion is decoupled from the chain-scale viscosity, likely because the NR diameter facilitates NR relaxations within the entanglement network. In MD simulations designed to mimic this experimental system, a hop-like

mechanism was identified at long-times when $2R_{NP} < d_{tube}$, although the MD simulations over-predict the NR diffusion coefficient in well-entangled polymer melts.[233]

We also note that NP diffusion in dilute and concentrated solutions has also been studied and these three-component systems are analogous to melts, although with additional complex interactions and different confining length scales.[211,215,216,219] NP diffusion has been measured in several polymer solutions with a variety of techniques including XPCS, SPT, and FCS.[222,241–245] The relevant viscosity in NP-polymer solutions depends on the NP and polymer concentrations and the interactions between the NP, solvent, and polymer. Generally, insights regarding NP diffusion from NP-polymer solutions can be used to inform NP diffusion in polymer melts (and visa versa) and may be relevant to understand PNC fabrication from solution.

1.6.4 Diffusion in attractive PNCs

Although athermal and spherical NPs in a polymer melt can be considered the simplest PNC system, PNC systems with strong NP-polymer attraction have a number of practical advantages so understanding the role of NP-polymer interaction on NP diffusion is critical. Early theories considered the effect of NP-polymer attraction in terms of interfacial polymer packing[215], while more recent descriptions introduce two competing mechanisms: "core-shell" diffusion and "vehicular" diffusion.[214] In core-shell diffusion, which dominates for $R_{NP} > R_g$, adsorbed polymers diffuse along with the NP, thereby increasing the hydrodynamic size ($R_{eff} \approx R_{NP} + R_g$) and slowing diffusion relative to SE behavior.[214] In vehicular diffusion, which dominates for $R_{NP} < R_g$, NPs diffuse with the local polymer environment until successive desorption and readsorption events ("hops") lead to decoupled polymer and NP dynamics, thereby enhancing NP diffusion relative to SE.[214]

The transition between core-shell diffusion and vehicular diffusion have been observed as a function of molecular weight[246] (Figure 1.15) and NP size[109,208]. As shown in Figure 1.15 for

amine-functionalized OAPS diffusion in PPG as measured via DLS, the small NPs ($2R_{NP}$ ~ 2 nm) diffuse via core-shell diffusion ($D<D_{SE}$) in short, unentangled melts and via vehicle diffusion ($D>D_{SE}$) in longer, lightly entangled melts.[246] The observed crossover corresponds to where R_{NP}~R_g, N~N_e, and when $D_{NP} \sim D_{poly}$. These experimental results are consistent with observations via MD simulations designed to mimic the OAPS/PPG system and the previously described theory.[214,246]

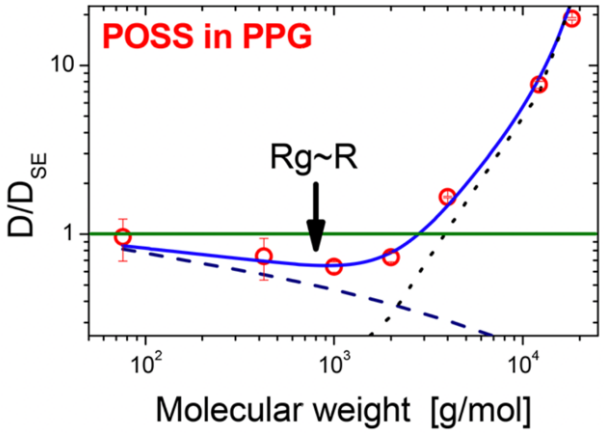

Figure 1.15: Crossover from core shell diffusion ($D<D_{SE}$) to vehicle diffusion ($D>D_{SE}$) for OAPS diffusion in PPG as a function of molecular weight. Adapted with permission from Ref 246. Copyright 2018, American Chemical Society.

Core-shell diffusion[208] and vehicular diffusion[109] has also been observed in well-entangled P2VP melts using RBS and attractive NPs of different size. For 26-nm diameter SiO_2 in P2VP ($2R_{NP} > d_{tube}$), the measured diffusion coefficient was slower than predicted by Equation 1.4 and the difference was found to increase with M_w.[208] The difference between D_{NP} and D_{SE} was quantitatively accounted for by an increased hydrodynamic radius that was found to scale with $M_w^{1/2}$[208], as predicted in core-shell diffusion and also observed in PPG-based attractive PNCs.[225,246] For attractive OAPS in P2VP ($2R_{NP} < d_{tube}$), vehicle diffusion was observed when the timescale and M_w-dependence of NP diffusion was compared to the those of polymer segmental relaxations and chain diffusion.[109] As shown in Figure 1.16, OAPS relaxations were found to scale weakly with $M_w^{0.7}$, fall between segmental relaxations and relaxations of entanglement strands, and D/D_{SE}

enhancements were found to reach ~10^4 at $N/N_e \sim 20$ (not shown).[109] Together, these experimental observations are consistent with vehicle diffusion, where a similar M_w scaling is predicted theoretically and observed in simulations.[214]

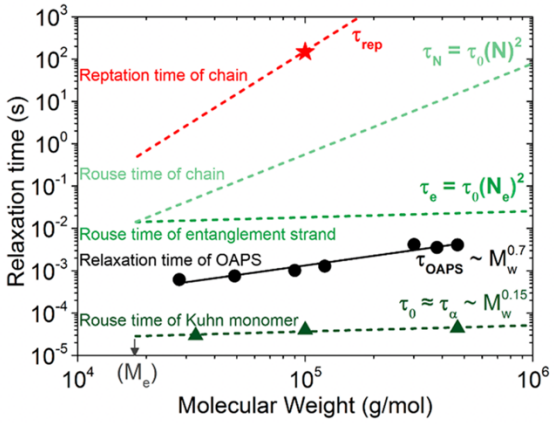

Figure 1.16: Comparison of relaxation times for poly(2-vinylpyridine) (P2VP) at various length-scales and attractive OAPS NPs as a function of P2VP molecular weight. The Rouse times of a Kuhn monomer (τ_0, BDS) and P2VP reptation time (τ_{rep}, ERD) were measured on bulk P2VP. OAPS relaxation times (τ_{OAPS}) are calculated directly from RBS measurements. All measurements are made at 140°C. Reprinted with permission from Ref 109. Copyright 2019, American Chemical Society.

The diffusion of attractive NPs in a polymer melt has also been probed with atomistic[247–249] and coarse-grained[124,166,192,214,229,250,251] MD simulations. For small fullerenes, NP diffusion in various polymers[247,248] can be observed at microsecond timescales with atomistic detail where only one fullerene is included to prevent fullerene aggregation and crystallization. Hopping diffusion was observed in attractive fullerene-polymer melts, such as polyimide[248] or polystyrene (PS)[247], and absent in a non-interacting polypropylene (PP)[247] melt. The comparison of fullerene dynamics in PS and PP shows NP hopping occurs when small NPs adsorb to and desorb from polymer segments, as predicted in vehicle diffusion.[247] Fickian diffusion occurs in both cases at long times, and NP diffusion is slower in more attractive melts.[247] For larger NPs using coarse-grained MD simulations, NP diffusion is observed to be systematically slower for polymer melts with increased NP-polymer interaction, although the degree to which NP diffusion is slowed depends on system-

specific parameters such as NP size and interaction strength, among other parameters.[124,229,250] Although most PNC simulations apply NP-polymer interaction through a LJ potential, which can be considered comparable to physical bonding in PNCs, the case of ionic interactions was also studied using MD simulations.[251]

1.6.5 Non-diffusive NP dynamics

Non-diffusive NP dynamics, characterized by MSD ~ t^{α} where $\alpha \neq 1$, is predicted at length- and timescales before the diffusive regime, such as ballistic motions.[38,211–213] As previously mentioned, subdiffusion ($\alpha < 1$) is predicted for $2R_{NP} > b$ due to the caging of NPs within the correlation network of polymer melts (on the order of b) or the entanglement mesh (on the order of d_{tube}).[212,213] Experimentally, a crossover from subdiffusion to Fickian diffusion was observed at length scales of ~R_{NP} using NSE measurements and PEG-functionalized polyhedral oligomeric silsesquioxane dispersed in PEG.[227] This is consistent with the aforementioned theory by Rubinstein and coworkers.[211] In general, this regime is largely unexplored, especially for larger NPs, because observations of motion on the order of or less than R_{NP} in the melt necessitates excellent spatial and temporal resolution and unique length- and time-scales.

Non-diffusive NP dynamics have been widely reported in XPCS in various PNC systems and experimental conditions.[131,159,260–265,252–259] Systematic measurements of ~100 nm-diameter PS-grafted SiO_2 NP relaxations (τ_{NP}) in unentangled PS as a function of M_w revealed a temperature dependence to the stretching (or compressing) exponent, γ, on the intermediate scattering function (ISF) and the scaling of n, where $\tau_{NP} \sim q^{-n}$.[253] For example, sub-diffusion ($n>2$, $\gamma<1$) is observed at high temperatures, super-diffusion ($n<2$, $\gamma>1$) is observed at lower temperatures, and the crossover is at $1.25T_g$ where Brownian diffusion is observed ($n\sim2$, $\gamma\sim1$).[253] In another XPCS study of attractive 11 nm-diameter PEG-grafted SiO_2 NPs dispersed in PMMA of varying molecular weight,

Brownian diffusion is observed in unentangled melts but superdiffusion (n = 1, $\tau_{NP} \sim q^{-1}$) is observed above the entanglement molecular weight and the NP velocity is reasonably independent of M_w (Figure 1.17).[159] Observations of nondiffusive NP dynamics have also been reported in PNCs containing dilute[159] and concentrated[256,257] NP volume fractions, grafted[159,253] and bare[255] NPs, athermal[253,254] and attractive[159,254,255] interactions, and under various measurement conditions[260]. Interestingly however, Brownian diffusion has also been observed in XPCS of various PNC systems and conditions.[234,266,267]

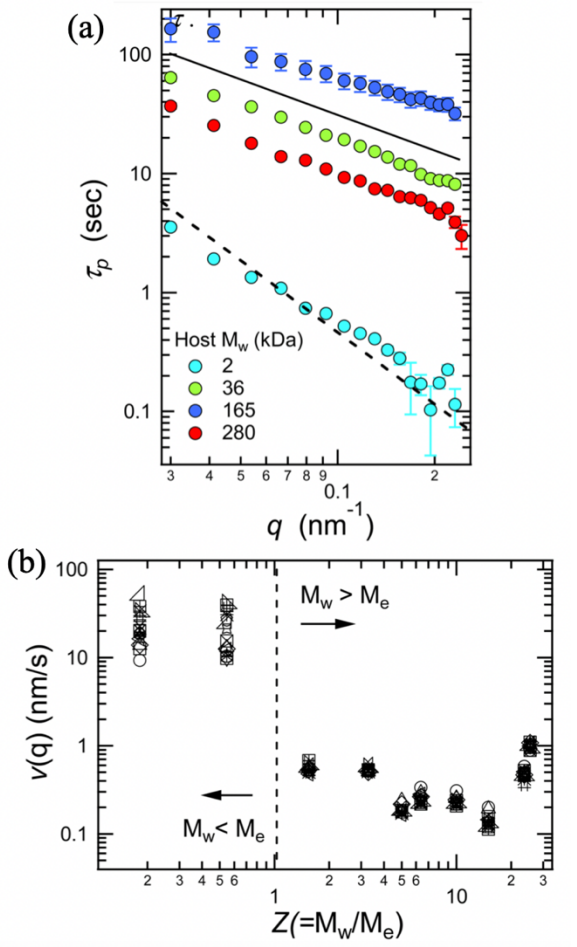

Figure 1.17: (a) Nanoparticle relaxation time as a function of q for PEG functionalized SiO_2 in PMMA of varying molecular weight. Solid line denotes superdiffusion (q^{-1}) and dashed line denotes Brownian diffusion (q^{-2}). (b) NP velocity extracted as the slope of (a) as a function of entanglements per chain. Different symbols represent different q. Adapted with permission from Ref 159. Copyright 2016, American Chemical Society.

The origins of anomalous NP dynamics in XPCS remain somewhat unclear. Superdiffusion, akin to a velocity, may occur when a probe experiences kinetic forces without drag forces (ballistic motion) or when a probe interacts with a gradient or field, among other scenarios. Fundamentally, XPCS measures the ensemble-averaged characteristic decorrelation time of the sample electron density distribution as a function of wave-vector, q.[268] Structural decorrelation on the order of $2\pi/q$ does not require NP diffusion on the order of $2\pi/q$, so the diffusion length can be somewhat unclear in XPCS. However, since XPCS samples length-scales beyond ~100 nm, it is unlikely that the observed super-diffusion rises from probing short-length scale ballistic motions, which are likely $<< R_{NP}$. Some authors surmise that superdiffusive dynamics show the NPs are coupling to internal stress fields, either caused by nonequilibrium and kinetically trapped chain conformations and stress fields in the PNCs or deformation caused by particle motion, both of which can provide elastic energy leading to superdiffusion.[159,256,258] This claim remains debated. Other authors surmise that observed non-diffusive motion results from NP-NP correlations, even in the dilute NP limit when no clear structure factor peak is observed. However, an apparent molecular weight effect in PNCs with similar structure (Figure 1.17) and diffusive measurements in lightly aggregated PNCs indicate that NP-NP correlations are not the predominant origin of anomalous dynamics.[159,234,255–257] As a final note, XPCS requires high-brilliance X-ray radiation for prolonged periods of time, and although beamlines monitor sample degradation and try to reduce exposure time and flux, the potential impact of beam damage (albeit largely unknown) has been noted.[269–271] Future studies should aim to further understand the origin of this non-diffusive behavior and develop new and complimentary methods to systematically probe NP motion on similar timescales and compare directly to XPCS.

1.7 Outline of Thesis Chapters

This thesis fundamentally examines multiscale polymer and nanoparticle dynamics in model polymer nanocomposites using experiments and simulations. As discussed in Section 1.2, many macroscopic properties of PNCs are dictated by microscopic dynamic processes, including the dynamics of the polymer segments, chains, and NPs. However, a fundamental understanding of these dynamic processes remains poorly understood, especially with respect to the expansive parameter space presented by these multicomponent materials. As such, this thesis aims to navigate the hierarchy of PNC dynamics and highlight the coupling nature of NPs and polymers in melt PNCs.

Although each chapter is introduced below, the organization of this dissertation is as follows. Chapter 2 and Chapter 3 survey segmental dynamics in attractive PNCs while Chapter 4 and Chapter 5 survey chain-scale motion in athermal and attractive PNCs, respectively. Multiscale polymer and NP dynamics in attractive PNCs with very small NPs are surveyed in Chapter 6. Finally, Appendix E presents an experimental protocol to vary the NP-polymer interaction while Appendix F and Appendix G present preliminary results for NP diffusion in attractive PNCs and the bound polymer layer in PNC solutions (respectively).

Chapter 2 uses temperature-modulated differential scanning calorimetry (TMDSC) and quasi-elastic neutron scattering (QENS) to systematically study the influence of highly attractive NPs to polymer segmental dynamics, particularly at small length scales (~1 nm) and fast timescales (~1 ns). Using P2VP/SiO_2 PNCs, we measure the segmental mobility and characterize the segmental diffusion coefficient as a function of NP concentration, temperature, and matrix molecular weight. We show that segmental mobility is decreased in PNCs relative to bulk at all temperatures, primarily due to relaxations at the NP-polymer interface. Interestingly, we find that this reduction in segmental dynamics is very weakly dependent on P2VP molecular weight, which

stands in contrast to the documented molecular weight effect on segmental dynamics in attractive polymer nanocomposites at lower temperatures, as observed by TMDSC.

In Chapter 3, we further probe the segmental dynamics in P2VP/SiO_2 PNCs more mechanistically using the unique capability of deuterium and hydrogen labeling that QENS offers. Specifically, we study neat polymer and PNCs composed of fully protonated P2VP (where the dynamics of all protons are measured) and backbone deuterated dP2VP (where only the dynamics of the pendent pyridine ring are measured). In the melt state at $T>T_g$, we find that protons on the pendent group are slightly more mobile than backbone protons, but the normalized diffusion coefficient of segments is ~35% slower than bulk in both PNC samples. This observation highlights the connection between backbone and pyridine motion, even in PNCs where the motion is temporally slowed by attractive NPs, and provides fundamental insights into the segmental diffusion process in PNCs.

To probe polymer motion at longer length-scales, Chapter 4 presents coarse-grained molecular dynamics simulations of a monolayer of hexagonally-packed NPs in a polymer melt. In doing so, we observe the magnitude and length-scale over which homogeneously confining NPs impact the polymer conformations and diffusion. We show conformations under strong confinement (i.e. the interparticle distance, ID, is less than twice the polymer radius of gyration, $2R_g$) are more impacted than around an isolated NP, and the effect depends on the ratio of R_{NP}/R_g rather than either independently. We then show the polymer diffusion is slowed by the presence of NPs and persists more than five times beyond the length-scale over which polymer conformations are perturbed, which is ~R_g. Furthermore, by analyzing the directional van Hove distributions, we show polymer preferentially diffuses away from the NP monolayer, diffusion through the monolayer is slowed as a function of confinement, and diffusion away from the NP monolayer remains bulk-like.

In Chapter 5, we develop and apply ion scattering measurements that separate and directly measure the fraction of free polymer and polymer adsorbed to attractive NPs entirely in the melt state. By annealing thin PNC films of P2VP/SiO_2 deposited on bulk polymer matrices, free polymer from the PNC rapidly diffuses into the underlying matrix while the spontaneously-formed bound polymer remains with the NPs. Correlations of the fraction of bound chains and the NP surface area provide measurements of the bound polymer layer thickness (~R_g) and show the average surface area occupied by adsorbed chains in the melt is much smaller than predicted from an isolated chain or measured in solution. The bound polymer fraction decreases as a function of annealing time and decreases more rapidly at higher temperatures and for lower molecular weights, but even after annealing more than 10^6 reptation times, some polymer remains bound to the NPs.

In Chapter 6, we study multiscale dynamics of polymer segments, polymer chains, and NPs in mixtures of entangled P2VP with very small, attractive octa(aminophenyl) polyhedral oligomeric silsesquioxane (OAPS, R_{NP} ~ 0.9 nm). With increasing OAPS concentration, both the segment reorientational relaxation rate (measured by dielectric spectroscopy) and polymer chain center-of-mass diffusion coefficient (measured by elastic recoil detection) are substantially reduced. This commensurate slowing of both the segmental relaxation and chain diffusion process is fundamentally different than the case of PNCs composed of larger, immobile nanoparticles (Chapter 2 and Chapter 5). Next, using RBS to probe the NP diffusion process, we find that small OAPS NPs diffuse anomalously fast in these P2VP-based PNCs. The OAPS diffusion coefficients are found to scale very weakly with molecular weight, $M_w^{-0.7\pm0.1}$, and our analysis shows that this characteristic OAPS diffusion rate occurs on intermediate microscopic time scales, lying between the Rouse time of a Kuhn monomer and the Rouse time of an entanglement strand. The motion of the polymer and the NPs in this unique system support the recently developed theory of vehicle diffusion.

Chapter 7 summarizes the conclusions of this dissertation and includes a discussion of several directions of recommended future work. Appendix A, B, C, and D provide supporting information for Chapters 2, 3, 5, and 6, respectively. Appendix E discusses procedures and methodology for functionalizing SiO_2 NPs to control the NP surface energy. Appendix F discusses measurements of NP dynamics in entangled polymer melts using X-ray Photon Correlation Spectroscopy (XPCS). Appendix G presents preliminary small-angle neutron scattering measurements that probe the bound polymer layer in PNC solutions.

CHAPTER 2: Segmental Diffusion in Attractive Polymer Nanocomposites: A Quasi-Elastic Neutron Scattering Study

Content in this chapter was published in 2019 in *Macromolecules*, volume 52, issue 2, pages 669-678, in a modified version. The authors of this chapter are Eric J. Bailey, Philip J. Griffin, Madhusudan Tyagi, and Karen I. Winey.

2.1 Introduction

The addition of nanoparticles (NPs) to a polymer matrix, forming a polymer nanocomposite (PNC), can significantly enhance the thermal, mechanical, and functional properties of the host matrix.[2,4] Furthermore, PNC materials have wide-ranging tunable properties that can be dominated by the polymer, the nanostructured filler, or the interfacial region. As such, they are appealing materials for a variety of fields. Several questions still exist regarding the dynamic properties of free and interfacial chains. Polymer dynamics in polymer nanocomposites and polymer melts significantly influence or dictate their processability, applications, glass transition temperature (T_g), and various macroscopic properties (such as creep, toughness, and transport). In addition, due to the large surface area to volume ratio of NPs, PNCs are a model system to study the perturbation to polymer dynamics caused by a solid interface.

At the largest length scale, elastic recoil detection measurements have been conducted to probe center-of-mass polymer chain diffusion in PNCs with NPs that are athermal[170], attractive[272], grafted[182] and anisotropic[196,197,201,273]. This work has recently been reviewed.[26] Similar dynamics were probed using nuclear-magnetic-resonance techniques as well.[189] On a smaller length scale, segmental dynamics in PNCs have received more attention due to their relevance toward ion transport, small molecule separation, and the glass transition. This topic has also recently been reviewed from different perspectives.[29,36,54,270,274] However, additional fundamental studies are

needed to explore the complex parameter space and understand the underlying physics of interfacial and confined polymer dynamics.

There are several methods that can be used to analyze segmental dynamics including nuclear magnetic resonance (NMR), dynamic mechanical measurements (DMA), broadband dielectric spectroscopy (BDS), temperature-modulated differential scanning calorimetry (TMDSC), neutron spin echo (NSE) and quasi-elastic neutron scattering (QENS). The approximate timescales associated with many of these measurement techniques, as they pertain to segmental dynamics, are schematically represented in Figure 2.1. Also included in Figure 2.1 is a characteristic polymer segmental relaxation (α-process) curve following Vogel-Fulcher-Tammann (VFT) temperature dependence,

$$\tau(T) = \tau_0 \exp\left(\frac{B}{T-T_0}\right) \qquad (2.1)$$

where τ_0, B and T_0 are fitting parameters related to high temperature relaxation time, fragility, and Vogel temperature, respectively. To probe the α-process with a particular technique, the measurement temperature must be chosen such that the α-process falls within the accessible temporal window of the technique. For example, TMDSC measurements are particularly useful for measurements near T_g (~0.5 – 50 s) and BDS is useful for its coverage of over 6 decades in relaxation times at temperatures above T_g.[57] QENS, the focus of this paper, has the advantage of spanning even shorter time scales while providing simultaneous temporal and spatial information to capture the timescales and geometries of measured motions.

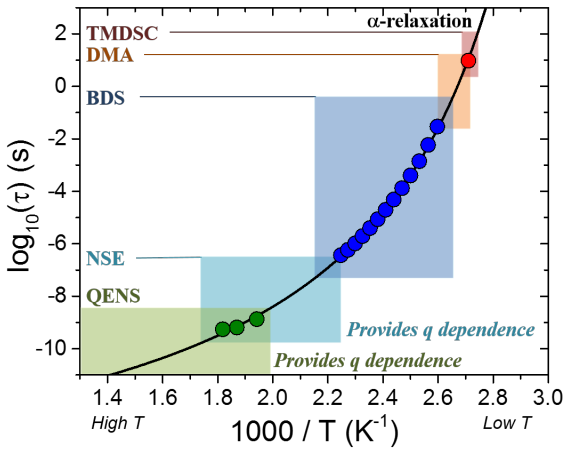

Figure 2.1: Primary segmental relaxation times (α-process) of bulk polymer as a function of inverse temperature. Approximate time scales for five techniques, and their corresponding temperatures, are depicted by shaded regions along the relaxation curve. Not depicted is NMR, which is used to characterize various polymer dynamic processes over several orders of magnitude. Black line represents VFT fit for bulk 40 kg/mol P2VP measured via TMDSC (red circle), BDS (blue circle), and QENS (green circle).

QENS measurements have been performed on filled rubber[107,275], polymer/layered silicate nanocomposites[24,276], and other PNC systems[77,95,127,141,260,277,278]. For example, in a PNC where free chains were removed by extraction, Roh et al. found slower relaxations and increased dynamic heterogeneity for 1,4-polybutadiene segments near aggregated carbon black NPs compared to segments in bulk polymer.[107] For crystalline poly(dimethyl siloxane)/SiO_2 PNCs, multiple polymer processes were analyzed and generally, bulk-like dynamics were measured below the polymer glass transition while slow dynamics attributed to interfacial polymer were identified at higher temperatures.[278] Additionally, QENS and NSE experiments on low molecular weight polyethylene glycol and SiO_2 (an attractive interaction) shows physically adsorbed chains are dynamically active with pico-second segmental dynamics at 413 K, but slowed relative to bulk.[77]

Recently, polymer nanocomposites comprising poly(2-vinyl pyridine) (P2VP) and colloidal silica (SiO_2) have emerged as model systems for studying the properties of attractive PNCs.[65,69,208] In these systems, it has been experimentally shown that a physically adsorbed bound polymer layer of thickness ~R_g spontaneously forms on the NP surface in solution and persists in

the melt state.[208] On the atomic level, hydrogen bonding between the nitrogen in P2VP and native hydroxyl groups on the surface of SiO_2 was directly observed by sum frequency generation and X-ray photoelectron spectroscopic techniques.[69] The segmental dynamics of P2VP/SiO_2 PNCs have also been studied by dielectric spectroscopy as a function of NP concentration[65], NP size[66], polymer molecular weight[73], and interfacial bonding strength[88]. An interfacial layer on the order of a few nanometers with suppressed segmental dynamics has been identified in these experiments, and the degree to which the dynamics are suppressed increases with decreasing polymer molecular weight, among other characteristics.[29,69,73] Analysis of small-angle X-ray scattering[73], pycnometry data[69], and various spectroscopic techniques[69] suggest that shorter chains pack more efficiently at the NP surface, leading to a greater fraction of physisorbed segments, slower interfacial dynamics, and a thicker interfacial layer. Despite this progress, a recent review by Sokolov et al. highlighted that the impact of temperature on the structure and dynamics of interfacial polymer, and whether the molecular weight effect is a kinetically trapped phenomena or an equilibrium state, remains an open question.

In this article, we present a systematic study of segmental dynamics in attractive polymer nanocomposites comprising P2VP and colloidal SiO_2 NPs using TMDSC ($T\sim T_g$) and QENS ($T\sim T_g$+150K). We show that motions of P2VP segments on ~1 nm length scales and ~1 ns time scales are well described by classic translational diffusion, even at NP concentrations of ~50 vol% where the average interparticle spacing is ~2 nm. The average segmental diffusion coefficient decreases with increasing NP concentration by up to a factor of ~5 and is mostly independent of temperature over the studied temperature range. In contrast to the well-documented molecular weight dependence of segmental diffusion in the deeply supercooled regime, our measurements of the same dynamic process at higher temperatures show reduced segmental dynamics that are largely independent of matrix molecular weight. Finally, by comparing TMDSC, BDS, and QENS, our results suggest that temperature has a significant impact on the NP-induced perturbation to

segmental dynamics in PNCs and highlights the unique and complementary insights that can be provided by QENS.

2.2 Experimental Section

Materials: All poly(2-vinylpyridine) (P2VP) was purchased from Scientific Polymer Products, Inc. and used as received. To study the molecular weight dependence of interfacial dynamics, unentangled (10 kg/mol), lightly-entangled (40 kg/mol), and well-entangled (190 kg/mol, $M/M_e \approx 11$) P2VP were also studied.[208] Throughout this paper, these samples will be referred to as 10, 40, and 190 kg/mol although the weight average molecular weights were measured using GPC and are listed in Table 2.1. All measured molecular weight dispersities were < 1.3. To study the role of NP concentration and temperature on polymer segmental dynamics, PNCs were fabricated with 40 kg/mol P2VP. Silica NPs were synthesized following the modified Stöber[279,280] method with a log-normal geometric mean diameter (d_{NP}) of 26.1 nm and standard deviation standard deviation $e^{\sigma} = 1.2$ as determined by analysis of transmission electron micrographs (TEM).[208]

Table 2.1: Nanocomposite details including P2VP molecular weight, NP concentration (ϕ_{NP}), calorimetric T_g of bulk polymer and PNCs, measurement temperatures for QENS, and degradation temperature taken as the temperature of 5% mass loss in bulk polymer. All P2VP molecular weight dispersities are < 1.3.

M_w (kg/mol)	ϕ_{NP} (vol%)	Bulk T_g (K)	PNC T_g (K)	ΔT_g (K) (T_g^{PNC}-T_g^{bulk})	QENS Temper-ature (K)	Bulk Degradation Temperature (K)
9.9	24.2	362.4	366.6	4.2	525	615
39.3	25.3	369.0	370.2	1.2	550, 535, 515, 480	626
188	25.4	376.2	376.7	0.5	535	626
39.3	52.7	369.0	372.3	3.3	550, 535, 515	626

PNC Preparation: PNC samples were made by solution mixing of P2VP/MeOH ($c_{polymer}$ < 2 wt %) with the appropriate amount of SiO_2/EtOH ($c_{NP} \approx$ 15 mg/mL) to achieve desired NP concentrations (25 or 50 vol%). Solutions were continuously stirred for at least 12 hours to ensure homogeneous dispersion of NPs. The P2VP/SiO_2 mixture in solution has good dispersion as found by dynamic light scattering, where a single peak at ~d_{NP} was observed. Bulk polymer and PNC solutions were drop casted in Teflon dishes and dried in ambient conditions for 24 hours, then annealed at T_g+60 K for at least 12 hours under vacuum. Representative TEM micrographs illustrate that NPs remain well-dispersed in the as-dried PNCs (Figure A.1). The presence of a physically adsorbed bound layer in P2VP/SiO_2 PNCs is known to promote good NP dispersion and prevent NP-NP aggregation.[88,208,210]

Thermogravimetric Analysis (TGA): Polymer degradation behavior and NP concentrations were measured via TGA using a TA instruments SDT Q600. For each measurement, a sample of 5-10 mg was placed in a platinum pan and heated from 300 K to ~1100 K at a rate of 5 K/min under air purge. NP concentrations listed in Table 1 were calculated with the TGA results and densities of 1.2 and 2.3 g/cm^3 for P2VP and SiO_2, respectively.[73]

Temperature-Modulated Differential Scanning Calorimetry (TMDSC): The calorimetric glass transition was measured via TMDSC with a TA Instruments Q2000. All

measurements were made upon cooling a sample of ≥ 5 mg of polymer at a rate of 5 K/min with a modulation time of 30 sec and amplitude of ±0.5 K over a temperature range of $T_g \pm 60$ K. T_g was defined as the inflection point of the heat flow thermograms and all results were reproduced.

Broadband Dielectric Spectroscopy (BDS): Segmental dynamics of bulk P2VP was measured with BDS using a Solartron ModuLab XM MTS with the femto-ammeter accessory. Polymer films were placed between steel electrodes and separated with 50 μm silica spacers. Samples were annealed in the cryostat at 420 K until the imaginary permittivity spectra stopped changing. Isothermal frequency sweeps from 10^{-1} – 10^{6} Hz were measured every 5 K between 380 and 450 K on cooling. Measurements were made after heating again to ensure reproducibility.

Quasi-Elastic Neutron Scattering (QENS): Inelastic neutron scattering measures the double differential scattering cross-section ($d^2\sigma/d\Omega d\omega$), which is related to the probability that a given incident neutron is scattered into a solid angle $d\Omega$ with an energy transfer $d\omega$. The double differential scattering cross-section has incoherent and coherent contributions, each of which can be expanded and related to the dynamic structure factors:

$$\frac{d^2\sigma}{d\Omega d\omega} = \left(\frac{d^2\sigma}{d\Omega d\omega}\right)_{inc} + \left(\frac{d^2\sigma}{d\Omega d\omega}\right)_{coh} = \frac{k_1}{k_0 4\pi} N \left[\sigma_{inc} S_{inc}(q,\omega) + \sigma_{coh} S_{coh}(q,\omega) \right] \quad (2.2)$$

where k_0 and k_1 are the magnitude of incident and final wave vectors, respectively, N is the number of nuclei, σ is the incoherent and coherent scattering cross sections of the nuclei, and S(q, ω) is the incoherent and coherent dynamic structure factors. Because σ_{inc}^{H} (~80 barns) is much larger than all other atoms in this system (σ_{other} < ~6 barns), we can generally assume that the signal is dominated by the incoherent contribution to Equation 2.2.[281] For example, using Equation 2.2, ~90% of the signal in P2VP is incoherent and even at our maximum SiO_2 concentration of 50 vol%, the polymer accounts for ~63% of the total scattering.[281] $S_{inc}(q, \omega)$ is the time and space Fourier transform of the self-part of the van Hove correlation function and combines spatial ($q=k_1-k_0$) and

temporal (ω) information for correlations between the single nuclei.[282] Quasi-elastic neutron scattering measures $S_{inc}(q, \omega)$ centered at ω=0, and is typically used to probe diffusive motions on molecular length scales.

QENS measurements were made at the High-Flux Backscattering Spectrometer (HFBS, NG2) at the NIST center of neutron research in Gaithersburg, MD, USA.[283] Samples containing at least 200 mg of polymer were folded and sandwiched into aluminum foil and placed in cylindrical aluminum cans for measurements. Each sample was approximately 50 μm thick.

First, in a fixed window scan (FWS), the elastic scattering intensity $S_{inc}(q, \omega=0)$ was measured as a function of temperature, starting at 50 K with a heating rate of 1 K/min. Second, $S_{inc}(q,\omega)$ was measured at select temperatures over a q-range of 0.25–1.75 $Å^{-1}$ and an energy range spanning -17–17 μeV (with a resolution of 0.8 μeV as defined by the elastic scattering of vanadium at 50 K). These q- and energy ranges correspond to molecular dynamic processes with length and time scales of approximately 3–25 Å and 40 ps–2 ns, respectively. The measurement temperatures were guided by extrapolating dielectric relaxation times (similar to Figure 2.1) and further refined by choosing a temperature where mean squared displacements measured via FWS were ~7 $Å^2$ or at least 3 $Å^2$ for the lowest temperature measurements. QENS spectra were collected for 12 hours under vacuum after a 30-minute equilibration at the measurement temperature. Analysis was primarily conducted in DAVE software.[284]

In this PNC system, relatively high temperatures are necessary to observe the segmental diffusion process in the dynamic window of QENS and are mostly unexplored. The thermal degradation temperatures of bulk P2VP, as defined by the temperature at which 5 wt% polymer is lost in TGA are >600 K (Table 1). (Full thermograms are presented in Figure A.2.) The maximum temperature of FWSs and QENS measurements are sufficiently below the onset of thermal degradation, by at least 75 K (Table 2.1). Nevertheless, a thorough analysis of molecular weight

(GPC), T_g (TMDSC) and thermal degradation (TGA) of samples after QENS measurements are presented in Section A.9. Although the thermal degradation behavior did not change after measurements (Figure A.10), the molecular weight and glass transition temperature decreased slightly (Table A.1 and Figure A.9, respectively). It is important to note that molecular weights measured after QENS measurements are still categorically different and span the unentangled to well-entangled regimes. These changes in chain length and T_g are expected from slight polymer degradation, but do not affect the reported measurements of segmental dynamics or main conclusions of this work.[285] To confirm this, Section A.9 also includes a time-dependent analysis of QENS, showing the sample measurement was the same at the beginning and end of the experiment. This result demonstrates the reliability of these QENS measurements.

2.3 Results

The glass transition temperature (T_g) of P2VP/SiO_2 PNCs as measured by TMDSC are shown in Figure 2.2 and listed in Table 2.1. The absolute T_g shown in Figure 2.2 increases with P2VP molecular weight (MW) and NP concentration (Figure 2.2, 40 kg/mol). It is well-established that the addition of highly attractive NPs causes an increase in T_g resulting from the slowing down of the primary structural relaxation (α-process) at the NP-polymer interface.[29] As such, it is expected that increased NP concentration causes an increase in T_g due to the larger volume fraction of 'interfacial' polymer affected by the NP surface. Furthermore, the impact of the same concentration of NPs is much more pronounced for unentangled polymer (~4 K for 10 kg/mol P2VP) than in well-entangled polymer (<1 K for 190 kg/mol P2VP). This increased perturbation for lower molecular weight PNCs has recently been reported and described by differences in interfacial packing.[69,73,88] Importantly, our measurements agree with calorimetric measurements of T_g on similar systems.[65,73,88]

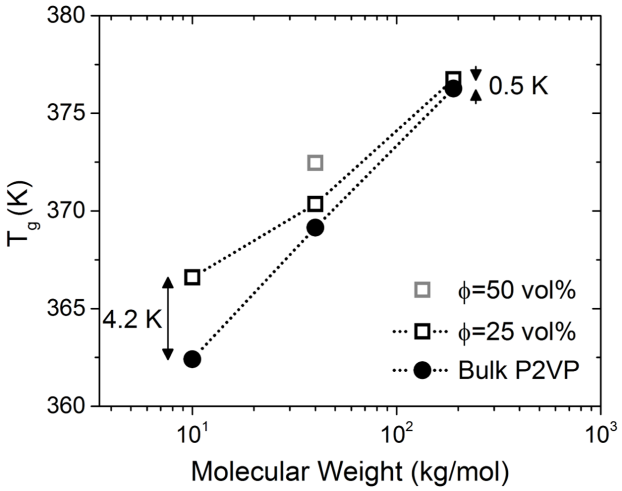

Figure 2.2: Absolute glass transition temperature (T_g) as measured by TMDSC for each molecular weight and NP concentration studied. Difference in T_g between P2VP with 25 vol% SiO_2 and bulk P2VP is labelled for 10 and 190 kg/mol P2VP.

2.3.1 Effect of NP Concentration on Segmental Mobility

To further understand segmental dynamics in these PNCs at elevated temperatures, we use neutron scattering to measure PNCs with modest molecular weight (lightly entangled, 40 kg/mol) and NP concentrations of 25 and 50 vol%. First, the elastic scattering of each sample was measured as a function of temperature from 50 K to 550 K in a FWS. The mean-squared displacement ($\langle x^2 \rangle$) was determined using the Debye-Waller approximation, as discussed in Section 3 of Supplemental Information.[286,287] Figure 2.3 displays the fitting results where $\langle x^2(T) \rangle$ is shown relative to $\langle x^2(T=T_g^{bulk} - 100\ K) \rangle$ and the temperature is plotted relative to T_g^{bulk}. Data without normalization is provided in Figure A.3.

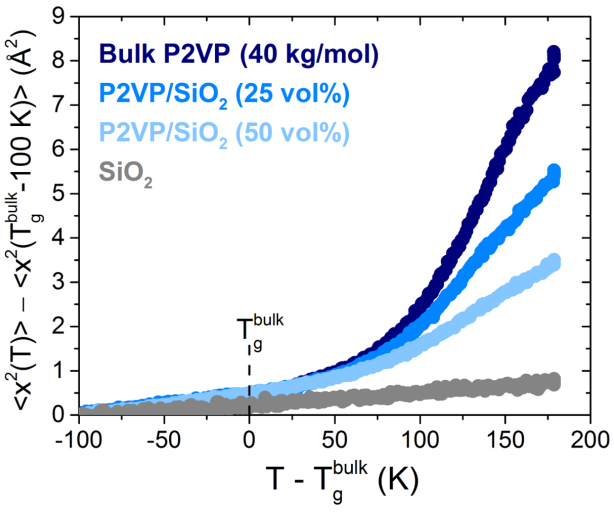

Figure 2.3: Average segmental mean-squared displacement (MSD) obtained from FWS of bulk 40 kg/mol P2VP and P2VP/SiO_2 PNCs with concentrations of 25 and 50 vol%. MSD is defined relative to T_g-100 K and temperature is defined relative to bulk calorimetric T_g. The MSD of nuclei in dried SiO_2 are shown for comparison and display expected linear Debye-like thermal motion.

P2VP segments in bulk and PNCs show similar low mobility for $T < T_g$, consistent with thermal harmonic vibrations in the glassy state.[286] For $T > T_g$, polymer segments exhibit a dramatic increase in $\langle x^2 \rangle$ as they become more mobile and are able to relax in the melt state. The bulk polymer and both PNCs show the change in slope occurring at similar $T\text{-}T_g^{bulk}$, as expected from the small increase in calorimetric T_g with the addition of NPs. However, at $T>T_g$, polymer segments in P2VP/SiO_2 PNCs show significantly reduced mobility with increasing NP concentration. Also shown in Figure 2.3 is a sample of SiO_2 NPs for comparison. Because the incoherent scattering cross-sections of hydrogen (σ_{inc}^{H} ~ 80 barns) is much larger than Si (σ_{inc}^{Si} ~ 0 barns and σ_{coh}^{Si} ~ 2.1 barns) and O (σ_{inc}^{O} ~ 0 barns and σ_{coh}^{O} ~ 4.2 barns), we expect the SiO_2 signal to be dominated by hydrogens in surface hydroxyl groups.[281] The MSD of nuclei in the dried SiO_2 NPs show no change of slope and minimal mobility over all temperatures, as expected from thermal vibrations.[76,287]

Figure 2.3 shows the overall mobility of hydrogens in the sample but it is difficult to separate various types of polymer motion by monitoring only the elastic scattering intensity. For

example, any protons mobile on the experimental length and time scale will contribute to $\langle x^2 \rangle$, regardless of their motion being diffusion, reorientations, rotations, or other motions. To better understand and characterize the segmental mobility and dynamic processes, isothermal QENS measurements of $S_S(q,\omega)$ were made. According to Figure 2.3, measurement temperatures of at least ~T_g+100 K will place segmental dynamics in the experimental length and time scale. Figure 2.4a shows a representative QENS spectrum of bulk 40 kg/mol P2VP at 550 K and q=1.21 Å^{-1} and is compared to P2VP with NP concentration of 25 and 50 vol% in Figure A.4.

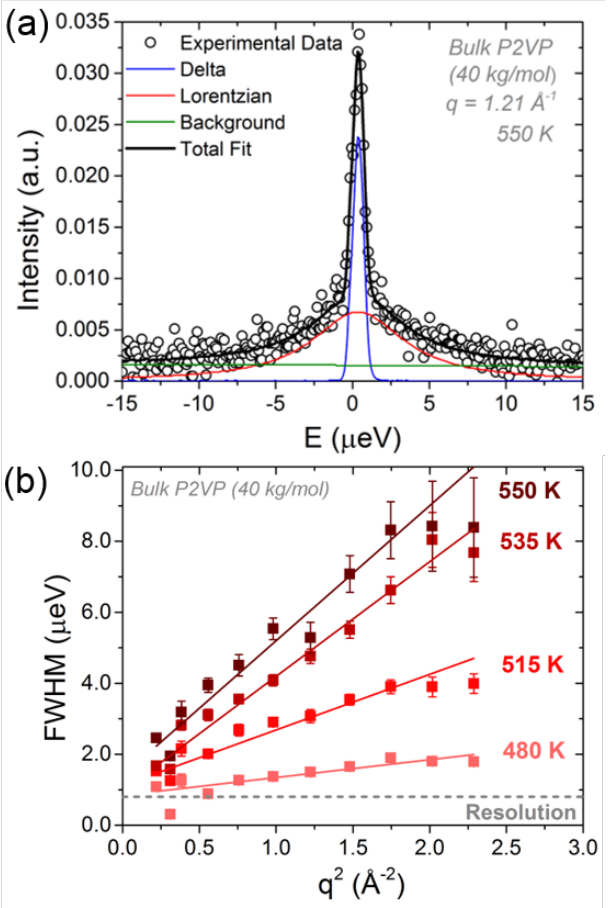

Figure 2.4: (a) Representative fit of experimental QENS spectra for bulk 40 kg/mol P2VP at 550 K (T_g+180 K) and q=1.21 Å^{-1}. (b) Quasi-elastic broadening (full width at half max of Lorentzian contribution) plotted as a function of q^2 for bulk P2VP at different temperatures. Measured broadening surpasses experimental resolution and clearly displays linear dependence, indicative of translational diffusive motions.

As shown in Figure 2.4a, a delta function is used to describe the elastic contribution, or signal from protons not moving within the experimental time window and length scale. A single Lorentzian is used to describe the quasi-elastic broadening (dynamics) and a linear function is included to represent background signal and dynamics much faster than the time window. The experimental data is fit by the linear combination of each contribution after convolution with a Gaussian representing experimental resolution. With this relatively simple single Lorentzian model, the data show no significant or systematic residuals (Figure A.4) and therefore more complex models, such as the addition of another Lorentzian, are unwarranted.

Figure 2.4b shows the full width at half max (FWHM) of the Lorentzian component for bulk 40 kg/mol P2VP plotted as a function of q^2 for several temperatures. The quasi-elastic broadening is found to increase linearly with q^2, indicative of translational diffusive motions where the slope is related to the diffusion coefficient ($FWHM \sim Dq^2$).[59] One may expect signatures of Rouse dynamics at low q (where $FWHM \sim q^4$)[59,141], but this is not apparent in our data. With a Kuhn segment length of ~1-2 nm for P2VP, the length scales probed by QENS are likely smaller than those associated with Rouse dynamics.[74] The apparent non-zero y-intercept in Figure 2.4b is expected from the presence of q-independent reorientational motions (such as pyridine ring fluctuations or β-relaxations) as well as potential contributions from multiple scattering events, which are expected to be minimal for the present sample dimensions. More complex models, such as jump diffusion[59], are often applied to polymeric systems but do not appreciably improve the fits as compared to the translational diffusion model for both bulk P2VP and PNCs. Importantly, the observed quasi-elastic broadening is substantially larger than the energy resolution, especially for $T \geq 515$ K. As expected, at higher temperatures, the observed FWHM increases as segmental mobility increases.

Using 535 K as an example, Figure 2.5a shows the quasi-elastic broadening is reduced with increasing SiO_2 NP concentration. The q-dependence of the FWHM for all systems and all

measurement temperatures are included in Figure 2.4b and S5. Using the translational diffusion model, the segmental diffusion coefficients (D_α) were extracted from the slope of Figure 2.5a and are plotted as a function of inverse temperature in Figure 2.5b. These extracted diffusion coefficients can be directly compared to TMDSC and BDS through $\tau \sim (D_\alpha q^2)^{-1}$ where a q of 0.63 $Å^{-1}$ was chosen. As shown in Figure 2.1, the measured QENS relaxations times for bulk 40 kg/mol P2VP at T > 515 K are consistent with BDS and TMDSC measurements, suggesting that the observed dynamics are related to the primary structural relaxation process. A detailed discussion of analysis for BDS measurements and a comparison to literature is provided in Section A.7

At the high measurement temperatures ($T>T_g+100$ K) and over the narrow temperature range studied by QENS, D_α shows Arrhenius behavior for bulk and PNC materials (Figure 2.5b). Although $D_{\alpha,PNC} < D_{\alpha,Bulk}$, all materials exhibit similar activation energies. The effect of NP concentration is further highlighted by normalizing D_α relative to bulk measurements at the same temperature (Figure 2.5c) showing a monotonic decrease in the average polymer segmental diffusion coefficient with increasing NP concentration. Specifically, D_α drops by ~40% with 25 vol% NP and ~80% with 50 vol% NP concentration when P2VP is lightly entangled. Furthermore, over the narrow temperature range measured, the reduction in diffusion coefficient is independent of temperature within experimental error. This slowing of segmental dynamics with increased NP concentration is consistent with the increase in T_g (Figure 2.2) and decrease in MSD for all $T>T_g$ (Figure 2.3), despite the isolation of diffusive motions of protons.

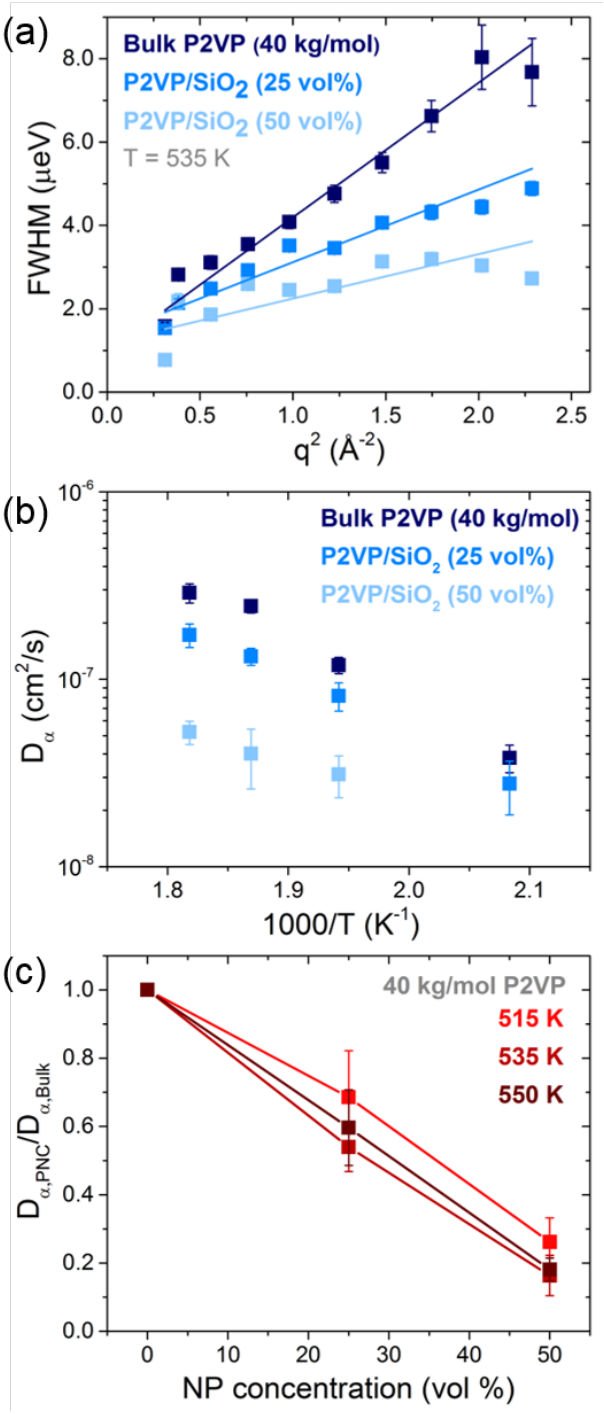

Figure 2.5: (a) FWHM of P2VP and P2VP/SiO_2 PNCs as a function of q^2 for measurements at 535 K. (b) Translational segmental diffusion coefficient as a function of temperature for all 40 kg/mol bulk and PNC measurements. (c) Reduced segmental diffusion coefficient (relative to bulk) as a function of NP concentration.

Assuming monodisperse NPs randomly dispersed in the polymer matrix, the average interparticle distance (ID) is given as $ID=d_{NP}\left[\left(2/\left(\pi\phi_{NP}\right)\right)^{1/3}-1\right]$ where d_{NP} and ϕ_{NP} are the NP diameter and volume fraction, respectively.[96] Thus, at ϕ_{NP} = 25 and 50 vol%, ID is ~9.5 nm and ~2.2 nm, respectively. From dynamic and static measurements from various techniques, the length scale of the perturbed interfacial layer (from the perspective of segmental dynamics) is often reported as ~2-5 nm from the NP surface.[29] As such, to a first approximation, the 50 vol% PNC can be considered an "all-interfacial" PNC wherein nearly all of the polymer segments are within the interfacial layer. Therefore, Figure 2.5c suggests that the interfacial layer in this strongly attractive PNC system is dynamically active at these high temperatures and the measured segmental diffusion coefficient from QENS is slowed by nearly one order of magnitude.

2.3.2 Effect of Chain Length on Interfacial Dynamics

To study the effect of molecular weight on interfacial dynamics, we studied PNCs with 25 vol% SiO_2 dispersed in P2VP with molecular weights ranging from unentangled to well-entangled (10, 40, and 190 kg/mol), Table 2.1. The results from FWSs for each polymer and PNC are shown in Figure 2.6. To account for the molecular weight dependence of T_g^{bulk} (Figure 2.2), $\langle x^2 \rangle$ is normalized to $T=T_g^{bulk} - 100$ K and temperature is presented relative to T_g^{bulk}. Data from all three MWs essentially collapse onto a master curve for bulk polymer and 25 vol% PNCs, showing that segmental mobility is largely independent of molecular weight (even in the case of PNCs).

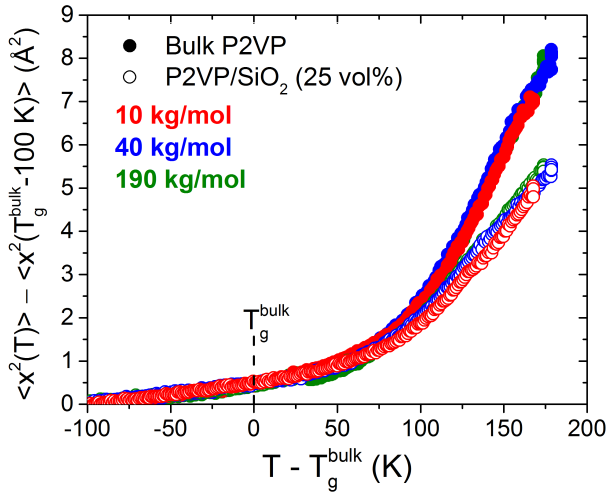

Figure 2.6: Average mean-squared displacement of segments for different polymer molecular weights as a function of temperature. MSD is presented relative to T_g^{bulk} – 100 K as a function of temperature relative to T_g^{bulk}.

Isothermal QENS measurements were performed at 525, 535, and 535 K for PNCs and bulk polymers with MWs of 10, 40, and 190 kg/mol, respectively. At these temperatures, which are all ~T_g^{bulk}+160 K, segments in bulk exhibit a similar average MSD (~7 Å^2 relative to $\langle x^2 \rangle$ at T=50 K), as shown in Figure A.3. Given the weak temperature dependence of $D_{\alpha,PNC}$ / $D_{\alpha,Bulk}$ (Figure 2.5c), we will compare these QENS measurements as isothermal.

All bulk and PNC materials exhibit classic characteristics of translational segmental diffusion (FWHM ~ $D_\alpha q^2$), as shown in Figure 2.5a and Figure A.7. Figure 2.7a shows that D_α for bulk P2VP is approximately independent of MW, differing by less than 30% from each other. Small variations in bulk D_α are attributed to slight differences in measurement temperature relative to T_g (Table 2.1, Figure 2.2) and fragility. The measured D_α values for 25 vol% PNCs are also shown in Figure 2.7a and the segmental diffusion coefficients are significantly suppressed upon the addition of attractive NPs.

To quantitatively compare the impact of molecular weight on segmental diffusion in PNCs, $D_{\alpha,PNC}$ is normalized by $D_{\alpha,Bulk}$ in Figure 2.7b. The error bars in Figure 2.7b represent the propagated

error in fitting the q^2 dependence of the quasi-elastic broadening and do not include the errors associated with small differences in NP concentration, measurement temperatures, etc. For all molecular weights of P2VP, the addition of 25 vol% SiO_2 NPs causes a substantial reduction in the average segmental diffusion coefficient. For PNCs with 10 kg/mol and 190 kg/mol P2VP, $D_{\alpha,PNC}/D_{\alpha,bulk}$ is 42±5% (T=525 K) and 61±8% (T=535 K), respectively. These conclusions are similar to those from the FWS presented in Figure 2.6, that the addition of NPs significantly reduces the segmental dynamics in PNCs but the effect is weakly dependent on molecular weight. In contrast, a much stronger molecular weight dependence was observed in the difference between T_g in PNCs and bulk (ΔT_g): 4.2 K for 10 kg/mol and 0.5 for 190 kg/mol (Figure 2.2). In addition, at the highest molecular weight of 190 kg/mol, although T_g approaches the bulk value, the dynamics measured by QENS at high temperature are still measurably reduced.

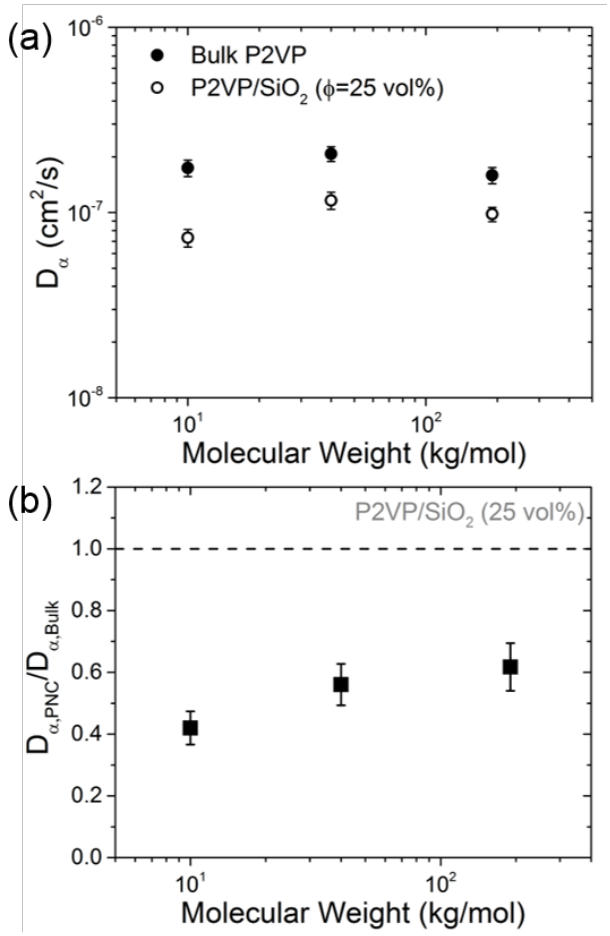

Figure 2.7: (a) Measured diffusion coefficient as a function of molecular weight for bulk and 25 vol% PNCs. (b) Reduced diffusion coefficient as a function of polymer molecular weight.

2.4 Discussion

These QENS measurements at high temperatures correspond to time and space correlations at fast time scales (~1 ns) and short length scales (< ~2 nm). In this regime, we observed that the time scale of polymer relaxation increases with the length scale squared, consistent with translational diffusive motion. We expect that the observed diffusion process is dominated by the primary structural relaxation (α-process), rather than a secondary relaxation (β-process).[65,127,288,289] Unlike our observations of slower segmental dynamics in PNCs, recent neutron and light scattering measurements showed β-relaxations faster than bulk in P2VP/SiO_2 PNCs at 300 K.[127] Our α-process assignment is further supported by the agreement between TMDSC, BDS, and QENS

measurements of bulk P2VP in Figure 2.1. Note that the α- and β-processes are expected to converge at high temperatures, but BDS, NMR, or QENS measurements at lower temperatures might be able to separate their contributions.

The bulk polymer and PNCs in our measurements exhibit similar q^2-dependence of quasielastic broadening, differing only in the value of the observed segmental diffusion coefficient (Figure 2.5c). Surprisingly, this suggests that the measured dynamics are significantly perturbed temporally and relatively unperturbed spatially in our q-range corresponding to ~0.5 – 2 nm. It is reasonable to expect segments beyond 2 nm from the NP surface to relax spatially bulk-like (from the perspective of QENS) because their local environment is similar to bulk polymer. Since most segments, especially in PNCs with 25 vol% NPs (ID~9.5 nm), are far enough from the NP surface, our measurements show no significant changes in the q^2-dependence of the dynamics. To further confirm this hypothesis, measurements over a larger q-range are necessary. Nevertheless, since we observe temporal perturbations without spatial perturbations, our results imply that the impact of a NP surface is farther ranging temporally than spatially.

The reduction in normalized D_α with increased concentration of attractive NPs measured by QENS at high temperatures (Figure 2.5c) captures the slow segmental motion observed in BDS[65] and TMDSC (Figure 2.2). In BDS, the mean molecular relaxation time in similar PNCs is nominally unchanged[290] and requires detailed analysis to reveal a second relaxation that is nearly two orders of magnitude slower.[58] In contrast, our QENS analysis provides an average diffusion coefficient that is significantly reduced suggesting that this method is insensitive to the faster diffusion corresponding to bulk-like P2VP. Others have reported similar findings when comparing inelastic neutron scattering and other techniques, including NMR[77] and ellipsometry[76]. This has been explained by differences in dynamic sampling, wherein inelastic neutron scattering is biased to the slower processes.[76] This is consistent with our data. We extract an average diffusion

coefficient in PNC systems that is slower than that of bulk, even when the interparticle distance is nearly 10x larger than the measurement length scale. The discrepancy between neutron scattering and other techniques has also been described in terms of technique sensitivity and dynamic range, where the spectral shape is analyzed over only one order of magnitude in QENS (Figure 2.1). This is also consistent with our PNC data being described by a single Lorentzian, despite the known heterogenous dynamic environment PNCs. Our direct comparison of TMDSC and QENS, along with similar measurements from BDS[65], demonstrate that considering differences in experimental probes and sensitivities is critical in future comparisons, especially in heterogeneous materials such as PNCs.

In QENS, when a segment relaxes slower than the experimental time scale (~2 ns), it appears immobile and therefore contributes to the elastic peak and is excluded from the QENS broadening analysis. This effect can be directly quantified by the elastic incoherent structure factor (EISF), which represents the fraction of immobile nuclei and is calculated by the area of the elastic contribution relative to the sum of the elastic and quasielastic contributions. The EISF for each sample measured at ~T_g+160 K is shown as a function of q in Figure 2.8a. For each bulk sample, nearly 80% of segments are mobile at q ~ 1 $Å^{-1}$ but upon the addition of NPs, a smaller fraction of nuclei are mobile on this nanosecond time scale. Thorough analysis and fitting of the q-dependence of the EISF is beyond the scope of this study, but it is worth noting that our data follows a similar trend to comparable systems in literature.[59,276]

The addition of hydroxyl-terminated SiO_2 NPs introduces additional scattering intensity that will contribute to the elastic fraction and therefore affect the EISF. To account for this contribution, we assume an upper estimate for the hydroxyl surface density of ~4.9 nm^{-2} and amorphous SiO_2 and P2VP densities of 2.3 and 1.2 g/cm^3, respectively, and calculate the predicted incoherent and coherent scattering intensities of each sample using Equation 2.2.[281,291] For NP loadings of 25 and 50 vol%, the polymer scattering accounts for 83% and 63% of the total scattering

contributions. It is important to note that the incoherent and coherent scattering from SiO_2 does not affect the measured quasielastic broadening or D_α because the nuclei are immobile on the experimental length and time scales (Figure 2.3) and therefore contribute solely to the elastic scattering. This increase in elastic scattering was accounted for in the EISF, but in all samples, the reduction in mobile nuclei was found to be more than expected from just the addition of SiO_2 NPs. This difference can be attributed to nuclei of the polymer that are slowed beyond the temporal window of the experiment and therefore appear immobile, most likely belonging to segments closest to the attractive NP interface.

Using a simple three-phase model including SiO_2, immobile polymer, and mobile polymer, the "interfacial width" can be extracted by correlating the measured fraction of immobile polymer to the increased NP-polymer interfacial volume resulting from increased NP concentration. The calculated interfacial width is shown in Figure 2.8b, where the error bars represent the standard deviation of calculations for $0.55 < q < 1.6$ Å^{-1}. The interfacial with is ~1 nm and is independent of NP loading (see 40 kg/mol) and molecular weight. This interfacial width does not delineate the slow segments from the bulk-like segments because the remaining segments are still slower than bulk (Figure 2.5c). Instead, this interfacial width represents the estimated average distance from the NP surface after which segments relax within the window of QENS. Without accounting for scattering from SiO_2 NPs, the interfacial width falsely appears to be ~2.5 nm but the MW dependence remains unchanged.

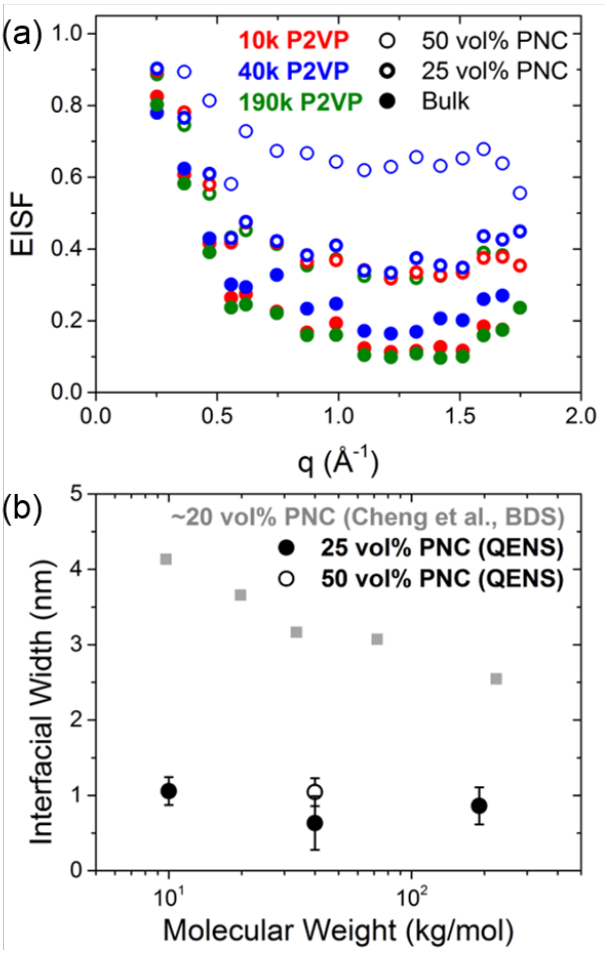

Figure 2.8: (a) Elastic incoherent structure factor versus q for all bulk and PNC samples measured at ~T_g+160 K. (b) Extracted interfacial width of segments immobile on the experimental length and time scale. Gray squares are BDS measurements adopted from Cheng et al.[73]

The extracted interfacial widths via BDS[73] and QENS (Figure 2.8b) show surprisingly distinct molecular weight dependences. Whereas the interfacial thickness in BDS decreases from ~4 nm at low MW to ~2.5 nm at high MW (consistent with arguments of MW-dependent interfacial packing[69,73]), the interfacial thickness in QENS is consistently ~1 nm over the same molecular weight range. Although these are structural insights inferred from dynamic measurements, the same behavior is observed in direct measurements of segmental dynamics. In TMDSC (Figure 2.2) and BDS[73] measurements, the increase in glass transition temperature and decrease in segmental

dynamics (respectively) are highly dependent on matrix MW, whereas we observed that $D_{\alpha,PNC}/D_{\alpha,Bulk}$ in QENS is nearly independent of molecular weight.

Although QENS, TMDSC, and BDS probe the same dynamic process (Figure 2.1), a notable difference between these experimental methods is the measurement temperature, which has two important implications. First, it remains unclear how the structure, dynamics, and interactions of the interfacially bound polymer segments depend on temperature. Thus, TMDSC ($T\sim T_g$), BDS ($T<T_g+60$ K) and QENS ($T\sim T_g+160$ K) may probe fundamentally different perturbations to the segmental dynamic process. Limited experimental data suggests a reduced interfacial width at elevated temperatures, which is in line with the observations in Figure 2.8b.[29] Second, the loops and trains of the adsorbed polymers may depend on processing conditions, even after long annealing.[29] In fact, processing details including concentrations of polymer and NP solutions, solvent quality, and annealing conditions, may impact the adsorbed polymer conformations and subsequently the interfacial dynamics. As such, it is important for the field to consider and clearly report these details. At elevated temperatures, not only is the entropy of interfacial chains promoted and local free volume increased, but the relative strength of the hydrogen bond is decreased. Samples measured for several hours at the high temperatures as required for QENS may provide enough time and thermal energy for segments to sample their local environment and energetic landscape and reach a more equilibrium conformation. Future studies of annealing time and temperature are needed to fully understand the influence of processing on interfacial dynamics.

Not only can QENS provide complimentary dynamic measurements to other techniques but it offers several unique capabilities, making it a useful complement to the field of segmental dynamics in PNCs. In this work, the use of spatial correlations in bulk and PNCs showed that although the observed segmental dynamics are temporally slowed, they are relatively unperturbed spatially. The fast time scales probed by QENS captures dynamics at elevated temperatures to elucidate the role of temperature on interfacial segmental dynamics. In addition, the ability to

quantify the fraction of mobile and immobile species allowed the extraction of structural parameters from dynamic measurements. Finally, unique capability of neutron scattering that has yet to be fully exploited is selective H/D labeling to isolate and investigate different polymer dynamics and processes within the chain (through intrachain deuteration) or spatially in the PNC (through interchain deuteration).

2.5 Conclusion

Quasi-elastic neutron scattering was used to study segmental dynamics in highly attractive polymer nanocomposites (PNCs) at high temperatures (~T_g+150 K). We isolate the role of nanoparticle (NP) concentration, temperature, and matrix molecular weight on segmental dynamics in model PNCs made of P2VP and 26 nm colloidal SiO_2. We monitor the elastic scattering as a function of temperature to reveal proton mobility over a wide temperature range and measure the dynamic structure factor under isothermal conditions to probe dynamics on length and time scales of ~ 1 nm and ~ 1 ns, respectively. We show segmental mobility is strongly reduced for all $T>T_g$ upon the addition of NPs. At the QENS length and time scales, we observe classic translational diffusion of segments in bulk and in PNCs, even when the average interparticle separation distance is ~2 nm (50 vol% SiO_2). Simultaneously, the average segmental diffusion coefficient is reduced by ~80% (relative to bulk) at NP concentrations of 50 vol%, showing strong temporal suppression without spatial perturbations. Similar observations are made for PNCs with unentangled and well-entangled matrix polymers. The decrease in segmental mobility for all $T>T_g$ and a reduced diffusion coefficient are highly dependent on NP concentration, but nearly independent of matrix molecular weight.

Several dynamic probes have been used to study segmental dynamics in highly attractive PNC systems. By comparing our QENS results to solely dynamic measurements on slower time-scales (and therefore lower temperatures), we highlight categorically different observations on

similar PNC systems. Namely, calorimetric measurements (measured at $T \sim T_g$) show a much stronger molecular weight dependence than QENS (measured at $T >> T_g$). These discrepancies provide insights into the effect of temperature on the observed segmental dynamics in attractive PNCs. Furthermore, the unique ability of space and time correlations and selective labeling in neutron scattering presents a valuable future direction to mechanistically understand segmental diffusion in various PNC systems.

CHAPTER 3: Correlation Between Backbone and Pyridine Dynamics in Poly(2-Vinyl Pyridine)/Silica Polymer Nanocomposites

Content in this chapter is in preparation to be submitted for publication in a peer-reviewed journal. The authors of this chapter are Eric J. Bailey, Madhusudan Tyagi, and Karen I. Winey.

3.1 Introduction

Polymer nanocomposites (PNCs), comprised of nanoparticles (NPs) dispersed in a polymer matrix, have attracted significant attention in recent decades due to their superior properties relative to the bulk homopolymer.[4,29] For example, the addition of NPs to a polymer matrix can improve the mechanical properties of glassy and melt polymers[39,40] and enhance small molecule transport[43,46]. However, a microscopic and mechanistic understanding regarding the origin of these altered macroscopic often remains elusive. In the case of mechanical and transport properties, segmental dynamics often underly these properties in the melt. As a result, it is advantageous to develop a fundamental understanding of the impact of NPs on different molecular motions in PNCs to optimize properties and to guide the design and development of PNCs.

In model attractive PNCs comprised of poly(2-vinyl pyridine) (P2VP) and 26-nm diameter silica (SiO_2), broadband dielectric spectroscopy (BDS) reveals the primary structural α-relaxation in proximity to the NP surface is ~100x slower than bulk.[65,73] These slow segmental relaxations are accompanied by slight increases in the glass transition temperature as measured by calorimetry as well.[55,64,65] We recently reported quasi-elastic neutron scattering (QENS) measurements on the same PNC system and showed reduced segmental mobility in PNCs relative to bulk and ~80% slower segmental diffusion at 50 vol% NP concentration at $T>>T_g$.[55] We also observe a layer near the NP surface (~1 nm thick) that relaxed at timescales slower than the available temporal range, which has been observed in the same system by a variety of techniques.[68,69,207] QENS has the additional capability to probe the spatial dependence of relaxations, unlike other strictly temporal

measurements (such as BDS and TMDSC) and therefore provides valuable insights to understanding relaxation processes in other PNCs systems.[46,107,270,275] In P2VP/SiO_2, we found that the spatial dependence of the segmental relaxation time was comparable between bulk and PNC, implying spatially-similar relaxations in bulk and PNCs (beyond ~1 nm from the NP) despite the slower average relaxation rate.[55] The secondary segmental dynamics in PNCs, typically corresponding to non-diffusive pendant reorientations, has received less attention. In one contribution, a combined QENS, BDS, and Brillouin light scattering study of P2VP/SiO_2 observed picosecond dynamics below the glass transition temperature (T_g) and correlated them to changes in mechanical properties.[127]

In this article, we present QENS measurements on PNCs to further understand the segmental dynamics at short length scales (~1 nm) and fast time scales (~ 1 ns). By measuring bulk polymer and PNCs comprised of fully-protonated P2VP and partially-deuterated (backbone deuterated) d3P2VP, we aim to decouple the dynamics of the pendant group and backbone chain with and without NPs. Partial deuteration of polymers has been successful in differentiating molecular motions and contributions to relaxations in QENS in other systems.[37,151] The separation of backbone and pendant motion in PNCs is critical to understanding the previous measurements of segmental dynamics and how polymers segments relax in the presence of attractive NPs.

3.2 Experimental Details

P2VP (30.9 kg/mol, 1.1 PDI) and d3P2VP (33.6 kg/mol, 1.2 PDI) samples were purchased from Scientific Polymer Products and Polymer Source, respectively, and used as received. Polymer molecular weight distributions were measured via GPC. The glass transition temperature of both polymers, as measured by differential scanning calorimetry, was 370 K. Colloidal SiO_2 NPs dispersed in water (Ludox AS-40, d_{NP} = 28±3 nm) were obtained from Sigma-Aldrich and measured via SAXS and TEM. Following previous works[178], concentrated NP solutions in water

were diluted with DMF, distilled at 130˚C, and repeated until the H_2O content as measured by Karl Fisher titration was <0.1 wt%. P2VP and d3P2VP were dissolved in DMF (~5 wt% polymer) and for PNCs, were mixed with SiO_2/DMF solutions (~20 g/L SiO_2). Solutions were stirred continuously overnight to ensure formation of the bound polymer layer in solution, which is known to lead to good NP dispersion.[208,292] Solutions were drop cast in a hot PTFE dish (383 K) then vacuum annealed at T_g+100 K for 24 hours. For QENS measurements, at least 200 mg of polymer was encased in aluminum foil and placed in cylindrical aluminum cans during measurement.

NP concentrations were measured via TGA where ~5 mg samples were heated beyond 1100 K in platinum pans to measure the total SiO_2 mass. Small-angle X-ray scattering (SAXS; $0.008 < q < 0.12$ Å^{-1}) was conducted at the Multi-angle X-ray Scattering (MAXS) facility at the University of Pennsylvania to characterize the NP dispersion in PNC films. QENS measurements were conducted at the High-Flux Backscattering Spectrometer (HFBS, NG2) at the NIST Center of Neutron Research in Gaithersburg, MD, USA.[283] Fixed window scans (FWS) and QENS measurement conditions and parameters are reported in our previous publication.[55] Importantly, HFBS probes $0.25 < q < 1.75$ Å^{-1} and $-17 < h\upsilon < 17$ μeV (with a resolution of 0.8 μeV), so the probed molecular motions are approximately 3 − 25 Å and 40 ps − 2 ns.

3.3 Results and Discussion

This model attractive PNC system of P2VP/SiO_2 is known to form well-dispersed mixtures due to the strong NP-polymer attraction which forms a bound polymer layer and prevents NP-NP aggregation.[208,292] SAXS patterns that were shifted for clarity are shown in Figure 3.1 and show that P2VP and d3P2VP PNCs exhibit similar NP structure. In addition, the plateau at low q and the undulations similar to NPs in solution indicate a lack of NP-NP aggregates in these PNC films, as expected from previously reported PNCs.[55,208,292] The NP concentration in both PNC films is ~25 vol% (~40 wt%), as measured by TGA in the inset of Figure 3.1.

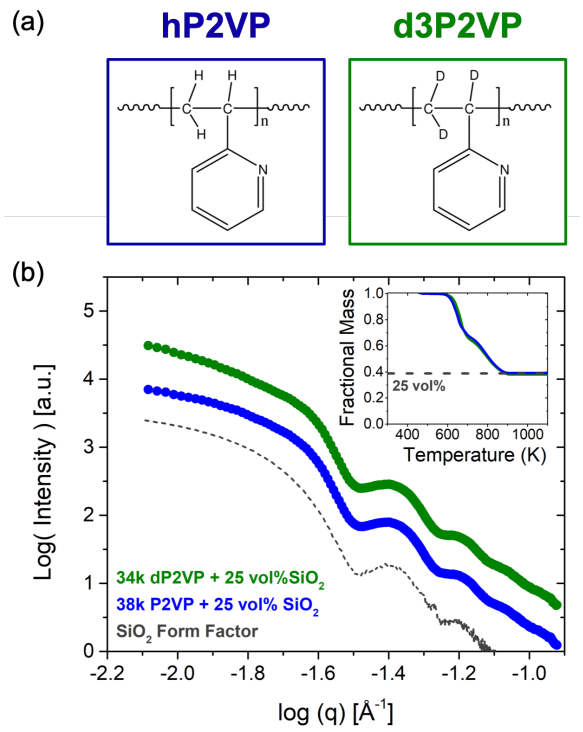

Figure 3.1: (a) Chemical structure of P2VP (blue) and d3P2VP (green). (b) SAXS of PNCs and SiO_2 NPs in solution, all shifted vertically for clarity. (inset of b) TGA measurements of PNCs showing similar NP concentrations.

Since the incoherent scattering cross section (σ) for hydrogen ($\sigma_H \sim 80$ barnes) is much larger than other atoms (σ_D, σ_C, σ_{Si}, σ_O, $\sigma_N < 6$ barnes), QENS is primarily sensitive to the motion of protons in these samples.[281] Thus, QENS measurements of P2VP/SiO_2 and d3P2VP/SiO_2 can identify the similarities and differences between backbone and pyridine pendant motion in P2VP/SiO_2 PNCs. Specifically, all protons contribute equally in protonated P2VP PNCs, while QENS of d3P2VP PNCs is dominated by dynamics associated with only the pyridine ring. Unfortunately, d4P2VP with a deuterated pendant pyridine group, which would isolate only backbone motion, is difficult to synthesize and unavailable commercially.

To characterize the segmental mobility of neat P2VP, neat d3P2VP and both PNCs over a broad temperature range, the elastic scattering intensity was monitored as a function of temperature

from 50 to 535 K in a fixed window scan (FWS). The mean-squared displacements of segments ($<x^2>$) shown in Figure 3.2 were extracted using the Debye−Waller approximation:

$$\frac{I_{elastic}}{I_0} = \exp\left(-\frac{q^2}{3}\langle x^2\rangle\right) \qquad (3.1)$$

Where $I_{elastic}/I_0$ is the elastic scattering intensity at any given temperature normalized by the elastic scattering at T = 50 K. In practice, $\langle x^2\rangle$ is obtained directly as the slope of $-3\cdot\ln\left(\frac{I_{elastic}}{I_0}\right)$ plotted as a function of q^2 for $q^2 < 1.22$ Å^{-2}.[55,76] This analysis assumes motions beyond the resolution of the instrumental resolution and produce a change in the elastic scattering can be modeled as simple harmonic springs and therefore indicates the average proton mobility in the sample.

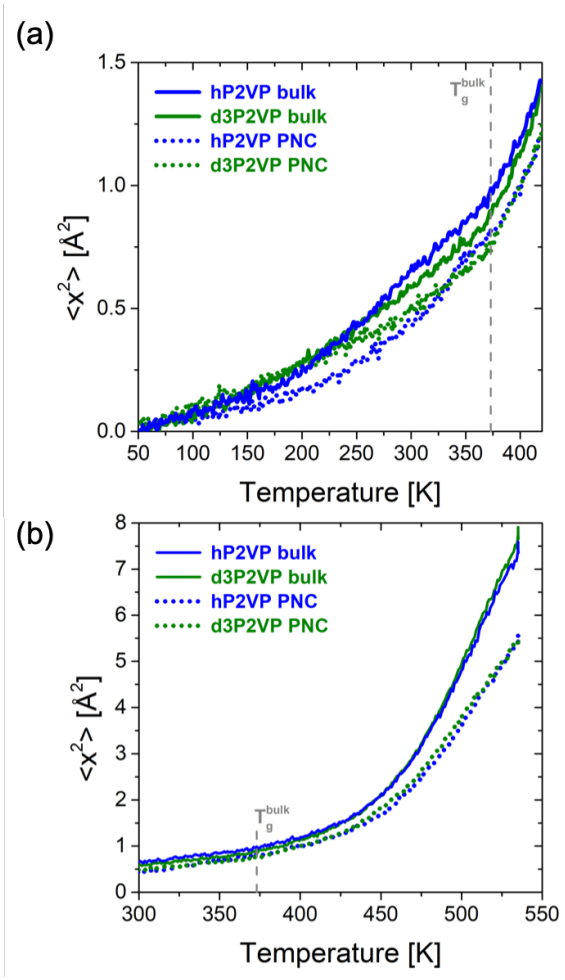

Figure 3.2: Fixed window scans of bulk polymers and PNCs with 25 vol% SiO_2, plotted as mean-squared displacements of segments ($\langle x^2 \rangle$) as a function of temperature. For clarity, (a) focuses on $\langle x^2 \rangle$ at low temperatures and (b) focuses on $\langle x^2 \rangle$ at high temperatures.

At low temperatures in Figure 3.2a, $\langle x^2 \rangle$ is less than ~1 Å^2 which is consistent with measurements of polymer glasses since the α-relaxation process is inactive at $T<T_g$.[76,95] The d3P2VP PNC sample appears more similar to bulk d3P2VP than the P2VP PNCs is to bulk P2VP. This is likely because the pyridine ring motion is local enough to occur at these low temperatures[127], even in the PNC, so d3P2VP is dominated by the most mobile protons. As the temperature approaches the calorimetric T_g, both PNC samples diverge from their respective bulk polymer. In Figure 3.2b, a sharp increase in $\langle x^2 \rangle$ is observed for $T>T_g$ in all samples due to the activation of the α-process and other segmental motions. At these higher temperatures, convergence is observed

between d3P2VP and P2VP neat polymer as well as both PNCs, although the d3P2VP may be slightly more mobile in both cases. In both P2VP and d3P2VP, the segmental mobility decreases by the addition of attractive SiO_2 NPs, in agreement with previous QENS measurements[55]. The small differences between P2VP and d3P2VP samples in Figure 3.2b indicate that the proton mobility on the pyridine ring does not differ significantly from protons on the backbone. This observation is in direct contact to semiconducting P3HT[293] and PVAc melts[294], both of which exhibit side chain dynamics decoupled from backbone dynamics.

To further characterize the segmental dynamics, QENS measurements were conducted at 515 and 535 K, where segments are highly mobile ($\langle x^2 \rangle > 4$ Å^2, Figure 3.2). As shown in the representative QENS spectra in Figure 3.3, all samples show significant broadening beyond the experimental resolution and the broadening in PNCs is markedly reduced from bulk. In other words, segmental dynamics are active in all samples but clearly slower in PNCs. These QENS spectra can be fit with a linear combination of a delta function for the elastic scattering peak, a single Lorentzian for the segmental motion, and a linear background, all of which are convoluted with experimental resolution obtained from measurements of bulk vanadium. This fitting is more thoroughly described elsewhere.[55] This relatively simple fitting procedure, i.e. one Lorentzian used to account for the mobile species, describes all spectra well and produces featureless residual plots.

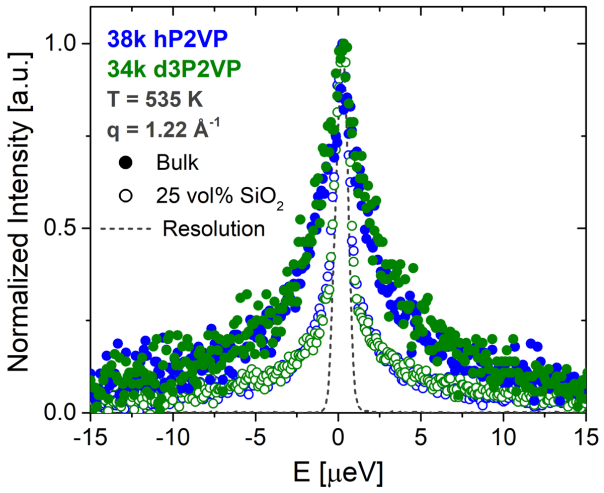

Figure 3.3: Normalized QENS spectra for bulk (solid symbols) and PNCs (open symbols) for P2VP (blue) and d3P2VP (green) samples at T=535K and q=1.22 $Å^{-1}$. Grey line shows experimental resolution obtained from measurements of vanadium.

The full-width at half maximum (FWHM) of the Lorentzian, which is inversely related to the average relaxation time of the protons, is extracted and plotted as a function of q^2 for 515 K and 535 K in Figure 3.4a and b, respectively. While we report the FWHM of each sample at 515 K, we refrain from fitting these data because all samples exhibit similar FWHM (< ~4 μeV) with nonnegligible scatter. However, it can be qualitatively deduced that the d3P2VP samples shows faster dynamics than P2VP samples, especially at higher q, and both PNCs are less mobile than their bulk counterparts.

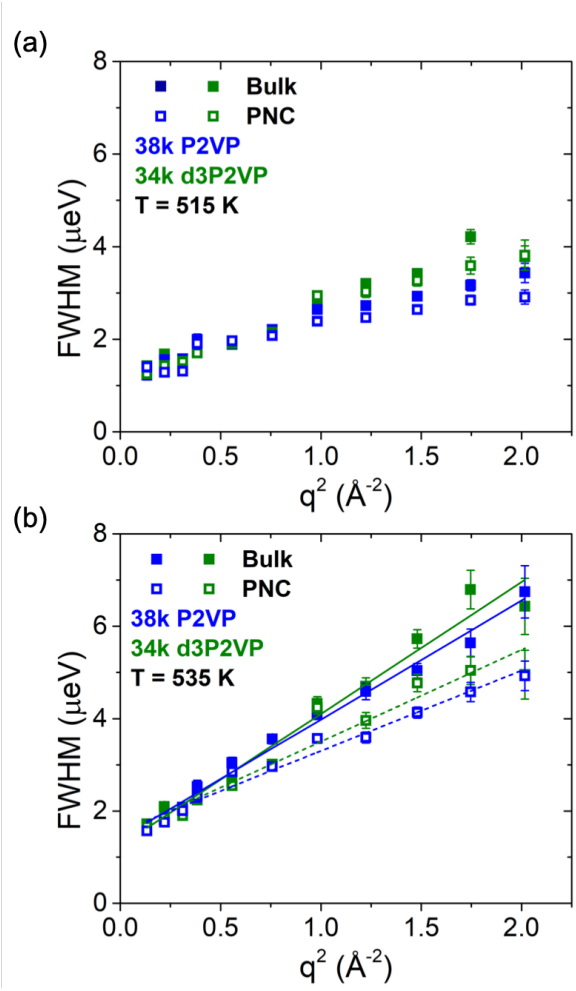

Figure 3.4: FWHM extracted from QENS spectra as a function of q^2 for P2VP (blue) and d3P2VP (green) bulk polymer (closed symbols) and PNCs (open symbols) at (a) T = 515 K and (b) T = 535 K. Lines in (b) are linear fits to data, as discussed in the text.

In Figure 3.4b at 535 K, the d3P2VP samples exhibit slightly faster dynamics than their P2VP counterparts for both bulk polymers and PNCs for all q. The FWHM of each sample varies linearly with q^2, which indicates diffusive motion (i.e. $\tau^{-1} \sim q^2$) on these short timescales where the slope is related to the diffusion coefficient, D_α. These fits are presented with the data in Figure 3.4b, and the extracted D_α is presented in Figure 3.5. Interestingly, the y-intercept of each sample is similar, FWHM ~1.4 μeV. Although assigning a dynamic motion to this feature is beyond the scope of the study, we suspect it represents fast, q-independent, motion of protons in the pyridine ring.

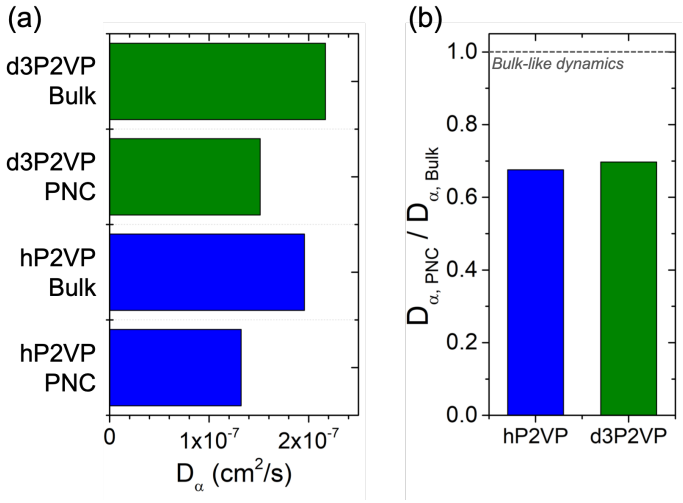

Figure 3.5: (a) Diffusion coefficients of segments in each material system at T= 535 K. (b) Normalized diffusion coefficient of PNCs.

The fit results of D_α from data in Figure 3.4b (T = 535 K) are shown in Figure 3.5. Considering the bulk polymers first, D_α is only ~12% faster in d3P2VP as compared to P2VP. This implies the motion of the pyridine ring is slightly faster than the motion of the backbone and they are highly coupled at 535 K. The observation is consistent with expectations that pendant groups are more mobile than the chain backbone, but the motions are highly coupled at high temperatures ($T>>T_g$). In both PNCs, D_α is reduced by ~35% relative to bulk (Figure 3.5b). In other words, the observed spatial and dynamic perturbation imposed by the NPs is quantitatively the same for P2VP and backbone-deuterated d3P2VP.

There are two main explanations for the agreement observed in Figure 3.5b. First, the motion in P2VP may be dominated by the more-mobile pyridine rings (commonly referred to as a β-process), so deuteration of the backbone proves inconsequential. However, we surmise that this is not the case. Agreement between TMDSC, BDS, and QENS in our previous work[55] supports the notion that QENS samples backbone reorientation, known as the α-process. In addition, systematic deviations of D_α in Figure 3.5a support the notion that backbone protons contribute in the P2VP

samples. The second explanation is that the backbone and pyridine motion are highly correlated and coupled in both neat polymer and PNCs at $T >> T_g$. Not only is this explanation supported by Figure 3.2b, but it is well-established that primary (α) and secondary (β, γ, etc.) relaxations converge at high temperatures, such as those used in this work. Therefore, our results imply that this coupling remains true in the presence of highly attractive NPs while segmental and chain dynamics are slowed significantly.[65,207,208] This supports the conclusion that although the segmental dynamics are slowed in PNCs, the spatial relaxation and way in which the segments relax are largely unaltered from bulk.[55]

3.4 Conclusions

We used QENS to characterize segmental dynamics in P2VP/SiO_2 PNCs comprised of fully protonated P2VP and backbone-deuterated d3P2VP. While all protons are sampled evenly in P2VP, d3P2VP selectively probes the motion of the pendant group. By monitoring the mobility of segments as a function of temperature, we observed that pyridine motion in the PNC is similar to bulk for $T<T_g$, but mobilities of pyridine pendants and backbone protons converge at $T>T_g$. In both P2VP and d3P2VP PNCs, however, the dynamics were reduced relative to their bulk counterparts at all temperatures. From measurements of QENS at $T>>T_g$, we observe diffusive dynamics of protons in all samples on time and length scales of ~1 ns and ~ 1 nm. Even though the segmental diffusion coefficient observed in d3P2VP samples (which are dominated by the pendant group) are systematically faster than P2VP samples, the normalized diffusion coefficients in 25 vol% PNCs are both ~35% slower than bulk. This observation highlights the connection between backbone and pyridine motion, even in PNCs where the motion is temporally slowed by attractive NPs. These results provide further insight toward developing a fundamental understanding of the mechanistic impact of NPs to segmental dynamics in PNCs.

CHAPTER 4: Chain-Scale Polymer Conformations and Dynamics Through a Monolayer of Confining Nanoparticles

Content in this chapter is in preparation to be submitted for publication in a peer-reviewed journal. The authors of this chapter are Eric J. Bailey, Robert A. Riggleman, and Karen I. Winey.

4.1 Introduction

It is well known that static and dynamic properties of a polymer melt can be altered by the addition of nanoparticles (NPs).[4,26,29] These hybrid materials, called polymer nanocomposites (PNCs), have received considerable attention for several decades due to their potential applications in critical areas such as electronics, biomedical engineering, and energy.[4] Despite the diverse research through experiments, simulations, and theory, the connection between microscopic parameters and macroscopic properties remains elusive, motivating the need for further fundamental studies. The structure, conformation, and dynamics of polymer chains near NPs influence various properties of interfacial polymers including mechanical, transport, and functional properties and more broadly the processability of PNCs. However, due to the broad and interrelated parameter space and complex nature of PNC materials, the NP-induced perturbation to static and dynamic properties is not well established.

The experimental determination of polymer chain conformations (e.g. the radius of gyration, R_g) in PNCs with small angle scattering is challenging. Using small angle neutron scattering (SANS), experimental observations of increased chain dimensions,[295] decreased chain dimensions,[209] and unperturbed conformations[296] have been reported, as compiled recently[297]. In one contribution, meticulous fitting of combined X-ray and neutron scattering revealed an interfacial layer in attractive PNCs over which the structure (e.g. density, conformations, chain packing) are perturbed, but individual chain conformations were unavailable.[209] In part due to the ensemble-averaging and isotropic nature of PNCs and SANS, molecular dynamics simulations are

more conducive for meticulous interrogation of polymer conformations, as reviewed recently.[110] Starr et al. used MD simulations of a single faceted NP in a polymer melt to show polymer chain flattening at the NP surface (for $R_{NP} > R_g$) and the recovery of bulk conformations beyond ~R_g from the NP surface.[79,120] Other authors have conducted similar simulations in the dilute regime with various NP sizes, chain lengths, NP-polymer interactions, where expanded[79,298–302] and unperturbed[153,154,192] conformations were reported but all conformations were within ~20% of bulk. Fewer simulations addressed strongly confined PNCs (high NP concentration) by including several NPs in the simulation box with random order or on a lattice.[303,304] Namely, for a variety of NP sizes (R_g/R_{NP} ~ 1-8), repulsive NPs did not perturb the average conformations but chains swelled with increasing loading of small, attractive, NPs.[304] In part due to the sometimes conflicting results and dense parameter space, a mechanistic understanding of how NPs perturb polymer conformations, especially under strong confinement, has not been developed.

The dynamics of polymer chains are also known to be perturbed near NPs. It is reasonably established by the convergence of simulations and experiments on different material systems that small length-scale polymer segmental dynamics are slow near attractive and weakly interacting NPs.[29,55,65,66,119] At longer length-scales, the chain-scale polymer diffusion is known to be affected by the presence of NPs. Elastic recoil detection (ERD) has been used to measure tracer polymer diffusion into PNCs with spherical NPs for various NP loadings, tracer MWs, NP sizes (R_{NP}), and NP-polymer interactions.[170,181–183,272] In each case, the polymer diffusion coefficient was slower in the PNC (D) than in bulk (D_0) and D/D_0 was found to depend on only the confinement parameter ($ID/2R_g$) where ID is the average accessible interparticle distance between nearest NPs. Furthermore, $D/D_0 < 1$ was observed even at $ID/2R_g \sim 10$, which implies that the temporal effect of NPs on polymer diffusion is spatially long-lasting. We note that this behavior, where D/D_0 is related to $ID/2R_g$ is restricted to PNCs with immobile NPs and isothermal measurements and deviations have been observed.[109,188]

Although MD simulations of polymer diffusion can be challenging due to computational expense, especially for high NP loadings and long polymer chains, insights have been gained from MD simulations and other calculations, as recently reviewed.[32] For example, the addition of attractive NPs was found to slow polymer diffusion relative to bulk as a function of NP concentration.[192] However, a nonmonotonic trend was observed in PNCs with repulsive NPs where $D/D_0 > 1$ at low NP concentrations and $D/D_0 < 1$ when tortuosity dominates at higher NP concetrations.[192] In another set of MD simulations, polymer diffusion was found to be reduced relative to bulk with increasing NP concentration and the slowing more significant than predicted by totuosity.[305] More recently, scaling of D/D_0 with $ID/2R_g$, similar to experimental observations, was observed in dynamic Monte Carlo simulations but a scaling factor that depends on temperature, NP size, NP-polymer interaction was needed to collapse the various PNC systems.[194] Furthermore, the convergence of $D/D_0 \sim 1$ occurred at $ID/2R_g \sim 3$ which is much more rapid than observed in experimental systems. Despite numerous observations, a systematic understanding of the how D/D_0 depends on $ID/2R_g$ and the origin of the spatially long-lasting effect of NPs on polymer diffusion remains unclear.

In this article, we use coarse-grained molecular dynamics simulations to study polymer conformations between highly confining NPs and probe the spatial and temporal impact of a monolayer of NPs on polymer diffusion. By placing a monolayer of hexagonally packed NPs in a dense polymer melt we isolate the confined region and observe the transition from bulk-polymer behavior to confined behavior. In doing so, we systematically provide fundamental insights to the more complex PNC environment. We show that polymer conformations under strong confinement ($ID/2R_g < 1$) are more impacted than around an isolated NP, and the effect depends on the ratio of R_{NP}/R_g rather than either independently. In fact, these conformations can be quantitatively replicated by executing a simple random walk in a similarly confining environment. We then show the perturbation to polymer diffusion is impacted far beyond the region over which polymer

conformations are perturbed. We show the local polymer diffusion coefficient ~R_g from the NPs is slowed as a function of confinement, and the slowing persists even ~$5R_g$ from the NPs. Furthermore, by analyzing the directional van Hove distributions, we show polymer preferentially diffuses away from the NP monolayer and diffusion through the monolayer is slowed as a function of confinement. While only considering a monolayer of NPs, we recover the functional form observed experimentally in the more complex PNC environment, though the suppression of diffusion is expectedly weaker. Unlike experiments, however, for constant degrees of confinement ($ID/2R_g$), we find that larger NPs perturb diffusion more strongly as may be expected from tortuosity arguments. These molecular dynamics simulations highlight the impact of a monolayer of NPs and provide fundamental insights into the temporal and spatial effect of confining NPs on polymer conformations and diffusion.

4.2 Simulation Method

We conduct coarse grained molecular dynamics (MD) simulations that follow the well-established Kremer-Grest model.[306] The units reported herein are normalized to the monomer size (σ), potential strength (ε), and monomer mass (m) where time, $\tau = \sigma(m/\varepsilon)^{1/2}$. All simulations were run with the LAMMPS MD simulation package using the velocity-Verlet algorithm[307] in an NVT ensemble with a the Langevin thermostat and periodic boundaries applied in all dimensions.

The NPs in these simulations were constructed from an amorphous melt of non-bonded monomers beads with density (ρ) of 0.9 σ^{-3}. All beads beyond R_{NP} from the center of the simulation were discarded leaving a spherical NP with amorphous bead structure and an effective radius approximately equal to the defined $R_{NP.}$ These NPs were then assembled into a hexagonal lattice monolayer in the x-y plane. The minimum interparticle distance (ID) is used to define the separation of nearest neighbor NPs, whose centers are displaced by $ID+2R_{NP}$ (Figure 4.1a). While this defines the x and y dimensions of the box, the z-dimension was typically at least 10 R_g (to incorporate a

sufficient volume of bulk-like polymer). Box dimensions and other relevant parameters are listed in Table S1. Finally, polymer chains were added to the simulation box on a lattice above and below the NP monolayer and the system was equilibrated, as described below. The precise value of the z dimension was adjusted to achieve a polymer monomer density far from the NP monolayer of 0.85 σ^{-3}. The simulation box after equilibration is presented in Figure 4.1b.

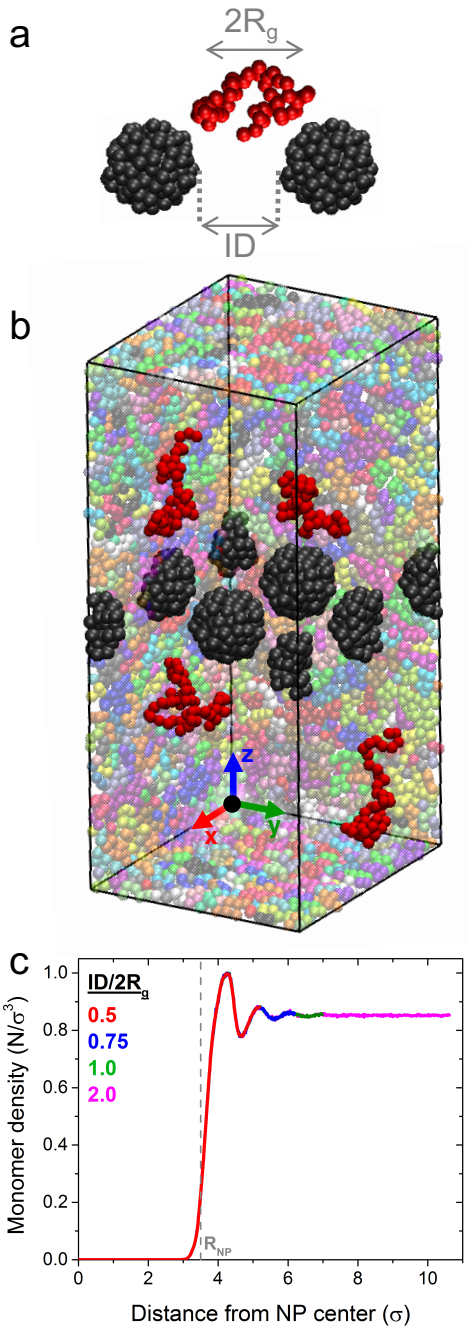

Figure 4.1: (a) A representation of the polymer chains and NPs and (b) a representative image of the simulation box including NPs (dark grey), and polymer chains (various colors) with four representative chains highlighted (red). All images are obtained from the simulation of $ID/2R_g = 1$, $N = 50$, and $d_{NP} = 7\sigma$. (c) Monomer density profile as a function of distance from the NP surface for $ID/2R_g = 0.5 – 2$.

All nonbonded monomer-monomer interactions are governed by a repulsive Lennard-Jones (LJ) potential and bonded monomers are connected via a FENE anharmonic spring potential. Beads in the NP interact with polymer monomers through the same repulsive LJ potential as nonbonded monomers, making this an athermal system. A spring force was independently applied to NP beads, fixing their equilibrium position but allowing them to vibrate to prevent artificial crystallization caused by peaks and valleys on the NP surface. This makes the center-of-mass (COM) of the NPs immobile throughout the simulation, which is a reasonable approximation because chain diffusion in PNCs[170,272] is ~100 times faster than NP diffusion in polymer melts[208], especially for $R_{NP} \sim R_g$.

Equilibration of the system was monitored by conformation and dynamic properties of the polymer. For regions $>5R_g$ from the NP monolayer, monomer density and polymer conformations (R_g) were found to equilibrate to bulk values rapidly ($<\sim 10^5\ \tau$). During equilibration, the average monomer travelled $>>2R_g$ and reached the diffusive regime where $MSD \sim t^1$. For systems with N=200, equilibration was assisted by bond swap algorithm followed by standard MD for times sufficient for full chain diffusion. For experimental sampling, a Langevin thermostat was used at T = 1 and the timestep used was 0.002τ for N=50 and 0.006τ for N=200.

Most results discussed in this work are systems with N=50 beads per polymer chain ($R_g = 3.6\sigma$) and NPs with $2R_{NP} = 7\sigma$. However, in certain cases, systems with N=200 ($R_g \sim 7.2\sigma$) and $2R_{NP} = 3.5\sigma$ and 14σ are reported. In general, we explore levels of confinement of $ID/2R_g = 0.5$, 0.75, 1, and 2, Figure 4.1a. The NP-polymer interface in each system with N=50 and $d=7\sigma$ can be observed in Figure 4.1c. Due to the amorphous surface structure and lightly vibrating beads, there is slight monomer penetration into the NP on the order of $\sim 0.5\sigma$. In addition, density fluctuations away from the NP surface are minimal and independent of degree of confinement. Analysis of polymer conformations and dynamics will be described later.

To further understand polymer conformations in these systems, observations from MD simulations are compared to simple random walks generated in a similar environment. Specifically, smooth-walled NPs matching the size and location of NPs in MD simulations were placed in space. Then, the starting location of the random walk was randomly generated and N steps of 1σ were generated in random directions. All starting locations and subsequent steps beyond R_{NP} from the NP center were accepted and all locations and steps within the NP were declined except those within 1σ of the NP surface which were accepted conditionally. To be specific, an exponential function that dictates acceptance criteria was used near the NP surface (from R_{NP}-1 to R_{NP}) to match the amorphous NP surface structure, both of which lead to a slightly less sharp NP surface (Figure 4.1c). This yields a qualitatively similar NP-polymer interface and shows good agreement at the chain-scale with MD simulations, as will be discussed later. Since R_{NP} matches MD simulations and the random walks have no excluded volume, we vary the number of steps per chain (n) to match R_g of MD simulations in bulk. For comparison to N=50 in MD, we use n=83 to get a bulk R_g of ~3.6σ in both simulations.

4.3 Results and Discussion

4.3.1 Polymer Conformations: Effect of Confinement

We first present calculations of the chain conformations at various locations in the simulation box. It is useful to describe the conformation of a polymer chain by reporting component of R_g perpendicular to the nearest NP surface ($R_g^{\perp}$), which follows the radial symmetry imposed by the NPs. $R_g^{\perp}$ is calculated using Equation 4.1:

$$R_g^{\perp} = \frac{1}{N^2}\left\langle \sum_{i=0}^{N-1} \sum_{j=i+1}^{N} \left(\frac{(\vec{r_i} - \vec{r_j}) \cdot (\vec{r_i} + \vec{r_j})}{|\vec{r_i} - \vec{r_j}|} \right)^2 \right\rangle \qquad (4.1)$$

where r_i represents the location of bead i with respect to the center of the nearest NP and N is the number of beads in the chain. In bulk polymer where there are no NPs, the origin of the simulation box is used rather than the center of the nearest NP.

Figure 4.2 shows spatially resolved and time-averaged maps of $R_g^{\perp}$ within the NP monolayer (x-y plane, top) and through the NP monolayer (x-z plane, bottom) for N=50 chains in PNCs with $R_{NP} \sim R_g$ for three different confining environments. The value of $R_g^{\perp}$ is normalized to $R_g^{\perp}$ far from the NP surface ($R_g^{\perp,\infty}$), which matches $R_g^{\perp}$ in bulk polymer. Using $ID/2R_g = 2$ in Figure 4.2 as an example, $R_g^{\perp}$ is compressed at the NP surface, but eventually returns to an unperturbed conformation. The perturbed area is constant in thickness around the NP in both planes and uniformly around the NP surface. As the confinement is increased, or the NP-NP separation distance is decreased, the perturbed area maintains the same thickness but eventually perturbed areas from different NPs begins to overlap ($ID/2R_g = 0.5$, Figure 4.2). In fact, nearly all conformations in the x-y plane are perturbed when $ID/2R_g = 0.5$ and none resemble bulk-like conformations. Regarding the x-z plane, the conformation significantly above and below NP monolayer are bulk-like while conformations between the NPs are compact. Although we only report $R_g^{\perp}$, our observation of chain flattening against the NP surface is also apparent in analysis of the 3-D R_g or R_{ee} for any individual component.

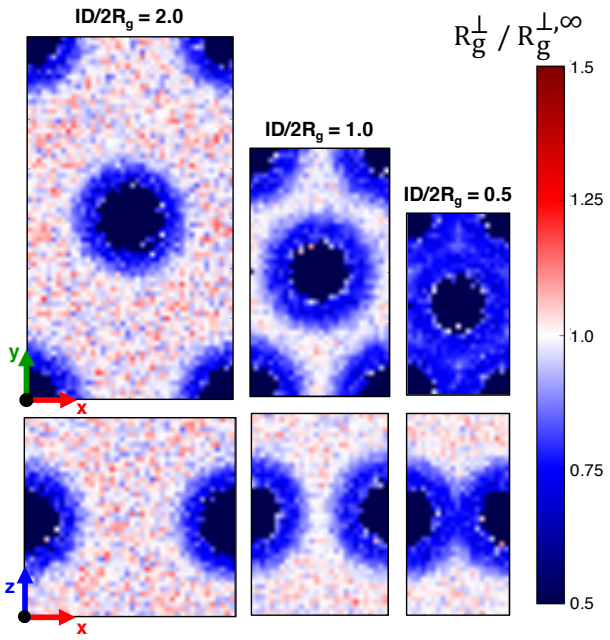

Figure 4.2: Map of polymer conformations, plotted as $R_g^{\perp} / R_g^{\perp,\infty}$ in the x-z plane (through the NP monolayer) and x-z plane (excluding the bulk regions above and below the NP monolayer) on the top and bottom, respectively.

Figure 4.2 allows visualization the spatial influence of NPs and confinement on polymer conformation, but we further investigate these perturbed conformations by isotropically averaging the conformation as a function of distance from the nearest NP surface in Figure 4.3a. The chain compression directly at the NP surface is mostly independent of confinement and reduces $R_g^{\perp}$ ~25% relative to the unperturbed state. In addition, we observe that polymers beyond ~R_g from the NP surface retain their bulk-like conformation, similar to observations reported by Starr et al. on an isolated NP in a polymer melt of shorter polymer chains (N=20).[79] It is important to note that the position of chains in this calculation were defined by their COM position from the NP surface, which explains the apparent penetration into the NP in Figure 4.3a. It is possible for chains to wrap around the NP such that the COM is within the NP excluded volume without the presence of a single monomer within the excluded volume.

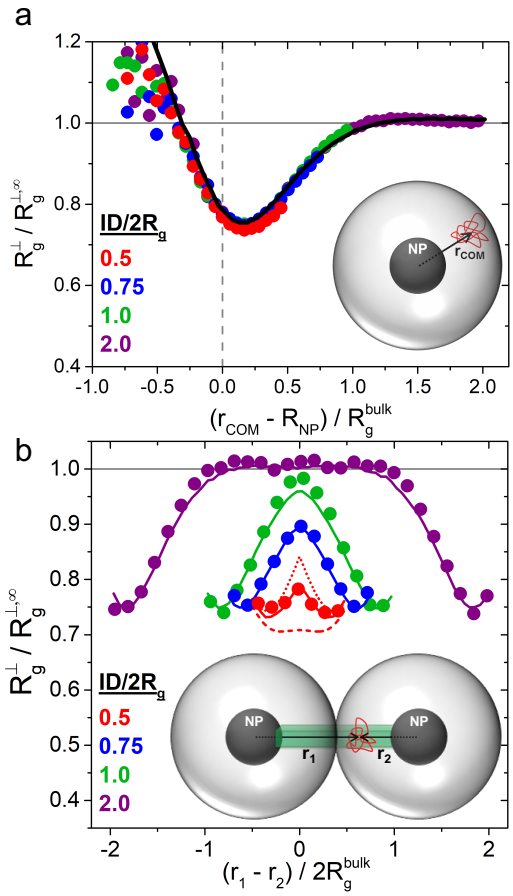

Figure 4.3: (a) Isotropically-averaged and normalized polymer conformation as a function of distance from the NP surface. Symbols represent MD simulations and the solid line represents a random walk around an isolated NP. (b) Normalized polymer conformation as a function of location between two confining NPs. Symbols represent MD simulations, dotted and dashed lines represent the predicted perturbation from only the nearest NP and both confining NPs (respectively), and solid lines represent random walk generation in the same confining environment. All MD simulations are for N=50 and d = 7σ.

The analysis in Figure 4.3a restricts the maximum distance from the NP surface to be ID/2 to ensure an isotropic average around the nearest NP. In contrast, Figure 4.3b analyzes the conformations directly between confining NPs, as schematically represented in the inset of Figure 4.3b. In each case, chains residing directly between the NPs are considered at position 0, the NP surfaces are the ID/2R_g away from the center position (i.e. +/-2 for ID/2R_g=2), and chains with COM inside the NP are excluded for clarity. Because the least confined system has ID ≥ 2R_g, bulk conformations are retained even between NPs. The most confined systems in Figure 3b show

conformations directly between the NPs remain perturbed from bulk, as qualitatively observed in Figure 4.2. It is interesting to note that the perturbation directly at the interface of the nearest NP is still independent of confinement, but chains with COM residing in between the NPs are more heavily perturbed compared to conformations near a single NP.

When considering the perturbation imposed by two confining NPs, as opposed to a single isolated NP, there are two extreme cases. First, the conformation of the polymer may be dictated by only the nearest NP. If this is true, the profile between NPs should follow the isotopically averaged profile observed in Figure 4.3a, which is represented by the dotted red line for the $ID/2R_g=0.5$ system in Figure 4.3b. This case underestimates the perturbation, indicating both NPs contribute to some degree to the perturbed conformation. The second extreme case is that both confining NPs perturb the conformation as much as the case of an isolated NP. Mathematically, this can be estimated by multiplying the perturbation at r_1 in Figure 4.3a by the perturbation at r_2. This case is represented by the dashed red line for the $ID/2R_g=0.5$ system in Figure 4.3b and clearly over estimates the perturbation. Thus, when $ID < 2R_g$, both confining NPs influence the conformation of the polymer chain, but their perturbations are not simply multiplicative.

To further probe conformations in these confining environments, we now compare the observed conformations to random walks in a similar confinement geometry, as described in the previous method section. The calculated conformations from random walks around an isolated NP are shown by a solid line in Figure 4.3a. Even though the simple random walk uses a smooth NP and no excluded volume, it quantitatively captures the main observations from MD simulations. For example, conformations beyond R_g from the NP surface remain bulk-like and conformations at the NP-polymer interface are flattened by ~20%. Using the same method, we now generate random walks in the confined environments between nearest-neighbor NPs and compare directly to MD simulations in Figure 4.3b (solid lines). For all degrees of confinement, the observations using random walks match those from MD simulations. This result shows that the flattened

conformations observed are simply a result of confined random walks. Furthermore, we suspect that for athermal systems, this simple method can be used to rapidly predict conformations in complex environments.

4.3.2 Polymer Conformations: Effect of NP size

We now explore the conformations of polymer chains with different chain lengths (N=50 and N=200) near NPs of different sizes ($2R_{NP}$ = 3.5, 7, and 14 σ). In each case, R_{NP}/R_g is approximately 0.5, 1, or 2. As shown in the MD simulations in Figure 4.4, conformation profiles with matching R_{NP}/R_g collapse onto the same curve and systems with larger R_{NP}/R_g show larger perturbations at the NP interface. For example, when $R_{NP}/R_g \sim 0.5$, polymer conformations are relatively unperturbed, experiencing a ~5% decrease in $R_g^{\perp}$ when the chain COM is ~$0.5R_g$ from the surface of the NP. In fact, some swelling is observed with the addition of small NPs. We also note that for each system, regardless of R_{NP}/R_g, the conformations begin to approach bulk-like values ~R_g from the NP surface. We observe the same effects using the random walk model reported in Figure 4.3, as shown in Figure B.3. This further supports the notion that conformations in complex confining environments and around various NPs, even when the NP and polymer have similar radii of curvature, are simply confined random walks.

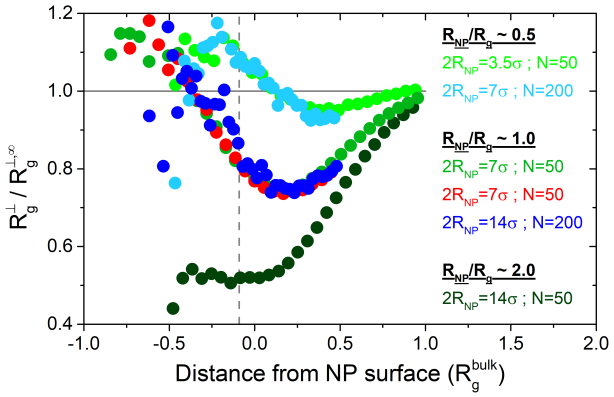

Figure 4.4: Isotropically-averaged normalized polymer conformations as a function of distance from the NP surface showing the effect of NP size relative to bulk R_g (R_{NP}/R_g) for systems with different NP sizes and chain lengths.

4.3.3 Polymer Diffusion: Effect of Confinement

We now aim to probe polymer diffusion near and through the confining NP monolayer. In the simplest analysis, we extract the polymer chain diffusion coefficient in the z direction (D_z, perpendicular to the NP monolayer). The average D_z for N=50, $2R_{NP} = 7\sigma$, and $ID/2R_g = 0.5$ is 7.6×10^{-4} σ^2/τ, compared to bulk polymer which is 8.7×10^{-4} σ^2/τ (Figure B.4 and Table B.1). Clearly, polymer diffusion is slower in systems with NPs, as reported in simulations and experiments. The observed reduction in diffusion from this simple analysis is noteworthy because the majority of volume is bulk polymer in our simulation box, yet polymer diffusion is still measurably perturbed. This demonstrates a spatially long-lasting impact of NPs on polymer diffusion, which was also reported in experiments. However, more complex analysis is needed to probe this perturbation further.

We first highlight the local polymer diffusion near and far from the NP monolayer by observing the variation in polymer diffusion as a function of distance from the NP monolayer. To be specific, we analyze monomer trajectories for time periods up to 60,000τ and for each trajectory and time period, calculate the average z position ($\bar{z}$). As shown schematically in Figure 4.5a, this

definition of $\bar{z}$ provides a measure of the most common z position that the diffusing species sampled during it's trajectory. Then, we generated several mean-squared displacement vs time curves after grouping monomers with similar $\bar{z}$ positions together (Figure 4.5b, $ID/2R_g = 0.5$). Each curve shows that MSD varies linearly with time for $t > \sim 30{,}000\tau$, which indicates diffusive dynamics where the slope is related to the diffusion coefficient ($MSD = 2Dt$). The MSD curves far from the NP monolayer (cyan in Figure 4.5b) closely match bulk polymer (solid line in Figure 4.5b), meaning the bulk-like region of the simulation exhibits diffusion dynamics similar to bulk-like polymer. In contrast, the dynamics directly outside the NP monolayer (pink in Figure 4.5b) are significantly suppressed relative to bulk or far from the NP monolayer.

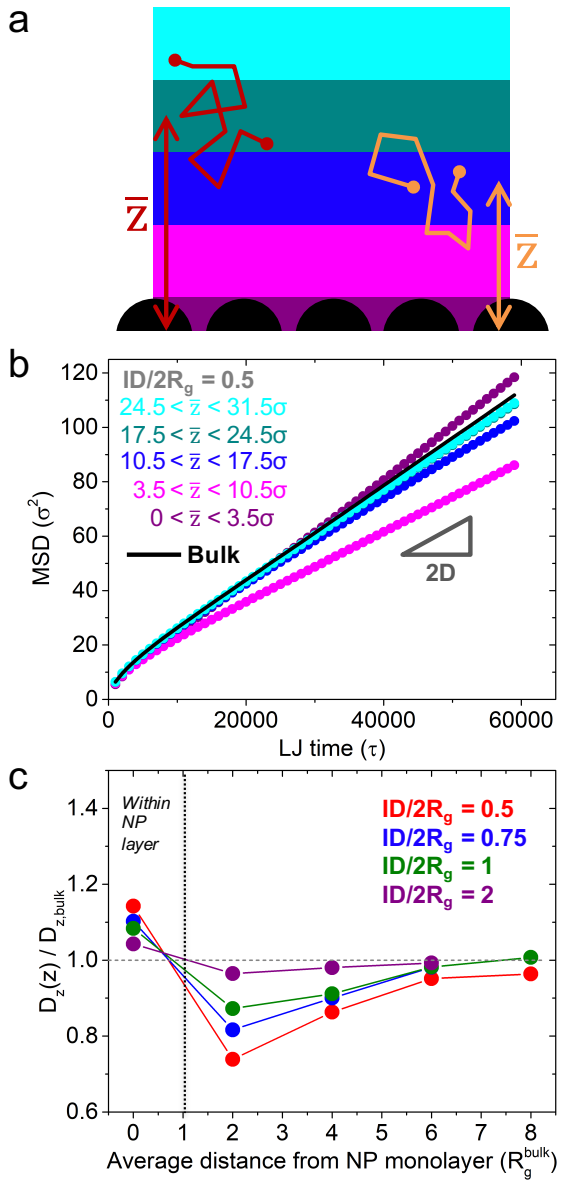

Figure 4.5: (a) Schematic representation of analysis to assign a z position to a given polymer trajectory. (b) Time averaged mean-squared displacement as a function of time for various $\bar{z}$, as schematically represented in (a), for ID/2R_g = 0.5 (symbols) and bulk (solid line). (c) Normalized local polymer diffusion coefficient as a function of distance from the NP monolayer.

In Figure 4.5c, we summarize the spatial dependence of polymer diffusion by plotting the z-directional local diffusion coefficient, $D_z(z)$, normalized to D_z of bulk, as a function of distance from the NP monolayer for systems with different degrees of confinement. Generally, we observe

three different regimes that occur at different distances from the NP monolayer: fast polymer diffusion within the monolayer, slow polymer diffusion just outside the NP monolayer, and bulk-like polymer diffusion far from the NP monolayer. In addition, we observe that these three regions occur for each level of confinement, but the deviations from bulk are more extreme under stronger confinement.

For polymer diffusion within the NP monolayer, Figure 4.5 shows that chains diffuse more rapidly than bulk. This result is reminiscent of the enhanced polymer diffusion observed under intermediate levels of confinement in athermal pores or between althemal substrates, where analogous systems exhibited D/D_0 ~1.2.[308–310] Furthermore, previous simulations of polymer diffusion in PNCs with smooth and repulsive NPs showed that diffusion near the NP surface is enhanced due to the reduced segmental friction near the NP.[192] This regime is likely not significantly affected by tortuosity because movement in the z direction is often accompanied by an increase in accessible volume. In contrast to the enhanced diffusion within the monolayer, the strongest reduction in polymer diffusion is observed directly outside the NP monolayer. In the most confined case of $ID/2R_g$=0.5, diffusion ~$2R_g$ from the center of the NP monolayer is nearly 30% slower than bulk diffusion. This is likely where tortuosity penalties are present because as chains approach the NPs, they are approaching the confinement region with reduced accessible volume. Finally, at long distances, diffusion within 5% of bulk is recovered in all systems. Importantly, if we determine the system-average diffusion coefficient from this analysis by calculating a weight-average of the $D_z(z)$ where the weight is the number of chains in each binned z, we recover the macroscopic D_z reported in Appendix B. This self-check supports the validity of this local analysis and the attribution of a position to individual trajectories.

The slow polymer diffusion near the NP monolayer observed in Figure 4.5 is spatially long lasting. In systems with NPs, the diffusion coefficient remains slower than bulk until ~$6R_g$ from the NP monolayer. Recall from Figure 4.3a that conformations reach bulk-like values after only

~R_g. This decoupling of dynamics and conformations has been recently reported at the segment scale, but our results suggest that it extends to the chain-scale as well. Furthermore, the long-lasting nature of polymer diffusion has been observed experimentally where $D/D_0 < 1$ even when ID is $>20R_g$.[182] In this analysis, the maximum MSD accessed is $< 120\sigma^2$ (~10σ average displacement), and the region over which diffusion is perturbed is more than 21σ. This means that the NPs perturb polymer diffusion even when the average bead does not interact with the NP monolayer.

To further understand polymer diffusion through the NP monolayer, we calculate and analyze one-dimensional van Hove distributions of polymer beads. In this analysis, we calculate the probability (P) of finding a polymer bead at a given z location given a certain lag time (Δt) and starting location (z_0). The van Hove distribution for bulk polymer is shown in Figure 4.6a for three different Δt. As expected, $P(z, \Delta t)$ in bulk follows a symmetric Gaussian distribution that broadens with increasing Δt. In fact, the variance of the distribution (Γ) increases with $\Delta t^{1/2}$ (Figure 4.6b) for $\Delta t > \sim 30{,}000\tau$ indicating diffusive motion with a diffusion coefficient matching D_z (Figure B.5).

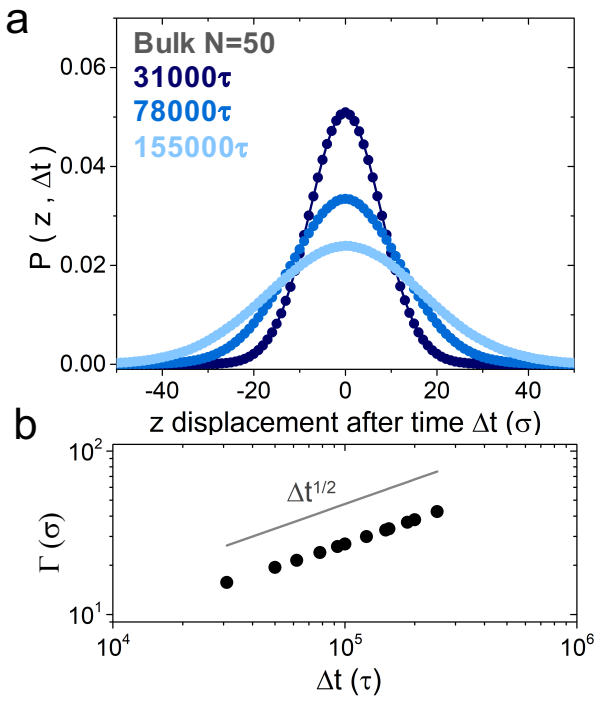

Figure 4.6: (a) Van Hove distribution of monomers in bulk polymer at various times, Δt. (b) Extracted variance (Γ) as a function of Δt showing diffusive behavior ($\Gamma \sim \Delta t^{1/2}$).

We demonstrate the analysis for van Hove distributions in the presence of NPs with $ID/2R_g = 0.5$, $\Delta t = 78{,}000\tau$, and $z_0 = 4\sigma$, meaning the initial bead locations are just beyond the NP monolayer (Figure 4.7a). We ascribe $z<0$ to motion toward or through the NPs and $z>0$ to motion away from the NPs. The distribution shown in dashed red in Figure 4.7a is the raw distribution which shows a clear depression in $P(z,z_0,\Delta t)$ in the NP monolayer as a result of the decreased local volume fraction of polymer (Figure B.2) . The distribution shown in solid red in Figure 4.7a represents the corrected van Hove distribution, obtained by dividing the raw distribution by the normalized local polymer volume fraction at each z position in the box and then renormalizing the distribution. The corrected van Hove distribution effectively accounts for the space occupied by the NPs but retains the dynamic information about the polymer.

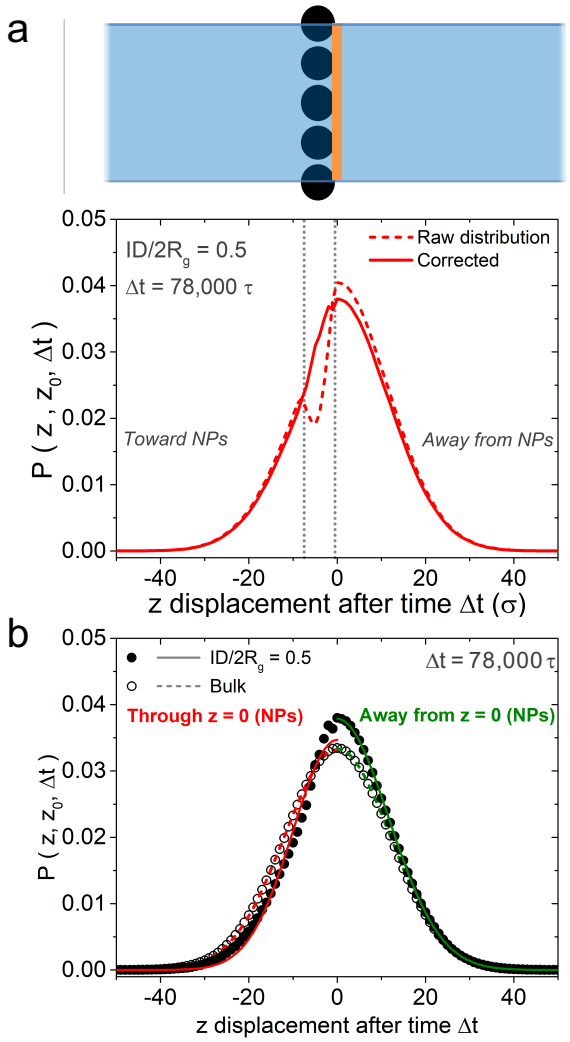

Figure 4.7: (a) Van Hove distribution of $ID/2R_g$ = 0.5 for Δt = 78,000τ and corresponding schematic representation of the simulation box. Dashed line represents the raw van Hove distribution and the corrected distribution obtained by dividing by the relative local polymer volume fraction. (b) Corrected van Hove distribution of $ID/2R_g$ = 0.5 (solid symbols) compared to bulk (open symbols). Directional fitted Gaussian profiles are shown in red and green lines.

The van Hove distributions of bulk polymer and $ID/2R_g$=0.5 are directly compared in Figure 4.7c. Although the maximum of each distribution is located at a z displacement of 0, the van Hove from the $ID/2R_g$=0.5 system is narrower and asymmetric relative to bulk. This observation means that diffusion through the NP monolayer is slower than bulk, as expected from Figure 4.5c,

and more chains diffuse away from the NP monolayer than through it. To further quantify this behavior, we use a Gaussian function to independently fit the distributions to the left and right while restricting the center to be at a z displacement of 0. The fits are included in Figure 4.7 for bulk (dashed) and $ID/2R_g = 0.5$ (solid). Although the fit of the distribution through the NP monolayer is imperfect and is likely a result of the correction for polymer volume fraction, we note that the parameters extracted from the fit (Γ and amplitude) accurately represent the width and integrated amplitude of all distributions.

We begin by analyzing the width of the distribution in each direction and converting it to a diffusion coefficient, $D = \Gamma/(2t)$, to separate diffusion toward the NP monolayer and diffusion away from the NP monolayer. Figure 4.8 shows the diffusion coefficients as a function of degree of confinement, $ID/2R_g$. While diffusion away from the NP monolayer remains bulk-like, diffusion through the NP monolayer is restricted up to almost 40% under the most confined case. Furthermore, the trend in diffusion through the NP layer is reminiscent to the functional form observed experimentally: $D/D_0 = \exp(-R_g/ID)$.[184] Of course, the magnitude of reduced diffusion that we observe is less than observed experimentally, likely because our system is 1-D diffusion through a monolayer rather than isotropic diffusion through infinitely many layers.

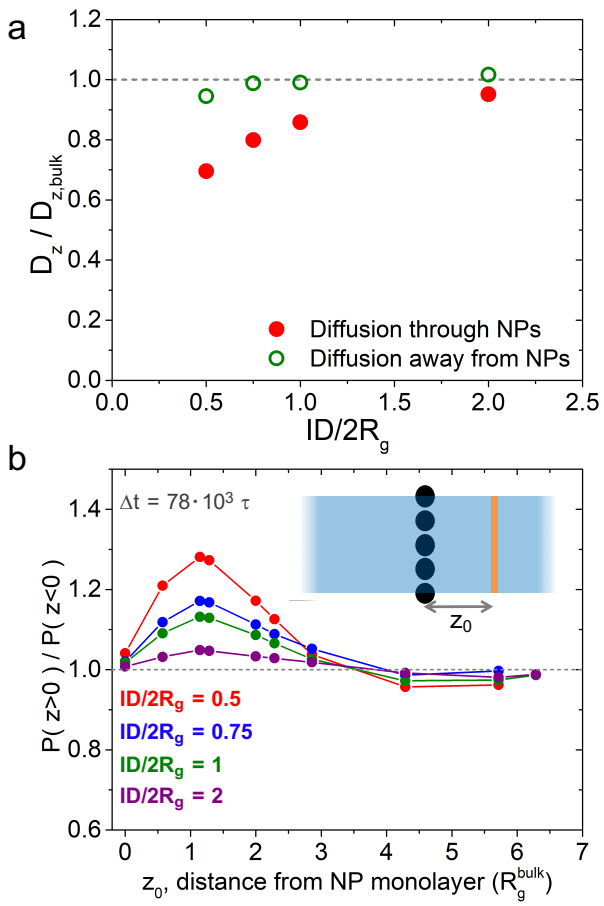

Figure 4.8: (a) Normalized diffusion coefficient away from NPs (green open symbols) and through NPs (red solid symbols) as a function of ID/2R_g. (b) The asymmetry, plotted as P(z>0)/P(z<0), as a function of the initial and center location of the van Hove distribution of z_0 for $\Delta t = 78{,}000\tau$. Inset shows schematic representation of z_0. All data presented is obtained from simulations with $d_{NP}=7\sigma$ and N=50.

We next characterize the asymmetry in the presence of NPs while simultaneously probing the length scale over which diffusion is perturbed. We highlight the asymmetry by calculating the ratio of the probability of a bead diffusing toward the NPs, P(z>0), and away from the NPs, P(z<0), as a function of the starting location, z_0. Although representative van Hove distributions are presented in Figure B.6, the ratio of P(z>0)/P(z<0) is plotted as a function of z_0 for $\Delta t = 78{,}000\tau$ in Figure 4.8b. In qualitative agreement with Figure 4.5c, the asymmetry in diffusion away from and

toward the NP monolayer persists ~$3R_g$ from the NP monolayer. Although the general trend observed in Figure 4.8b is true for all Δt, increasing Δt leads to longer-lasting asymmetry. The results in Figure 4.8b suggest that for chains near the NP monolayer, more chains diffuse away from the NP monolayer than through the NP monolayer and this effect is stronger for more confined systems. We note that this analysis takes advantage of the symmetry in the simulation and direction is considered relative to the NPs, not positive or negative in the z direction. Therefore, the simulation still has a net flux of zero through the NP monolayer but the asymmetry in Figure 4.8b partially highlights the geometric and tortuosity effect of the NP monolayer.

In Figure 4.8, we show that the monolayer of confining NPs slows diffusion toward the NPs but does not perturb diffusion away and that more chains diffuse away from the layer than through it. The latter is expected from excluded volume because fewer chains can enter the monolayer than diffuse away.[170,179] However, the slow diffusion observed through the monolayer may be impacted by excluded volume but is also likely influenced by configurational entropy of the chain, as suggested experimentally.[188] Although we expect more tortuous trajectories in real PNCs due to the spatial distribution of NPs, our use of a hexagonal lattice with fixed and varying ID uniquely highlights the perturbation.

4.3.4 Polymer Diffusion: Effect of NP size

Finally, we now study the same degree of confinement ($ID/2R_g = 1$) and the same chain length (N=50) but vary the NP size. While the NP surface to surface distance remains the same, the diameter of the NP changes the thickness of the NP monolayer and the NP concentration in the monolayer. Using the same analysis presented in Figure 4.8a, we separate diffusion toward and away from the NP monolayer in Figure 4.9. While slow NP diffusion toward the NP monolayer and bulk-like diffusion from the NP monolayer is observed regardless of NP size, we find that larger NPs slow diffusion toward the NP more strongly. Interestingly, this result is in contrast to

experimental observations[181,272] where polymer diffusion in PNCs with different NP sizes scaled with $ID/2R_g$ but is in agreement with recent MD simulations[194] which shows polymer diffusion in PNCs was more impacted by larger NPs. It is important to note that experimental system were not purely athermal, polymer were entangled, and diffusion was monitored over more than $100R_g$, all of which may contribute to the discrepancies between these simulation and previous experiments.

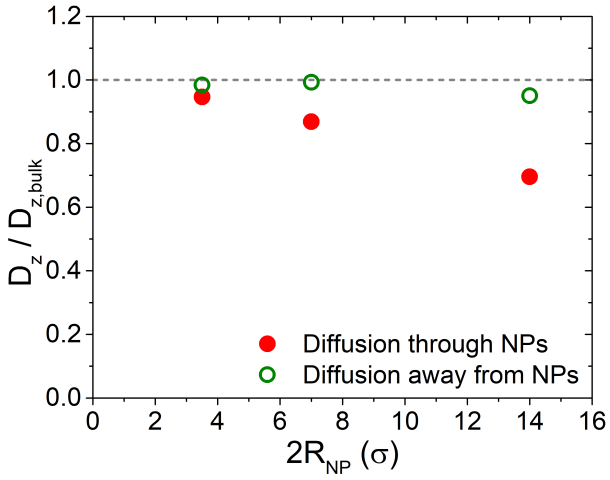

Figure 4.9: Diffusion coefficient through the NP monolayer (red closed symbols) and away from the NP monolayer (green open symbols), normalized to bulk, as a function of NP size ($2R_{NP}$) for systems with N=50 and $ID/2R_g = 1$.

4.4 Conclusions

We use coarse-grained molecular dynamics simulations to study polymer behavior in the presence of a monolayer of hexagonally packed NPs in a polymer melt. Using this unique simulation box, we study the polymer conformations within the NP monolayer and the spatial and temporal impact of the NP monolayer on polymer diffusion through confining NPs. We show that polymer conformations under strong confinement ($ID/2R_g < 1$) between two NPs are more impacted than around an isolated NP and the effect depends on the ratio of R_{NP}/R_g rather than either independently. Furthermore, we show that these conformations originate from a confined random

walk which provides mechanistic insight into predicting conformations in complex confining environments.

We also show that polymer diffusion in systems with NPs is slower than bulk. We show that the local polymer diffusion coefficient within ~R_g of the NP layer is slowed as a function of confinement, and the slowing lasts even ~$5R_g$ from the NPs, despite the fact that perturbation to polymer conformations only persist ~R_g from the NPs. Furthermore, by analyzing the directional van Hove distributions, we show polymer preferentially diffuses away from the NP monolayer and diffusion through the monolayer is slowed as a function of confinement. While only considering a monolayer of NPs, we recover the functional form observed experimentally in the more complex PNC environment, but expectedly a weaker suppression of diffusion. Unlike experiments, however, for constant degrees of confinement, we find that larger NPs perturb diffusion more strongly. These molecular dynamics simulations highlight the impact of a monolayer of NPs and provide fundamental insights into the temporal and spatial effect of confining NPs on polymer conformations and diffusion. The observations from these simplified systems help provide context for more complicated PNC systems and help develop fundamental intuitions to understand chain-scale polymer behavior in PNCs.

CHAPTER 5: Characterizing the Areal Density and Desorption Kinetics of Physically Adsorbed Polymer in Polymer Nanocomposite Melts

Content in this chapter was accepted and published online in 2020 in *Macromolecules*, DOI: 10.1021/acs.macromol.9b02205, in a modified version. The authors of the chapter are Eric J. Bailey, Philip J. Griffin, Russell J. Composto, and Karen I. Winey.

5.1 Introduction

Polymer nanocomposites (PNCs), or materials comprised of nanoparticles (NPs) dispersed in a polymer matrix, are appealing candidates for a variety of applications and technologies, including functional materials, membranes and coatings, and various consumer products.[4] In these materials, the polymer layer adsorbed to nanoparticles, often called bound polymer, can enhance properties and improve NP dispersion, especially for PNCs with attractive NP-polymer interactions.[4,25,26,29] For example, this bound layer is responsible for mechanical strengthening[39,127] and improved ion and small molecule transport,[14,42] among other properties. In addition, the presence of bound layers can sterically prevent NP-NP aggregation, akin to a covalently grafted polymer brush but with less synthetic effort.[210,292,311,312] Importantly, the stability of the various PNC properties and NP morphology are predicated on the stability and lifetime of this bound layer, which remain poorly understood and challenging to measure.[4,25,29]

The conformations of polymers adsorbed to interfaces are perturbed relative to bulk and contain trains (chains of adsorbed segments in direct contact with the surface), loops (sections of non-adsorbed segments between trains), and tails (non-adsorbed chain ends).[110,313] As observed in various experiments, the bound polymer layer thickness (l_b) around a NP in solution[206,210,314] or in the melt[55,73,209,210] is less than or approximately the radius of gyration of the chain (R_g).[4,29] Molecular

dynamics simulations reveal a similar length-scale and show adsorbed chains have conformations that are flattened perpendicular to the NP surface and extend ~R_g from the NP surface.[79,110]

Polymer dynamics are also perturbed near NP-polymer interfaces.[26,29,54,66,73,315] For example, in a mixture of poly(2-vinyl pyridine) (P2VP) and highly-attractive silica (SiO_2) nanoparticles studied by dielectric spectroscopy, P2VP segments beyond ~5 nm from the NP surface relax at timescales similar to bulk while P2VP segments within the bound layer relax nearly 100x slower than bulk.[65,88] One may reasonably expect that these slow segmental relaxations lead to slow dynamics at longer length and time scales, an effect that has been observed near flat substrates.[185,205,316,317] For example, polystyrene diffusion from a hydroxyl-covered silicon substrate was nearly one order of magnitude slower than bulk, and some chains remained immobile on the timescale of the experiment.[185] In the same system, solvent washing for up to 150 days revealed two populations of adsorbed chains: tightly bound chains comprised predominately of trains and loosely bound chains comprised predominately of loops and tails.[316]

Using this evidence of slow segmental dynamics near NPs in PNCs and heterogeneous populations of adsorbed chains at the substrate interface in thin films, it is reasonable to expect slow chain-scale dynamics at the NP interface in PNCs with attractive interactions. These anticipated populations are schematically represented in Figure 5.1. In the initial condition depicted in Stage 1, some chains reside in close proximity to the NP interfaces and others reside farther from NPs in bulk-like regions. Free chains in the PNC, i.e. those far from the NP surface, are able to relax and diffuse at timescales similar to bulk. Thus, after annealing in the melt state on the order of the bulk chain mobility, this population of polymer will relax at the chain-scale, diffuse, and be replaced by other free chains (Stage 2). At longer times, weakly bound chains, i.e. those with few or short trains, are expected to desorb from the NP surface and exchange with free polymer. At this stage, only tightly adsorbed chains will remain from the initial PNC configuration (Stage 3). At sufficiently long times in Stage 4, even these tightly adsorbed chains will desorb, so that all chains

diffused relative to the initial configuration in Stage 1. Naturally, the timescales associated with these stages depends on various parameters such as NP size, polymer molecular weight, NP-polymer interactions, and temperature.

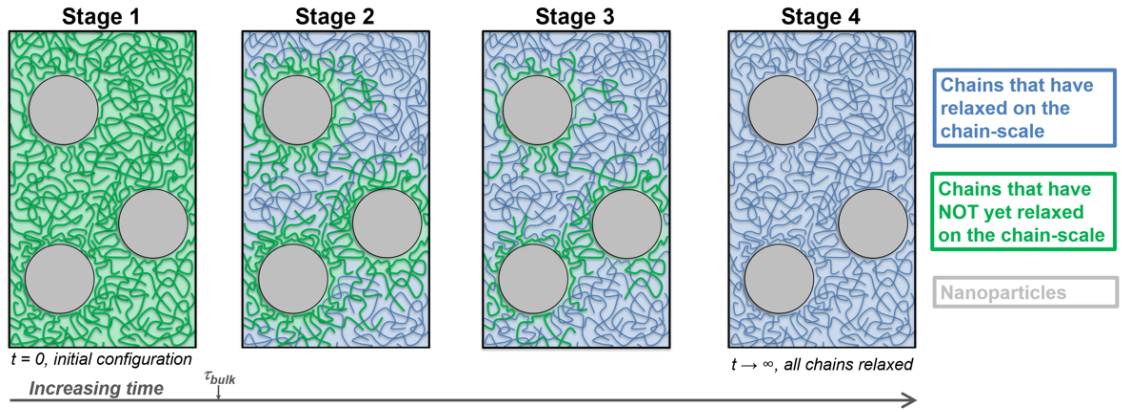

Figure 5.1: (a) Schematic representation of chain scale relaxations in attractive PNCs. The first chains to relax at the chain-scale from the initial condition (Stage 1) the bulk-like polymers far from a NP surface, while chains that are bound to the NP remain in their initial configuration, Stage 2. Next, chains that are loosely bound to the NP surface relax, Stage 3. Finally, at sufficiently long times, all chains have relaxed in Stage 4.

Distinguishing Stages 1 – 4 in PNCs remains an experimental challenge. By contrast, the directionality of thin films facilitates the separation of bound and free populations. However, some progress has been made in PNCs. For example, free chains can be removed by repeated solvent-washing, centrifuging to separate NPs with adsorbed polymer from free polymer, and then removing the free polymer.[141,206,210,318] Recently, this technique was used to fabricate deuterated P2VP-coated SiO_2 NPs that were dispersed in protonated P2VP and small angle neutron scattering (SANS) revealed a decreasing bound layer thickness with increased annealing time (i.e. from Stage 2 towards Stage 3). Interestingly, l_b was found to decrease from ~3 nm to ~0.6 nm when annealing at T_g+75°C, but l_b remained constant after annealing at T_g+50°C, indicating that the desorption process is highly temperature sensitive.[206] These scattering measurements measure the change in scattering length density, which depends on isotope concentration and local mass density[209] and subsequently assign a uniform bound layer thickness. Unfortunately, the extent to which the bound

layer and interfacial polymer conformations are perturbed by solvent-washing, if at all, remains unclear. In another study with conventional sample preparation, the bound polymer layer thickness was inferred by measuring the SiO_2 NP diffusion in P2VP melts. These measurements revealed an effective hydrodynamic radius larger than the core NP radius by ~R_g, implying that adsorbed chains remain adsorbed during NP diffusion. Although the length-scale of the bound polymer was determined and Stages 1 and 2 were distinguished, this NP diffusion study did not capture the internal structure or the stability of the bound polymer at long times. With limited data sets and few experimental methods, the understanding of chain-scale dynamics and properties of the bound layer in melt PNCs, and the dependence on various parameters, remains incomplete.

In this article, we develop ion scattering methods to quantify the fraction of bound and free polymer as a function of NP concentration, polymer molecular weight, annealing temperature, and annealing time. Whereas most techniques define the bound layer through segment-sensitive properties[55,65,69,71,73,209] or rely on solvent-assisted separation of bound and free polymer[206,210,292,314,316,318,319], the experiments presented herein probe the chain-scale structure and dynamics of bound polymers directly in the melt state. At short times (Stage 2) our analysis shows that bound chains extend ~R_g from the NP surface in the melt and reveals the average surface area per bound chain. The bound polymer fraction decreases at long annealing times and depends on annealing temperature and molecular weight. These results highlight the importance of chain-scale considerations on the structure and desorption dynamics in attractive PNC melts, motivate more investigations at the chain-scale, and provide fundamental insights for stabilizing bound polymer layers.

5.2 Experimental Section

Materials: The poly(2-vinylpyridine) (P2VP) polymers were purchased from Scientific Polymer Products and used as received. Partially deuterated poly(2-vinylpyridine), dP2VP, of 130

kg/mol was synthesized at the Center for Nanophase Materials Science at Oak Ridge National Laboratory. Other dP2VP of 110 kg/mol and 31 kg/mol were purchased from Polymer Source, Inc. and used as received. All polymer molecular weight averages were characterized by GPC and polydispersities (compared to narrow polystyrene standards) are < 1.4. Silica (SiO_2) nanoparticles (NPs) were synthesized following the modified Stöber method[279,280] with a log-normal geometric mean diameter (d_{NP}) of 26.1 nm and standard deviation of 3.9 nm as determined by analysis of transmission electron micrographs (TEM).[208]

Bilayer Sample Fabrication: Bilayer samples were comprised of a thin (<150 nm) dP2VP-based PNC film deposited on a matrix of neat P2VP polymer, as depicted in Figure 5.2a. Neat P2VP matrices were made by doctor blading a solution of P2VP in methanol (MeOH) (c_{poly} ~ 50 g/L) on an ozone-cleaned silicon wafer. Doctor bladed films were dried for several hours at room temperature, then annealed at ~T_g+80°C under vacuum for at least 48 hours. The resulting films were ~20 μm in thickness.

The PNC films were made from solution as follows. The dP2VP was mixed with MeOH and allowed to completely dissolve by stirring overnight. Then, requisite amounts of SiO_2 in ethanol (EtOH) were added to dP2VP/MeOH. The resulting polymer and NP concentrations were c_{poly} < ~20 g/L and c_{NP} < 7 g/L, respectively. This solution was stirred at room temperature for at least 48 hours to ensure proper mixing and provide ample time for the spontaneous formation of the bound polymer layer in solution.[208] To deposit the PNC films, a thin layer of 2000 kg/mol polystyrene (PS) was first spin coated on an ozone-cleaned silicon wafer with thickness ~30 nm. This sacrificial PS layer mitigates potential SiO_2 aggregation at the polar substrate and promotes release of the adsorbing dP2VP PNC film from the wafer. The dP2VP/SiO_2/MeOH PNC solution was then spin coated onto the PS-treated silicon substrate to a thickness between 100 to 150 nm.

To form the bilayer samples (Figure 5.2a), the PNC film was lifted from the substrate in DI water (such that the PS layer is facing toward the water and the dP2VP layer is facing up) and

transferred to the preannealed P2VP matrix. This diffusion couple is placed on a hot plate at T_g+50°C for < 20 seconds to weld the bilayer films and prevent delamination of the PNC film. Bulk diffusion couples (neat dP2VP on P2VP) that are used for comparison and to determine the diffusion coefficient of the free polymer are fabricated in the same manner as PNC tracer films, without the addition of NPs.

Bilayer films are annealed at the requisite temperatures under a nitrogen environment (~0.4 atm) after at least four nitrogen purges. Temperature equilibration (within ±1°C) during purging was < 1 min. For anneals less than 5 minutes, only one purge was used.

Ion Beam Measurements: The depth profile of dP2VP was measured using elastic recoil detection (ERD), which has been used to measure the tracer diffusion coefficient through the PNC film[109,169,170,188] and is described elsewhere[169]. ERD offers a depth resolution (full width at half maximum) of ~110 nm and depth penetration (for deuterium) of ~700 nm, which is large compared to both the NP and polymer size. In ERD, He^{2+} ions are accelerated at 3 MeV and incident onto the sample at 70° off-normal. Light elements, such as hydrogen and deuterium, are forward recoiled to a detector at the complimentary angle. A thin (~10 μm) Mylar film is used to block forward recoiled He^{2+} ions. The measured energies are converted to depth profiles through the stopping power of He^{2+} into the sample, the stopping power of deuterium or hydrogen leaving the sample, and the stopping power through the Mylar film.

The depth profile of SiO_2 NPs was measured using Rutherford backscattering spectrometry (RBS), which has been used to measure the diffusion of tracer NPs into polymer matrices,[109,169,208] as described elsewhere.[169] RBS offers a depth resolution of ~80 nm and a penetration depth (for Si) of ~1 μm. In RBS, He^+ ions are accelerated to 3 MeV and incident on the sample in normal geometry. Backscattered He^+ ions are collected at a detector 10° off normal. The energies of

collected He ions are converted to depth profiles by the stopping power of He^+ into and out of the sample.

5.3 Results

5.3.1 Evidence of Bound Polymer

Figure 5.2 shows a schematic representation of the experimental samples and process (Figure 5.2a) and representative experimental data (Figure 5.2b and Figure 5.2c). As shown in Figure 5.2b, the as-cast PNC bilayer samples contain a mixture of dP2VP (solid green) and SiO_2 NPs (black) in the top ~150 nm film. We selected material systems and annealing conditions such that $D_{NP} < D_{poly}$. Therefore, after short annealing times the NPs remain in the top ~150 nm (Figure 5.2c, black), while free polymer diffuses into the underlying matrix (Figure 5.2c, green). Compared to the diffusion of neat dP2VP (Figure 5.2c, open circles), the PNC bilayer sample annealed at the same conditions contains excess dP2VP in the top film (where the NPs are located) and a corresponding depletion of dP2VP beyond ~200 nm. These data clearly demonstrate the ability of these experiments to separate the dP2VP that quickly diffuses away from the PNC layer and the dP2VP that is slower to diffuse and thereby establish the timescale for Stage 2. Analysis of these profiles reveal the amount of bound polymer and by extending to longer anneals, reveal the progressing from Stage 2 to Stage 3.

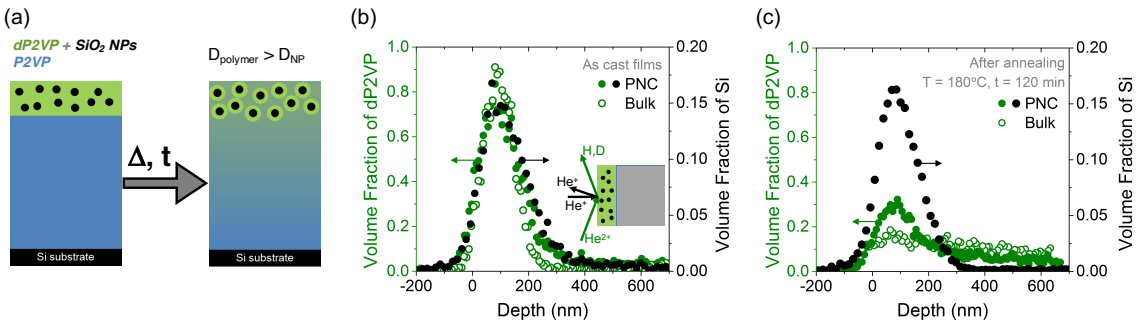

Figure 5.2: (a) Schematic representation of experimental samples before and after annealing. Blue and green represent P2VP and dP2VP, respectively, while black represents SiO_2 NPs. (b,c) ERD (green) and RBS (black) depth profiles for 110 kg/mol dP2VP samples with SiO_2 NPs (closed circles, ϕ_{NP} = 19 vol%) and without NPs (open circles) for samples before annealing (b) and after annealing for 120 min at T_g+80°C (c). Inset of (b) depicts measurement geometry for ERD (green) and RBS (black). The underlying P2VP matrix in this representative dataset is 250 kg/mol.

5.3.2 Extracting the Fraction of Bound Chains

Akin to Figure 5.1, the analysis of the dP2VP depth profiles considers two populations: bound polymer residing in the top PNC film (ϕ_{bound}) and free polymer diffusion into the matrix (ϕ_{free}). Thus, the depth profiles are fit to a linear combination of ϕ_{bound} and ϕ_{free} that is convoluted with a Gaussian representing experimental resolution.

$$\phi(z) = \text{Res} * \{\phi_{bound}(z) + \phi_{free}(z)\} \quad (5.1)$$

where

$$\phi_{bound}(z) = X_{bound} \cdot \phi_{poly} \text{ when } 0 < z < h \quad (5.2)$$

$$\phi_{free}(z) = (1 - X_{bound}) \cdot \left(\frac{1}{2}\left[\text{erf}\left(\frac{h-z}{\sqrt{4Dt}}\right) + \text{erf}\left(\frac{h+z}{\sqrt{4Dt}}\right)\right]\right) \quad (5.3)$$

where z is the depth, Res is the resolution function, ϕ_{poly} is 1-ϕ_{NP}, h is the thickness of the PNC film, D is the free chain diffusion coefficient, t is the annealing time, and X_{bound} represents the number fraction of bound dP2VP chains. A representative fit is provided in Figure 5.3a.

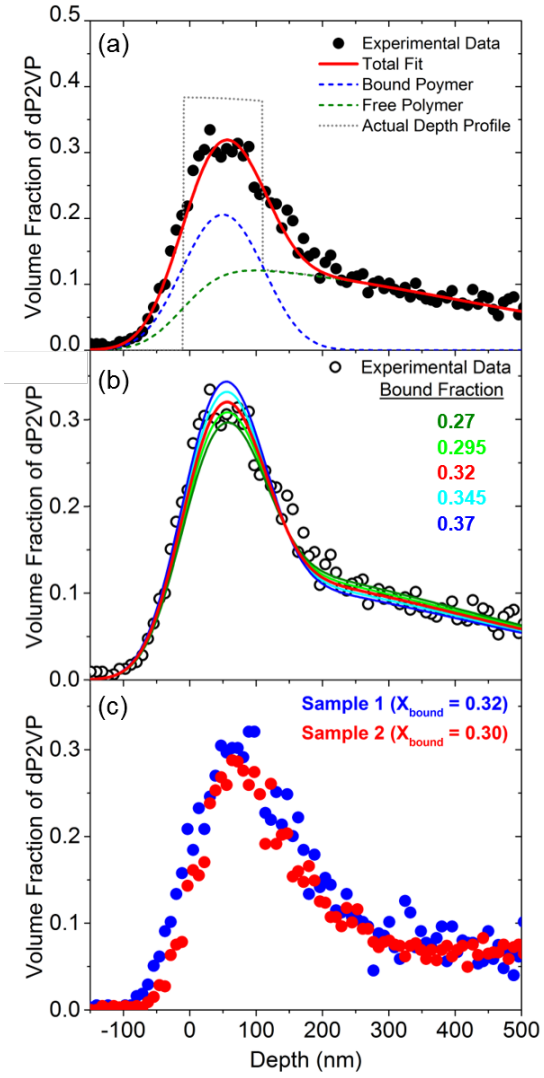

Figure 5.3: (a) Representative volume fraction of dP2VP as a function of depth (circles), total fit (red solid line), contributions from bound polymer (blue dashed line) and free polymer (green dashed line), and the actual depth profile without experimental resolution (grey dotted line). (b) Comparison of fit quality for various values of X_{bound}, where the limits are considered poor fits, to demonstrate fitting errors. (c) Comparison of duplicate samples and measurements showing reproducibility. Data displayed is for 110 kg/mol dP2VP deposited on 250 kg/mol P2VP, ϕ_{NP} = 19 vol%, T= T_g+80°C, and t = 45 min (a,b) or 180 min (c).

A step function is used to describe the deuterated polymer in the PNC layer (Equation 5.2), which after annealing is the signature of bound polymer. The ϕ_{poly} and h values in Equation 5.2 are known from RBS and ERD measurements of the unannealed bilayer sample (Figure C.2). The concentration profile of free polymer is described by Equation 5.3 and is the solution to Fick's

second law for a finite source diffusing into a semi-infinite medium, as previously reported.[109,170,208] The diffusion coefficient of neat dP2VP into the P2VP matrix (D_{bulk}, Figure C.4) is used to approximate the diffusion of free dP2VP chains through the NPs in the PNC layer and in the underlying matrix. Note that the D used to fit the annealed PNC bilayer samples may be reduced from the bulk diffusion coefficient by at most ~25% to improve the fit to ERD data.[170,272] In addition, the tracer PNC film thickness, h, may vary upon annealing due to asymmetric diffusion between dP2VP and P2VP, i.e. the Kirkendall effect.[320] Thus, the thickness in Equation 5.2 is allowed to vary between the resolution of ERD (~110 nm) and the ERD-measured thickness of unannealed samples, typically 125-150 nm. Importantly, these two parameters (D and h) can be separately evaluated because they have distinct contributions to the overall depth profile of dP2VP. Thus, after selecting the appropriate D ($0.75 \cdot D_{bulk} \leq D \leq D_{bulk}$) based on the slope at $z > 200$ nm, h is selected by the region $100 < z < 200$ nm. As a result, X_{bound} is the only remaining fit parameter used to describe the relative concentrations at $z < 200$ nm (bound polymer) and $z > 200$ nm (free polymer).

It is important to note that X_{bound} is explicitly defined as the excess dP2VP fraction residing with the NPs in the thin PNC layer after a given annealing time and not necessarily the fraction of chains in direct contact with the NP surface. However, at short annealing conditions, the rate limiting step for polymer diffusion into the underlying matrix is most likely desorption from the attractive NP rather than slow diffusion through the PNC film (i.e. confinement effects imposed by NPs). Previous studies have established that the reduction in polymer diffusion coefficient (relative to bulk) through comparable PNCs is dependent on the interparticle distance (ID)[181] relative to the chain size ($2R_g$).[170,272] For the most confining PNC conditions studied herein, the tracer diffusion is expected to be only ~2x slower than bulk polymer.[170,272] Furthermore, this anticipated slow diffusion of free polymer in the PNC lasts only in the PNC film, which is ~150 nm in total thickness. In reality, the population described by ϕ_{bound} diffuses orders of magnitude slower than bulk. Thus,

when chains desorb, they are able to freely diffuse into the underlying matrix, thereby leading to the experimental realization of Figure 5.1.

Finally, the extracted values of X_{bound} may have uncertainties associated with fitting the model or sample-to-sample variability. Figure 5.3b shows how the fit varies from experimental data for different values of X_{bound} with other variables fixed. We consider $X_{bound} = 0.32$ as the best fit, but show variance of ±0.05, where the extremes clearly deviate from the concentration profiles, particularly at z = 75 nm and 250 nm. Figure 5.3c shows replicated samples under the same conditions to demonstrate small variances between identical samples. Thus, we estimate an error bar ±0.03 on X_{bound}.

5.3.3 Effect of NP Concentration

To explore the role of NP concentration (ϕ_{NP}), we measure the depth profile of dP2VP-130 (130 kg/mol dP2VP) with SiO_2 NP concentrations of 4, 11, and 16 vol%. All samples were annealed for 45 minutes at 180°C (~T_g+80°C) and the underlying matrix was 110 kg/mol P2VP. At these annealing conditions, the characteristic diffusion length of neat dP2VP-130 is more than 500 nm. Thus, free polymer diffuses into the underlying film during annealing (Figure 5.4a), while the slower NPs and the NP-bound polymer remain near the surface (Figure 5.4b).

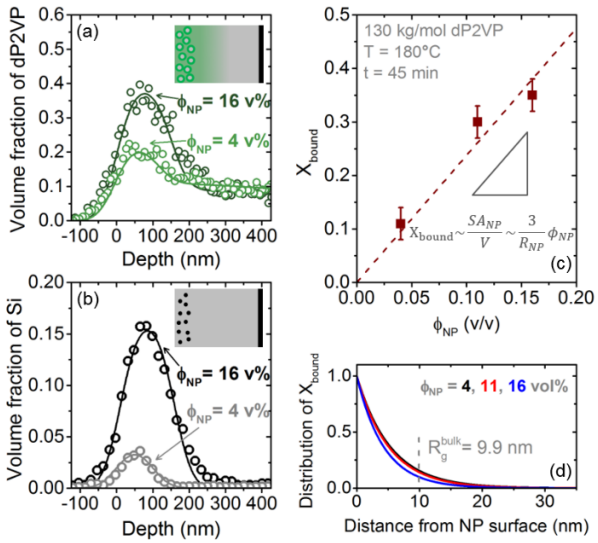

Figure 5.4: (a) ERD measurements of dP2VP-130 concentrations and (b) RBS measurements of NP concentrations as a function of depth after annealing PNC samples of ϕ_{NP}=4 vol% (light) and 16 vol% (dark) for 45 min at T= 180°C. (c) X_{bound} as a function of ϕ_{NP} showing linear dependence. (d) Extracted concentration of bound polymer as a function of distance from the NP surface (assuming exponentially decaying distribution) showing a bound layer thickness on the order of R_g. The underlying P2VP matrix is 110 kg/mol.

As shown in Figure 5.4c, the extracted X_{bound} of dP2VP increases linearly with NP concentration from the origin. In PNCs with individually dispersed NPs, the bound fraction is expected to scale linearly with the NP surface area, and thereby ϕ_{NP}. Thus, the linear relationship in Figure 5.4c is consistent with our assertion that X_{bound} reflects the polymers adsorbed to the NP surface, namely Stage 2. Note that X_{bound} is ~34% at ϕ_{NP} = 16 vol%, indicating that the majority of polymer chains are free to diffuse and relax at timescales similar to neat polymer.

To gain more insight into the quantitative meaning of X_{bound}, the concentration profile of the bound polymer around a single NP can be calculated by assuming an exponential decay as a function of distance from the NP surface.[73,88,209,313] Using a construct with a single NP in a volume defined by ϕ_{NP} and R_{NP}, the bound polymer (X_{bound}) was represented by spherically integrating the exponential profile around the NP surface:

$$X_{bound} = \frac{4\pi \int_{R_{NP}}^{\infty} r^2 \, e^{\frac{-(r-R_{NP})}{l_b}} dr}{{}^4/_3 \pi R_{NP}^3 \left(\frac{1-\phi_{NP}}{\phi_{NP}}\right)} \quad (5.4)$$

where l_b is the characteristic length of the exponential decay of the bound polymer concentration. Figure 5.4d shows the extracted concentration profiles of the bound layer. The bound layer extends ~R_g from the NP surface with l_b ~ 4.9±0.7 nm. This value of l_b is independent of ϕ_{NP}, as expected, and is smaller than the chain size (R_g ~ 9.9 nm[206,208]), in agreement with other measurements of the bound layer thickness.[29,206,208,210] The result that $l_b \leq R_g$ further supports our assertion that (i) annealing at 180°C for 45 minutes is sufficient for free polymer to spatially separate from NP-bound polymer, i.e. Stage 2, and (ii) that our definition and extraction of X_{bound} accurately reflects the bound fraction. In addition, the result that l_b is independent of ϕ_{NP} suggests that polymer bridging has little effect on our results, despite the fact that polymer bridging has been observed through mechanical measurements at small NP concentrations (ϕ_{NP} < 5 vol%)[40] and that ID at 16 vol% (~16.2 nm)[181] is slightly smaller than $2R_g$ (19.8 nm).

5.3.4 Desorption of Bound Polymer

The diffusion of free dP2VP into the underlying P2VP matrix is relatively rapid (< 1 hr), as demonstrated in the experimental realization of Stage 2 in Figure 5.4. However, polymers that are initially adsorbed to NPs may desorb and become free to diffuse at longer times (Stages 3 and 4).[206,316] Importantly, the NP diffusion must be restricted to access sufficiently long annealing times. To impede NP diffusion (Figure C.5) without perturbing free polymer diffusion[170,321], the underlying P2VP M_w was increased from 110 kg/mol to 250 kg/mol.[208,214,216]

First, we measure the bound fraction remaining in the PNC after long annealing times in an effort to observe Stage 4. Figure 5.5 presents measurements of PNCs comprised of dP2VP-31 and dP2VP-110 with ϕ_{NP} = 19 vol% deposited on 250 kg/mol P2VP after ~12 hours of annealing

at 160°C, 180°C, and 200°C. Importantly, all dP2VP depth profiles show the presence of bound polymer, meaning that Stage 4 is not observed under these experimental conditions. For all temperatures studied, dP2VP-31 exhibits a lower bound fraction than dP2VP-110, which is consistent with a smaller l_b expected for lower M_w. For a fixed annealing time (~12 hrs), more polymer desorption has occurred at higher temperatures. Although we observe a sharp decrease in X_{bound} between 160°C and 180°C, only a modest decrease in X_{bound} is observed upon further increasing the temperature to 200°C.

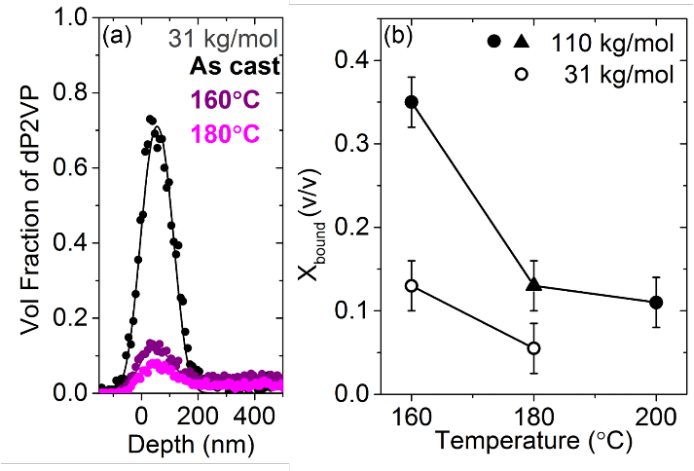

Figure 5.5: (a) Depth profiles for dP2VP-31 that are unannealed (black) and annealed at 160°C (purple) and 180°C (magenta) for 12 hours. (b) Measured X_{bound} for dP2VP-31 (open symbols) and dP2VP-110 (closed symbols) as a function of annealing temperature for annealing times of 12 hours (circles) or 13 hours (triangle). The P2VP matrix is 250 kg/mol and the PNC layer has ϕ_{NP} = 19 vol%.

To probe the kinetics of desorption, i.e. the transition from Stage 2 to Stage 3, X_{bound} was measured as a function of annealing time. As shown in the depth profiles for dP2VP-31 (Figure 5.6a) and dP2VP-110 (Figure 5.6b), the dP2VP concentration in the top PNC layer generally decreases as the annealing time increases. For dP2VP-31 and dP2VP-110 annealed at 180°C and 200°C, the extracted X_{bound} are plotted in Figure 5.6c as a function of annealing time. Figure 5.6c shows a systematic decrease in X_{bound} with increasing annealing time and demonstrates ongoing

dP2VP desorption from SiO_2 NPs. Furthermore, for these times, smaller values of X_{bound} are observed for the lower M_w dP2VP-31 (open circles) and at higher temperatures (red symbols), consistent with Figure 5.5b. For dP2VP-31, after an initial decrease in X_{bound} upon annealing, a plateau of X_{bound} ~5% is observed at both 180°C and 200°C. For longer dP2VP-110 at 180°C, the initial X_{bound} persists and a decrease in X_{bound} occurs at longer annealing times. Thus, we observe slower desorption kinetics for larger polymers and at lower temperatures.

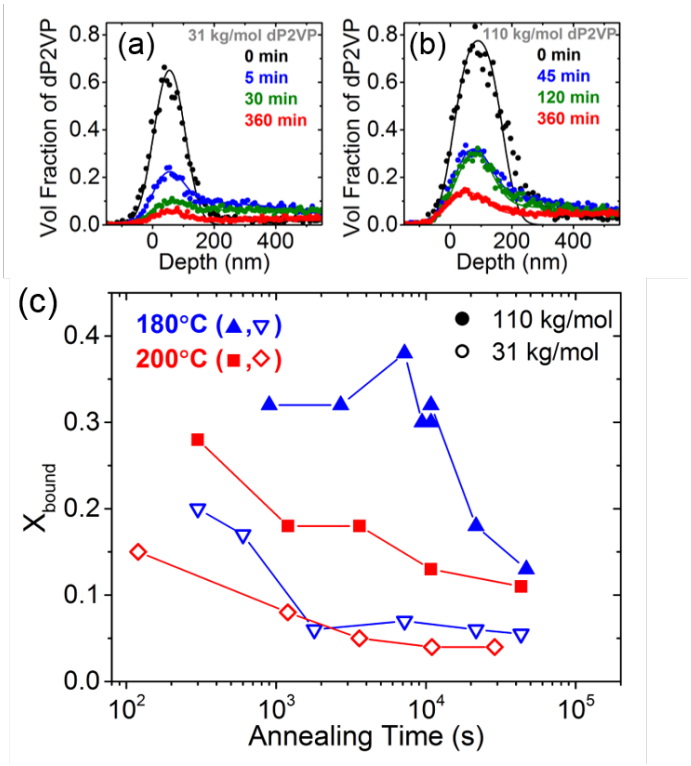

Figure 5.6: ERD depth profiles for dP2VP-31 (a) and dP2VP-110 (b) for various annealing times for T = 180°C. (c) Extracted X_{bound} as a function of time. The P2VP matrix is 250 kg/mol and the PNC layer has ϕ_{NP} = 19 vol%. Error bars of 0.03 in (c) are omitted for clarity.

In summary, at short annealing times as demonstrated in Figure 5.4, we experimentally separate and identify bound polymer from free polymer (Stage 2). Then upon further annealing, as demonstrated in Figure 5.6c, we observe polymer desorption from Stage 2 to Stage 3. Although the rate at which chains desorb depends on M_w and temperature, in all cases, polymers that are initially

bound become free after additional annealing. At long times (as demonstrated in Figure 5.5 and Figure 5.6c), some polymer remains adsorbed to the NPs in each data set, meaning that complete desorption (Stage 4) was not observed at these experimental conditions.

5.4 Discussion

5.4.1 Ion Beam Methods to Probe Bound Polymer in PNCs

Before further discussing the results presented above, this section will highlight the advantages and challenges of combining ERD and RBS to measure the static and dynamic properties of bound polymer in PNCs. These ion scattering methods are unique in that they measure chain-scale structure and dynamics of bound polymer by isolating and quantifying bound polymer directly in the melt. Previous studies have probed chain-scale mobility of polymers (polymer diffusion) in PNCs[109,170,272] and other studies have probed segmental dynamics at the NP interface[65,88], but few studies have probed chain-scale phenomena at the interface[206,208,210]. In addition, many studies that probe the bound polymer layer use solvent to isolate the bound polymer layer, which may change the polymer conformations of the bound layer relative to the melt.[206,210,314] Below, we summarize the unique attributes and limitations of these measurements.

Conventional PNC Fabrication Methods: PNC samples for these ion beam measurements are fabricated by conventional solvent-based fabrication procedures so that the observations are widely applicable. To be specific, we mix a single polymer component with solvent and NPs and spin coat the film. Thus, the bound layer is formed naturally and spontaneously in solution and densified as solvent is removed. All post-processing is conducted in the glassy state and separation of bound and free polymer is done purely in the melt state.

Separate Free and Bound Polymer: Using the sample geometry in Figure 5.2a, isolation of free and bound polymer is achieved by the comparatively faster diffusion of free polymers from

the PNC layer into the homopolymer layer. This spatial separation of free and bound polymer, as discussed in Figure 5.3, enables straightforward data interpretation using the simple model presented in Equation 5.1. The ability to selectively and independently measure the depth profile of the NPs (RBS) and deuterated polymer (ERD) in various samples and for different annealing conditions (t, T) permits informed fitting of experimental data, and ultimately, accurate delineation of bound and free polymer.

Measurement of Bound Fraction: This ERD/RBS measurement directly measures the amount of bound polymer in the PNC, as opposed to a length-scale of the bound layer or the local dynamics within it. As a result, new information is available. Although straightforward approximations can lead to the bound layer thickness (Figure 5.4d, Figure C.3) and measurements as a function of time can lead to chain-scale dynamics (Figure 5.6c), additional information such as the average NP surface area occupied by adsorbed chains can be reported (as discussed below). Note that this method, unlike scattering methods or measurements of hydrodynamic sizes, is not sensitive to the size, shape, or size dispersity of the NPs. However, the experimental signal depends intimately on the interfacial area which presents an inherent paradox: high NP concentrations are desired to maximize the signal in the measurement and low NP concentrations are desired so adjacent NPs are non-interacting and polymer bridges between different NPs are minimized. Thus, a good practice is to measure the bound layer at multiple NP loadings, Figure 5.4.

Broad Potential for Studying Experimental Parameters: This experimental method offers a wide array of accessible experimental parameters, many of which were studied herein, such as temperature, time, M_w, and ϕ_{NP}. Ex-situ annealing provides a wide range of time and temperature without complicating the ERD/RBS measurements. The two main requirements for the PNC system are the necessity of deuterated polymer and slower NP diffusion than polymer chain diffusion. For the former, it is important to note that partially deuterated polymer can be used, and these measurements require very little deuterated polymer (~10 μg per sample). For the latter, this

relation is naturally true for many annealing conditions and several PNC systems. When necessary, the NP diffusion can be slowed by increasing the viscosity or even lightly crosslinking the underlying matrix (e.g. Figure C.5). For matrix materials that significantly differ from the tracer polymer, it will be important to characterize how the differences impact the measurement. Although not a requirement, these ERD/RBS measurements are more convenient for glassy polymers (i.e. T_g < 25°C). Beyond these straightforward requirements to the materials, the ERD/RBS method is applicable to a broad range of PNC systems and experimental parameters.

Measuring Concentration Profiles: The ability to quantify the polymer and NP concentrations as a function of depth into the sample are critical to the success of these measurements. Here, we use ERD and RBS measurements that require specialized equipment not commonly available. Other techniques that are more widely available, such as secondary ion mass spectrometry (SIMS), are likely capable of similar measurements of the bound layer in PNCs. Depth-profiling techniques are insensitive to areal information so complimentary measurements might be needed to probe areal properties (e.g. NP dispersion).

5.4.2 Characterization of Areal Density

With direct measurement of the number fraction of bound chains (X_{bound}) and precise knowledge of the NP surface area (through R_{NP} and ϕ_{NP}), we can report the average surface area occupied by an adsorbed chain, a parameter that is often difficult to quantify in the melt. At 180°C, about 32% of the dP2VP-110 remains as bound polymer after 45 min (Figure 5.6c). These annealing conditions are identical to those in Figure 5.4c and were long enough to separate free and bound polymer but short enough to minimize desorption of initially bound dP2VP (Stage 2), as supported by the extracted bound polymer layer thickness (Figure C.3). The measured X_{bound} values can be related to the total NP surface area to reveal the average NP surface area occupied by each dP2VP chain ($<SA_{chain}>$):

$$\langle SA_{chain} \rangle = \left(\frac{3}{R_{NP}}\right)\left(\frac{\phi_{NP}}{1-\phi_{NP}}\right)\left(\frac{M_w}{X_{bound}\rho_{poly}N_A}\right) \quad (5.5)$$

where ρ_{poly} is the neat polymer mass density and N_A is Avogadro's number. Equation 5.5 assumes all bound chains are dP2VP. Note that at longer annealing times where dP2VP/P2VP exchange is likely, calculating $<SA_{chain}>$ is unreliable and therefore not reported.

For dP2VP-110, $<SA_{chain}>$ is ~14 nm^2/chain in the melt state, which corresponds to an effective areal density of 0.072 chains per nm^2. For comparison, the projected areal coverage of an unperturbed polymer (πR_g^2) isolated on the NP surface is much larger $<SA_{chain}>$~260 nm^2/chain. This result suggests that the adsorbed dP2VP has relatively few (or short) trains and several (or large) loops and tails. Moreover, this areal density highlights that bound chains are highly interpenetrating within the bound layer. In contrast, a similar P2VP/SiO_2 system was repeatedly solvent washed to remove free polymer and is reported to have a polymer concentration of ~12 wt%, corresponding to $<SA_{chain}>$~60 nm^2/chain.[206] The smaller $<SA_{chain}>$ measured by ion scattering in the melt appears to be the result of solvent washing producing less bound polymer than in the melt. This observation can be reconciled in terms of the polymer density in the bound layer. For an isolated chain, since the polymer density is low, the chains near the interface occupy more of the surface area. As the polymer density increases in a polymer solution and more so in the melt, the densification leads to more polymers near the interface and therefore more that are bound. This quantitative comparison further highlights the differences between the bound layer in solution and in the melt.[210]

For dP2VP-31, $<SA_{chain}>$ is 5.8 nm^2/chain (areal density of 0.17 chains per nm^2) at the shortest annealing time accessible at 180°C (5 min). The measured $<SA_{chain}>$ relative to the projected chain size, $<SA_{chain}>/\pi R_g^2$, is 8.0% and 5.3% for dP2VP-31 and dP2VP-110, respectively. This difference suggests a larger percentage of segments in dP2VP-31 chains are adsorbed on the surface of the NP. This observation is consistent with the model previously proposed from BDS,

pycnometry, SAXS, and IR and X-ray spectroscopies studies which indicate that shorter chains pack more efficiently at an interface.[69,73,88] It is also somewhat surprising that the chains in both PNCs occupy, on average, relatively small amounts of the NP surface yet still exhibit long-lived adsorption. Although we begin to interpret these dynamic results further in the next section, it is important to note that our analysis of $<SA_{chain}>$ reveals an average areal density and whether the distribution is narrow, broad, or multi-modal remains unclear. As others have discussed[29,206,210,316], we expect the $<SA_{chain}>$ of individual chain can deviate strongly from the average and can be phenomenologically described as ranging from weakly- to strongly-adsorbed.

5.4.3 Collapse of Desorption Data

Data in Figure 5.6c characterizes the desorption of bound polymer as a function of time for different annealing temperatures and M_w. To gain insights into the mechanism and microscopic parameters that influence the lifetime of the bound layer, we scale the annealing time to different polymer dynamic processes. Since the P2VP/SiO_2 interaction and adsorption is fundamentally at the segment scale, Figure 5.7a shows X_{bound} as a function of annealing time normalized by the segmental relaxation time, τ_α, of neat polymer (obtained from Ref [55]). Although the data from 180°C and 200°C seem to overlay on each other, τ_α fails to capture the effect of M_w, suggesting that bound polymer desorption also requires consideration of polymer chain length or cooperative motion. Since this measurement fundamentally monitors the diffusion of the chain from the NP surface, Figure 5.7b shows X_{bound} as a function of annealing time normalized by the chain-scale mobility, given by the reptation time in bulk polymer ($\tau_{rep} = R_g^2/D_{chain}$, Figure C.4). The X_{bound} data for two molecular weights, three annealing temperatures, and a range of annealing times collapse reasonably well. The current data set spans a range of 10^2–10^6 τ_{rep} and the bound fraction decreases by nearly 6x, from ~30% to ~5%, over that timescale. On average, these chains desorb ~10^4 times slower than bulk τ_{rep} and even after annealing for times longer than ~10^6 τ_{rep}, some polymer remains

adsorbed. Chain desorption occurring after more than 10^{10} τ_α or 10^3 τ_{rep}, if they desorb at all, is particularly noteworthy considering the relatively small average $\langle SA_{chain} \rangle$ we calculated using Equation 5.5. We speculate that the chains with relatively few adsorbed segments (and therefore lower local SA_{chain}) are the ones we observe desorbing while those with more absorbed segments (and therefore higher local SA_{chain}) are the bound chains that persist beyond ~10^6 τ_{rep}. It remains unclear how the polymer conformations and distribution of them within the bound layer change during annealing, desorption, resorption, and exchange.

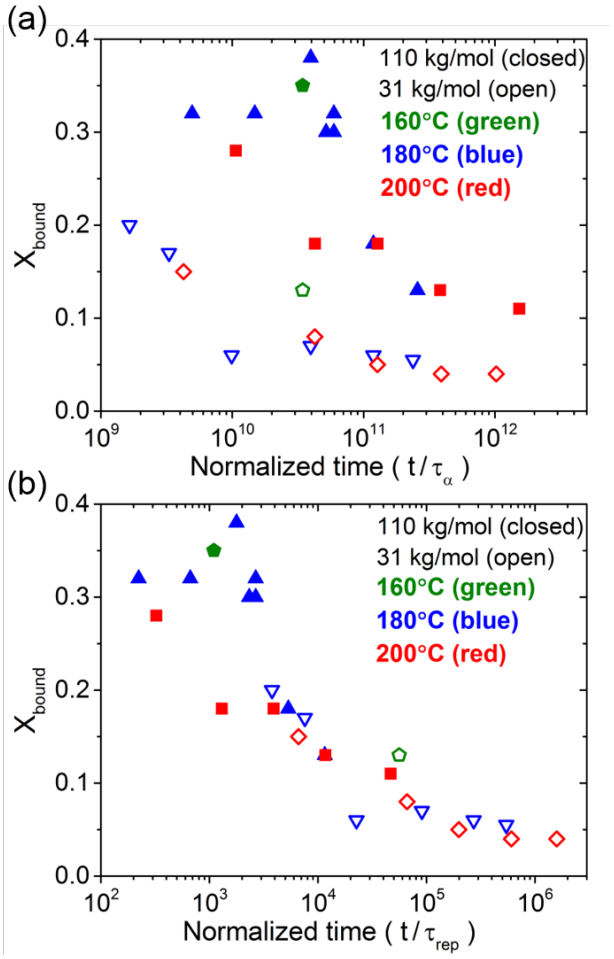

Figure 5.7: Rescaled desorption data from Figure 5.6c. The experimental X_{bound} is plotted as a function of (a) annealing time normalized to segmental relaxation time (τ_α) and (b) annealing time normalized to chain reptation time (τ_{rep}).

While it remains to be tested if this collapse will apply to a broader range of PNCs and conditions, the effective collapse of the current data implies significant cooperativity and chain length dependence of desorption of P2VP from SiO_2. The observed correlation between polymer desorption and t/τ_{rep} in Figure 5.7b highlights two important dependences: temperature and chain length. The temperature dependence is largely captured by the temperature dependence of polymer dynamics (i.e. friction coefficient) as opposed to an activation energy. In fact, normalization of the annealing time to either τ_α or τ_{rep} reasonably collapses data from the same M_w, which is consistent with the fragility of chain-scale and segmental mobilities often being comparable.[322] The desorption kinetics may become decoupled from polymer dynamics as the temperature approaches T_g, but desorption will slow precipitously and may be experimentally inaccessible. The dependence of desorption on chain length, where $t/\tau_{rep} \sim N^3$ for entangled chains, could be influenced by the fact that larger chains have (i) slower intermediate and chain dynamics in bulk, (ii) more adsorbed segments per chain, and (iii) likely more or longer trains per chain. It is important to note that all polymer in our measurements are entangled ($M>M_e$), and although it remains unclear how the entanglement network and constraint release is perturbed in the bound layer[109,152,208], this may contribute to the observed chain-length dependence in Figure 5.7.

Our results clearly demonstrate that polymer desorption from attractive NPs in the melt is more than a segmental phenomenon, is cooperative in nature, and is complex. Despite our observation in Figure 5.7, it remains unclear if desorption is dictated by a segmental relaxation rate and chain-length dependent adsorption energy or, conversely, a chain-scale relaxation rate and a chain-length independent adsorption energy. One may reasonably expect the timescale of desorption to be related the product of a segmental relaxation time and exponential of the adsorption energy. In this light, one can imagine incorporating another term into the normalization of Figure 5.7 that accounts for an adsorption energy that changes with molecular weight. This difference in

adsorption energy may result from a different average length of trains, distribution of loops and trains, or reflect some longer-lasting cooperativity. The current data set is insufficient for this level of analysis or the definition of this adsorption energy. Alternatively, the collapse in Figure 5.7b may suggest that the chain-scale relaxation plays a dominant role and the effective energy term is on the order of ~10^4 and constant with molecular weight. A physical interpretation of this may be that the rate limiting step for desorption is chain diffusion away from the NP surface. In other words, interfacial segments can desorb and readsorb (which occurs on the order of 10^{-5} sec according to BDS)[65,73] until the chain diffuses away from the NP surface (which occurs on the order of 10^3 sec according to Figure 5.6c). Although our results in Figure 5.7 begin to interrogate the complex and multiscale questions associated with polymer desorption from a NP surface, many answers remain elusive. Future experimental and theoretical efforts are required to provide more insight into the underlying physics, development of a mechanistic description, and documentation of the microscopic properties and parameters that dictate bound layer desorption in polymer melts.

5.5 Conclusions

The combination of ERD and RBS experiments separates, identifies, and quantifies spontaneously-formed bound polymer layers in polymer nanocomposite melts and reveals new static and dynamic properties of bound polymers. Unlike most measurements of bound polymers in PNCs that rely on solvent-assisted removal of free chains[206,210,292,314,316,318,319] or define bound and free polymer through segment-sensitive techniques[55,65,69,71,73,209], these ion scattering methods define the bound layer in the melt through deviations in the chain-scale dynamics. Three populations of chains are observed in our measurements: free chains diffusing at bulk-like timescales, weakly adsorbed chains that desorb at timescales ~10^4 times slower than bulk polymer diffusion, and strongly adsorbed chains that remain bound for these experimentally-accessible timescales. These ion scattering measurements reveal a bound layer thickness of ~0.5Rg, that

bound polymer extends ~Rg from the NP surface, and the average surface area occupied by bound chains in the melt, which is much smaller than predicted by an isolated chain model or measured in solution. Polymer desorption increases with annealing time and the polymer desorption kinetics depends on temperature and chain length. This study provides a framework to understand bound polymer structure and desorption in the melt and to guide the design and evaluation of more stable interfacial layers. Our results and observations motivate theoretical and further experimental inquiries into the kinetics and mechanisms of polymer desorption from NPs and their dependence on various PNC properties.

CHAPTER 6: Multiscale Dynamics of Small, Attractive Nanoparticles and Entangled Polymers in Polymer Nanocomposites

Content in this chapter was published in 2019 in *Macromolecules*, volume 52, issue 5, pages 2181-2188, in a modified version. The authors of the chapter are Eric J. Bailey, Philip J. Griffin, Russell J. Composto, and Karen I. Winey.

6.1 Introduction

Understanding nanoparticle (NP) and polymer dynamics over their hierarchy of length and time scales is a complex problem relevant to drug delivery, filtration technology, and the properties and processability of polymer nanocomposites (PNCs).[4,25,26,29,323] Because NPs and polymers share overlapping energy, length, and time scales, their motional processes are interrelated and therefore significantly impact each other. This is especially true for very small NPs in well-entangled polymer matrices, where the radius of the nanoparticle (R_{NP}) is on the order of the radius of gyration of the polymer (R_g) or the entanglement tube diameter (d_{tube}).

It is now well established that polymer dynamics at small length scales (e.g. segmental relaxations) are perturbed near a NP surface[26,29,36,54,55] and are highly dependent on system-specific parameters, including NP-polymer interfacial interaction[88,116] and NP size[66,108]. For example, poly(2-vinylpyridine) (P2VP) segmental dynamics are ~100 times slower near the surface of moderately-sized, attractive silica NPs (SiO_2, R_{NP} = 13 nm), but remain bulk-like beyond ~5 nm from the NP surface.[65] Similar behavior is reported in MD simulations of attractive PNCs.[315] However, the magnitude of reduced segmental dynamics is dependent on the NP-polymer interaction while the length-scale over which relaxations are perturbed is nominally independent of interactions and reported as ~3 nm.[315] For attractive PNCs with NPs on the order of the segment size (R_{NP} = 0.9 nm), experiments coupled with theory and simulations designed to mimic the sizes

and interactions in the experimental system report categorically different behavior as compared to PNCs with larger NPs.[108] For example, in PNCs with smaller NPs, segmental relaxations slow precipitously and become more dependent on temperature (more fragile) with increasing NP concentration (ϕ_{NP}).[108] In addition, the glass transition temperature increases up to 30°C at ϕ_{NP} = 54 vol% but the step in specific heat capacity remains unchanged, both of which are not true for PNCs with larger NPs.[108]

At longer length scales, polymer chain diffusion through PNCs has been measured as a function of NP concentration[170], NP and polymer size[181], NP-polymer attraction[272], and NP interface softness[182]. In each case, the polymer chain diffusion coefficient through PNCs decreases with decreasing interparticle separation distance (achieved by increasing ϕ_{NP} or decreasing R_{NP}). It is important to note that the NPs in these experiments are effectively immobile on the timescale of polymer diffusion, with the exception of a recent subset of systems with anisotropic NPs.[200]

It is crucial to consider the hierarchy of polymer dynamics from the segment to chain scale when studying the diffusion of NPs in a polymer melt because the relevant polymer dynamics depend on the size of the NP, polymer chain length, and NP-polymer interaction.[159,212,213,216,234] A continuum hydrodynamic description of the translational diffusion of spherical particles, D_{SE}, in a polymer melt is given by the Stokes-Einstein (SE) equation with static boundary conditions:

$$D_{SE} = \frac{k_B T}{6\pi\eta_0 R_{NP}} \qquad (6.1)$$

where k_BT is the thermal energy term and η_0 is the zero-shear viscosity of the polymer medium.[35] However, the SE prediction often fails to describe NP diffusion in polymer melts, especially when $R_{NP} < R_g$ (or d_{tube}) or in systems with strong NP-polymer attraction.[38,214,216] Both of these cases, small NPs and strong interactions, are especially important to understand because it is at these limits where uniform NP dispersion is most often realized.[29,296] It has been shown that athermal gold NPs (R_{NP} = 2.5 – 10 nm) diffuse in entangled poly(butyl methacrylate) melts (M/M_e = 12,

where M_e is the entanglement molecular weight) approximately 10 – 100 times faster than the SE prediction.[221] Diffusion of small NPs in athermal or repulsive polymer melts at timescales faster than D_{SE} was also observed in MD simulations[228,229] and predicted in self-consistent generalized Langevin equation theory.[216] To describe the diffusion of small NPs, η_0 is sometimes replaced with a length-scale-dependent viscosity smaller than the macroscopic value and corresponding to approximately the NP size, however, Equation 6.1 is commonly used for comparison.[159,216,228,234] A more recent theory by Yamamoto et al. that includes NP-polymer attraction predicts two competing mechanisms of NP motion called core-shell and vehicle diffusion.[214] In the core-shell mechanism, NPs and adsorbed polymer chains diffuse together with an effective size larger than R_{NP}. This core-shell diffusion has been observed experimentally in mixtures of P2VP and SiO_2 ($R_{NP} > R_g$), where SE behavior was retained by using an increased effective NP size to capture the presence of an irreversibly bound polymer layer.[208] In vehicle diffusion, NPs are predicted to diffuse with the local polymer environment until the NP desorbs and re-adsorbs in a new environment, which usually leads to fast NP diffusion relative to Equation 6.1.[214] A crossover between core-shell (where $D/D_{SE} \sim 0.6$) and vehicle diffusion (where $D/D_{SE} \sim 20$) was recently measured using dynamic light scattering (DLS) in mixtures of sticky NPs ($R_{NP} = 0.9$ nm) in polypropylene glycol (PPG) melts with $M/M_e < 6$.[246]

In this article, we combine measurements of polymer dynamics at the segment and chain scale with measurements of NP diffusion to probe polymer and NP dynamics in PNCs with small nanoparticles ($R_{NP} << R_g$), entangled polymers, and attractive NP-polymer interactions. The PNCs are comprised of well-entangled poly(2-vinylpyridine) (P2VP) ($M/M_e \approx 1 – 26$ where $M_e = 18$ kg/mol and $R_g = 4.5 – 18.7$ nm)[208] and octaaminophenyl silsesquioxane (OAPS) NPs ($R_{NP} \approx 0.9$ nm)[108]. The polymer dynamics on the chain-scale are suppressed by up to ~60% relative to bulk at NP concentrations of 25 vol%. This reduction in chain dynamics is largely due to a slowing of polymer segmental dynamics, which likely results from favorable pyridine-amine interactions. In

addition, relative to the hydrodynamic SE prediction based on the NP size and zero-shear melt viscosities, the NP diffusivity is dramatically enhanced (up to a factor of 10,000). NP diffusion coefficients in this system are modestly dependent on polymer molecular weight, scaling as $\sim M_w^{-0.7\pm0.1}$, which is comparable to recent theoretical predictions of the vehicle mechanism in well-entangled attractive polymer melts.[214] By measuring and correlating multi-scale polymer and NP dynamics, we conclude that the transport of small, attractive NPs in entangled polymer melts occurs via the vehicle mechanism, where NPs diffuse via successive adsorption/desorption events that likely take place on Rouse time scales.

6.2 Experimental Section

Materials and PNC preparation: All poly(2-vinylpyridine) (P2VP) was received from Polymer Source or Scientific Polymer Products and used as received. All polymer molar mass moments and distributions were verified by gel permeation chromatography (relative to narrow polystyrene standards), and all dispersities were < 1.3, as listed in Table D.1. Partially deuterated poly(2-vinylpyridine) (dP2VP) was synthesized at the Center for Nanophase Materials Science at Oak Ridge National Laboratory. The deuterium to hydrogen ratio (measured by elastic recoil detection) is approximately 1:2 and the weight-averaged molecular weight and dispersity (measured by GPC) are 100 kg/mol and 1.2, respectively. Dry octaaminophenyl silsesquioxane (OAPS) powder was used as received.

PNCs were fabricated by solution mixing and drying. Solutions of OAPS in MeOH (c_{OAPS}~20 g/L) and P2VP in MeOH (c_{P2VP}~50 g/L) were fabricated and allowed to stir for several hours. Once completely dissolved, the requisite amount of OAPS/MeOH was added dropwise to P2VP/MeOH solutions while stirring. P2VP/OAPS/MeOH solutions were stirred for at least 24 hours before deposition and annealing, as further described below.

Differential Scanning Calorimetry (DSC): The polymer glass transition temperature (T_g) was measured via DSC with a TA Instruments Q2000. All measurements were made upon cooling a sample of ~5 mg at a rate of 10°C/min between 175°C and 25°C. T_g was defined as the inflection point of the heat flow thermograms. DSC samples were fabricated by drop casting P2VP/OAPS/MeOH solutions onto Teflon, air dried, then annealed at T=170°C under vacuum for ~24 hours. Results for T_g of P2VP/OAPS PNCs as a function of OAPS concentration and molecular weight are provided in Figure D.2. T_g for bulk 100 kg/mol P2VP is measured to be ~96°C.

Broadband Dielectric Spectroscopy (BDS): Polymer reorientational segmental dynamics were measured using a Solartron ModuLab XM MTS with the femto-ammeter accessory. BDS samples were processed as described for DSC samples, but after annealing, were melt pressed to the appropriate size and placed between steel electrodes and separated with 50 μm silica spacers. Samples were annealed in the cryostat at 160°C until the imaginary permittivity spectra at all frequencies remained constant (within 5%) over several hours. Isothermal frequency sweeps from 10^{-1} – 10^{6} Hz were measured every 3 K on cooling from 179°C to 107°C. Select measurements were made after heating again to ensure reproducibility.

Elastic Recoil Detection (ERD): The polymer chain translational diffusion coefficient was measured into P2VP/OAPS PNCs using ERD, an ion scattering technique used to measure the depth profile of light elements such as deuterium and hydrogen. Solutions containing P2VP/OAPS/MeOH were doctor bladed on a silicon wafer, air-dried, then annealed for at least 48 hours at T=160°C under vacuum. The resulting thickness was at least 20 μm. Tracer films were made by spin coating a thin layer of 2000 kg/mol polystyrene (PS) (~30 nm) on an ozone-treated silicon wafer, then a ~50 nm film of 100 kg/mol dP2VP from MeOH on the PS layer. To form the diffusion couples (Figure 6.1a), bilayer tracer films were floated off the silicon wafer and transferred to the pre-annealed PNC matrix for subsequent annealing at T=140°C under vacuum.

Polymer diffusion couples were then measured via ERD where a He^{2+} ion beam is accelerated to 3 MeV and incident on the sample in forward scattering geometry (70° off normal), as described in detail in Ref [169] and further discussed elsewhere.[170,272] A mylar film before the detector is used to obstruct He ions but allow forward-recoiled deuterium ions to be detected.

Rutherford Backscattering Spectrometry (RBS): Nanoparticle diffusion into bulk P2VP was measured as a function of P2VP molecular weight (M_w) using RBS, an ion scattering technique used to measure the depth profile of heavy elements, such as Si herein. The P2VP matrix of varying molecular weights was doctor bladed from solutions of P2VP/MeOH on a silicon wafer and annealed for at least 48 hours at T=160°C under vacuum. The resulting thickness was at least 20 μm. The tracer films were made by spin coating a thin layer of 2000 kg/mol polystyrene (PS) (~30 nm) on an ozone-cleaned silicon wafer, followed by a ~150 nm film spin coated from the P2VP/OAPS/MeOH. Tracer films were then floated in DI water and transferred to the pre-annealed bulk P2VP matrix for subsequent annealing at T=140°C under vacuum (Figure 6.3a). The same P2VP M_w was used in tracer and matrix films. The OAPS concentration in the tracer film was fixed to 25 vol%. This concentration is large enough to provide sufficient Si signal in RBS, but low enough to minimally affect polymer viscosity, and below the reported aggregation concentration.[108] OAPS diffusion couples were measured with RBS where He^+ ions are accelerated to 3 MeV and incident normal to the sample surface. Backscattered He ions are collected at a detector 10° off normal. RBS is described in detail in Ref [169] and discussed elsewhere[208,236].

6.3 Results

6.3.1 Polymer Dynamics

We first probe the dynamics of P2VP in P2VP/OAPS PNCs by measuring the diffusion coefficient of the chain (D_{poly}) as a function of OAPS concentration. As described elsewhere[170,272]

and schematically depicted in Figure 1a, elastic recoil detection (ERD) was used to measure the depth profile of 100 kg/mol dP2VP (M/M_e~5.5, R_g ~ 8.6 nm) as it diffuses into PNC films with different NP concentrations after different annealing times. At OAPS concentrations of 25 vol%, the highest concentrations studied here, yet still below the previously reported aggregation threshold[108], the expected NP-NP separation distance for randomly packed OAPS (R_{NP} = 0.9 nm) is only ~2.5 nm. We confirm reasonable OAPS dispersion in P2VP using X-ray scattering between 2 Å and 370 nm, as described in Figure D.3. Furthermore, measured Si depth profiles in Figure D.4 show uniform distribution of OAPS through the depth of the film with no measurable surface aggregation. OAPS dispersion at NP concentrations up to 25 vol%, which is not common in PNCs containing POSS[297,324], suggests strong and favorable NP-polymer interactions between OAPS and P2VP.[108,246]

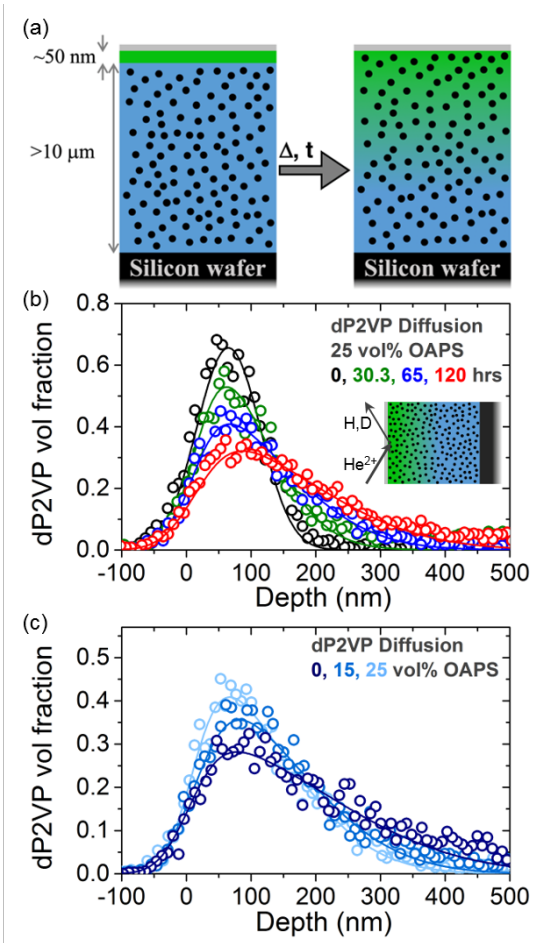

Figure 6.1: (a) Schematic representation of unannealed and annealed diffusion couples used to measure dP2VP diffusion into P2VP/OAPS. Measured concentration profiles from ERD of 100 kg/mol dP2VP diffused at 140°C into (b) 25 vol% OAPS PNCs after 0, 30.3, 65, and 120 hours and (c) PNCs of different NP concentrations after 65 hours. Symbols represent experimental data and solid lines represent fits used to extract diffusion coefficient. Inset of (b) depicts schematic of ERD measurement. In schematics, grey represents the sacrificial PS layer, green and blue represent dP2VP and hP2VP (respectively) and black circles represent OAPS NPs. Schematics not drawn to scale.

Representative diffusion profiles of dP2VP diffusing into P2VP with 25 vol% OAPS at 140°C at various diffusion times are shown in Figure 6.1b. As expected, dP2VP diffuses farther into the underlying matrix after longer annealing times. The dP2VP diffusion coefficient is extracted from the experimental data by fitting each concentration profile with Fick's second law describing a finite source diffusing into a semi-infinite medium.[170,325] Figure 6.1c displays dP2VP

profiles measured at the same annealing temperature and time as a function of OAPS concentration. For the same annealing conditions, dP2VP diffusion is slowed as the NP concentration in the underlying matrix is increased. The extracted polymer diffusion coefficients as a function of NP concentration are shown in Figure 6.2a. The error bars, which are smaller than the size of the data points, are calculated from the standard deviation of at least three annealing times.

Whereas the addition of small molecules[326], including POSS[324], often enhances dynamics and plasticizes a polymer melt, we observe the opposite effect in this attractive mixture. The observed monotonic reduction in D_{poly} can be qualitatively understood by a slowing of segmental dynamics and increase in glass transition temperature, as previously reported in the same system.[108] To compare dynamics at the segment and chain-scale, the segmental reorientational relaxation time (τ_α) was measured by dielectric spectroscopy at 140°C and is presented in Figure 6.2a (see Figure D.5 for dielectric measurements at various temperatures). As the OAPS concentration increases, τ_α increases showing slower relaxations, consistent with DSC measurements (Figure D.2) and literature.[108]

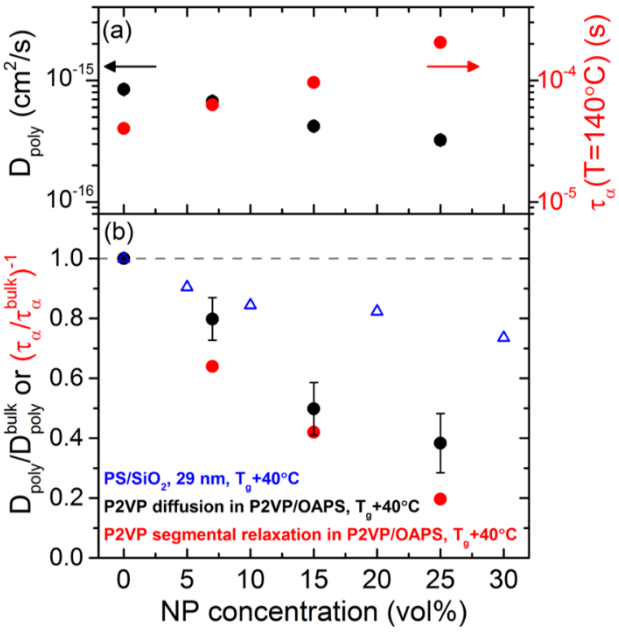

Figure 6.2: Measured dP2VP diffusion coefficient (black) and segmental relaxation times (red) as a function of OAPS concentration (M_w = 100 kg/mol and T = 140°C). (b) Normalized P2VP diffusion coefficient (black) and segmental relaxation time (red) as a function of NP concentration. Included for comparison in (b) is polystyrene diffusion in PNCs with immobile, athermal NPs (R_{NP} = 15 nm) at T = 140°C (blue).[188]

By comparing the normalized chain and segmental dynamics in PNCs to bulk P2VP in Figure 6.2b, we find the addition of these Kuhn bead-sized NPs slows segmental dynamics slightly more than chain dynamics. For example, at the highest NP loading, chain diffusion is slowed by ~60% relative to bulk, while the segmental dynamics are slowed by ~80%. To further understand these reductions in polymer dynamics, we interpret our results in terms of the reptation model, where polymer diffusion in an entangled matrix is defined as:

$$D_{poly} \approx \frac{R_{ee}^2}{\tau_{rep}} \approx \frac{R_{ee}^2}{N^2}\left(\frac{k_B T}{\xi b^2}\right)\frac{N_e}{N} \propto \frac{R_{ee}^2 N_e}{N^3}\frac{1}{\tau_\alpha} \qquad (6.2)$$

where R_{ee} is the polymer end-to-end distance, N is the degree of polymerization, N_e is the degree of polymerization of an entanglement strand, ξ is the monomeric friction coefficient, and b is the Kuhn length.[35] The term $k_BT/\xi b^2$ is proportional to the segmental relaxation rate, τ_α^{-1} (Equation 6.2).[35] Thus, according to the reptation model, the observed differences between D_{poly} and τ_α in Figure 6.2b could be related to dilation of chain dimensions (increasing R_{ee}) or disentanglement effects (increasing N_e). Recent small angle neutron scattering experiments on a similar system of poly(methyl methacrylate) and weakly attractive POSS observed no change in R_{ee} in PNCs relative to bulk.[297] Thus, it is unlikely that differences in chain dimensions are responsible for differences in polymer dynamics in our system. Moreover, disentanglement has been observed in recent rheology measurements of this P2VP/OAPS system.[108] Furthermore, in an athermal system of poly(ethylene oxide) and small gold NPs, neutron scattering also revealed tube dilation of ~20% at a NP concentration of 20 vol%.[131] Given these observations, we surmise that the observed enhancements in D_{poly} relative to τ_α are primarily related to disentanglement and tube dilation likely

resulting from excluded volume, but the specific impact of NP-polymer attraction in our system remains unclear. Figure 6.2b also includes a quantitative comparison to the reduction in chain-scale diffusion of polystyrene (PS) diffusing into athermal PNCs comprised of PS and phenyl-capped SiO_2 (SiO_2-Ph, R_{NP} = 15 nm).[188] At T = 140°C and at all ϕ_{NP}, the addition of small OAPS into P2VP (attractive) is more impactful and more dependent on ϕ_{NP} than the addition of larger SiO_2-Ph into PS (athermal).[188]

6.3.2 Nanoparticle Dynamics

To fully understand the dynamics in these attractive P2VP/OAPS PNCs, we next measure the diffusion of OAPS NPs in P2VP of various molecular weights. As described elsewhere[208,236] and shown schematically in Figure 6.3a, Rutherford backscattering spectrometry (RBS) was used to measure the depth profile of OAPS infiltration into bulk P2VP. A representative set of fitted diffusion profiles for OAPS diffusion into 90 kg/mol P2VP at 140°C is presented in Figure 6.3b. OAPS diffusion was measured in seven P2VP melts ($2R_{NP}/d_{tube}$~0.25) with M_w ranging from 28 to 467 kg/mol spanning M/M_e~1 to 26 and R_g/R_{NP}~5 to 21, as listed in Table S1.

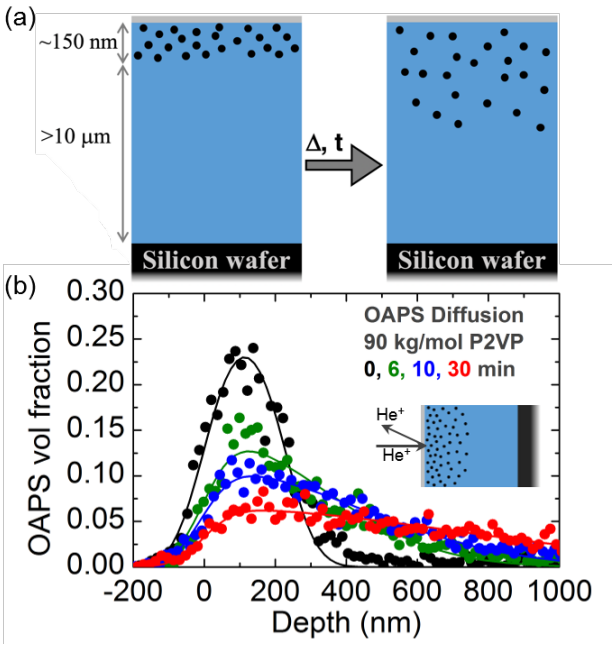

Figure 6.3: (a) Schematic of unannealed and annealed diffusion couples used to measure OAPS diffusion into bulk P2VP polymer melts. (b) Representative concentration profiles from RBS of OAPS in 90 kg/mol P2VP after 0, 6, 10, and 30 minutes at 140°C. Inset of (b) depicts schematic of RBS. In schematics, grey represents the sacrificial PS layer, blue represents P2VP and black circles represent OAPS NPs. Schematics not drawn to scale.

The measured D_{OAPS} presented in Figure 6.4a monotonically decreases with increasing P2VP M_w, but only weakly, scaling as $M_w^{-0.7\pm0.1}$. Furthermore, these NP diffusion coefficients are substantially larger than those predicted by SE (D_{SE}, Equation 6.1), calculated using the zero-shear viscosity (η_0) of bulk P2VP[208] (see Figure D.6 for details). Recent rheology measurements[108] of P2VP/OAPS showed only a subtle change in η_0 upon the addition of up to 25 vol% OAPS, which is equivalent to the maximum local OAPS concentration in unannealed tracer films and more concentrated than the local environment OAPS NPs experience during these diffusion measurements (~5 vol%, Figure 6.3b). We have verified the negligible change in η_0 (~30% increase relative to bulk) in 5 vol% OAPS PNCs using small amplitude oscillatory shear measurements (Figure D.6).

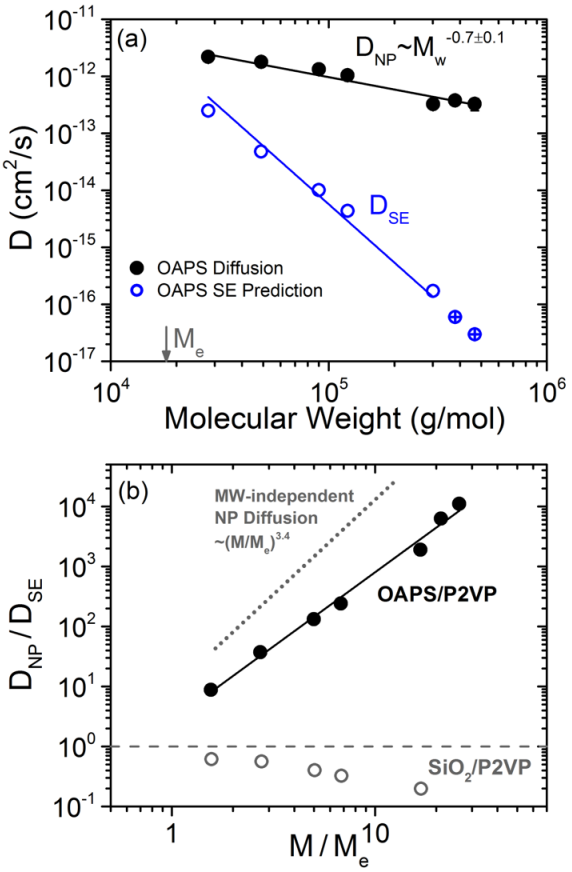

Figure 6.4: (a) Measured OAPS NP diffusion coefficient (solid black circles) and Stokes-Einstein prediction (blue open circles) as a function of P2VP molecular weight. Data shown in blue circles with crosses were calculated using extrapolated values of η_0, as described in Figure D.6. (b) OAPS diffusion coefficient normalized to SE prediction as a function of number of entanglements per chain (solid black circles). Earlier experimental measurements[208] (open circles) of larger attractive NPs (R_{NP} = 13 nm) are shown for comparison.

In this attractive P2VP/OAPS system, we observe fast NP diffusion relative to SE (D_{OAPS}/D_{SE}) by 10^1–10^4 over the molecular weight range studied (Figure 6.4b). These results are consistent with an extrapolation to large M_w of the recent DLS study of a similar system (OAPS in PPG) that found a crossover from $D < D_{SE}$ to $D > D_{SE}$ at $R_g \sim R_{NP}$ (as well as $M \sim M_e$).[246] In stark contrast to our previous studies of SiO_2 NP diffusion (R_{NP} = 13 nm) in P2VP that diffuse via the core-shell mechanism (Figure 6.4b, open circles), decreasing the size of the NP by a factor of ~14

changes D/D_{SE} by up to 10^4 at high M_w (Figure 6.4b).[208] This clearly demonstrates the fundamental importance of NP size on transport mechanisms.

The weak molecular weight dependence found for D_{OAPS} in P2VP/OAPS PNCs suggests that NP motion is coupled to polymer dynamics between segmental relaxations (approximately M_w independent) and longer-range Rouse relaxations (scaling with M_w^{-1}) and is decoupled from chain-scale relaxations (scaling with $M_w^{-3.4}$). Recent theoretical predictions by Yamamoto et al. predict that small NPs with enthalpic attraction to the polymer matrix diffuse in entangled polymers via a vehicular mechanism.[214] In vehicle diffusion, NPs diffuse with the local polymer environment until successive desorption and adsorption events lead to Fickian NP diffusion.[214] The frequency of desorption events and lifetime of NP-polymer adsorption depend on system-specific parameters, especially NP size and NP-polymer interaction. Although the NP-polymer interaction and desorption time in P2VP/OAPS are difficult to experimentally probe, our observations that NP motion is coupled to subdiffusive polymer relaxations (Figure 6.4a) support the theory of vehicle diffusion.

6.4 Discussion

By directly measuring the dynamics of polymer segments, the chain, and the NPs in this P2VP/OAPS model system, we can quantitatively and mechanistically understand how small, enthalpically-attractive NPs diffuse in entangled polymer melts and how they impact polymer dynamics at various length scales. Figure 6.5 summarizes and quantitatively compares directly measured or estimated polymer and nanoparticle dynamics in this P2VP/OAPS system.

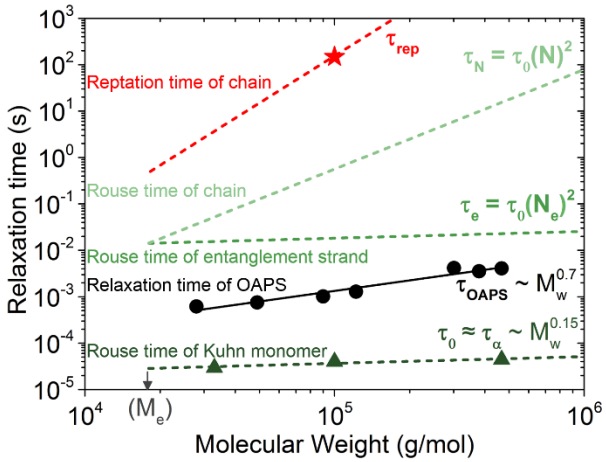

Figure 6.5: Comparison of relaxation times for P2VP at various length scales and OAPS NPs as a function of M_w. The Rouse times of a Kuhn monomer are taken directly from BDS measurements of bulk P2VP and are used to calculate the Rouse time of an entanglement strand and the chain. The P2VP reptation time and OAPS relaxation time are calculated directly from ERD and RBS measurements, respectively. All measurements are made at 140°C.

We consider the segmental relaxation time (τ_α) to be approximately equal to the relaxation time of a single Kuhn monomer, and therefore the shortest Rouse time of P2VP (τ_0). According to the Rouse model[35], the relaxation time of an entanglement strand (τ_e) is given by $\tau_e = \tau_0(N_e)^2$ where N_e for P2VP[74,108,208] is ~23. Our assignment of τ_0 is supported by recent rheology and dielectric measurements of bulk P2VP, which found $\tau_e/\tau_\alpha \sim 10^3$ or $\sim N_e^{2}$.[108] Although τ_α is often considered molecular weight independent, we measure a weak M_w dependence of τ_α in bulk P2VP at 140°C, scaling with $M_w^{0.15}$, which follows the slight increase in T_g (Figure D.2 and Figure D.7). The reptation time of the chain (τ_{rep}) can be calculated from the measured diffusion coefficient in Figure 6.2a through $\tau_{rep} = (R_g)^2/(6 \cdot D_{poly})$, and is expectedly slower than the Rouse prediction (τ_N) which neglects entanglement effects. Similarly, the relaxation time of the OAPS NPs can be calculated as $\tau_{OAPS} = (R_{NP})^2/(6 \cdot D_{OAPS})$. The measured τ_0 and τ_{rep} data shown in Figure 6.5 are for 100 kg/mol bulk P2VP (Figure 6.2a) and all measurements presented are at 140ºC.

With experimental evidence that OAPS diffusion is slower than Kuhn segment relaxations but faster than P2VP chain diffusion, we can further understand the polymer dynamic results

presented in Figure 6.2. For traditional PNCs (such as PS/SiO_2-Ph), the slowing of chain diffusion has been described with excluded volume[184] and entropic[170,188] arguments. However, chain-scale entropic effects can be considered negligible in P2VP/OAPS diffusion, because the OAPS position is fully decorrelated on the timescale of conformation fluctuations ($\sim\tau_{rep}$), NPs fully penetrate polymer conformations, and all chains likely sample similar conformations. These justifications are not true for larger and less mobile NPs. Furthermore, in PNCs with larger NPs ($R_{NP} \geq R_g$), the mean molecular relaxation time is largely unchanged overall[116,178], even though friction is known to be significantly increased at the NP-polymer interface[65]. As a result, while segmental relaxations are less perturbed than chain diffusion in traditional PNCs, the perturbations are similar in P2VP/OAPS PNCs (Figure 6.2b), thus highlighting the fundamentally different mechanism causing reduced chain-scale polymer diffusion in PNCs with small, attractive, and highly mobile NPs.

In P2VP/OAPS PNCs, we conclude that polymer segments and small NPs relax together making the segments slower than in bulk and significantly increasing the friction on the chain. This conclusion is supported by observations that the step in heat capacity at T_g remains unchanged upon the addition of OAPS NPs[108], which we confirm in our DSC measurements, suggesting that these small and attractive NPs are dynamically active during segmental relaxations. Since the friction at the segmental scale is increased, chain-scale diffusion is similarly slowed while also being slightly enhanced by other factors (e.g. disentanglement, Equation 6.2). This mechanism of chain-scale retardation through segmental friction is categorically different than previous measurements of polymer diffusion in PNCs with larger SiO_2 (R_{NP} > 6 nm) and likely results from the enthalpic attraction, size, and mobility of OAPS NPs.[170,181,182,188,272]

Given that these attractive OAPS NPs are coupled to M_w-dependent polymer dynamics (Figure 6.4a), and the measured OAPS diffusion is faster than the P2VP chain diffusion (Figure 6.5), we conclude that NP desorption from the P2VP chain occurs. Since $\tau_0 < \tau_{OAPS} < \tau_e$ for all M_w

P2VP (Figure 6.5), the desorption time of OAPS NPs (τ_{des}) must also lie somewhere between the Rouse time of a single Kuhn bead and that of an entanglement strand. For systems with this dynamic behavior (specifically $\tau_\alpha < \tau_{des} < \tau_{rep}$) recent theory predicts vehicle diffusion and D_{NP} scaling of $M_w^{-0.5}$.[214] Figure 6.4a, for OAPS diffusion in P2VP, shows qualitative and also approximate quantitative agreement with this theory (scaling with $M_w^{-0.7\pm0.1}$). Importantly, the prediction of $D_{NP} \sim M_w^{-0.5}$ assumes M_w-independent segmental relaxations[214], thus, the slightly larger exponent observed experimentally can be attributed to the M_w-dependence of segmental dynamics ($D_\alpha \sim M_w^{-0.15}$, Figure D.7). Further potential differences in theoretical predictions and experimental measurements are expected from differences in the NP-polymer interaction strength and the exact timescales of τ_{des} and τ_0.

Although our dynamic measurements provide support of vehicular diffusion, to fully and definitively prove this mechanism, additional measurements must be conducted by altering the NP desorption time, potentially through changes in NP size, NP surface chemistry, or temperature (in the case of hydrogen bonding PNC systems). As NP desorption is slowed through increasing R_{NP} or strengthening the NP-polymer interaction, a stronger molecular weight dependence and smaller D/D_{SE} can be expected as the NPs will be more coupled to polymer dynamics.[208,214] Independently controlling NP-polymer interaction strength (without significantly changing NP dispersion) and NP size (without significantly changing the NP-polymer interactions) remains an experimental challenge.[4,25,29]

6.5 Conclusions

Polymer segmental dynamics, polymer chain dynamics, and NP diffusion coefficients, were directly measured in mixtures of entangled P2VP ($M/M_e \sim 1 – 26$) and OAPS ($R_{NP} = 0.9$ nm), which exhibit favorable NP-polymer interactions. In this system, the P2VP chain diffusion slows

by ~60% relative to bulk at 25 vol% OAPS, an effect consistent with increased friction at the segmental scale with potential contributions from disentanglement. In addition, OAPS NPs diffuse at timescales between polymer segmental dynamics and chain-scale diffusion and D_{OAPS} is weakly dependent on molecular weight, scaling with $M_w^{-0.7\pm0.1}$. We observe enhancements in D_{OAPS} relative to hydrodynamic Stokes-Einstein predictions of up to 10^4, providing experimental support of recent theoretical predictions describing vehicle diffusion in well-entangled polymer melts.[214] By measuring polymer and NP dynamics, we show that small attractive NPs diffuse with polymer segments commensurate with the NP size, thereby slowing the polymer segmental motion and other dynamic processes (e.g. reptation) that occur at longer length and time scales. We conclude that in this attractive PNC system with small NPs and entangled polymers, successive adsorption/desorption events on Rouse-like timescales lead to NP diffusion coupled to sub-diffusive polymer dynamics but decoupled from the polymer chain diffusion, as proposed by the vehicular mechanism.

CHAPTER 7: Conclusion and Future Outlook

7.1 Conclusions

Many macroscopic properties of PNCs are dictated by microscopic dynamic processes, including the dynamics of the polymer segments, chains, and NPs. However, due to the overlapping characteristic length, time, and energy scales of the NPs and polymers, the interactions and dynamics within these materials are complex and poorly understood. This is especially true with respect to the expansive parameter space presented by these multicomponent, hybrid materials. Thus, fundamental studies into different dynamic processes are critical to design, develop, and manufacture new PNC materials. Thus, this thesis examines multiscale polymer and nanoparticle dynamics in model polymer nanocomposites using experiments and simulations to provide fundamental and mechanistical insights.

Chapter 2 uses quasi-elastic neutron scattering (QENS) to systematically study the influence of highly attractive NPs on the dynamics of polymer segments at small length scales (~1 nm) and fast timescales (~1 ns). Using poly(2-vinylpyridine) (P2VP) mixed with up to 50 vol% colloidal silica (SiO_2), we measure the segmental mobility and characterize the segmental diffusion coefficient as a function of NP concentration, temperature, and matrix molecular weight. We show that segmental mobility is decreased in PNCs relative to bulk at all temperatures and at high temperatures, segments are ~5x slower than bulk at 50 vol% loading. Interestingly, we find that this reduction in segmental dynamics is very weakly dependent on P2VP molecular weight, which stands in contrast to the documented molecular weight effect on segmental dynamics in attractive polymer nanocomposites at lower temperatures, as observed by temperature modulated differential scanning calorimetry in this work.

In Chapter 3, we further probe the segmental dynamics in P2VP/SiO_2 PNCs more mechanistically using the unique capability of deuterium and hydrogen labeling offered by QENS.

Specifically, we study neat polymer and 25 vol% PNCs composed of fully protonated P2VP (where the dynamics of all protons are measured) and backbone deuterated dP2VP (where only the dynamics of the pendent pyridine ring are measured). For $T<T_g$, we show the mobility of protons on the pendent group are less affected by the attractive NPs than the protons on the backbone. In the melt state at $T>T_g$, we find that protons on the pendent group are slightly more mobile than backbone protons, but the normalized diffusion coefficient of segments is ~35% slower than bulk in both PNC samples. This observation highlights the connection between backbone and pyridine motion, even in PNCs where the motion is temporally slowed by attractive NPs. These results, along with those from Chapter 2, show that segments are perturbed temporally more than spatially and provide fundamental insights into the segmental diffusion process in PNCs.

To probe polymer motion at longer length-scales, Chapter 4 presents coarse-grained molecular dynamics simulations of a monolayer of hexagonally-packed, athermal NPs in a polymer melt. In doing so, we observe the magnitude and length-scale over which homogeneously confining NPs impact the polymer conformations and diffusion. We show conformations under strong confinement (i.e. the interparticle distance, ID, is less than twice the polymer radius of gyration, $2R_g$) are more impacted than around an isolated NP, and the effect depends on the ratio of R_{NP}/R_g rather than either independently. We then show the polymer diffusion is slowed by the presence of athermal NPs and the slow diffusion persists far beyond the length-scale over which polymer conformations are perturbed, which is ~R_g. Although the strongest suppression to chain diffusion occurs within ~R_g of the NP monolayer, diffusion is slowed even ~$5R_g$ from the NPs. Furthermore, by analyzing the directional van Hove distributions, we show polymer preferentially diffuses away from the NP monolayer, diffusion through the monolayer is slowed as a function of confinement, and diffusion away from the NP monolayer remains bulk-like.

In Chapter 5, we study chain-scale motion in highly attractive PNCs from Chapter 2. We develop and apply ion scattering measurements that separate and directly measure the fraction of

free polymer and polymer adsorbed to immobile, attractive NPs entirely in the melt state. By annealing thin PNC films of P2VP/SiO_2 deposited on bulk polymer matrices, free polymer from the PNC rapidly diffuses into the underlying matrix while the spontaneously-formed bound polymer in the melt remains with the NPs. Correlations between the fraction of bound chains and the total NP surface area provide measurements of the bound polymer layer thickness (~R_g) and show the average surface area occupied by adsorbed chains in the melt is much smaller than predicted from an isolated chain or measured in solution. The bound polymer fraction decreases as a function of annealing time and decreases more rapidly at higher temperatures and for lower molecular weights. However, even after annealing more than 10^6 reptation times, some polymer remains bound. We find that the desorption time is related to the chain-scale mobility in the bulk as opposed to the segmental relaxation times measured in Chapter 2. These new measurements and observations provide early insight into the mechanism of chain desorption from attractive NPs.

In Chapter 6, we study multiscale dynamics of polymer segments, polymer chains, and NPs in mixtures of entangled P2VP with very small, attractive octa(aminophenyl) polyhedral oligomeric silsesquioxane (OAPS, R_{NP} ~ 0.9 nm). With increasing OAPS concentration, both the segment reorientational relaxation rate (measured by dielectric spectroscopy) and polymer chain center-of-mass diffusion coefficient (measured by elastic recoil detection) are substantially reduced, with reductions relative to bulk reaching ~80% and ~60%, respectively, at 25 vol % OAPS. This commensurate slowing of both the segmental relaxation and chain diffusion process is fundamentally different than the case of PNCs composed of larger, immobile nanoparticles, such as those discussed in Chapter 2 and Chapter 5. Next, using RBS to probe the NP diffusion process, we find that small OAPS NPs diffuse anomalously fast in these P2VP-based PNCs. The OAPS diffusion coefficients are found to scale very weakly with molecular weight, $M_w^{-0.7\pm0.1}$ and our analysis shows that this characteristic OAPS diffusion rate occurs on intermediate microscopic time scales, lying between the Rouse time of a Kuhn monomer and the Rouse time of an entanglement

strand. The motion of the polymer and the NPs in this unique system support the recently developed theory of vehicle diffusion.

In summary, this thesis presents experiments and simulations that provide fundamental and mechanistic insight into dynamics of segments and chains in PNCs and the motion of NPs in polymer melts. The segmental dynamics presented in Chapter 2 and Chapter 3 show slow segmental relaxations near large attractive NPs. Chapter 4 and Chapter 5 examine how chain scale motion is perturbed by athermal and attractive NPs (respectively). Chapter 5 shows that the slow relaxations observed in Chapter 2 and Chapter 3 persist to the chain scale and lead to slow (or nonexistent) chain diffusion. Finally, Chapter 6 (with NPs faster than the polymer chains) describes categorically different dynamic behavior than Chapters 1-5 (with NPs slower than polymer chains). All together, this thesis demonstrates the importance of considering multiple length, time, and energy scales in PNCs and provide insights into the effect of various PNC parameters on microscopic dynamics. This work has also presented valuable future directions of research, which are presented and discussed in Section 7.2.

7.2 Future Work

7.2.1 Probing the Role of NP-Polymer Interactions on Various PNC Properties

The experimental work presented in this thesis focuses on systems with strong and attractive NP-polymer interactions in the form of hydrogen bonding between segments and the NP surface. Understanding the role of NP-polymer interaction on dynamics is critically important. This presents an experimental challenge, however, because changing the material (i.e. the polymer or NPs) leads to changes in other properties, which then have to be taken into account in comparisons. For example, comparing PNCs with different polymers leads to changes in critical characteristics such as the polymer backbone stiffness, glass transition temperature, entanglement molecular

weight, and tube size. In addition, it is well established that PNCs with weaker NP-polymer interactions exhibit poor NP dispersion in the melt state. Comparing systems with different dispersion states is undesirable because dynamics in PNCs are primarily perturbed at the NP-polymer interface, so changes in the interfacial area need to be considered but are difficult to measure.

One opportunity to probe NP-polymer interaction while minimizing the effect of other variables is to compare P2VP/SiO_2 PNCs where the SiO_2 is partially or fully functionalized with non-polar moieties. These molecular caps on the NP surface will not only change the NP surface energy, but will also remove hydrogen bonding sites for P2VP and sterically hinder the formation of trains on the NP surface. As a result, fully functionalized SiO_2 in P2VP should act akin to SiO_2 and PS, lacking strong favorable attraction, and will likely aggregate. However, if the NPs are functionalized at low areal densities, the opportunity for hydrogen bonding will decrease, but remain possible. Thus, there is likely a set of partially functionalized NPs that will have different surface energies and less hydrogen bonding opportunities than unmodified SiO_2, but will still be dispersed in P2VP.

Proceeding with this line of research necessitates two sequential studies. First, a thorough study of NP dispersion is essential to understand the transition from dispersed to aggregated NPs as a function of functionalization surface density. After the dispersion state in the PNCs is well understood, measurements of multiscale dynamics can proceed.

For measurements of NP dispersion, PNCs of low and high NP concentration (~5 and ~15 vol%) should be fabricated with NPs of different functionalization densities. These PNCs should be drop-casted, dried, and annealed until the structure stops changing. The dispersion state of each PNC should be studied with ultra-small angle X-ray scattering and transmission electron microscopy to understand the ensemble average structure and real-space representation (respectively). Preliminary measurements have been conducted on PNCs with 100 kg/mol P2VP

filled with 15 vol% MEK-STL (~50 nm diameter) that are unmodified or functionalized with octylsilanes at a density of ~0.6 caps/nm^2. For comparison with a system known to aggregate, PNCs with 100 kg/mol PS and unmodified SiO_2 were also fabricated. All PNCs were annealed at T_g+60°C for 15 days since a kinetic study has not been completed and the NP morphology was different from the as-cast condition. Kinetic studies are underway. The structure factors, S(q), are obtained by dividing the PNC scattering pattern by the form factor of the NPs to reveal the NP-NP correlations (Figure 7.1). The STL-un NPs (unmodified MEK-STL NPs) in P2VP exhibit a peak in S(q) at a location that closely matches the predicted interparticle separation distance for a random dispersion of NPs in these conditions, indicating that the NPs are well dispersed. For the same STL-un NPs in PS, the NPs are aggregated as indicated by the peak in S(q) at slightly smaller distances than the average NP diameter (indicating the touching of adjacent NPs) and a deep correlation well below 0.01 Å^{-1}. Finally, the STL-oct NPs (octyl-functionalized MEK-STL NPs) in P2VP exhibit an aggregated morphology, but one that appears to be more dispersed than PS/STL-un. A peak matching the location of PS/STL-un and a lack of a peak at low q indicates a partially aggregated system, but more analysis and TEM imaging is required to more clearly define the NP morphology. Future studies should follow this protocol, but sample more NP loading, more NPs including fully and partially functionalized NPs, and potentially include a kinetic aspect of documenting the dispersion after different annealing conditions.

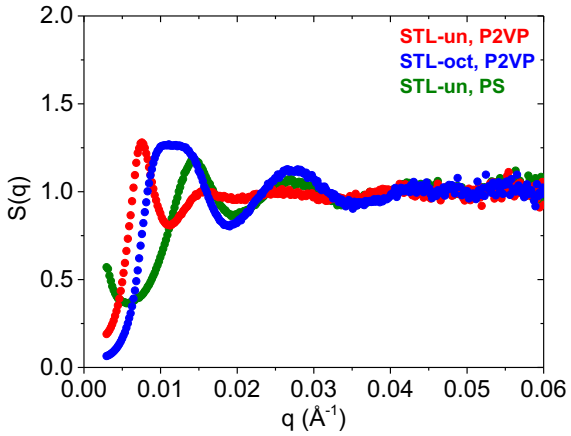

Figure 7.1: Structure factors from SAXS measurements for PNCs with P2VP and unmodified SiO_2 (STL-un/P2VP, red), P2VP and octyl-functionalized SiO_2 (STL-oct/P2VP, blue), and PS and unmodified SiO_2 (STL-un/PS, green). All PNCs are composed of ~50 nm Nissan MEK-STL NPs at 15 vol%, all polymer is 100 kg/mol, and each sample was annealed.

For measurements of multiscale dynamics, PNCs with similar dispersion states (none of which were achieved in Figure 7.1) should be measured with a variety of probes. For segmental dynamics, temperature modulated differential scanning calorimetry (TMDSC) can be used to probe the macroscopic glass transition temperature and segmental dynamics. Broadband dielectric spectroscopy (BDS) can be used to highlight segmental dynamics in the melt state and may be able to isolate the signal from interfacial relaxations. At longer length scales, polymer desorption can be measured from different NP surfaces using the technique discussed in Chapter 5, as will also be discussed in Section 7.2.2. Finally, measurements of NP diffusion will be insightful. As discussed in Section 1.6, most experimental measurements of NP diffusion in polymers are either grafted NPs or highly attractive, but simulations have been reported and theory has been developed for weakly interacting systems (see Section 1.6). In fact, the interesting situation where neither core-shell diffusion[208,225,246] nor vehicular diffusion[109,246] (Chapter 6) dominate, and both coexist, may be realized. These material systems present an interesting opportunity to either confirm theoretical predictions or provide more insights to guide them.

7.2.2 Further Studies on the Structure and Dynamics of Bound Polymer in the Melt

Chapter 5 of this thesis developed and demonstrated a technique that can measure new structure and dynamic properties of bound polymer directly in the melt state. Although measurements of NP concentration, polymer molecular weight, and annealing conditions were reported, there are several opportunities for new and impactful research. First and foremost, Chapter 5 presents interesting results that suggests the desorption of adsorbed chains correlates with the bulk-chain mobility, but this observation needs more robust testing. More complete temperature dependence measurements with different molecular weights (including unentangled polymer) is necessary to fully test the collapse of experimental data in Section 5.4.3. We hypothesize that even loosely bound chains will be unable to desorb at reasonable timescales at low temperatures. Similarly, sufficiently low M_w polymer which have a few long trains will likely behave differently than high M_w polymer with several trains of varying lengths and more conformational entropy. A more thorough study of annealing conditions and polymer molecular weight is needed to observe these effects and further develop a mechanistic understanding of polymer desorption.

Given the difficulty of isolating bound polymer and measuring chain-scale properties like thickness, areal adsorbed chain density, and desorption kinetics, much of the PNC parameter space remains unexplored. First, NP size (or radius of curvature) relative to the chain size is a potential future direction. One may expect bound chains to desorb more rapidly from smaller NPs due to less contact area and more convex curvature. An interesting comparison can be made between small NPs, large NPs, and flat substrates[185]. The experiments outlined in Chapter 5 are currently suitable for this set of measurements. Another potential direction, as discussed in Section 7.2.1, is the role of NP-polymer interaction. Using partially or fully functionalized NPs (Appendix E), the role of NP-polymer interaction on the bound layer thickness, adsorbed density, and desorption kinetics can

be revealed. For highly attractive systems like P2VP/SiO_2, bound polymer exists even after ~10^6 reptation times (Chapter 5). In weakly attractive PS and SiO_2 flat substrates, bound polymer remained after solvent washing for more than 140 days.[316] In melt PNCs, it is unclear if bound polymer will remain adsorbed after similarly long times if the NP-polymer interaction is weakened. Measurements on other model PNC systems, such as PMMA/SiO_2, is also suggested and may provide additional insights.

There are also interesting structural properties that can be studied using the methods introduced in Chapter 5. Measurements of the areal density of adsorbed chains and bound layer thickness provide insight into how chains pack at the NP interface. Importantly, these measurements are done after relatively short annealing times, so preventing the motion of NPs is not necessary. The measurements presented in Chapter 5 were on PNC films directly after spin coating (i.e. no pre-annealing). An interesting future direction is to study how pre-annealing the PNC film further densifies the bound polymer layer and changes the structure. In addition, the question of competitive adsorption can be addressed using these experiments. For example, in a solution of bimodal M_w, the polymer that preferentially adsorbs to the NP surface can be measured by the bound layer thickness and adsorbed areal density. Other questions include how the bound polymer species depends on the order in which the polymers are introduced, how much pre-annealing is done, and how different the chain lengths are. These fundamental questions of competitive adsorption can help identify the underlying thermodynamics of adsorption and help engineer the bound polymer layer for various applications.

In addition, new experimental methods should be developed to probe these properties that do not rely on access to an ion beam and ERD/RBS capabilities. In an extension of the SANS method recently reported[206], time-resolved SANS using preferentially adsorbed deuterated and protonated polymer can probe bound polymer dynamics. As bound chains desorb and matrix chain adsorb, the scattering length density will change. This change in scattering contrast can be extracted

and analyzed to reveal the kinetics of exchange. While sample preparation and optimizing the PNC parameters to observe bound polymer exchange may be challenging, the development of this technique can open a direction of research that can address research questions including but not limited to those presented in this section.

7.2.3 Probing the Bound Polymer Layer in NP-Polymer Solutions

Section 7.2.2 discussed potential measurements of the bound polymer layer in the melt state, but studying the bound polymer layer in solution is also critical (see Appendix G). NP-polymer solutions present additional interactions that change bound layer properties, making the energetics more complex and the parameter space more vast. NP-polymer solutions are also academically and industrially relevant. PNCs are traditionally fabricated from solution, so understanding the properties in solution will help engineer properties in the melt. There is also relevance to biological media and, more directly, colloidal systems.

Measurements of small-angle neutron scattering (SANS) and dynamic light scattering (DLS) are ideal for this investigation. DLS provides a measurement of hydrodynamic size in solution, but can be used to identify polymer adsorption as shown in Figure 7.2 for PS and P2VP mixed with SiO_2 in DMF. For the attractive system of P2VP/SiO_2, polymer adsorbs to the NP surface and increases the hydrodynamic size by ~$2R_g$ relative to only SiO_2. Conversely, the non-attractive case of PS and phenyl-capped SiO_2 exhibits a NP size that is essentially unchanged from SiO_2. Similar measurements can be used to more thoroughly navigate the energetics of NP-polymer solutions. Furthermore, measurements as a function of polymer concentration may reveal the adsorbed chain density in solution (analogous to the SA_{chain} in the melt reported in Chapter 5). At low concentration, the NP size should be unchanged from bare SiO_2 but eventually the NP size should plateau at ~d_{NP}+$2R_g$. The concentration of the plateau will reveal the polymer coverage on the NP.

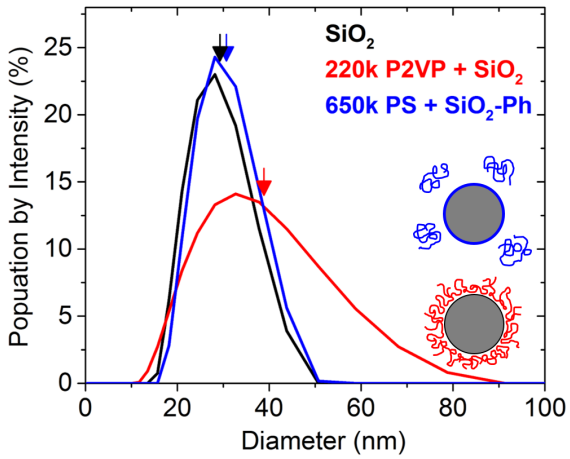

Figure 7.2: DLS measurements of SiO_2 (black), 220 kg/mol P2VP + SiO_2 (red), and 650 kg/mol PS + phenyl capped SiO_2 (SiO_2-Ph, red) in dimethylformamide (DMF). Polymer concentration was ~5 g/L in NP-polymer solutions and solvent-transferred Ludox AS40 SiO_2 was used in each case.

SANS can be used to more thoroughly study the bound polymer layer in solution, particularly using contrast matching and hydrogenated and deuterated polymer. Preliminary measurements are presented in Appendix G. Contrast-matching the solvent with the NPs in dilute solutions ensures that only the polymer will be contributed to the scattering pattern. If polymer is not adsorbed, a Debye function will describe the data, but if polymer is adsorbed to the particle, the data will follow a hollow shell form factor with an inner diameter equal to the NP diameter. This difference is expected to be clear (Figure G.2). Since the scattering contrast is related concentration and SLD of each component, meticulous fitting should reveal the polymer concentration (density) within the bound polymer layer and the length scale associated with the bound layer. Furthermore, the stability of the bound polymer can be probed by changing the temperature or adding a good solvent for the NP and polymer or a low M_w polymer. The unique ability to measure only the polymer makes SANS measurements of bound polymer in solution a worthwhile and insightful endeavor with several potential variables to explore.

Using SANS, the kinetics of adsorption and desorption can also be probed. These timescales are presently unknown and certainly depend on solution properties, but experimental conditions such as temperature, material systems, and measurement parameters may be tuned to make this study possible. To study the kinetics of adsorption, the solution can be made by mixing a polymer solution and a NP solution and immediately measuring the SANS pattern continuously. If polymer adsorption is immediate, the time-dependent measurements will align. If not, the formation of the bound layer can be observed in real time. For polymer desorption, or exchange in solution, two dilute solutions of NP-polymer-solvent can be mixed. Importantly, one solution should be made with only hydrogenated polymer and the other should be made with only deuterated polymer. The mixed sample, assuming no structure factor is present, will be the summation of both solutions. However, if polymer exchange occurs such that hydrogenated chains desorb and reabsorb into deuterated bound layers, the scattering contrast of the system will change. This change in scattering contrast can be analyzed as a function of time and related to the fraction of chains that desorbed and readsorbed. Alternatively, the same experiment can be conducted with a NP solution in a bath of free polymer. Similarly, as chains exchange, the scattering contrast will change. Preliminary measurements of both cases will help understand which scattering pattern is tractable and which is more difficult to describe analytically.

7.2.4 Understanding the Role of Processing on the Dispersion and Bound Polymer Properties

It remains mostly unclear if PNCs reach their equilibrium morphology or if they are often kinetically trapped in a non-equilibrium morphological and structural state. This delineation is of critical importance. First, if PNCs cannot access their equilibrium state, comparison with current equilibrium-based theory and simulation require caution and new theory and simulation efforts or

methods are needed to incorporate nonequilibrium effects. Second, if PNCs are in kinetically trapped states, engineers should be able to use processing methods and parameters to further tune and control PNC macroscopic properties.

There is evidence of nonequilibrium effects in common PNC research, including the long-lived bound polymer that was highlighted in Chapter 5. It has been shown that the final NP dispersion states[292,311] depend on the solvent quality used during fabrication. Preliminary SAXS measurements of PMMA/SiO_2 PNCs after different drying conditions are presented in Figure 7.3. These measurements show that the rate at which solvent is removed, which was controlled by temperature, changes the NP dispersion state. The clear difference in NP morphology in the same PNCs but with different processing conditions indicates non-equilibrium effects. Recently, the bound layer structure and properties were analyzed in PNCs made from good and poor solvent.[70] In these PEO/SiO_2 PNCs, a thicker bound layer and more perturbed dynamics were observed in PNCs fabricated from poor solvent (ethanol) relative to a good solvent (water).[70]

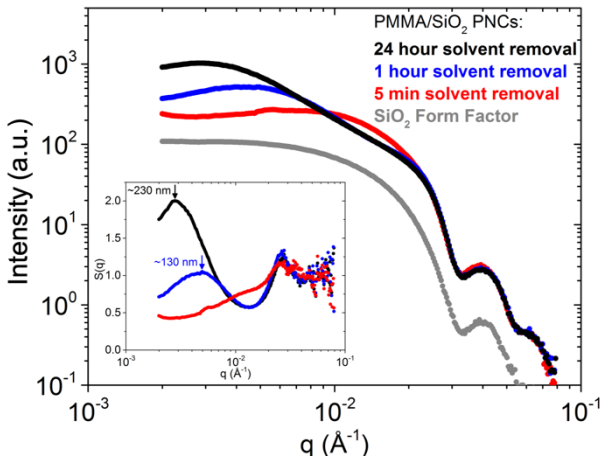

Figure 7.3: SAXS characterization of PMMA/SiO_2 PNCs fabricated by solvent evaporation at different drying rates. Structure factor showing NP-NP correlations (inset). Differences in the NP morphology show that PNCs depend on the processing conditions.

An intriguing future direction is to systematically change the processing conditions and probe the resulting NP structure and multiscale dynamics, particularly of the polymer and polymer

segments. For example, the fraction of loops, tails, and trains of bound polymer should depend on the quality of the solvent during their formation, among other factors. For example, chains that are more expanded in a good solvent may adsorb to NPs with longer trains than a compressed chain in a poor solvent which may have more loops. If this is true, it should be possible to engineer more stable bound polymer layers through solvent selection. Measurements of bound polymer desorption (chain-scale) and BDS or TMDSC (segment-scale) may show these differences.

Fabricating the model PNCs from different fabrication methods can also be a worthwhile direction of future work. These new methods may reveal new morphological states in the same PNC system or promote (temporary) dispersion when it may not be achievable with other techniques. Such fabrication methods may include traditional drop casting, vacuum-assisted drop casting, precipitation in a poor solvent (such as hexane or water), and freeze drying. If NPs that are difficult to disperse in a polymer melt at equilibrium can be kinetically trapped in a dispersed state initially, there is an opportunity to study the kinetics of NP aggregation in the melt. Furthermore, PNCs can be quenched below T_g in their dispersed and aggregated morphology, providing an excellent comparison of the role of NP morphology on glassy properties (i.e mechanical or transport properties).

7.2.5 Narrowing the gap between simulations and experiments

As a final direction of research, it is critical to develop the direct comparison between experiments and molecular dynamic (MD) simulations. MD simulations present the unique opportunity to mechanistically and quantitatively understand PNC dynamic processes, rapidly explore the dense parameter space, and isolate, control, and measure individual variables and properties. For maximum impact, the continuous goal should be to directly verify simulations with

experiments which will help make simulations more predictive and their results attainable experimentally.

Chapter 4, for example, aims to more thoroughly understand previous experimental measurements of polymer diffusion in various PNCs. However, discrepancies between Chapter 4 results and experiments were highlighted, which leaves work for the future. For example, a more thorough testing of the confinement parameter, $ID/2R_g$, requires changing the polymer molecular weight and NP size simultaneously. This is challenging given the simulation box setup in Chapter 4 because as the chain length increases, the spatial region over which diffusion can be observed also increases causing the simulation size to grow. More traditional simulation boxes with NPs periodically arranged or randomly placed may be more suitable to fully test the confinement parameter. In addition, incorporating attractive NP-polymer interactions will help highlight if NP-polymer interaction influence polymer diffusion through confining NPs, which was not observed experimentally[272]. Using concepts from Chapter 5, this may produce a population of chains that freely diffuses but at timescales slower than bulk, and another population that remains adsorbed to the NPs. Furthermore, these simulations may provide more mechanistic insight into Chapter 5, but polymer desorption may be too slow to observe with coarse-grained MD simulations.

More broadly, specific parameters and measurements need to be developed to verify and directly compare experimental measurements with simulated PNC systems. Although the relation of Kremer-Grest parameters to experimental parameters in polymer melts have been reported[63], several PNC parameters remain unclear. For example, the NP-polymer interaction is often modelled by a LJ potential, but the range of interaction strengths (ε) that match experimental systems remains unclear. This is a challenging comparison to make. Furthermore, the appropriate structure of the NP that eliminates artificial packing and enhanced density at the interface and properly simulates the energetic landscape remains unclear. This is largely due to a limited understanding of NP interfaces experimentally and the present inability to directly compare

interfacial properties between simulations and experiments. In the future, research efforts to align MD simulations and in experiments in PNCs will help explore the expansive parameter space and accelerate new discoveries.

APPENDIX A: SUPPORTING INFORMATION FOR CHAPTER 2

A.1 TEM Images of 40 kg/mol PNCs

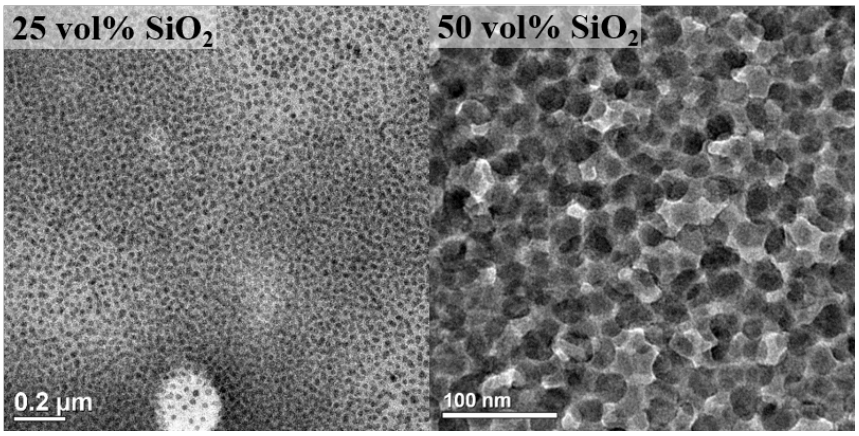

Figure A.1: (left) Representative TEM image for 25 vol% PNC (spin coated) with 40 kg/mol P2VP matrix. As expected from the strong NP-polymer attraction, long-range uniform dispersion is observed. Bright and dark patches are likely variations in thickness or bubbles caused by solvent evaporation during spin coating. (right) Representative TEM image for 50 vol% PNC drop casted directly onto TEM grid.

A.2 Thermal Degradation of Bulk Polymers

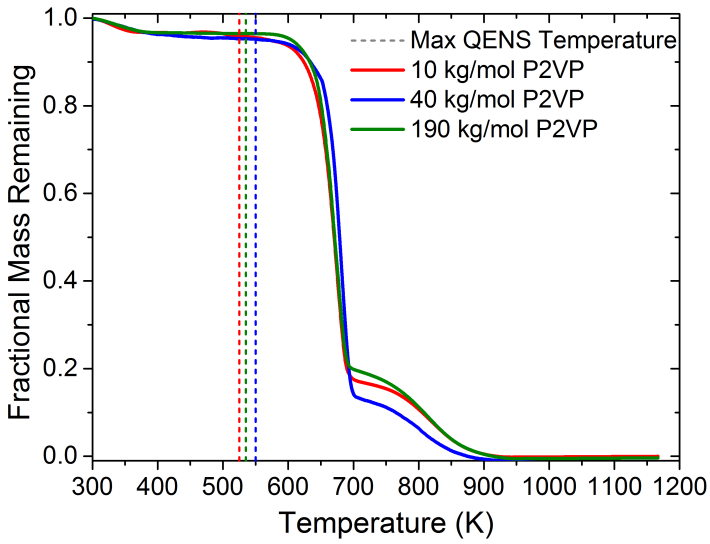

Figure A.2: Thermogravimetric curves used to characterize the thermal degradation of P2VP for the three molecular weights studied. Feature at ~373 K is likely the evaporation of adsorbed water

or solvent that remains present after drying procedure (T_g+60 K for at least 12 hours under vacuum). Vertical dashed lines represent the highest measurement temperature for QENS experiments and are well below the decomposition temperature of P2VP.

A.3 Fixed Window Scan Analysis

The mean-squared displacement ($\langle x^2 \rangle$) was determined using the Debye-Waller approximation, as previously reported.[287] After manipulation, it is shown that the intensity of elastic scattering ($I_{elastic}$) normalized to the intensity of the same sample at 50 K (I_0) is related to $\langle x^2 \rangle$ through the square of the scattering vector, q:

$$-3 \cdot \ln\left(\frac{I_{elastic}}{I_0}\right) = \langle x^2 \rangle \cdot q^2 \qquad \text{(A.1)}$$

In practice, $\langle x^2 \rangle$ is obtained directly as the slope of $-3 \cdot \ln\left(\frac{I_{elastic}}{I_0}\right)$ plotted as a function of q^2. Nonlinear deviations are expected to occur at large q due to the breakdown of Debye-Waller approximation.[76] Rather than accounting for this with higher order terms that add several variables and complexity, we use a linear fit restricted to $q^2 < 1.22$ Å^{-2} (length scales at least 5.7 Å). Similar methodologies have been reported elsewhere.[76,287]

A.4 Raw Fixed Window Scans

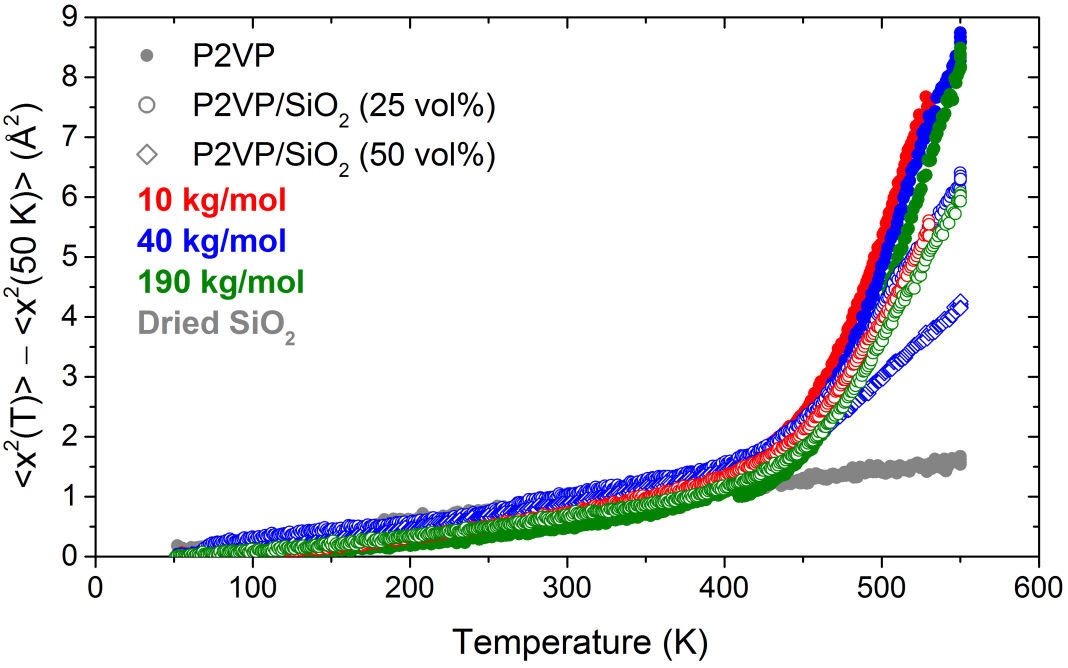

Figure A.3: Average mean-squared displacement of segments obtained from fixed window scan of bulk P2VP and P2VP/SiO_2 PNCs for all molecular weights and loadings. MSD is defined relative to T = 50 K, the minimum temperature measured. All samples show an expected linear increase in MSD at $T < T_g$ and an abrupt increase in MSD at $T \sim T_g$. Dried SiO_2 NPs, which have surface hydroxyl groups, are included for comparison.

A.5 Representative Fits and Residuals

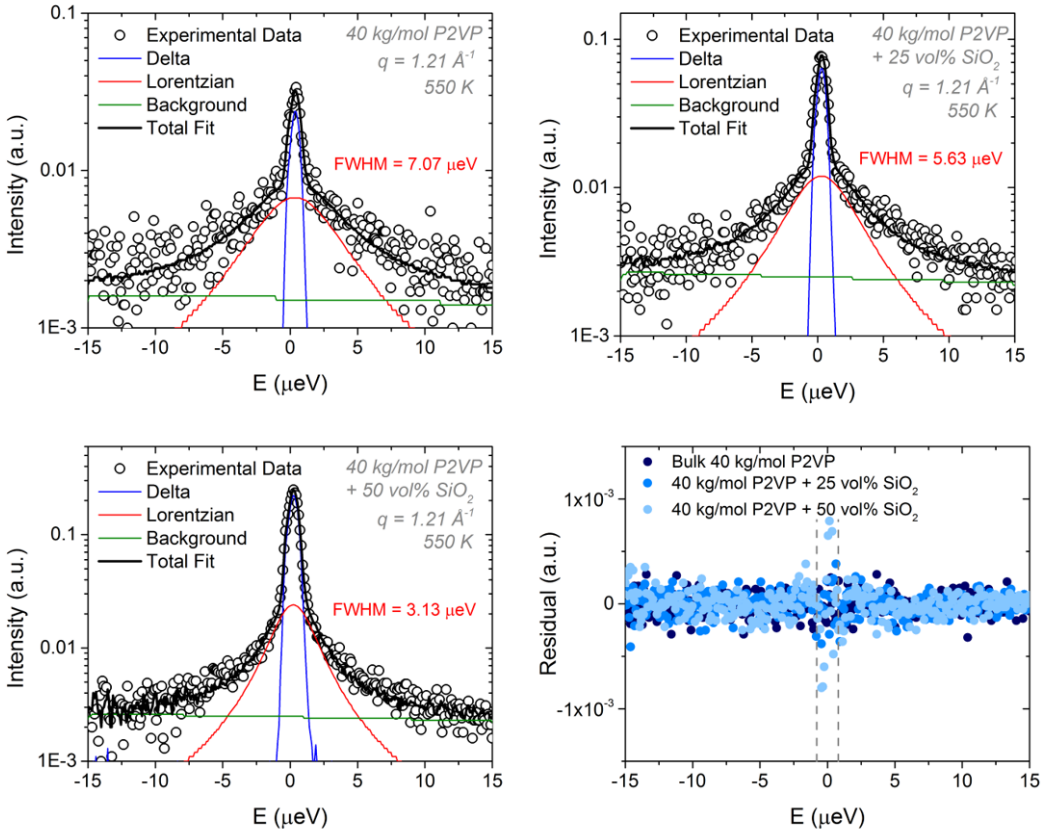

Figure A.4: Representative QENS spectra (550 K and q = 1.21 $Å^{-1}$) for bulk 40 kg/mol P2VP, and 40 kg/mol P2VP filled with 25 and 50 vol% SiO_2. Residuals of fitted spectra show no significant deviation or systematic trends, especially beyond the instrument resolution where dynamic information is captured.

A.6 Extracted QENS Broadening for 40 kg/mol Bulk and PNCs

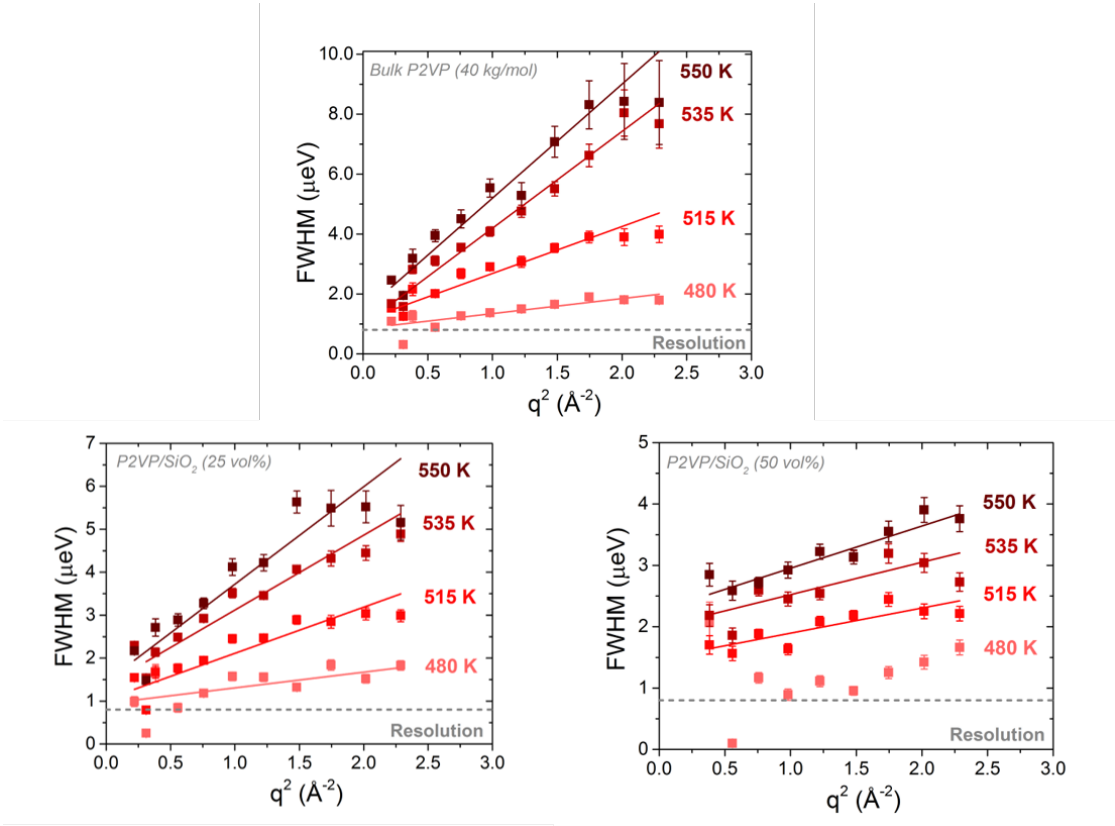

Figure A.5: Quasi-elastic broadening (full width at half-maximum, FWHM) of Lorentzian contribution to the fit of QENS spectra for bulk 40 kg/mol P2VP and PNCs of 25 and 50 vol% as a function of temperature. Note that P2VP/SiO_2 50 vol% was measured at 480 K but fails to follow FWHM~q^2, so a diffusion coefficient will not be reported.

A.7 Discussion of BDS Analysis

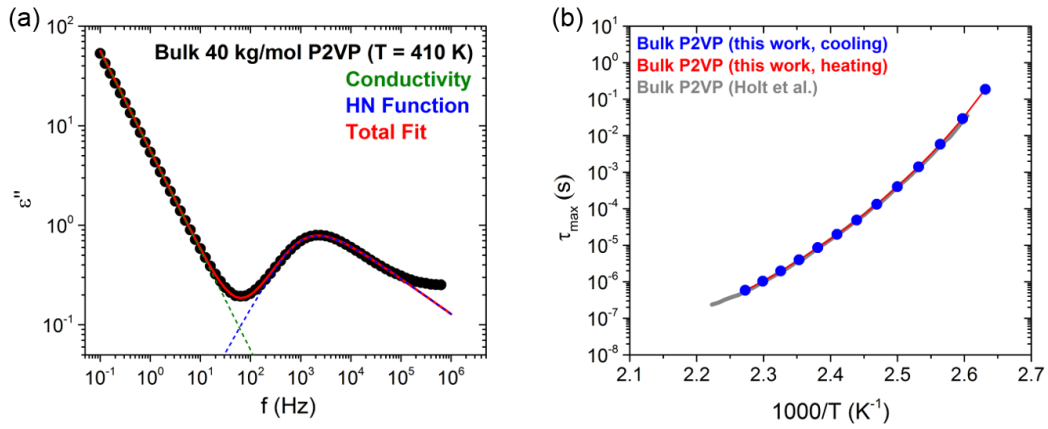

Figure A.6: (a) Representative imaginary part of the complex dielectric permittivity as a function of frequency obtained from 40 kg/mol bulk P2VP at 410 K upon cooling and fit with Equation A.2. (b) Relaxation time as a function of inverse temperature comparing measurements made upon cooling, subsequent heating, and in literature. Literature data were obtained from Ref 65.

The dielectric spectra were measured for bulk 40 kg/mol P2VP at various temperatures to compare to bulk relaxation times obtained from QENS and TMDSC. The complex permittivity was measured as a function of frequency and the imaginary part was fit using a linear combination of a Havriliak-Negami function and a conductivity term:[57]

$$\varepsilon''(\omega) = -\mathrm{Im}\left[\frac{\Delta\varepsilon}{\left(1+(i\omega\tau_{HN})^{\beta}\right)^{\gamma}} + \frac{\sigma}{i\varepsilon_0\omega}\right] \qquad \text{(A.2)}$$

where ω is the angular frequency, $\Delta\varepsilon$ is the dielectric strength, τ_{HN} is the Havriliak-Negami relaxation time, β and γ represent the symmetric and asymmetric broadening (respectively), σ is the dc conductivity and ε_0 is the vacuum permittivity. The mean molecular relaxation time (τ_{max}) can be calculated as:

$$\tau_{\max} = \tau_{\mathrm{HN}} \left(\sin\left(\frac{\beta\gamma\pi}{2(\gamma+1)}\right)\right)^{1/\beta} \left(\sin\left(\frac{\beta\pi}{2(\gamma+1)}\right)\right)^{-1/\beta} \qquad \text{(A.3)}$$

A representative fit is shown in Figure A.6a for 410 K. Figure A.6b shows the extracted relaxation times for P2VP measured upon cooling from 450 K to 380 K in steps of 5 K. Importantly, the relaxation times upon cooling and subsequent heating are essentially identical and agree with bulk P2VP measurements from literature (Figure A.6). Dielectric measurements of polymer nanocomposites have been studied extensively, and are therefore beyond the scope of this work.[58,65,73]

A.8 Extracted QENS Broadening for PNCs of Various Molecular Weights

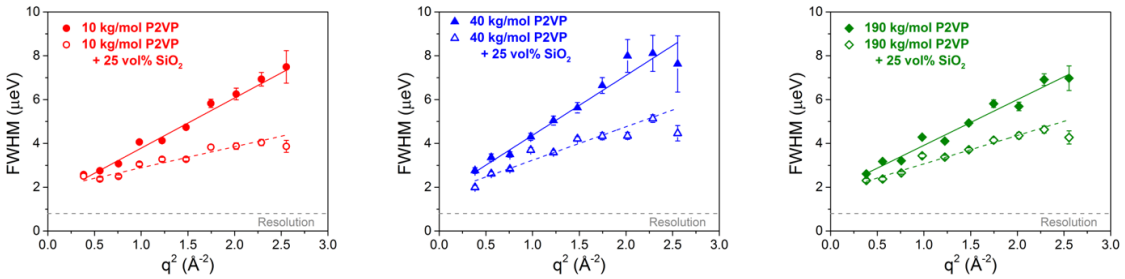

Figure A.7: Quasi-elastic broadening (FWHM) of Lorentzian contribution to the fit of QENS spectra for bulk P2VP and PNCs (with 25 vol% NPs) of different matrix molecular weights. In each case, the addition of NPs suppresses the diffusive dynamics.

A.9 Sample Degradation Analysis

Table A.1 presents GPC measurements of bulk P2VP samples before and after QENS measurements. 10 and 40k kg/mol samples were measured with a Shimadzu Prominence High Performance Liquid Chromatograph with two PLgel mixed-D columns (Agilent). On-line multi-angle light scattering (MALS) measurements were performed using a Wyatt Dawn Heleos II light scattering detector. Weight-averaged molecular weight was determined by MALS (dn/dc = 0.195), and molar mass distributions were determined relative to narrow-dispersity polystyrene standards using Wyatt Astra VII software. Samples were measured in THF at a flow rate of 1 mL/min. 190k samples were measured with the GPCMax with TDA from Malvern Instruments with three PLgel Mixed B column (Agilent). Samples were measured with 0.5% TEA in THF at a flow rate of 1 mL/min after calibration based on DRI detector signals with P2VP standards from Scientific Polymer Products, Inc.

Figure A.8 presents a time-dependent analysis of QENS data, showing no significant variation in the measured diffusion coefficient with measurement time. Figure A.9 and Figure A.10 present measurements of the glass transition temperature and degradation behavior, respectively, for samples before and after measurement.

Table A.1: Measured molecular weight of bulk P2VP samples before and after fixed window scans and QENS measurements. Note that 40 kg/mol QENS samples were measured at four temperatures while other MWs were measured at only one. PDI values, defined as M_w/M_n, are included in parenthesis.

Sample Name	M_w in kg/mol (PDI)	
	Before QENS	After QENS
10k Bulk	9.9 (1.03)	9.8 (1.03)
40k Bulk	39.3 (1.12)	33.1 (1.13)
190k Bulk	188 (1.24)	92 (1.85)

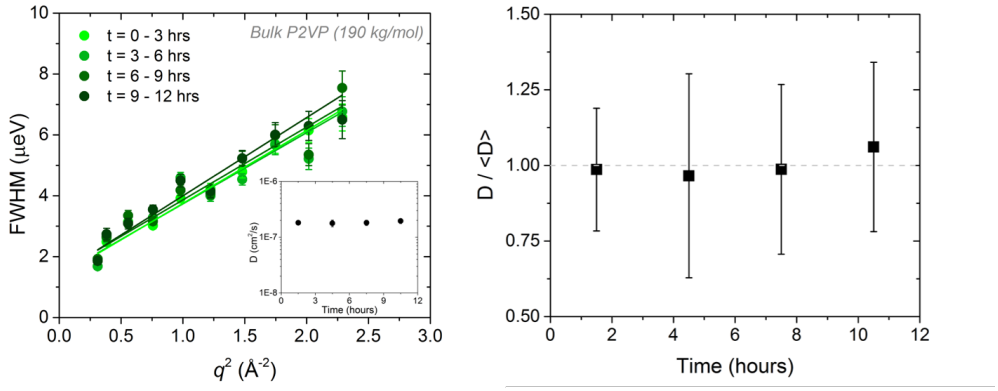

Figure A.8: Degradation analysis of bulk 190 kg/mol P2VP as a representative example. The QENS data was analyzed in four sequential 3-hour experiments and then analyzed individually and compared to the summed data. (left) FWHM of Lorentzian contribution to QENS for four measurement periods. Inset: Diffusion coefficient extracted over each measurement period. (right) Extracted diffusion coefficient (normalized to the average diffusion coefficient over entire measurement) plotted as a function of time. No systematic trend is observed and deviations from the average are well-within error.

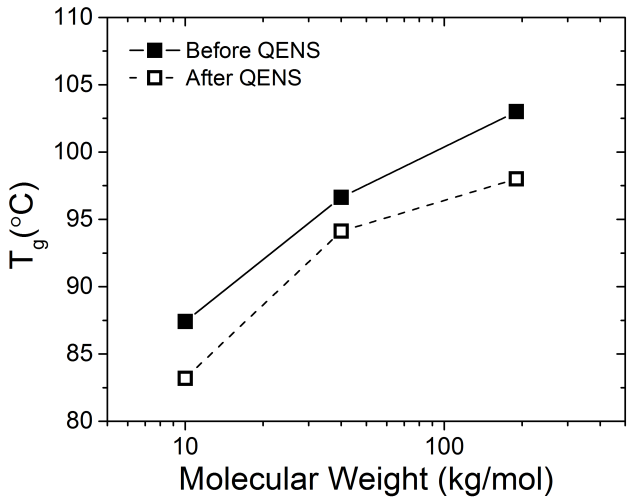

Figure A.9: Difference in calorimetric glass transition temperature (T_g) of bulk P2VP samples before and after fixed window scans and QENS measurements. The shape of the glass transition was unchanged (not shown).

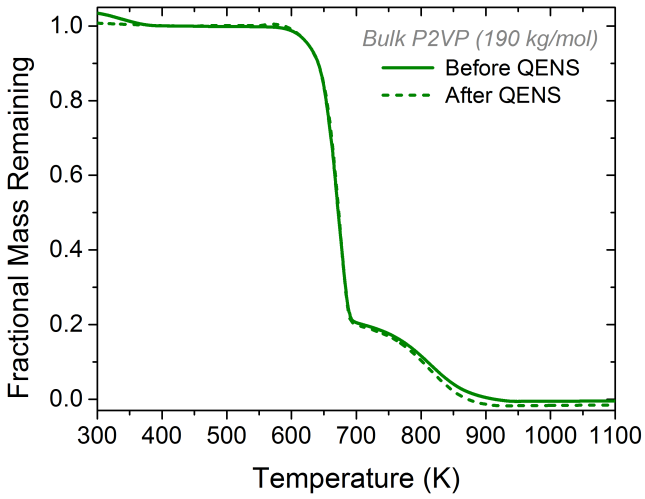

Figure A.10: Thermogravimetric curves for bulk 190 kg/mol P2VP (as a representative example) before and after fixed window scans and QENS measurements. Degradation temperature and behavior remained unchanged after the sample was subjected to measurement conditions.

APPENDIX B: SUPPORTING INFORMATION FOR CHAPTER 4

B.1 Table of Simulation Parameters

Table B.1: Table of simulation parameters for select systems including chain length (N), NP size (R_{NP}), box dimensions (Lx, Ly, Lz), macroscopic diffusion coefficient in z direction (D_z), and the maximum LJ time.

Confinement	**N**	**$2R_{NP}$**	**R_g/R_{NP}**	**Lx**	**Ly**	**Lz**	**D_z**	**LJ time**
Bulk	50		N/A	22.744	22.744	22.744	8.7E-4	
0.5	50	7	1	21.2	18.36	57.566	7.6E-4	1.7E7
0.75	50	7	1	24.8	21.48	42.167	7.7E-4	7.8E6
1	50	7	1	28.4	24.6	57.4	8.2E-4	1.2E7
2	50	7	1	21.4	37.07	47.4	8.5E-4	9E6
1	50	14	0.5	21.4	18.53	53.9	--	4.8E6
1	50	3.5	2	21.2	36.72	56.1	--	5.4E6

B.2 Polymer Density in Simulation Box

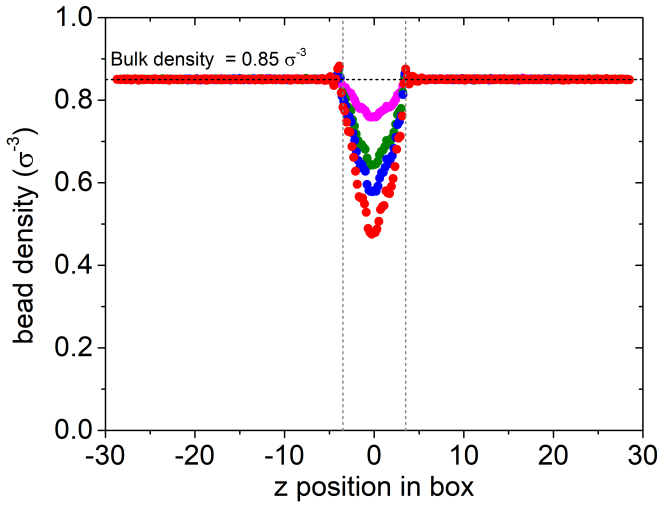

Figure B.1: Local polymer density as a function of z position in the simulation box.

B.3 Random-walk Conformation Maps

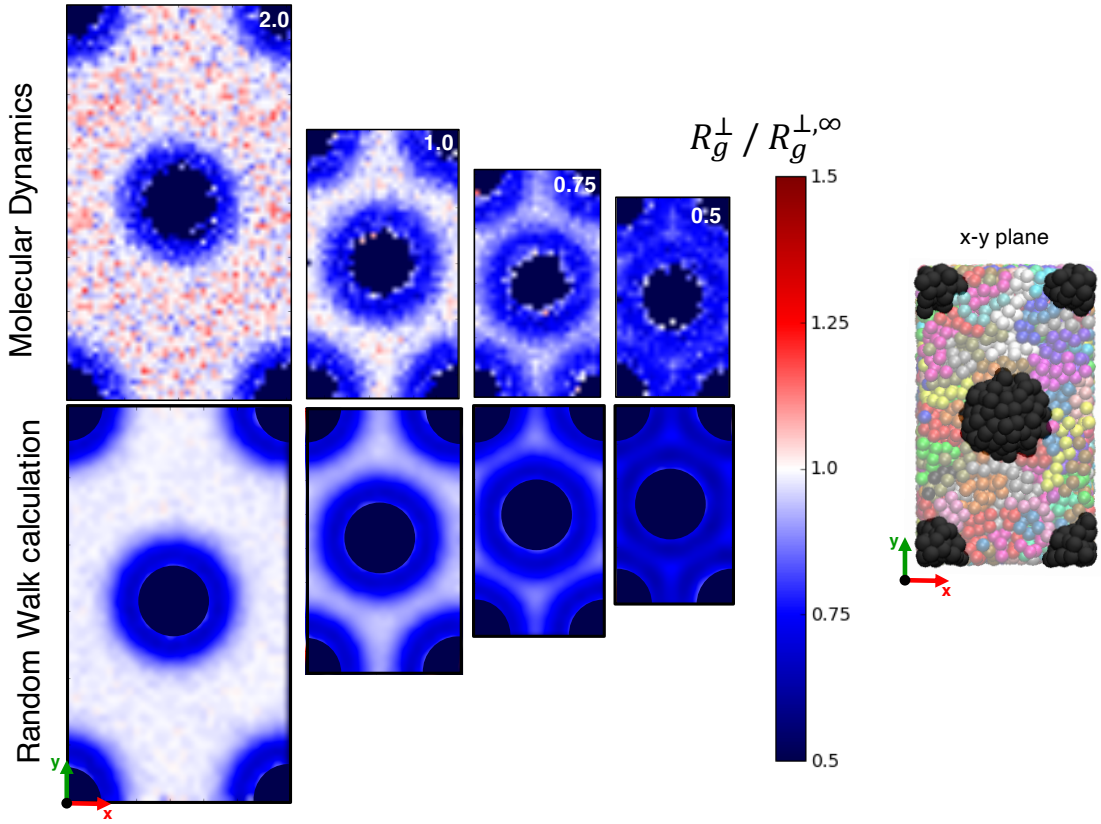

Figure B.2: Conformation map in x-y plane through NP monolayer for various degrees of confinements obtained from MD simulations (top) and random walk calculations (bottom). NP representations in maps from random walk calculation are added to exclude conformations where the COM of the conformation is within the NP excluded volume.

B.4 Random-walk Conformations Around NPs

Role of NP size *Role of chain length*

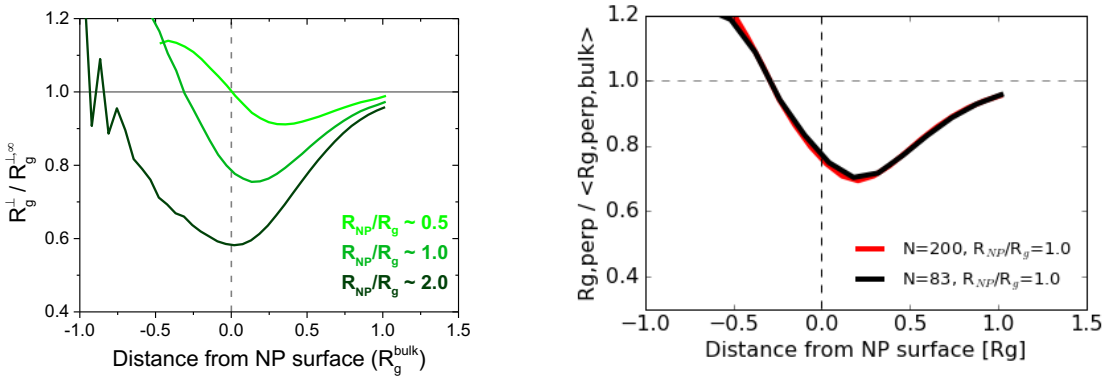

Figure B.3: Conformation profile plotted as normalized perpendicular component of R_g as a function of COM distance from the NP surface for different NP sizes (left) and chain lengths (right).

B.5 MSD of Bulk and PNC systems

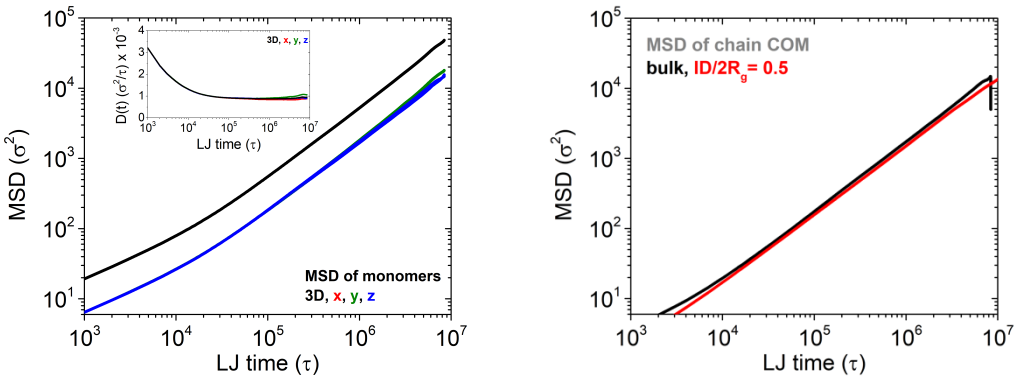

Figure B.4: Macroscopic mean-squared displacement as a function of LJ time for bulk N=50 chains (left). Comparison of MSD in z-direction for bulk and ID/2R_g=0.5 systems (right).

B.6 Diffusion Coefficient Extracted From van Hove Distribution as a Function of Time

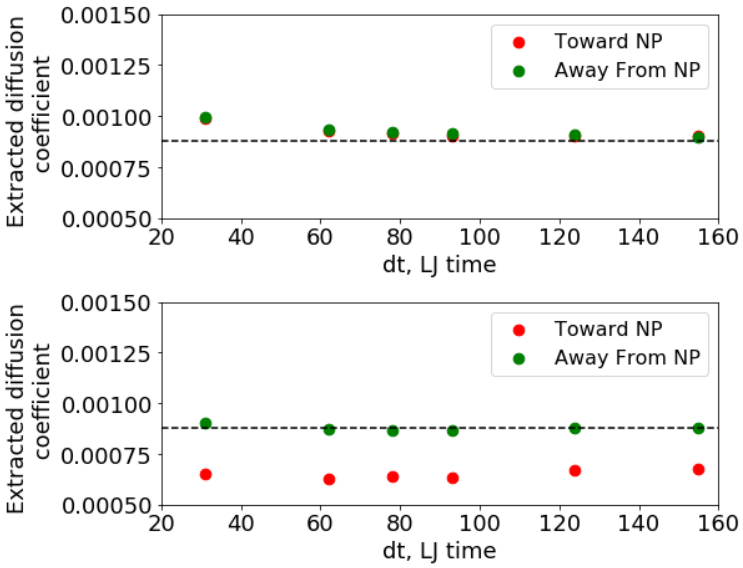

Figure B.5: Extracted diffusion coefficient from van Hove distribution analysis as a function of time for bulk polymer (top) and ID/2R_g = 0.5 (bottom). Dashed lines represent macroscopic diffusion coefficient of bulk polymer.

B.7 van Hove Distributions for Representative z_0

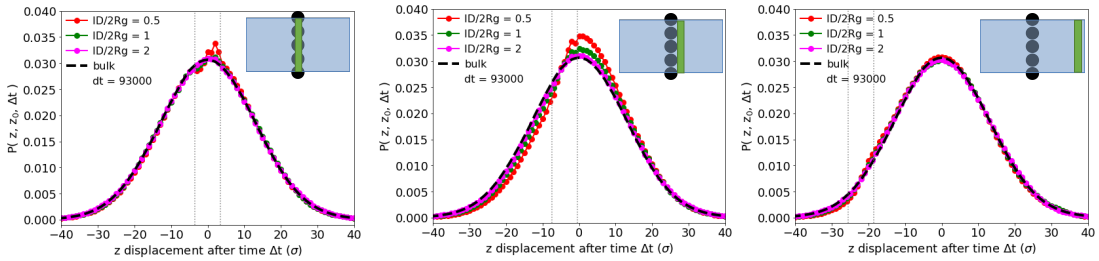

Figure B.6: van Hove distributions for bulk and confined systems for several starting locations, as depicted in the insets, and $\Delta t = 93{,}000\tau$. Figures include $z_0 = 0$ (left), $z_0 = 4$ (middle), and $z_0 = 22$ (right).

APPENDIX C: SUPPORTING INFORMATION FOR CHAPTER 5

C.1 Dispersion of SiO_2 NPs in P2VP

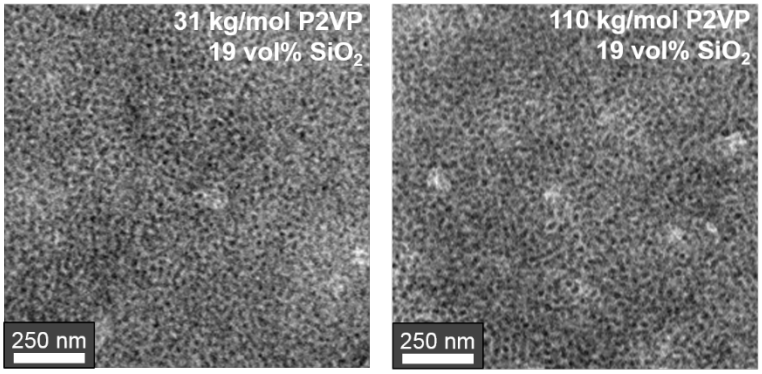

Figure C.1: Transmission electron micrographs showing homogeneous dispersion of SiO_2 nanoparticles in (a) 31 kg/mol and (b) 110 kg/mol dP2VP at 19 vol%, the highest concentration studied. The TEM specimens were prepared from ~150 nm thick P2VP/SiO_2 on ~30 nm PS that was floated from a silicon wafer in DI water and transferred to a TEM grid. Due to the high NP concentration and sample thickness (~180 nm total), there is extensive overlap of the NPs in the TEM image. However, P2VP/SiO_2 is known to form stable dispersions.[65,208,210] TEM images showing SiO_2 dispersion in various M_w P2VP (28 – 300 kg/mol P2VP and 10 vol%) after the same sample preparation can be found in Ref 208.

C.2 RBS measurements of unannealed bilayers

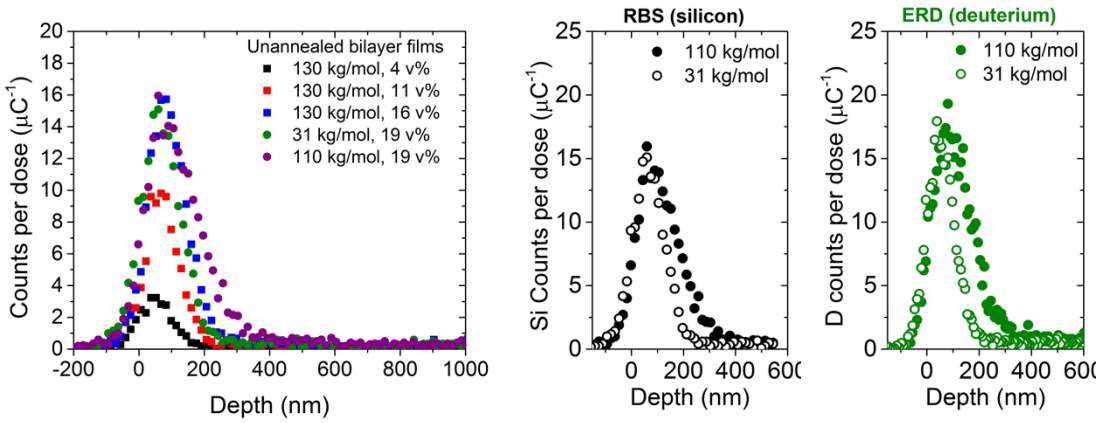

(a) (b) (c)

Figure C.2: (a) RBS measurements of all unannealed diffusion couples showing counts in Si peak as a function of depth. (b,c) Comparison of 31 and 110 kg/mol PNCs with RBS (b) and ERD (a). We note that the 31 kg/mol sample (open symbols, ~130 nm) is thinner than the 110 kg/mol sample (closed symbols, ~160 nm), but the NP concentration is the same (Table C.1). We also note that the ratio of counts in ERD and RBS (which is directly related to the relative amount of polymer and NP) are in good agreement for both samples.

Table C.1: Quantitative comparison of unannealed tracer films from Figure C.2a, which are defined by dP2VP M_w and ϕ_{NP}. The total Si signal from RBS normalized by the dose (I_{Si}) is calculated from Figure C.2a for -200 nm < z < 400 nm. The film thickness (h) and ϕ_{NP} were determined from fitting raw experimental data in SIMNRA. Between the different samples, the experimental I_{Si} should depend primarily on ϕ_{NP} and h, and as expected, $I_{Si}/(h*\phi_{NP})$ is constant (within ~10%) for all samples. This verifies that our assignment of h and ϕ_{NP} are reasonable.

dP2VP M_w (kg/mol)	ϕ_{NP} (vol%)	I_{Si}, Integrated RBS counts per dose (-200 nm < z < 400 nm)	h, film thickness (nm)	$I_{Si} / (h*\phi_{NP})$ (counts/nm)
130	4	29.3	105	0.0699
	11	87.5	125	0.0637
	16	155.8	150	0.0649
31	19	194.9	160	0.0641
110	19	154.0	130	0.0624

C.3 Bound layer thickness analysis for 31 and 110 kg/mol dP2VP PNCs

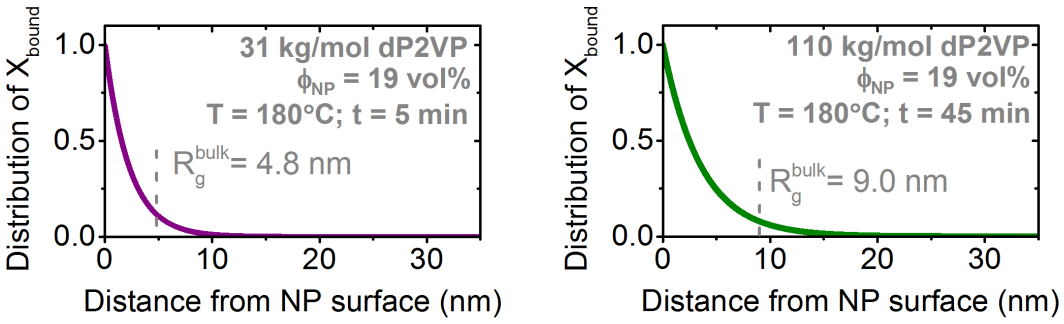

Figure C.3: Analysis of bound layer thickness for 31 kg/mol dP2VP (left) and 110 kg/mol dP2VP (right) PNCs comprised of 19 vol% SiO_2 and annealed for short times (5 min and 45 min respectively). In both cases, the bound layer thickness extends ~R_g from the NP surface, in qualitative agreement with Figure 5.4d. The underlying P2VP matrix in both cases is 250 kg/mol.

C.4 Measurements of bulk diffusion

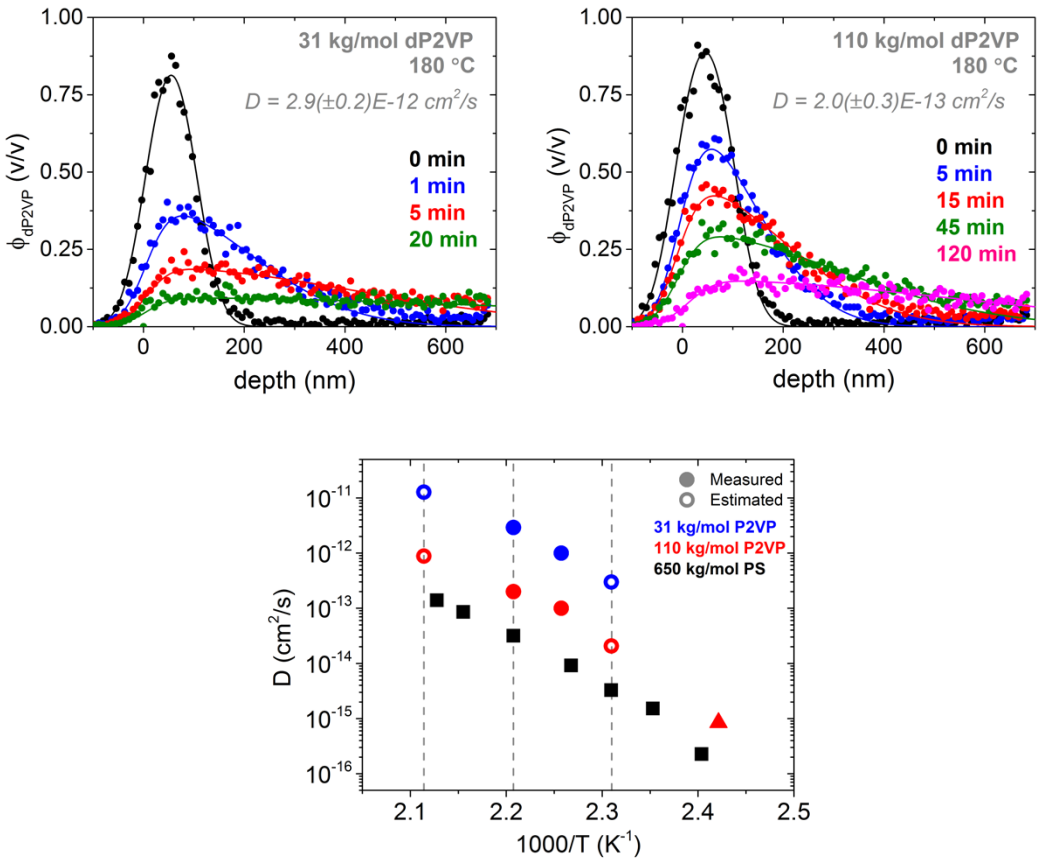

Figure C.4: Measured ERD depth profiles and diffusion coefficients for (top left) 31 kg/mol and (top right) 110 kg/mol dP2VP at 180˚C and varying annealing times. (bottom) Bulk diffusion coefficients as a function of inverse temperature. Measurements at 160˚C and 200˚C were extrapolated from measurements at lower temperatures (solid circles and triangles) assuming a similar fragility as bulk PS (solid black squares). Importantly, the fragility index of chain-scale dynamics for PS and P2VP are largely independent of molecular weight and have similar values (~90).[322] By comparing available D_{chain} measurements from PS (Ref 188) and P2VP (this work and Ref 109) in (bottom), this assumption seems reasonable. We also note that $D_{31k}/D_{110k} \sim (N_{31k}/N_{110k})^{-2.1}$, in reasonable agreement with the expected $D \sim N^{-2.3}$.[327]

Table C.2: Reptation times (τ_{rep}) defined as the square of the chain radius of gyration (R_g) divided by the chain diffusion coefficient (D_{chain}) and considered the time required for a chain to diffuse one characteristic length in the bulk. The chain diffusion coefficient (D_{chain}) is obtained from Figure C.4. These values are used to normalize for chain mobility in Figure 5.7.

dP2VP M_w (kg/mol)	$\tau_{rep} = R_g^2 / D_{chain}$ (s)		
	160˚C	180˚C	200˚C
31	0.78	0.08	0.02
110	39	4.1	0.92

C.5 Efficacy of restricting NP diffusion by increasing matrix M_w

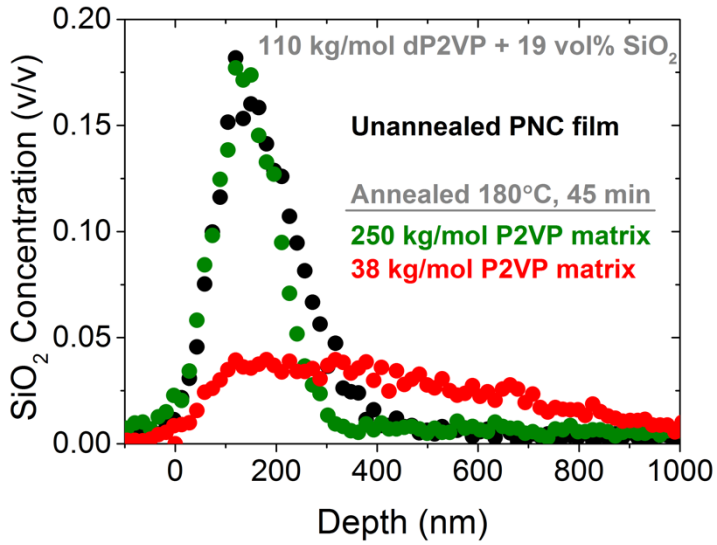

Figure C.5: Effect of matrix molecular weight on NP diffusion. NPs freely diffuse into 38 kg/mol P2VP and NPs remain in the top film when the bottom film is 250 kg/mol. The extracted diffusion coefficient from NPs into 38 kg/mol is in good agreement with Ref 208, suggesting that NPs are diffusing as individual entities in our PNCs samples, even for tracer PNC films with ϕ_{NP} = 19 vol%.

APPENDIX D: SUPPORTING INFORMATION FOR CHAPTER 6

D.1 Description of Materials

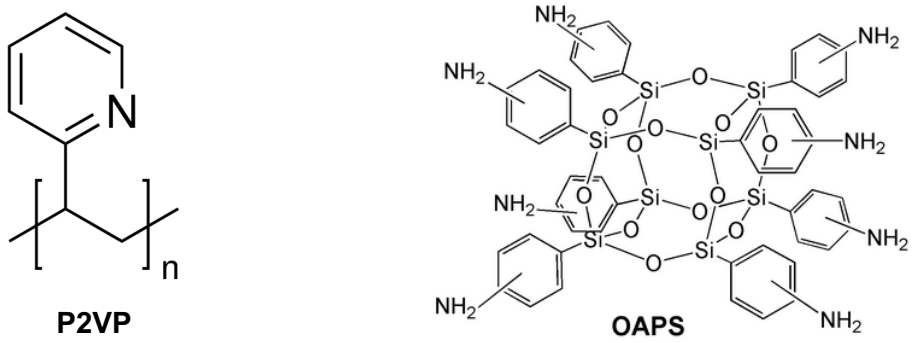

Figure D.1: Chemical structure of poly(2-vinylpyridine) (P2VP, left) and octa(aminophenyl) polyhedral oligomeric silsesquioxane NPs (OAPS, right)

Table D.1: List of measured polymer molecular weight, entanglements per chain (M/M_e), radius of gyration (R_g), and measured viscosity (η) for each polymer studied. Also included is the measured diffusion coefficient of OAPS NPs (D_{OAPS}), their Stokes-Einstein prediction (D_{SE}), and the measured enhancement relative to D_{SE}.

M_w (kg/mol)[a]	M/M_e[b]	R_g (nm)[c]	η (Pa*s)	D_{OAPS} (cm^2/s)	D_{SE} (cm^2/s)	D_{OAPS}/D_{SE}
P2VP						
28,000	1.6	4.6	1.21E4	2.2E-12	2.49E-13	8.8
49,000	2.7	6.1	6.28E4	1.8E-12	4.82E-14	37.4
90,000	5.0	8.2	3.00E5	1.33E-12	1.01E-14	131.9
122,000	6.7	9.6	6.95E5	1.05E-12	4.35E-15	241.2
301,000	16.7	15.0	1.76E7	3.25E-13	1.71E-16	1896.0
379,000	21.1	16.9	5.02E7[d]	3.8E-13	6.03E-17	6302.2
467,000	25.9	18.7	1.02E8[d]	3.3E-13	2.98E-17	11074.3
dP2VP						
99,000	5.5	8.6				

[a]All molecular weights were measured with GPC and polydispersities were < 1.3

[b]Entanglement calculation using M_e = 18 kg/mol

[c]R_g calculated assuming b = 1.8 nm

[d]Extrapolated values assuming $\eta \sim M_w^{-3.4}$

D.2 Glass Transition of P2VP/OAPS PNCs

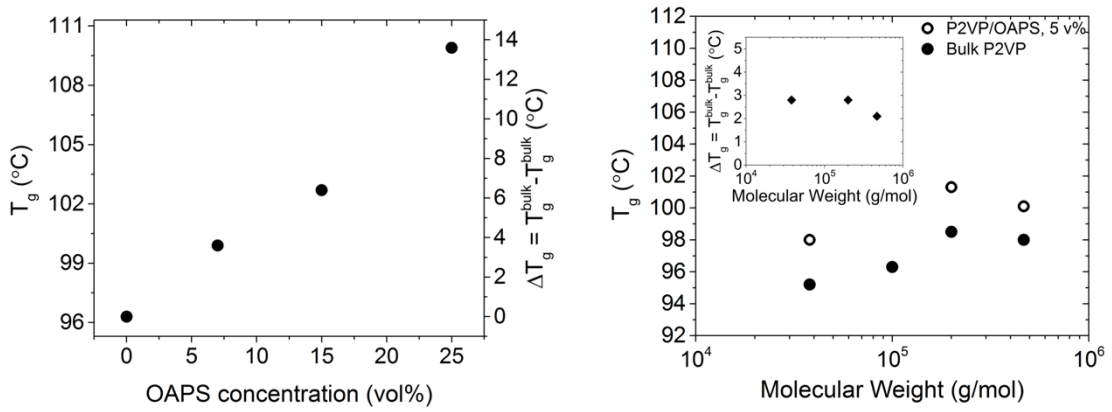

Figure D.2: (left) Calorimetric glass transition temperature (T_g) of P2VP/OAPS as a function of OAPS concentration. With increasing OAPS concentration (ϕ_{OAPS}), T_g increases monotonically as expected from reduced segmental dynamics and observed elsewhere.[108] (b) T_g of bulk P2VP (solid circles) and P2VP/OAPS PNCs at ϕ_{OAPS} = 5 vol% (open circles) as a function of molecular weight. Inset of (right) shows the change in T_g ($\Delta T_g = T_g^{PNC} - T_g^{bulk}$) as a function of molecular weight. Although there is a slight increase in T_g as a function of molecular weight, ΔT_g appears to be mostly independent of molecular weight, within 1°C, between 38 kg/mol and 467 kg/mol.

D.3 Dispersion of OAPS: X-ray Scattering

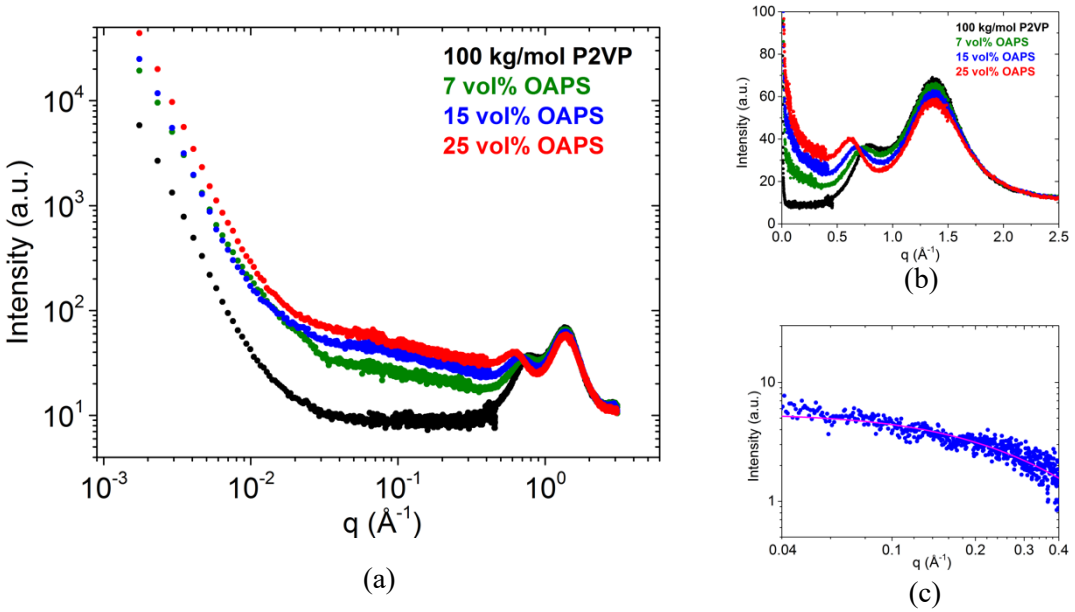

Figure D.3: (a) X-ray scattering characterization of P2VP/OAPS PNCs from 0.0017 $Å^{-1}$ < q < 3 $Å^{-1}$, or 0.2-370 nm. The plateau and lack of features for 0.02 $Å^{-1}$ < q < 0.5 $Å^{-1}$ suggests minimal aggregation and well-dispersed OAPS. We note that the low q upturn (q < 0.02 $Å^{-1}$) is also apparent in bulk P2VP and in the same PNC system and has been attributed to impurities or voids rather than large scale aggregates.[108] (b) Wide-angle X-ray scattering showing P2VP amorphous halo and no additional features in PNCs with OAPS (such as OAPS crystallization peaks), further supporting reasonable OAPS dispersion. (c) Isolation of OAPS scattering obtained by subtracting bulk P2VP from P2VP/OAPS PNC (15 vol%) between the low q upturn and amorphous halo. Line in (c) shows fit to data with fuzzy sphere model with radius of 0.9±0.5 nm, in good agreement with previous measurements and analysis.[108] We also note that P2VP/OAPS PNCs are optically transparent and homogeneous at all NP concentrations studied.

D.4 Dispersion of OAPS: Depth profile of matrix films

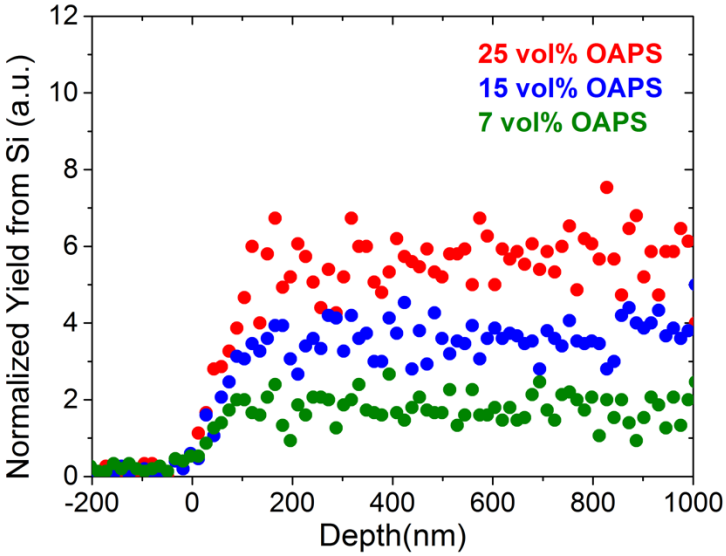

Figure D.4: Depth profile of Si measured with RBS showing uniform OAPS dispersion through the depth of doctor bladed and annealed films with no measurable surface aggregation.

D.5 Dielectric Measurements of P2VP/OAPS Nanocomposites: Role ϕ_{NP}

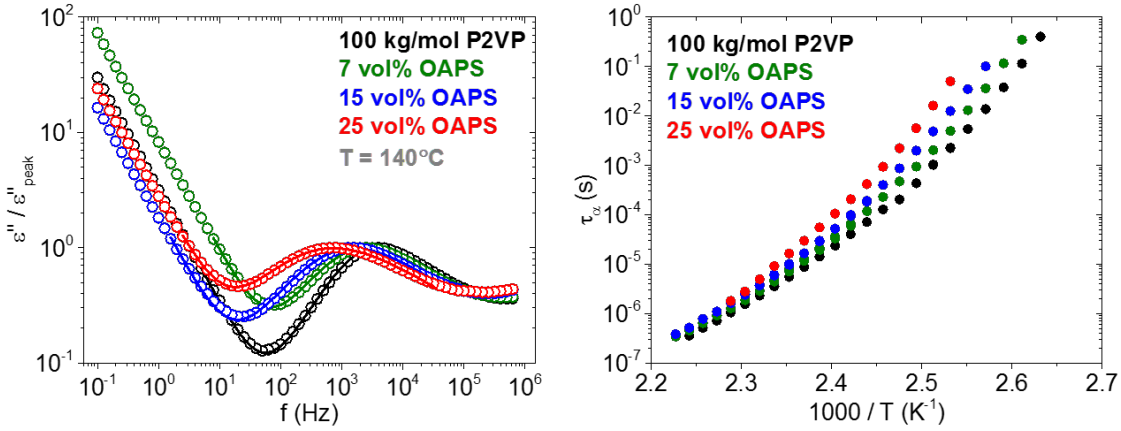

Figure D.5: (left) Dielectric spectra normalized to the maximum associated with α-relaxation at T=140˚C (same temperature as diffusion measurements) as a function of frequency. Symbols are experimental data and lines are fits comprised of a conductivity term and a single Havriliak-Negami function.[57] (right) Extracted segmental relaxation time as a function of inverse temperature for bulk P2VP and P2VP/OAPS PNCs. Dielectric results are in good agreement with literature.[55,108] We note that we expect Stockmeyer type A response of P2VP and that BDS measures rotational relaxation times, which are expected to deviate slightly from translational relaxation times by a factor of 1/2.[57]

D.6 Viscosity Measurements of P2VP and P2VP/OAPS

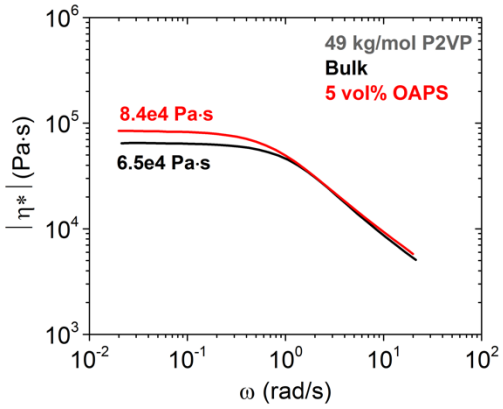

Figure D.6: Complex viscosity of 49 kg/mol bulk P2VP (black) and P2VP with 5 vol% OAPS (red), an approximate OAPS concentration relevant to NP diffusion measurements. Experimental details for measurements can be found in Ref 208.

Oscillatory shear measurements were performed using a Rheometrics Solids Analyzer II in a sandwich fixture under small applied oscillatory strain (amplitude = 1%). Samples were annealed at 190°C for 20 minutes, then cooled to the corresponding measurement temperature. The zero-shear viscosity was extracted from the low frequency imaginary shear modulus for 28 and 49 kg/mol P2VP at 140°C. For 90, 122, and 301 kg/mol P2VP, the zero-shear viscosity can not be obtained from the mechanical spectrum G' and G" measured at 140°C. Measurements of 90 and 122 kg/mol P2VP were performed at 150-190°C in steps of 10°C and measurements of 301 kg/mol P2VP were performed at 180°C and 190°C. In these cases, time-temperature superposition was applied to create master curve rheological spectra using T_{ref} = 140°C, and the zero shear viscosity was determined from these TTS master curves. The viscosity of 376 and 467 kg/mol P2VP was estimated by extrapolating the measured viscosities of the lower molar mass P2VP samples assuming scaling of $M_w^{3.4}$. All viscosities are listed in Table D.1.

D.7 Dielectric measurements of P2VP: Role of molecular weight

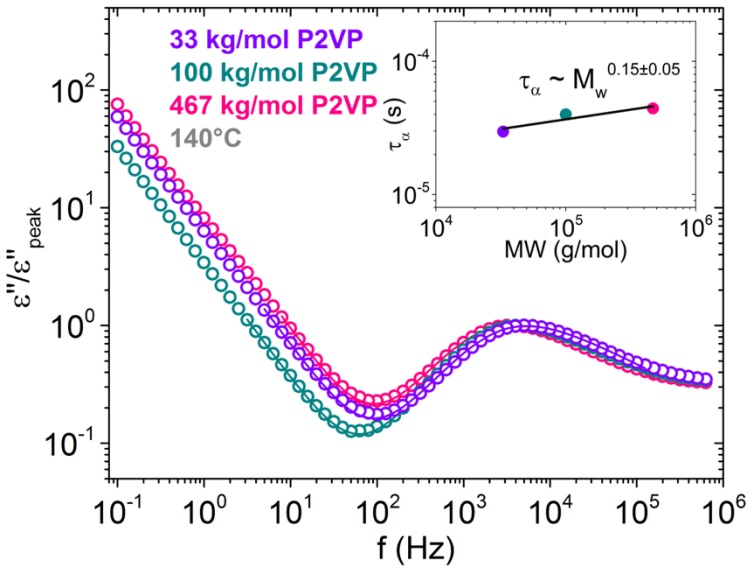

Figure D.7: Dielectric spectra normalized to the maximum associated with α-relaxation at T=140˚C (at the same temperature as diffusion measurements) for representative low, medium, and high molecular weight bulk P2VP. The extracted relaxation time (τ_α) is measured to scale weakly with $\tau_\alpha \sim M_w^{0.15\pm0.05}$, as can be expected due to slight differences in the glass transition temperature (Figure D.2).

D.8 Comparison of polymer diffusion with mobile and immobile NPs

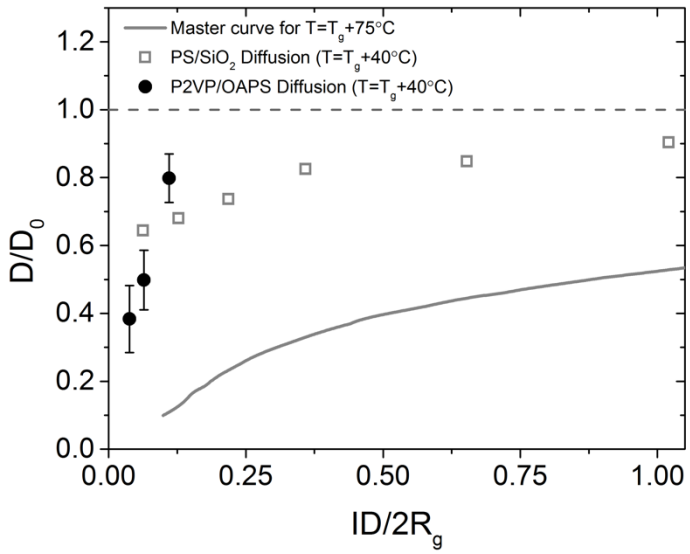

Figure D.8: Comparison of P2VP diffusion in OAPS/P2VP PNCs to the master curve developed from diffusion through immobile NPs at $T=T_g+75^{\circ}C$ (grey line)[272] and measurements of PS diffusion into PS/phenyl-capped SiO_2 at $T=T_g+40^{\circ}C$ (grey squares)[188] plotted as function of the interparticle distance (ID) relative twice the radius of gyration ($2R_g$). ID is determined assuming randomly distributed OAPS NPs (d_{NP}=1.8 nm), given by $ID = d_{NP}[(2/(\pi\phi_{NP}))^{1/3} - 1]$, where ϕ_{NP} is the NP volume fraction.

APPENDIX E: FUNCTIONALIZATION OF NANOPARTICLES

E.1 Introduction

This appendix describes best practices and outlines a method for functionalizing colloidal oxide nanoparticles (NPs). This method has been applied to Nissan silica (SiO_2) NPs, specifically MEK-ST (14 nm in diameter) and MEK-STL (53 nm in diameter), but can likely be used to functionalize other SiO_2 NPs. This method was used to functionalize NPs with For the reactants (or capping agents): phenyldimethyl-methoxysilane (PhDMMS), aminodimethyl-methoxysilane (ADMMS), and most commonly, octyldimethyl-methoxysilane (ODMMS). Other capping agents with similar silane chemistries should work as well. The typical batch size is 9 grams of SiO_2 in 100 mL of solvent. There is no fundamental limitation of batch size but changing the concentration may affect reaction rates. No systematic studies were done to determine the ideal concentration. This appendix begins by defining the necessary materials and equipment, then describes the preparation of glassware and solutions, and then outlines the conditions for running the reaction.

This appendix also describes methods for purifying and characterizing the functionalized NP solutions. After the reaction is run to completion, successive washing with a poor solvent is done to purify the NP solution, change the final solvent, and control the final NP concentration (c_{NP}). Since unreacted silane capping agents and reacted dimers are soluble in hexane but the NPs are not, repeated dilution with hexane followed by centrifuging allows isolation of functionalized NPs. To characterize the efficacy of the reaction, flocculation and thermogravimetric analysis (TGA) are used and described herein. Flocculation measurements fundamentally measure the change in surface energy in solution while TGA fundamentally measures the mass of molecular moieties on the surface on dried NPs.

E.2 Materials and Equipment for Reaction

Necessary equipment:

- A fume hood with access to nitrogen gas and running water
- Hot plate capable of simultaneous heating and stirring
- Oil bath capable of temperatures up to ~100°C and large enough to encompass the reaction vial
- Jack used to raise and lower reaction vial into oil bath
- Clamps and clamp stands
- Centrifuge capable of up to ~5000 rpm and up to 50 mL tubes

Necessary glassware:

- Glass condenser
- Three-neck round bottom flask (reaction vessel)
- Various glass pipettes, beakers, vials, and bottles

Additional accessories:

- Needles (23G), at least three
- Neoprene tubes for flowing nitrogen and other tubes for flowing water
- Metal tube clamps to secure tubes for water
- Rubber stoppers for reaction vial and condenser
- Centrifuge tubes (50 mL)

Materials:

- Anhydrous THF
- Hexane isomers
- SiO_2 NP stock solution
- Pure capping agent solution (stored in dry conditions)

Selection of capping agent:

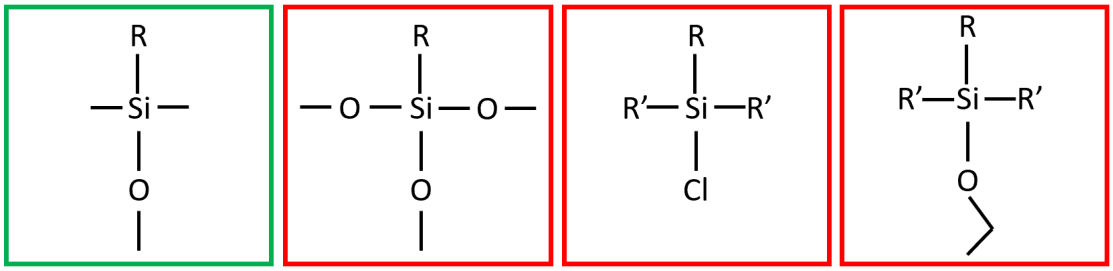

(a) (b) (c) (d)

Figure E.1: The silane on the right (green) is the suggested type for functionalizing silica, as described below.

When choosing a silane molecule for this procedure, there are important points to consider regarding the silane chemistry, as schematically presented in Figure E.1:

- The molecule needs to be soluble in THF, since that is the solvent that hosts the reaction. It also must be soluble in hexane so the solution can be purified after the reaction.
- Capping agents with one oxygen (C-O-C, ester group) (a) is preferred over capping agents with three (b). A single methoxy group limits the side reactions. Trimethoxy-silanes can polymerize with themselves and from oligomeric grafts on the NP surface or in solution rather than single groups. This complicates the NP interface and measurements of functionalization density.
- Methoxy-silanes (a) are preferred over those containing chlorine (c). A byproduct of the reaction with methoxy-silanes is methanol while a byproduct of chloro-silanes is hydrochloric acid. The former is far preferred. Also, the chloro-silane groups are more reactive which may promote undesired side reactions.
- The capping agent should be methoxy- (a) instead of ethoxy-silanes (d). Methoxy silanes are likely more reactive and less affected by steric hindrance.

E.3 Preparation of Materials

E.3.1 Preparing NP solution (for Nissan NPs in MEK)

1. Carefully move the NP stock solution without shaking it as aggregates tend to sediment over time. In a fume hood, draw from the top of the solution and transfer the appropriate amount of stock solution (usually 30mL) into a capped bottle with a stir bar.
2. Slowly add anhydrous THF (dropwise) to the NP solution while stirring. Always add a new solvent to a NP solution and not the other way around to slowly change the dielectric constant of the NP solution. An appropriate drop rate is ~1 drop per second until the NP solution is majority THF and an appropriate spin speed is ~250-400 rpm. A burette may be useful for dropwise adding THF, but be sure to minimize splashing in the beaker.
3. Continue adding anhydrous THF until the solution has an approximate concentration of 90 g/L (mass SiO_2 per volume total solvent) and the batch size is appropriate. For 30 mL Nissan MEK NPs (which comes from the manufacturer at ~300 g/L), 70 mL of THF is appropriate.
4. Allow the solution to stir for several minutes with a slight vortex.
5. Sonicate the solution for ~5 minutes.
6. Consider letting this solution sit overnight to see if the solution is unstable and if NPs sediment to the bottom of the beaker. If this problem persists after sonication, add the THF solution more slowly or dilute partially with MEK before adding THF.

E.3.2 Preparing capping solution

1. The capping agents should be stored in the glove box to minimize exposure to moisture since they can react with water. Before removing them from the glove box, calculate the

amount of capping agent needed for the reaction using the equation in the next subsection. This calculation should be completed before proceeding.

2. With a micropipette, take out the precise amount of capping agent needed and put it into a sealable vial. This amount is usually on the order of 10 μL – 1 mL but depends on the targeting areal density, NP size, and batch size.
3. Dilute the pure capping agent in the vial with at least three times the volume of anhydrous THF. This step helps the solution mix properly with the NP solution when added, helps dilute the reactant molecules, and helps ensure all of the caps are transferred to the reaction.
4. Seal the vial tightly, add parafilm, and put it aside until you are ready to start the reaction. It is best to do this just before you are ready to add it to the NP solution to minimize the time it is out of the glove box.

E.3.3 Determining the amount of capping agent to add

It is important to determine the appropriate amount of capping agent needed for the reaction. We use the amount of reactant added to control the areal density of functionalization on the NP surface. If the reaction is run in excess (targeting much more than 5 caps/nm^2) the resulting NPs can be considered fully functionalized. To produce less dense coverage on the surface, fewer caps can be added to the solution (e.g. targeting < 1 cap/nm^2). However, characterization is necessary to understand the relationship between the target and actual coverage. Unknown reaction rates, unknown side reactions, and steric hindrance, among other factors, lead to uncertainty in predicting the functionalization coverage. In fact, most capping molecules will not bond to the surface. Successful batches show the measured coverage is ~5-20% of the target coverage, but this should not be considered a general rule and it is unclear what primarily dictates this efficiency. Reactions of capping agents with the glassware, moisture in the NP solution, and other capping agents (forming a dimer) all contribute.

Below is the derivation and presentation of how to calculate the necessary amount of pure capping solution to add.

Table E.1: Definition of known variables used to calculate the amount of pure capping agent required for the reaction.

Variable	Definition
d_{NP}	diameter of silica [nm]
c_{NP}	concentration of NP solution in [mg/mL]
V_{soln}	volume of nanoparticle solution in the reaction [mL]
σ_{target}	targeted areal density of caps [caps per nm^2]

Variable	Definition
ρ_{NP}	density of silica [g/mL]
ρ_{cap}	density of the capping agent [g/mL]
MW_{cap}	molecular weight of the capping agent [g/mol]
N_A	Avogadro's number [$6.022*10^{23}$ in molecules/mol]

Table E.2: Definition of unknown variables used to calculate the amount of pure capping agent required for the reaction.

Variable	Definition
SA_{NP}	surface area per NP [nm^2]
SA_{tot}	total NP surface area in solution [nm^2]
N_{NP}	number of NPs in solution

Variable	Definition
V_{NP}	total volume of NPs [mL]
N_{cap}	number of caps needed
V_{cap}	volume of pure capping agent needed [mL]

Calculate the surface area per NP:

$$SA_{NP} = \pi * d_{NP}^2 \qquad \text{(E.1)}$$

Calculate the total volume of NPs in the solution:

$$V_{NP} = \frac{V_{soln} * c_{NP} * 10^{-3}}{\rho_{NP}} \qquad \text{(E.2)}$$

Calculate the total number of capping molecules needed:

$$N_{NP} = \frac{V_{NP} * 6}{\pi * {d_{NP}}^3 * 10^{21}} \qquad \text{(E.3)}$$

Calculate the total surface area of the NPs in the solution:

$$SA_{tot} = N_{NP} * SA_{NP} \qquad \text{(E.4)}$$

Calculate the number of caps needed for target coverage:

$$N_{cap} = SA_{tot} * \sigma_{target} \qquad \text{(E.5)}$$

Calculate the total volume of pure capping agent needed to add to the reaction:

$$V_{cap} = \frac{N_{cap} * MW_{cap}}{\rho_{cap} * N_A} \qquad \text{(E.6)}$$

E.4 Preparation of Glassware

It is important to thoroughly clean the 3-neck round bottom flasks before and after each reaction. The condensers should be rinsed with acetone on the inside.

1. With warm deionized water, wash the flasks in the sink with soap. Use a curved brush to wash every spot. Using DI water, not tap water, is important during cleaning.
2. Triple rinse the flasks with DI water to ensure all soap is removed.
3. Rinse the flask with methanol, toluene, and acetone, in that order. Repeat with particular solvents if it is not fully cleaned, using the solvent you think is best for the residue. Always end by rinsing with acetone because it is most volatile and easier to dry.
4. Let it dry in a glassware oven for about 15 minutes or until completely dry.

5. Pour about 30mL of anhydrous THF into the flask and add a stir bar. This is done to clean the interior of the flasks and condensers with warm THF (simulating the reaction conditions) and to also test the setup for leaks before the reaction starts.
6. Attach the condensers to the middle neck of the flask with green glassware clips and consider using PTFE covers to further secure the junction. Put stoppers on all other necks and the top of the condenser.
7. Set the oil bath temperature to 70°C. Add a stir bar (or paper clip) into the oil bath and stir it to ensure temperature homogeneity. Wait until the temperature has equilibrated.
8. Using a jack, lower the round bottom flask with anhydrous THF into the oil baths and turn on the water through the condenser.
9. Put the nitrogen inlet in one of the round bottom flask necks and route the outlet from the top of the condenser to an oil bubbler. Note this is not how it is depicted in Figure E.2. Each junction should be a needle through a rubber stopper.
10. Turn on the gas. Adjust the rate so that the oil bubbler has about 3 bubbles per second, but adjust as appropriate.
11. After several minutes, but no more than 30 minutes, move the nitrogen inlet from the round bottom flask neck to the top of the condenser. This final configuration is depicted in Figure E.2. This process is done to ensure the environment is entirely nitrogen and the oxygen and moisture are flushed out. Note that if the nitrogen inlet is left in the bottom the vessel, THF vapor may be removed with the N_2 flow, and the solution volume and concentration will change (which is undesirable).
12. Let this run for at least a few hours, preferably overnight, while checking all junctions, temperatures, flow rates, etcetera.

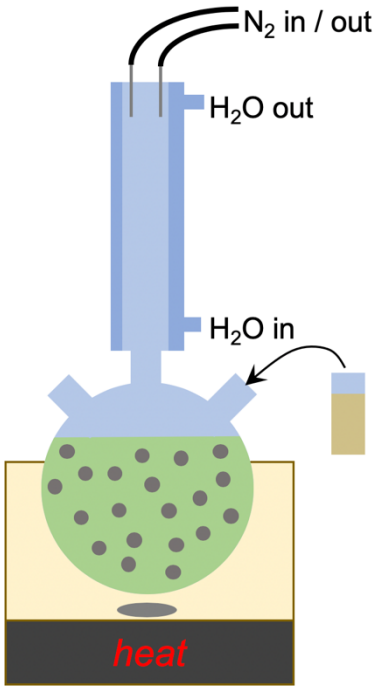

Figure E.2: Schematic representation of reaction setup. Some features are excluded for clarity, including tubing for water inlet and outlet, rubber stoppers on round bottom flask necks, condenser, thermometer, jack, and syringe and needle to add capping agent (mustard colored solution).

E.5 Running the Reaction

The directions for this section assumes the reader is proceeding from Section E.4.

1. Stop the water and nitrogen flow.
2. Detach the flask from the condensers and pour out the THF.
3. Vortex briefly then sonicate the particle solution made in Section E.3 for ~5 min.
4. Transfer the recently sonicated NP solution into the three neck round bottom flask (pour with a glass pipette to avoid spilling) and reattach it to the condenser. It is necessary to parafilm the stoppers if they swell with warm THF.
5. With a marker, mark the solution line on the flasks so evaporation or loss of solution can be monitored.
6. Lower the flasks into the oil baths. The stir speed should be fast enough to see a slight vortex but minimize unnecessary and uncontrolled contact with the flask walls.

7. Turn on the water.
8. Ensure the oil bath remains at 70°C and lower the flask into the oil bath.
9. Fix the N_2 inlet in the round bottom flask neck and outlet at the top of the condenser. Then turn the gas on. This allows the system to be filled with nitrogen faster and more effectively. Let this run for ~15 minutes, but no more than 30 minutes.
10. Move the N_2 inlet back to the tops of the condenser.
11. Now that the NP solution is at 70°C and completely under nitrogen, gather the capping agent made in Section E.3.
12. Attach a needle to a 20mL syringe and transfer the caps from the vial to the syringe. Note that the syringe must be compatible with THF.
13. Aiming for the middle of the solution, puncture the front-most stopper and slowly add the caps to the solution. Try to avoid running the capping agent along the wall of the flask.
14. Parafilm all stoppers on the flasks if they swell with warm THF to prevent loss of solution.
15. After adding the caps, the reaction has officially started so note the time. Close the hood and clearly write down the details of the reaction, materials, timing, and your contact information in the event something happens.
16. Let reaction run for 24 hours. Check on it periodically to make sure that water and nitrogen are still flowing. Also, check to make sure the solution maintains the same volume (i.e. none is evaporating). If the solution is decreasing in volume, either add anhydrous THF to the line marked in step 5 or find and fix the source of loss.
17. When stopping the reaction, use the jack to remove the flasks from the oil baths. Turn off the heat.
18. Once the solutions have reached room temperature, turn off the nitrogen and water.

19. Remove the flasks from the condensers, take off the stoppers and pour the solutions and stir bars into sealable bottles. Parafilm the bottles. They are now ready to purify.

E.6 Purifying the Functionalized NPs

This process is designed to remove 99.9% of the unreacted caps or dimers from solution by crashing particles out with hexane, centrifuging to collect them, and then redistributing them with THF. After successful functionalization, NPs are stable at higher fractions of hexane in THF/hexane mixtures, depending on their cap and density. But eventually, they will flocculate. Therefore, it is important to test the precipitation point beforehand with a small amount of solution so that one can calculate the maximum amount that can be cleaned while using the fewest centrifuge tubes.

There are two main ways to crash with hexane effectively. The first option is to crash the NP solution by adding hexane in a 50 mL centrifuge tube, centrifuging, removing the supernatant, redispersing the NPs, and repeating this process. This is more thoroughly discussed below as it is the preferred method. The second method is more time consuming but can be used to purify larger batches and may be better for NPs with dense functionalization of non-polar moieties. Here, the NP solution is added to a large beaker (~1000 mL or more) and flushed with hexane. This large beaker is then sealed, placed in an ice bath (to further decrease the solvent quality), and left undisturbed for several hours or overnight. Assuming enough hexane was added, the NPs will flocculate to the bottom of the large beaker. The clear supernatant can be carefully removed. By agitating the NPs at the bottom, the NPs in poor solvent can be transferred to centrifuge tubes and centrifuged to more effectively collect all of the NPs. While this option is more time consuming and still requires centrifuging after removing the supernatant from the large beaker, it can be used for larger batches and more non-polar NPs.

Steps for crashing NPs with hexane, centrifuging, and redispersing are presented below.

1. In an 8mL vial, add 0.5mL of capped particle solution and a clean stir bar.
2. Have this solution spin on a stir plate. When the NPs have flocculated, the solution will turn white and be opaque. Make sure that the background of the vial makes it easy to see whether the particles have flocculated.
3. Slowly add hexane, keeping track of how much is added.
4. Stop when the solution turns white and cloudy and calculate the ratio of hexane to NP solution. The following steps should be adjusted accordingly based off that ratio, or a higher ratio of hexane to ensure the NPs crash during purification.
5. By limiting the amount of total solution in a 50 mL centrifuge tube to 40 mL, calculate the amount of NP solution that can be added to the centrifuge tube using the ratio from step 4. For example, if the flocculation point is around 85% hexane, add 5mL (or less) of the capped particle solution to a 50mL centrifuge tube and pour 35mL of hexane into the tube.
6. Pour the proper amount of the NP solution into the centrifuge tube.
7. Pour the proper amount of hexane into the tube. Close the lid tightly, shake well, and vortex to mix the solution thoroughly.
8. Centrifuge for 3 minutes at 3000 rpm. When done, the bottom should have a white pellet and the top should be clear. Centrifuging too aggressively will result in a pellet that is compact and difficult to redisperse. Centrifuging too little will lead to a loose pellet and will result in a loss of NPs when the supernatant is removed. Centrifuging for longer times and at 5000 rpm has also been successful, but these conditions were not thoroughly tested.
9. Remove the top of the solution (the supernatant) in the tube and discard safely.
10. Fill with ~5 mL of THF then shake and vortex the NP solution. After vortexing, sonicate for ~5 min. If the solution isn't clear yet after the pellet has completely broken apart, consider adding more THF (or hexane to dilute the NP concentration further for non-polar NPs) as needed. Note, if more THF is added to redisperse the NPs than was originally

introduced, the NPs may not flocculate in the centrifuge tube after flushing with hexane. If this happens, the contents of the tube will need to be divided into two tubes. As a result, a best practice is to add ~90% of the THF that was originally added to redisperse the NPs. For example, if 5 mL of NP solution was added initially, consider adding 4.5 mL or less of THF to redisperse. Adding some hexane helps to dilute the NP solution and will help break up the pellet.

11. Sonicate the tube for ~5 minutes after the pellet is redispersed.
12. Repeat steps 7-11 at least two more times. Calculate the fraction of nonreacted caps or dimers that were removed by considering the solution volume that was removed and assuming caps/dimers are homogeneously distributed. Continue this process until 99.9% of caps are theoretically removed.
13. Note that after the last iteration, any solvent can be used to break up the pellet and redistribute the NPs. Thus, the final solvent and final concentration can be controlled. Obviously, only solvent that produces a stable solution can be used. A combination of solvents can also be used if that is desired.
14. Finally, store the solutions in closed bottles that are sealed with parafilm.

E.7 Characterization of functionalized NPs

E.7.1 Flocculation method

When functionalizing SiO_2 NPs with different moieties the NP surface energy will change. This can be directly observed by systematically documenting the flocculation point as hexane is added to the NP solution. This can be done by adding 1 mL of a predetermined concentration of NPs in a good solvent (suggested $c_{NP} \sim 40$ g/L) to two different vials. Then, in one vial add hexane

and in the other add the same good solvent. Add the solvents in small increments (less than 0.5 mL is suggested) while recording the total amount added. When the NPs crash out of the solution that has been diluted with hexane, the solution will turn white and opaque, especially relative to the solution diluted with the good solvent which should not change colors appreciably. Thus, the flocculation point can be determined from the difference in color and clarity between the two NP solutions. Figure E.3 demonstrates this experiment with MEK-STL in MEK by comparing unmodified NPs and octyl-functionalized NPs at the flocculation point of the unmodified NPs (1:1.5, MEK:hexane) and octyl-functionalized NPs (1:3, MEK:hexane).

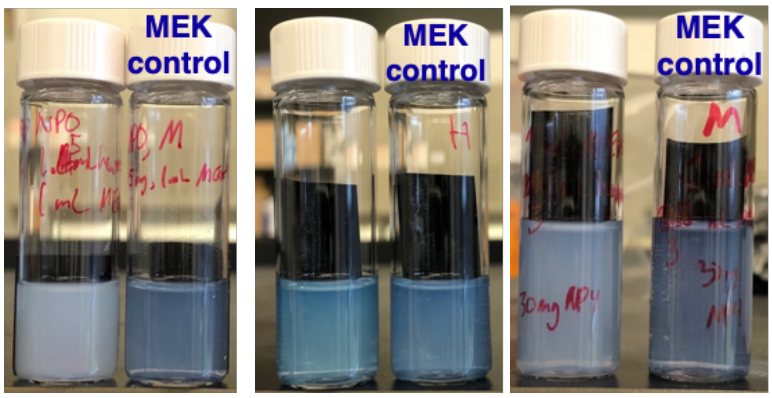

Figure E.3: (left) Unmodified MEK-STL NPs in MEK:hexane (1:1.5) and only MEK (MEK control). The NPs flocculate in the MEK:hexane solution. (center) Octyl-modified MEK-STL in MEK:hexane (1:1.5) and only MEK (MEK control). Both NP solutions remain stable indicating a change in the surface energy relative to the unmodified NPs. (right) Octyl-modified MEK-STL in MEK:hexane (1:3) and only MEK (MEK control). NPs in the MEK:hexane solution have flocculated, thus defining the flocculation point.

While it is difficult to determine the exact capping density from this method, this is a simple experiment that can be conducted rapidly in any laboratory after a reaction to confirm that it was successful. It is possible to more quantitatively conduct the experiment or analyze the results, but that is beyond the scope of this appendix.

E.7.2 TGA method

TGA is used to quantitatively analyze the degree of functionalization of the SiO_2 nanoparticles after a reaction. The observed weight loss in a TGA experiment of dried NP powder is due to adsorbed water, the capping agent or surface hydroxyls, and impurities leaving the surfaces of the nanoparticles. Note that the commercial Nissan NPs likely have covalently bonded molecules or adsorbed surfactants on the NP surface, but this information is proprietary. Separating the contributions and masses is challenging but if it is done correctly, TGA provides a quantitative number of caps on the NP surface.

E.7.2.1 Preparing the TGA sample:

1. Record the mass of an empty aluminum weighing dish.
2. With a micropipette, add the purified NP solution product to the dish. Add enough solution to have at least 60 mg of dried NPs. If the product concentration is unknown, deposit ~3 mL and use this step to measure the concentration.
3. Carefully bring the dish with solution to the hood and place it on a hot plate.
4. Heat the solution and dish to the boiling point of the solvent and wait well beyond the time it takes the the solvent to be visually evaporated.
5. Careful move the dish with dried NPs to a vacuum oven. Heat the oven to the same temperature as the hot plate and pull vacuum for ~ 1 hour. This will ensure most adsorbed water and remaining solvent is removed.
6. Record the mass of the boat and dried nanoparticles and confirm there are ~60 mg or more. This is an appropriate amount for a single TGA measurement of dried NPs.
7. Proceed to the TGA measurement. See below for suggested TGA thermal treatment. It is important to use platinum pans, not aluminum, because this experiment requires temperatures up to 900°C.

E.7.2.2 TGA heating procedure

1. Set breathing air (not argon or nitrogen) flow rate to 100 ml/min. This allows the carbon to convert to CO_2 and maximizes the signal in the measurement.
2. Ramp 10°C/min to 180°C. This thermal treatment ensures the adsorbed water and solvent is removed.
3. Isothermal for 20.00 min. This dwell time allows the measurement to stabilize and ensures adsorbed substances are removed. If the mass changes appreciably in this regime, repeat

the measurement on a new sample with a longer wait, at a higher temperature, or reconsider the drying procedure.

4. Ramp 10°C/min to at least 900°C. This thermal treatment is the one that removes the caps and measures the change in mass that will be analyzed. The heating rate is not critical to the measurement.
5. Isothermal for 15 min. This ensures the sample is no longer changing at the end of the run.
6. Air Cool. This step more rapidly cools the furnace.

E.7.2.3 Analysis of TGA

Here, analysis of TGA is briefly discussed. It is important to avoid analysis of weight loss from (i) adsorbed water or solvent, (ii) molecules on the unmodified NP surface from the manufacturer, and (iii) the loss of surface hydroxyls. The thermal treatment described above removes the contribution of adsorbed water and solvent if the initial mass of the sample is taken after the isothermal anneal 180°C. There are several ways to treat the impurities and hydroxyls in both the modified and unmodified NPs. TGA fundamentally measures the loss in mass, so a comparison between the modified to unmodified samples will highlight only the effect of the modification procedure. In other words, the manufacturer impurities and surface hydroxyls will be present in both samples, so the functionalization amount can be directly observed by normalizing by the unmodified sample. Thus, TGA is analyzed with the following equation and concept. We assume the difference in weight observed in TGA between unmodified and modified is equal to the difference in weight between the modification agent and the hydroxyl group that it replaces multiplied by the number of caps replaced:

$$W_{unmodified} - W_{modified} = N \times \Delta w \qquad \text{(E.6)}$$

where $W_{unmodified} - W_{modified}$ is the difference in the intrinsic remaining weight (i.e. weight normalized by the surface area) obtained directly from TGA measurements. Δw is the difference in weight between a hydroxyl, which is present on the unmodified SiO_2 surface, and the cap, which is present on the modified SiO_2. All of these variables are known, so the only unknown is N, the number of caps (normalized to the surface area). It is important to correct for units and properly calculate W_i normalized to the NP surface area and Δw for each moiety.

APPENDIX F: X-RAY PHOTON CORRELATION SPECTROSCOPY MEASUREMSNTS OF NANOPARTICLE DYNAMICS IN ENTANGLED POLYMER MELTS

F.1 Introduction

The diffusion of nanoparticles (NPs) in polymer melts is relevant to designing functional properties in polymer nanocomposites (PNCs) and dynamics in other complex media such as biological tissue and cells.[26,30,252] Despite various experimental research efforts using different NPs, polymer, and measurement conditions, much remains unknown.[109,208,221,236,246] However, many experimental measurements qualitatively agree with theoretical predictions for non-attractive[38,211–213,216] and attractive NPs[214] in polymer melts. Unlike most measurements of NP dynamics in a polymer melt, X-ray photon correlation spectroscopy (XPCS) consistently measures non-diffusive dynamics.[159,253,255,256,258,262] However, the origin of these motions remain unknown. Anomalous dynamics have been observed in PNCs with aggregated and dispersed NPs, grafted and bare NPs, and various PNC materials, preparation routines, and experimental conditions.

It is important to directly compare XPCS to other measurements using the same PNC system to fully understand the origin of non-diffusive motions observed in XPCS. This section describes measurements of XPCS that are directly comparable to measurements from Rutherford backscattering spectrometry.[208] The goal of this section is to present the preliminary results and highlight important findings, both of which will contribute to our understanding of XPCS and NP diffusion in polymer melts and guide future research efforts.

F.2 Materials and Methods

PNCs were fabricated with traditional drop casting techniques from methanol. All PNCs used in this study are composed of 0.5 vol% silica (SiO_2) dispersed in poly(2-vinylpyridine) (P2VP). P2VP/SiO_2/MeOH solutions were deposited in a Teflon dish (T = 130°C) and dried for ~10 minutes in the fume hood. Samples were then annealed at T=180°C under vacuum for ~6 hours. Note that the glass transition temperature of P2VP is ~100°C. Three different NPs were measured, including Nissan MEK-ST (12-nm diameter), Ludox AS40 (28-nm diameter), and Nissan MEK-STL (50-nm diameter). Ludox AS40 NPs are monodisperse but Nissan NPs are more polydisperse (PDI~ 1.35).[272] Most measurements were conducted with Ludox AS40.

Measurements were attempted in two sample holders: PNCs infiltrated into steel holders and PNCs sealed in fluid cells (Figure F.1). The steel plates with infiltrated polymer did not properly contain the polymer melts at $T>T_g$, even with Kapton tape. Polymer flowed out of the pores and fell with gravity and this behavior was apparent in the XPCS results which showed anisotropic dynamics after an azimuthal angle dependent analysis. Upon switching to the fluid cell (also called the gel and solution holder), more consistent and expected results were attained. The fluid cell has a steel casing fixed to the heating element with Kapton windows and O-rings forming a vacuum seal. All results presented here were collected in the fluid cell.

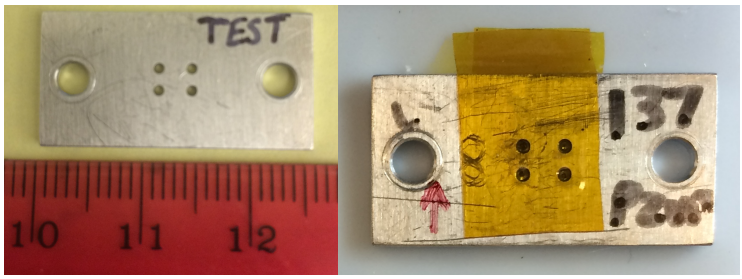

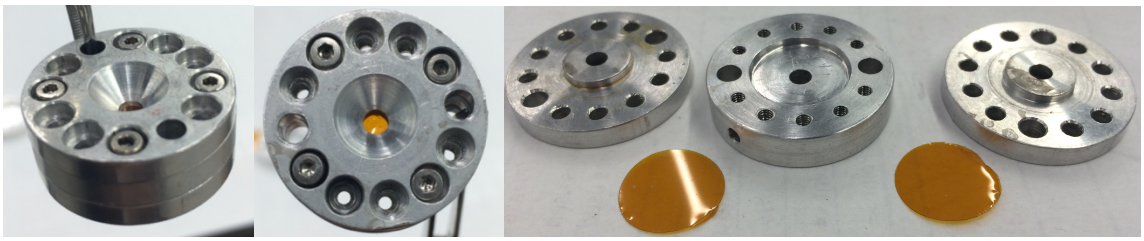

Figure F.1: (top) Steel plate sample holders used for XPCS measurements of solid samples which did not work for polymer melts. (bottom) Fluid cell with Kapton windows and O-rings (not shown) that successfully encapsulate polymer melts during XPCS measurements. The fluid cell was used for these XPCS measurements.

X-ray photon correlation spectroscopy (XPCS) uses coherent X-ray synchrotron radiation to measure dynamics in inhomogeneous samples by analyzing correlations between sequential 2D SAXS patterns.[268] A time-averaged autocorrelation is calculated for each pixel on the detector and binned radially to generate intensity time-autocorrelation functions, which are related to the intermediate scattering function of the scattering species, for several q. Each autocorrelation can be fit with a stretched exponential function to extract the relaxation time. The q-dependence of relaxation times (which often follows $\tau \sim q^{-a}$) reveals the time scale and geometry of the dynamics (e.g. a=2 for purely diffusive motion and a<2 for hyperdiffusive motion). XPCS measurements were conducted at the Advanced Photon Source at Argonne National Lab on beam line 8-ID-I. This beam line offers a q-range of 0.0024 $Å^{-1}$ – 0.07 $Å^{-1}$ (or 9 nm – 250 nm in real space), a dynamic range of 500 μs to ~10^3 s, and in situ temperature control up to ~210˚C. Most measurements were conducted at 180˚C, unless otherwise specified. Auto-correlation functions, g2, or normalized autocorrelation functions, g1, can be fit with a stretched exponential to reveal the timescale associated with NP relaxations.

F.3 Results and Discussion

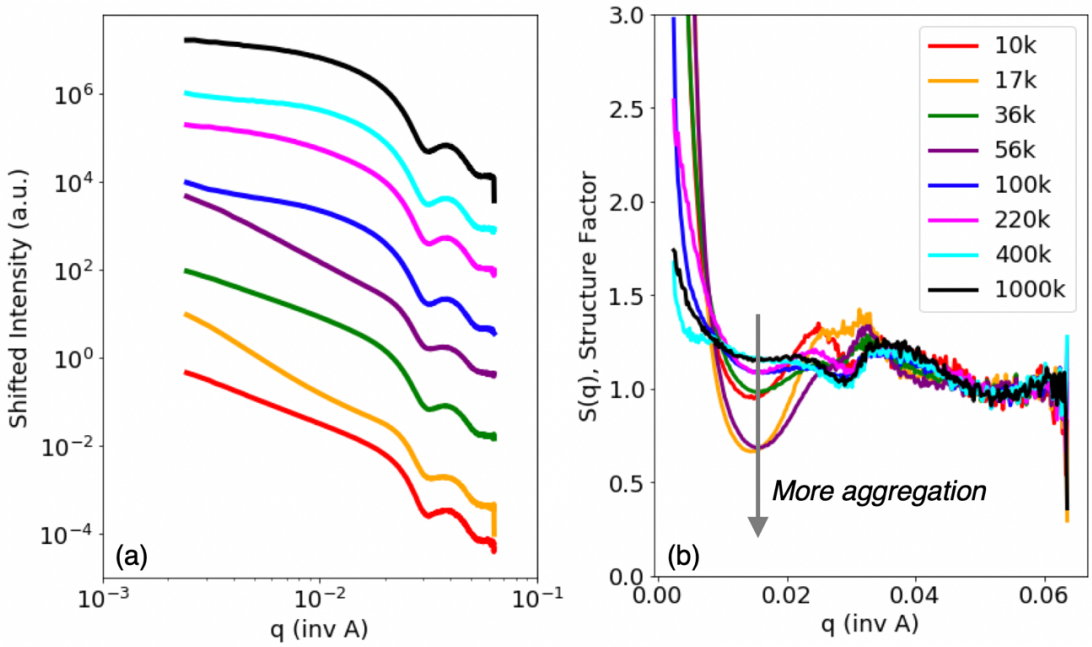

Figure F.2: (a) Small angle X-ray scattering patterns for PNC samples with 28 nm SiO_2 (0.5 vol%) and P2VP molecular weights of 10 (red), 17 (orange), 36 (green), 56 (purple), 100 (blue), 220 (magenta), 400 (cyan), and 1000 (black) kg/mol. (b) Structure factor of all PNCs obtained from samples in (a) after dividing by the form factor of the NPs measured in solution.

We first use the time-averaged small angle X-ray scattering patterns to probe the dispersion of the NPs in the polymer melt. Most PNCs exhibit good NP dispersion in the melt, with the exception of 17 and 56 kg/mol P2VP which appear to be aggregated (Figure F.2). For dispersed PNCs, Figure F.2a exhibits a plateau at low q and Figure F.2b shows a mostly featureless structure factor. P2VP/SiO_2 PNCs are known to exhibit good NP dispersion. For aggregated PNCs, Figure F.2a exhibits increasing signal at decreasing q and a deep correlation well at ~0.15 $Å^{-1}$. Because the 17 and 56 kg/mol P2VP samples are aggregated, they will be excluded from subsequent analysis.

NP dynamics were probed by conducting XPCS at $T>T_g$. Interestingly, samples required hours of in-situ annealing to replicate measurements more than one hour apart. As shown in Figure F.3, the normalized correlation function, g1, which is related to the intermediate scattering function,

changes for in-situ annealing of up to ~6 hours and NP dynamics get slower as annealing time is increased. Importantly, the SAXS profiles overlap during these measurements indicating the ensemble-averaged structure does not change even though the dynamics do. Also, the in-situ annealing did not seem to depend on the thermal history of the sample ex-situ and the amount of time required to anneal each sample varied.

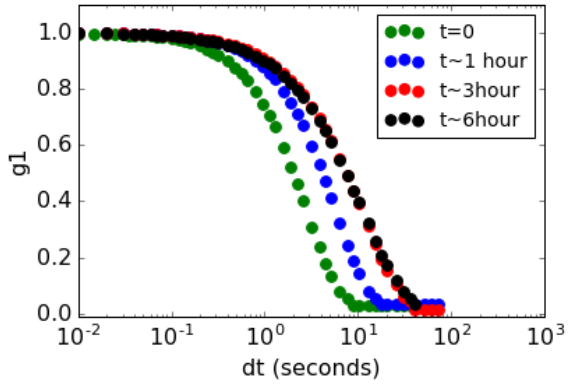

Figure F.3: Normalized autocorrelation function, g1, as a function of time a representative PNC at q = 0.15 $Å^{-1}$ for different amounts of in situ annealing.

The general measurement protocol was to monitor the NP dynamics as a function of annealing time at T = 180˚C until the dynamics remained constant. Figure F.4a presents the raw correlation function (g2) obtained from all dispersed samples PNC samples presented in Figure F.2. As the M_w of the P2VP is increased, the decorrelation is delayed to longer times, indicating slower NP motion. This slower motion in higher molecular weight P2VP is expected because for large NPs ($d_{NP} > d_{tube}$), NP motions is expected to be coupled to the polymer viscosity, where $\eta \sim M_w^{3.4}$.[208,216]

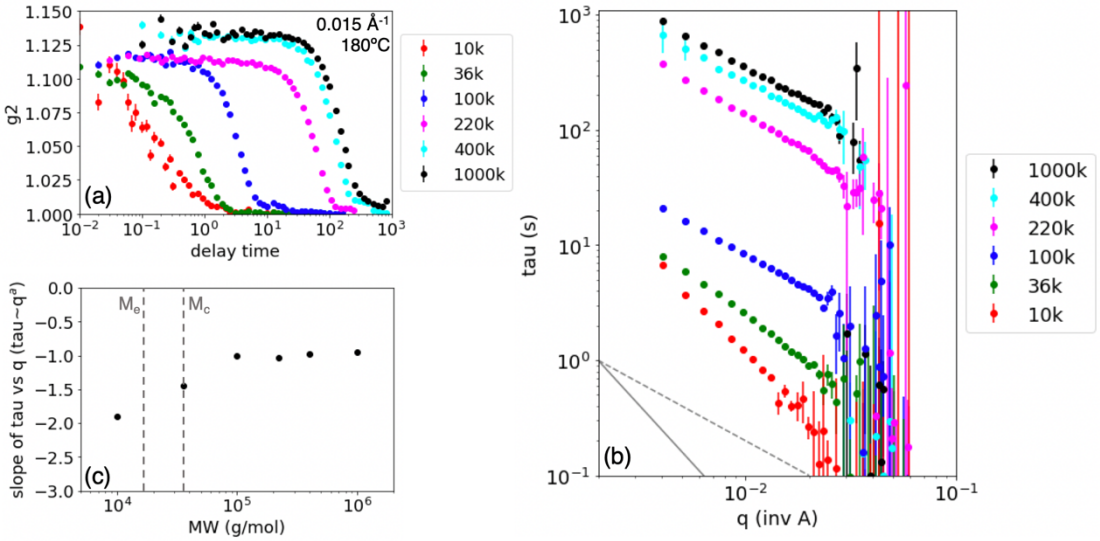

Figure F.4: (a) Raw correlation function, g2, as a function of time for q = 0.15 $Å^{-1}$ and T = 180ºC for 28-nm SiO_2 in P2VP of different M_w. (b) Extracted relaxation times, τ, for data presented in (a) as a function of q. Grey solid lines show diffusive motions ($\tau \sim q^{-2}$) and grey dashed lines show superdiffusive motions ($\tau \sim q^{-1}$).

Autocorrelation functions, such as the representative ones presented in Figure F.4a, are fit with a stretched exponential function. The stretching parameter, β, was found to be mostly q-independent but varied from sample to sample with values between 1 and 2. A value of 1 was commonly observed with diffusive motion and β>1 was generally observed with superdiffusion. The extracted relaxation time, τ, is plotted as a function of q in Figure F.4b. NP motion is slower in larger M_w polymer for all q. Furthermore, NP motion in lower M_w P2VP appears to have a stronger q-dependence. Figure F.4c highlights the slope of $\tau \sim q^a$ as a function of molecular weight to show this effect more clearly. For M_w greater than the critical molecular weight (M_c), hyperdiffusive motions are observed and $\tau \sim q^{-1}$, akin to a velocity. For the lowest molecular weight, unentangled 10 kg/mol P2VP, NP motion appears to follow Fickian diffusion ($\tau \sim q^{-2}$). This result, that NP motion in entangled polymer melts is apparently hyperdiffusive, was also observed using XPCS on measurements of grafted 10-nm SiO_2 NPs in PMMA.[159] Our similar observation in a

different PNC system with larger and bare NPs indicates that this is not specific to the material system. Measurements of similar SiO_2 NPs in P2VP using RBS[208] were restricted to $M_w > M_c$ and observed Fickian diffusion, in stark contrast to these XPCS measurements.

It is important to note that the relaxations times at any q (or equivalently the apparent velocity) in Figure F.4b do not scale strongly with M_w for $M_w > M_c$. PNCs with 220 kg/mol P2VP and 1000 kg/mol P2VP exhibit relaxation times that differ by, at most, a factor of 3 at each q. However, η differs by more than two orders of magnitude. This observation suggests that the observed NP motion is not correlated to polymer viscosity or the diffusion of the NPs. We note that the NP motion in 1000 kg/mol is expected to be beyond the XPCS experimental window and full decorrelation in Figure F.4a was not expected. However, measurements of the same sample at $T<T_g$, where NP motion is restricted, did produce an auto-correlation function that remained constant for 10^3 seconds. This suggests that XPCS is sampling some aspect of the active dynamics in these PNCs.

We next begin to interrogate the origin of the hyperdiffusive behavior by measuring XPCS at different measurement conditions and in different PNCs. We observed the same q-dependence in all data sets as a function of temperature, for T_g+50˚C - T_g+100˚C. Faster motion is consistently observed at higher temperatures. Lower temperatures are inaccessible because NP motion is too slow and higher temperatures approach the limit of the fluid cell. We find temperature has no impact on the q-dependence of the dynamics. The same is true for count rate, primary beam attenuation, and duration of sampling, among other beamline parameters. We also tested the role of NP concentration (ϕ_{NP}) and NP size. Figure F.5a shows the SAXS signal in the raw data increases with ϕ_{NP} and that PNCs with NP concentrations between 0.1 and 1 vol% exhibit good NP dispersion. Similarly, all PNCs in Figure F.5b, with NP diameters of 12 nm (ST), 28 nm (AS40), and 50 nm (STL), exhibit good NP dispersion. However, for 50 nm STL NPs, a clear plateau at

low q is beyond the experimental q-range, partially a result of the high polydispersity of these NPs which can be observed in Figure F.5b.

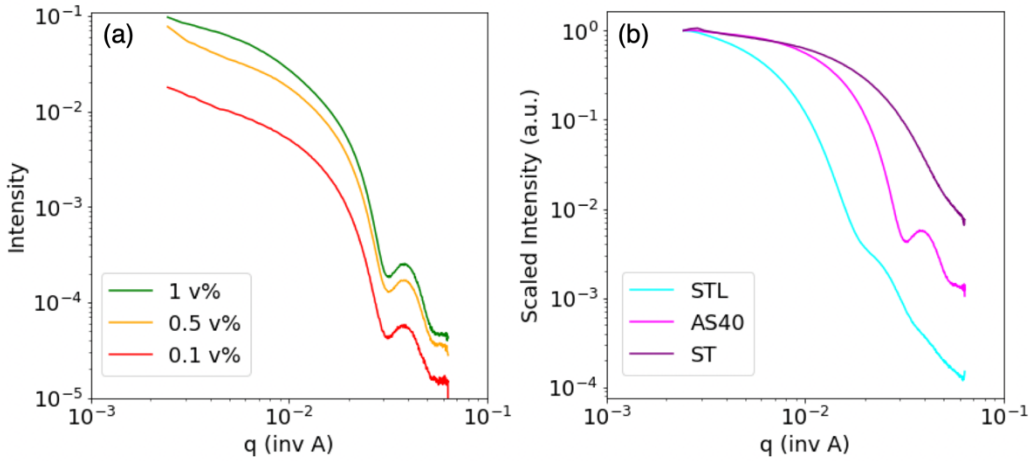

Figure F.5: Small angle X-ray scattering patterns for PNCs with different NP concentration (a) and different NP size (b). All PNCs are composed with 100 kg/mol P2VP. PNCs in (a) are made with 28-nm AS40 NPs. PNCs in (b) have 0.5 vol% SiO_2 and have NPs with diameters of 12 nm (ST), 28 nm (AS40), and 50 nm (STL).

Some speculate that the apparently hyperdiffusive motions observed in XPCS are a result of NP-NP correlations, but the details of this hypothesis are currently underdeveloped. If NP-NP correlations contribute to the hyperdiffusion, changes in NP concentration may result in changes in the q-dependence to the relaxation process. Figure F.6a shows the extracted relaxation times of PNCs comprised of 28 nm SiO_2 in 100 kg/mol P2VP for 180˚C with NP concentrations of 0.1, 0.5, and 1 vol%. While these PNCs are all in the dilute limit, their center-to-center NP distances assuming a random dispersion are 240, 140, and 110 nm. Notably, all of these length-scales are within the q-range of XPCS which highlights a paradox. Very low NP concentrations ($\phi_{NP} << 0.1$ vol%) are ideal to minimize NP-NP interactions and correlations, but measurements at those NP concentrations suffer from weak signal and are therefore difficult. This effect is even more important to consider for smaller NPs, which are scientifically more interesting.[216]

As shown in Figure F.6a, the q-dependence of the relaxation time is unchanged for different ϕ_{NP} as all NPs exhibit hyperdiffusive motions. In addition, while the 0.5 and 1 vol% samples overlay temporally, the motion observed at 0.1 vol% is measurably slower. If this is a true tracer experiment in the dilute limit, the resulting NP dynamics should be independent of NP concentration but that is not what is observed. Additionally, NP-NP correlations should be strongest and most prominent in the highest NP concentration (1 vol%), but this system exhibits essentially no difference from the 0.5 vol% sample. More measurements on duplicate samples and other NP concentrations are needed to understand the apparent role of NP concentration.

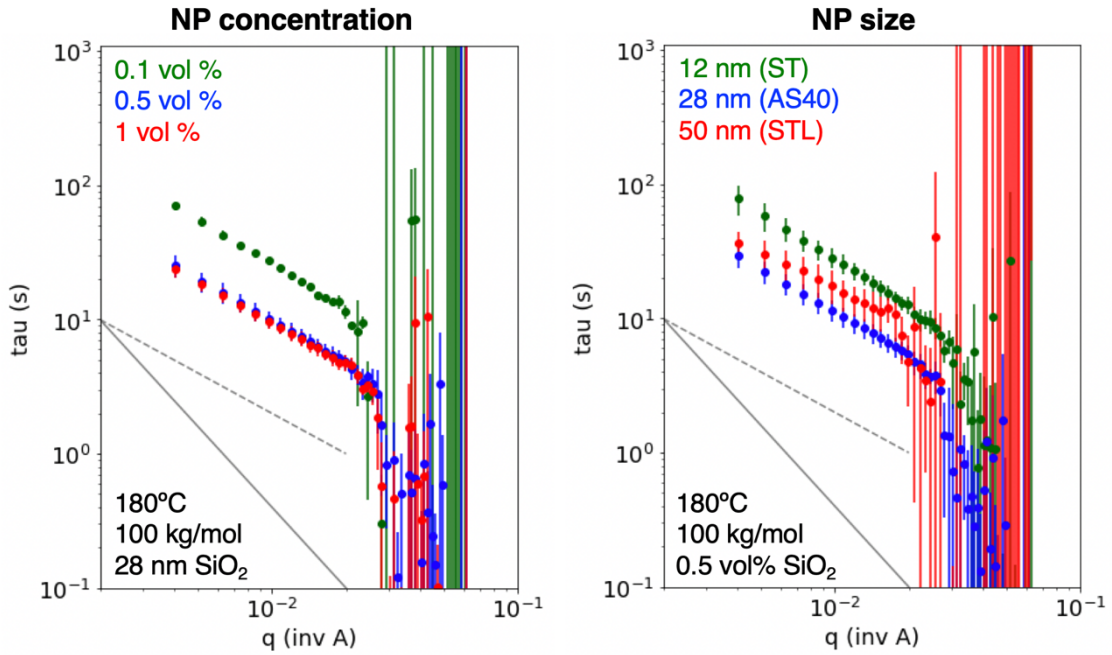

Figure F.6: Extracted relaxation times as a function of q showing PNCs with different NP concentrations (a) and different NP sizes (b). All PNCs have 100 kg/mol P2VP and were measured at 180˚C. PNCs in (a) all have 28 nm SiO_2 and all PNCs in (b) have ϕ_{NP} = 0.5 vol%.

Figure F.6b presents the XPCS results for PNCs with different NP sizes. All NP sizes produce hyperdiffusive motion and the timescale is slowest for the smallest NPs (12 nm). This result is unexpected because the motion of smaller NPs in polymer melts is known to be faster.

Unexpected differences in NP size have reported in XPCS measurements of PEO/Au PNCs as well.[131] It is important to note that while ϕ_{NP} was held constant in these measurements, the volumetric number density of NPs and the center-to-center distance changes.

The results presented in Figure F.6 are somewhat surprising. Regarding the timescale of the dynamics, it is unclear if the measured dynamics are significantly different from each other. We expect these measurements to be independent of ϕ_{NP} (Figure F.6a) but depend systematically on d_{NP} (Figure F.6b). We suspect the observations are a result of poor sample/experiment reproducibility and uncertainty or possibly the unclear nature of how XPCS samples these NP dynamics. Regarding the former, the annealing phenomena presented in Figure F.3 could not be systematically studied for different ϕ_{NP} or d_{NP} due to time, but the data presented in Figure F.6 are after the measured dynamics appeared to stop changing appreciably with in-situ annealing. A thorough study of XPCS using duplicate samples would help understand the uncertainty in the experiment and sample-to-sample variation.

The q-dependence presented in Figure F.6 is noteworthy. We showed that superdiffusion ($\tau \sim q^{-1}$) was observed for $M_w > M_c$ and regardless of beamline parameters (not shown) or PNCs parameters such as ϕ_{NP} and d_{NP} (Figure F.6), the superdiffusive behavior remained. This suggests that M_w may be the primary factor that produces these anomalous dynamics, but more work is necessary to fully understand the origin.

F.4 Conclusion

In these X-ray photon correlation spectroscopy measurements, we studied the motion of SiO_2 NPs in polymer melts of different molecular weight. Like other experimental works[159,253,255,256,258,262], we observe anomalous diffusion in PNCs with NPs dispersed in entangled polymer melts. While we observe diffusive motions in unentangled polymer melts, we observe superdiffusive NP relaxations in PNCs with $M_w > M_c$. We also observe that the NP motion is slower

in larger M_w polymer, but it does not scale with the polymer viscosity. We find that $\tau \sim q^{-1}$ in PNCs composed of entangled 100 kg/mol P2VP at all temperatures measured and regardless of beamline parameters such as sampling rate, measurement duration, primary beam attenuation, etc. We also find superdiffusive motion of NPs in 100 kg/mol P2VP at various NP concentrations (0.1 vol% - 1 vol%) and three NP sizes (12, 28, and 50 nm diameter). These results suggest that the origin of the superdiffusive signatures is dominated by molecular weight and the presence of entanglements, as opposed to beamline or PNC details.

F.5 Future Work

Before fully understanding the results presented in this section, two important details must be understood. First, it is critical to probe systematically the various uncertainties in these measurements. Unfortunately, the allotted beamtime was insufficient to fully study uncertainties and sources of error. The reproducibility of these measurements is in question because of the unexpected requirement for in situ annealing and the unexpected results presented in Figure F.6.

The second critical detail to interrogate and consider is beam damage on the sample, as some have mentioned.[270,271] The anomalous motion presented may be a result of localized polymer degradation, but this doesn't fully explain the apparent molecular weight dependence observed in Figure F.4c. Furthermore, our measurements are independent of radiation time, don't exhibit changes in the scattering intensity throughout the measurements, and are independent of the amount of beam attenuation. Addressing the problem of degradation is challenging because XPCS requires high brilliance X-ray radiation for prolonged periods of time. Nevertheless, the PNC system can be reconsidered, and the beamline parameters can be studied more broadly. However, a study to test beam damage requires a metric that can be used to identify it, which is presently unclear.

Finally, future XPCS measurements in the melt need to be done in conjunction with another technique, such as Rutherford backscattering spectrometry, single particle tracking, or dynamic

light scattering. It is important to select a material system that is ideal for both measurements, that the NPs are well-dispersed in the polymer matrix, and entangled polymer is available. If possible, using the same PNCs and preparation would be ideal, unlike the comparison of RBS and XPCS which require thin films and bulk samples (respectively). Regardless of the technique, this comparison remains challenging because the spatial and temporal window of XPCS is unique. Nevertheless, systematic measurements on the same PNCs will be insightful even if they're spatially or dynamically discontinuous.

APPENDIX G: SMALL-ANGLE NEUTRON SCATTERING MEASUREMENTS OF BOUND POLYMER LAYER IN NANOPARTICLE-POLYMER SOLUTIONS

G.1 Introduction

This section documents preliminary measurements of small-angle neutron scattering (SANS) to study polymer adsorption to nanoparticles (NPs) in solution. Polymer-nanoparticle solutions have academic and industrial relevance for polymer nanocomposite fabrication, colloidal suspensions more generally, and a variety of biological systems. For systems with strong NP-polymer attraction, polymer is known to adsorb to the NP in solution and this bound polymer layer can promote NP dispersion in the melt by sterically preventing NPs from aggregating.[208,210,292,314] However, the concept of polymer adsorption in solution involves consideration of several energetics including the six paired component enthalpic interactions (polymer-NP, polymer-solvent, solvent-NP, and three self-interactions), the conformational entropy of the chain, and the entropy associated with each species. In addition, the properties of bound polymer in solution remain largely unexplored experimentally, especially as a function of the various parameters these multicomponent systems offer.

SANS is an ideal measurement technique to study the bound polymer layer in solution. By contrast matching the solvent to the NPs using a mixture of protonated and deuterated solvent, the scattering pattern from SANS is governed by only the polymer in the sample. If the same sample is then measured in small angle X-ray scattering (SAXS), the scattering pattern is governed by only the NPs. These complimentary measurements present the opportunity to document and correlate the spatial organization of NPs and polymer in these systems. In addition, as discussed in Chapter

7.2, SANS is well-suited to probe the structure and dynamics of bound polymer using protonated and deuterated polymer to differentiate chains in the same sample.

This section describes preliminary measurements with the goal of providing insights for future SANS measurements of NP-polymer solutions. It includes a demonstration of contrast matching experiments, measurements of each individual component, and measurements as a function of polymer concentration and molecular weight. Using these data sets, we outline some initial findings that may guide future research efforts and direct the beginning of similar measurements in the future.

G.2 Materials and Methods

The experiments presented in this section use Ludox AS40 silica (SiO_2) NPs which are ~28 nm in diameter and are monodispersed (PDI ~ 1.1). These NPs are purchased in water (H_2O) and transferred to DMF or MeOH. To transfer to DMF, the stock NP solution was diluted with DMF and distilled at ~130˚C. This process was repeated until the H_2O content as measured by Karl Fisher titration was <0.1 wt%. To transfer to MeOH, the stock NP solution was diluted with MeOH. Dialysis was then conducted against a bath of MeOH and the water content in the bath was monitored with KF titration until the solution homogenized. The resulting water content was <0.5 wt%. The concentrations of SiO_2 in DMF and MeOH solutions were fixed at 40 g/L and all solutions were filtered with a 0.2 μm PTFE syringe filter.

To control the scattering length density of the solutions, deuterated solvents were often added to the NP solutions. In these cases, the deuterated solvent was added, dropwise, to the NP solution while stirring. After the addition of solvent, the NP solution was sonicated for at least five minutes.

The polymer used in this experiment is fully protonated P2VP or partially deuterated dP2VP ($C_7D_3H_4N$) of varying molecular weight purchased from Scientific Polymer Products, Inc.

Polymer solutions were left to stir for several hours. Before adding polymer to NP solutions, the solvent for the polymer was made to match the NP solution. When the polymer was fully dissolved, the polymer solution was dropwise added to the NP solution while stirring. The final solution was sonicated for at least 5 minutes and left to stir for several hours to promote polymer adsorption and homogenize the solution.

SANS measurements were conducted at the NGB 30 m SANS beamline at the Center for High Resolution Neutron Scattering (CHRNS) at the NIST Center for Neutron Scattering. The neutron wavelength was 6 Å and sample-to-detector distances of 1.33, 4, and 13.17 m were used to achieve a continuous q-range of 0.0035–0.1 $Å^{-1}$. Standard transmission fluid cells were sealed and used for all measurements. Sample collection took ~1-2 hours per sample to complete all sample-to-detector distances, depending on the sample conditions (e.g. scattering contrast and concentration). All scattering patterns were isotropic and 1D scattering patterns were obtained by azimuthal integration.

G.3 Results and Discussion

G.3.1 Contrast Matching SiO_2 NPs

To properly zero-average contrast (ZAC) match the SiO_2 NPs, it is important to properly measure the scattering length density (SLD) of the NPs. The best way to do this is to fix the NP concentration and vary the solvent scattering length density, usually through mixing hydrogenated and deuterated solvents in different ratios. Here, we use the stock NP solution (in H_2O) and dilute it with combinations of H_2O and D_2O. It is important to note that this should be done for all components (all polymer and NPs) before thorough measurements of multicomponent solutions. Due to time restraint, we only measured the SLD of SiO_2 for contrast matching purposes. We also

note that D_2O is hygroscopic, so a good practice is to measure the density (or the density relative to H_2O) before use to confirm that it is pure D_2O rather than a contaminated mixture of H_2O/D_2O.

We measure SiO_2 NPs at 1 vol% in H_2O:D_2O ratios of 100:0, 60:40, 55:45: 50:50, 40:60, and 6:94. Scattering patterns are plotted on a linear y-axis and the incoherent background is subtracted such that all patterns go to I=0 at high q (inset of Figure G.1). The square root of the total integrated intensity is calculated for each scattering pattern and plotted as a function of solvent SLD in Figure G.1. A linear fit is then applied to calculate the point at which the scattering intensity is expected to be zero, i.e. the zero-average contrast point. We find that the SLD of the Ludox AS40 SiO_2 NPs is ~3.59E-6 $Å^{-2}$, which is a reasonable value for amorphous SiO_2 assuming a density of 2.3 g/cm^3. This value is also in good agreement with other SiO_2 NPs (~3.5E-6 $Å^{-2}$)[150,209] but we emphasize that differences in synthesis may lead to slight differences in density and SLD, so it is important to repeat this measurement for NPs in future experiments.

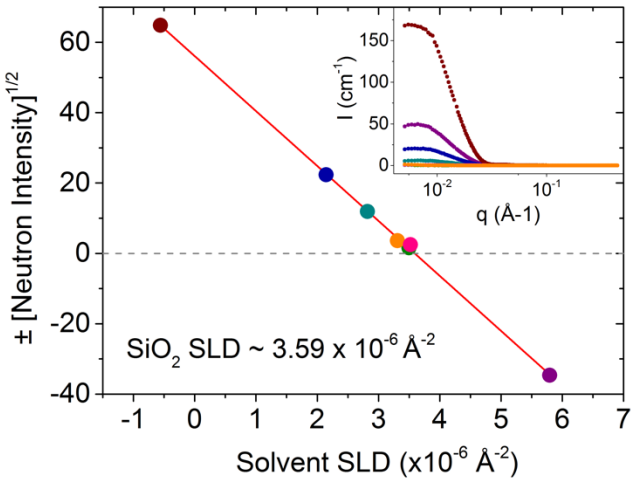

Figure G.1: Square root of the total scattering intensity from SiO_2 NP solutions at 1 vol% in mixtures of H_2O and D_2O with a linear fit used to extract the SLD of the NPs. (inset) Scattering patterns of various H_2O/D_2O mixtures after background subtraction.

G.3.2 SANS Pattern for Individual Components

We now present measurements of each component, P2VP and SiO_2, in dilute DMF solutions in Figure G.2. We use dP2VP rather than P2VP because dP2VP has a comparable SLD to SiO_2 (as indicated by the equal incoherent plateau at high q). Importantly, free polymer (purple) and bare NPs (grey) have unique features at different q positions. The NP scattering pattern follows the expected form factor for 28-nm spheres, but a structure factor is observed at low q meaning the solution is not dilute enough to only consider the form factor. Future measurements should be more dilute than 2 vol% for the same NP size to simplify the fitting and analysis. The polymer scattering pattern follows the expected Debye function with a feature at the polymer radius of gyration (R_g ~10 nm for 100 kg/mol P2VP).

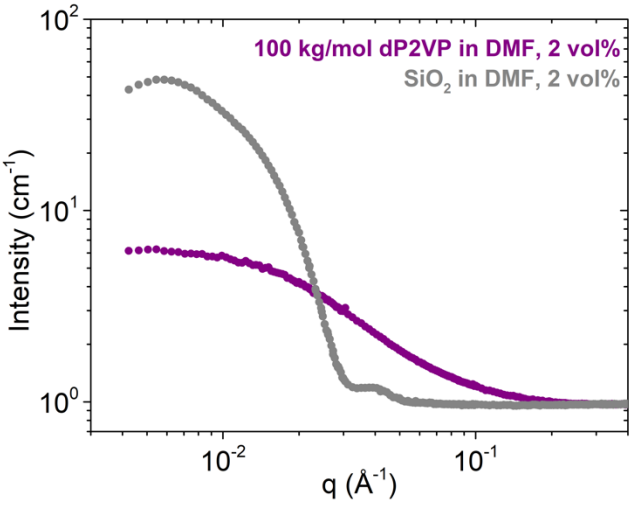

Figure G.2: SANS scattering patterns of SiO_2 (grey, diameter ~ 28 nm) and 100 kg/mol dP2VP (purple, R_g ~ 10 nm) in DMF, both at 2 vol%.

These measurements show that scattering from a feature with a shape similar to the NP is significantly different when compared to scattering from free polymer. This observation supports the notion that SANS can be used to study and differentiate free and adsorbed polymer in PNC solutions.

G.3.3 Measurements as a Function of Polymer Concentration

We measure NP-polymer solutions as a function of polymer concentration (c_{poly}) with the solvent and NPs near ZAC condition. Due to experimental limitation in the availability of deuterated solvents and available NP solutions, we used a mixture of hMeOH, dAcetone, and D_2O. Future systematic studies would be improved with a single-component solvent. We note that MeOH, Acetone, and H_2O are good, poor, and non-solvents, respectively. Formation of the bound polymer layer is promoted in systems with weak polymer-solvent affinity, because polymers energetically prefer to be adsorbed on the NP surface. We consider this combination of solvents to be a poor solvent.

Figure G.3 shows P2VP and SiO_2 solutions with 0, 3, 10, and 30 g/L P2VP in a hMeOH/dAcetone/D_2O solution at 1.5 vol% SiO_2. As expected, the SiO_2 solution without polymer shows minimal scattering at all q because the solvent SLD is engineered to match the NP SLD. As P2VP is added to the solution, more scattering is observed since the measurement is dominated by P2VP scattering. At small c_{poly}, the scattering pattern mimics the NP form factor in Figure G.2 as opposed to the form factor of free polymer. This suggests that polymer is adsorbing to the NP surface in this experiment. At the highest c_{poly}, the scattering pattern seems to follow a combination of both of the scattering patterns in Figure G.2. Although the oscillations for a spherical NP are observed, the background is increased and seems to follow $I \sim q^{-2}$ which is characteristic of free polymer scattering. This indicates the presences of both adsorbed and free polymer, but quantitative fitting of experimental data will confirm this assertion.

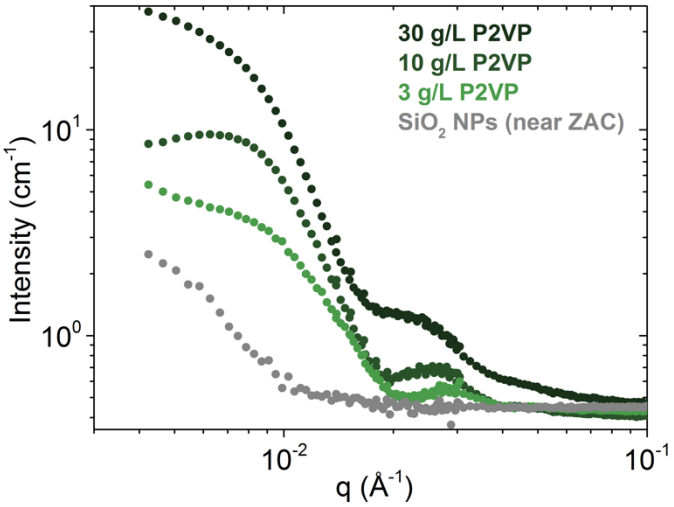

Figure G.3: SANS measurements of SiO_2 NPs with 100 kg/mol P2VP at c_{poly} = 0 g/L (grey), 3 g/L (light green), 10 g/L (green), and 30 g/L (dark green) in a mixture of hMeOH, dAcetone, and D_2O that has SLD comparable to the SiO_2. The SiO_2 concentration is 1.5 vol%.

G.3.4 Measurements as a Function of Polymer Molecular Weight

To further understand this measurement, we used the intermediate polymer concentration from Figure G.3 to measure the effect of molecular weight. For 100 kg/mol, c_{poly} = 10 g/L seemed to have the highest polymer concentration without observable free polymer scattering. We suspect this concentration, which is related to the areal density of adsorbed polymer, should depend on M_w, but we choose 10 g/L for all measurements.

Figure G.4 shows the scattering pattern for samples with different M_w. All samples show signatures of the NP form factor, suggesting the presence of adsorbed polymer in these solutions. Importantly, the feature mimicking the NP form factor at ~0.03Å^{-1} shifts to large q with higher M_w polymer. This suggests that the scattering object is growing in size, as expected for higher M_w. Fitting these SANS profiles is challenging, likely because of a structure factor resulting from NP concentrations too high or contributions of free polymer. However, models exist for approaching similar systems.[150,328] More systematic measurements of each component at their relevant

concentrations and corresponding SAXS measurements may provide enough insight to accurately fit the experimental data to extract the SLD and thickness of the bound polymer layer.

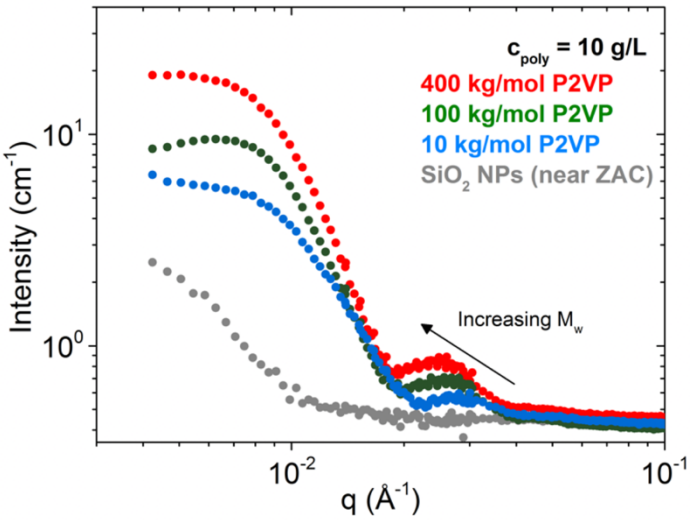

Figure G.4: SANS measurements of SiO_2 NPs (1.5 vol%) with 10 kg/mol (blue), 100 kg/mol (green), 400 kg/mol (red) P2VP at c_{poly} = 10 g/L in a mixture of hMeOH, dAcetone, and D_2O that has SLD comparable to the SiO_2. A solution containing only SiO_2 (grey) is shown for comparison.

G.4 Conclusions

The measurements presented above provide a demonstration of how SANS can be used to probe NP-polymer solutions and particularly measure the bound polymer layer. After measuring the scattering length density of the SiO_2 NPs, the solvent can be engineered to achieve ZAC so that the SANS scattering patterns are dominated by the polymer. Next, measuring the scattering pattern of individual components of the solution helps identify key features in more complicated samples and helps guide experimental design. P2VP/SiO_2 solutions as a function of c_{poly} mimic the spherical NP form factor at low c_{poly} and signatures of free polymer scattering begin to emerge at high c_{poly}. Finally, as the M_w of the polymer is increased, the scattering feature increases in size, but quantitatively fitting the experimental data is challenging.

G.5 Future Work

SANS measurements of NP-polymer solutions are ideal to study bound layer characteristics in solution. This section provided a demonstration and may help guide future experiments. In new experiments, it is important to measure the SLD (as was done in Figure G.1) for all of the individual components. In addition, it is important to meticulously measure SAXS of the NP solutions as a function of NP concentration to identify the best NP concentration. It is best to maximize the NP concentration for signal-to-noise ratios, but it is helpful to measure dilute solutions, where the scattering pattern can be approximated by only a form factor. SAXS measurements over the same q-range can help identify the ideal NP concentration. In addition, it is suggested to use a simpler solvent, preferably a mixture of the same protonated and deuterated solvent, but more complicated solvent mixtures can be successful.

For future measurements, scattering patterns should be collected in the same solvent type but different SLDs. For example, three different mixtures of deuterated and protonated MeOH would be suitable. These repetitive samples will help identify features and give further insight when trying to quantitatively fit the data. Another way to assist in fitting the data is to collect different components of the sample (at the same overall volume fraction) individually. If the fitting is mathematically divided into different components, as was useful in literature[150], these measurements will help identify different form factors and their values. Prior to attending the beam line for measurements, it may be constructive to build the expected form factors mathematically to help determine which samples need to be measured and the appropriate SLDs to use.

More discussion of SANS for studies of the bound polymer layer can be found in Chapter 7, including discussions about probing kinetics, competitive adsorption, and static bound layer properties.

References

(1) A.C. Balazs; T. Emrick; T.P. Russell. Nanoparticle Polymer Composites: Where Two Small Worlds Meet. *Science (80-.).* **2006**, *314* (5802), 1107–1110.

(2) Winey, K. I.; Vaia, R. A. Polymer Nanocomposites. *MRS Bull.* **2007**, *32*, 314–322.

(3) Arepalli, S.; Moloney, P. Engineered Nanomaterials in Aerospace. *MRS Bull.* **2015**, *40* (10), 804–811.

(4) Kumar, S. K.; Benicewicz, B. C.; Vaia, R. A.; Winey, K. I. 50th Anniversary Perspective: Are Polymer Nanocomposites Practical for Applications? *Macromolecules* **2017**, *50* (3), 714–731.

(5) Fernandes, N. J.; Koerner, H.; Giannelis, E. P.; Vaia, R. A. Hairy Nanoparticle Assemblies as One-Component Functional Polymer Nanocomposites: Opportunities and Challenges. *MRS Commun.* **2013**, *3* (1), 13–29.

(6) Paul, D. R.; Robeson, L. M. Polymer Nanotechnology: Nanocomposites. *Polymer (Guildf).* **2008**, *49* (15), 3187–3204.

(7) Pandey, N.; Shukla, S. K.; Singh, N. B. Water Purification by Polymer Nanocomposites: An Overview. *Nanocomposites* **2017**, *3* (2), 47–66.

(8) Kumar, S. K.; Krishnamoorti, R. Nanocomposites: Structure, Phase Behavior, and Properties. *Annu. Rev. Chem. Biomol. Eng.* **2010**, *1* (1), 37–58.

(9) Krishnamoorti, R. Strategies for Dispersing Nanopar Ticles in Polymers. *MRS Bull.* **2007**, *32*, 341–347.

(10) Hore, M. J. A.; Composto, R. J. Functional Polymer Nanocomposites Enhanced by Nanorods. *Macromolecules* **2014**, *47* (3), 875–887.

(11) Green, P. F. The Structure of Chain End-Grafted Nanoparticle/Homopolymer Nanocomposites. *Soft Matter* **2011**, *7* (18), 7914–7926.

(12) Kumar, S. K.; Jouault, N.; Benicewicz, B.; Neely, T. Nanocomposites with Polymer Grafted Nanoparticles. *Macromolecules* **2013**, *46* (9), 3199–3214.

(13) Azeredo, H. M. C. d. Nanocomposites for Food Packaging Applications. *Food Res. Int.* **2009**, *42* (9), 1240–1253.

(14) Merkel, T. C.; Freeman, B. D.; Spontak, R. J.; He, Z.; Pinnau, I.; Meakin, P.; Hill, A. J. Ultrapermeable, Reverse-Selective Nanocomposite Membranes. *Science (80-.).* **2002**, *296*, 519–523.

(15) Mutiso, R. M.; Winey, K. I. Electrical Properties of Polymer Nanocomposites Containing Rod-like Nanofillers. *Prog. Polym. Sci.* **2015**, *40* (1), 63–84.

(16) Byrne, M. T.; Guin'Ko, Y. K. Recent Advances in Research on Carbon Nanotube - Polymer Composites. *Adv. Mater.* **2010**, *22* (15), 1672–1688.

(17) Croce, F.; Appetecchi, G. B.; Persi, L.; Scrosati, B. Nanocomposite Polymer Electrolytes for Lithiumbatteries. *Nature* **1998**, *394* (July), 456–458.

(18) Kulkarni, D. D.; Choi, I.; Singamaneni, S. S.; Tsukruk, V. V. Graphene Oxide-Polyelectrolyte Nanomembranes. *ACS Nano* **2010**, *4* (8), 4667–4676.

(19) Hore, M. J. A.; Composto, R. J. Nanorod Self-Assembly for Tuning Optical Absorption. *ACS Nano* **2010**, *4* (11), 6941–6949.

(20) Raftopoulos, K. N.; Pielichowski, K. Segmental Dynamics in Hybrid Polymer/POSS Nanomaterials. *Prog. Polym. Sci.* **2016**, *52*, 136–187.

(21) Kim, H.; Abdala, A. A.; MacOsko, C. W. Graphene/Polymer Nanocomposites. *Macromolecules* **2010**, *43* (16), 6515–6530.

(22) Hu, X.; Zhang, W.; Si, M.; Gelfer, M.; Hsiao, B.; Rafailovich, M.; Sokolov, J.; Zaitsev, V.; Schwarz, S. Dynamics of Polymers in Organosilicate Nanocomposites. *Macromolecules* **2003**, *36* (3), 823–829.

(23) Chrissopoulou, K.; Anastasiadis, S. H. Effects of Nanoscopic-Confinement on Polymer

Dynamics. *Soft Matter* **2015**, *11* (19), 3746–3766.

(24) Anastasiadis, S. H.; Chrissopoulou, K.; Frick, B. Structure and Dynamics in Polymer/Layered Silicate Nanocomposites. *Mater. Sci. Eng. B* **2008**, *152* (1–3), 33–39.

(25) Kumar, S. K.; Ganesan, V.; Riggleman, R. A. Perspective: Outstanding Theoretical Questions in Polymer-Nanoparticle Hybrids. *J. Chem. Phys.* **2017**, *147* (2), 020901.

(26) Lin, C. C.; Parrish, E.; Composto, R. J. Macromolecule and Particle Dynamics in Confined Media. *Macromolecules* **2016**, *49* (16), 5755–5772.

(27) Richter, D.; Kruteva, M. Polymer Dynamics under Confinement. *Soft Matter* **2019**, *15* (37), 7316–7349.

(28) Simmons, D. S. An Emerging Unified View of Dynamic Interphases in Polymers. *Macromol. Chem. Phys.* **2016**, *217* (2), 137–148.

(29) Cheng, S.; Carroll, B.; Bocharova, V.; Carrillo, J. M.; Sumpter, B. G.; Sokolov, A. P. Focus: Structure and Dynamics of the Interfacial Layer in Polymer Nanocomposites with Attractive Interactions. *J. Chem. Phys.* **2017**, *146* (20), 203201/1-14.

(30) Volgin, I. V.; Larin, S. V.; Lyulin, S. V. Diffusion of Nanoparticles in Polymer Systems. *Polym. Sci. Ser. C* **2018**, *60* (S1), 122–134.

(31) Peng, H.; Nieuwendaal, R.; Soles, C. L. Polymer Dynamics in Constrained Geometries. In *Polymer Science: A Comprehensive Reference, 10 Volume Set*; Elsevier B.V., 2012; Vol. 7, pp 345–376.

(32) Karatrantos, A.; Composto, R. J.; Winey, K. I.; Kröger, M.; Clarke, N. Modeling of Entangled Polymer Diffusion in Melts and Nanocomposites: A Review. *Polymers (Basel).* **2019**, *11* (5), 876/1-29.

(33) Hore, M. J. A. Polymers on Nanoparticles: Structure & Dynamics. *Soft Matter* **2019**, *15* (6), 1120–1134.

(34) Tjong, S. C. Structural and Mechanical Properties of Polymer Nanocomposites. *Mater. Sci.*

Eng. R Reports **2006**, *53* (3–4), 73–197.

(35) Rubinstein, M.; Colby, R. H. *Polymer Physics*; Oxford University Press: New York, 2003.

(36) Priestley, R. D.; Cangialosi, D.; Napolitano, S. On the Equivalence between the Thermodynamic and Dynamic Measurements of the Glass Transition in Confined Polymers. *J. Non. Cryst. Solids* **2015**, *407*, 288–295.

(37) Arrese-Igor, S.; Arbe, A.; Frick, B.; Colmenero, J. Glassy Dynamics of Polystyrene by Quasielastic Neutron Scattering. *Macromolecules* **2011**, *44* (8), 3161–3168.

(38) Wyart, F. B.; De Gennes, P. G. Viscosity at Small Scales in Polymer Melts. *Eur. Phys. J. E* **2000**, *1*, 93–97.

(39) Genix, A. C.; Bocharova, V.; Kisliuk, A.; Carroll, B.; Zhao, S.; Oberdisse, J.; Sokolov, A. P. Enhancing the Mechanical Properties of Glassy Nanocomposites by Tuning Polymer Molecular Weight. *ACS Appl. Mater. Interfaces* **2018**, *10* (39), 33601–33610.

(40) Chen, Q.; Gong, S.; Moll, J.; Zhao, D.; Kumar, S. K.; Colby, R. H. Mechanical Reinforcement of Polymer Nanocomposites from Percolation of a Nanoparticle Network. *ACS Macro Lett.* **2015**, *4* (4), 398–402.

(41) Yang, S.; Akcora, P. Deformation of Chemically Heterogeneous Interfacial Layers of Polymer Nanocomposites. *ACS Macro Lett.* **2019**, *8*, 1635–1641.

(42) Mogurampelly, S.; Ganesan, V. Influence of Nanoparticle Surface Chemistry on Ion Transport in Polymer Nanocomposite Electrolytes. *Solid State Ionics* **2016**, *286*, 57–65.

(43) Bilchak, C. R.; Buenning, E.; Asai, M.; Zhang, K.; Durning, C. J.; Kumar, S. K.; Huang, Y.; Benicewicz, B. C.; Gidley, D. W.; Cheng, S.; et al. Polymer-Grafted Nanoparticle Membranes with Controllable Free Volume. *Macromolecules* **2017**, *50* (18), 7111–7120.

(44) Takahashi, S.; Paul, D. R. Gas Permeation in Poly(Ether Imide) Nanocomposite Membranes Based on Surface-Treated Silica. Part 1: Without Chemical Coupling to Matrix. *Polymer (Guildf).* **2006**, *47* (21), 7519–7534.

(45) Merkel, T. C.; Freeman, B. D.; Spontak, R. J.; He, Z.; Pinnau, I.; Meakin, P.; Hill, A. J. Sorption, Transport, and Structural Evidence for Enhanced Free Volume in Poly(4-Methyl-2-Pentyne)/Fumed Silica Nanocomposite Membranes. *Chem. Mater.* **2003**, *15* (1), 109–123.

(46) Jhalaria, M.; Buenning, E.; Huang, Y.; Tyagi, M.; Zorn, R.; Zamponi, M.; García-Sakai, V.; Jestin, J.; Benicewicz, B. C.; Kumar, S. K. Accelerated Local Dynamics in Matrix-Free Polymer Grafted Nanoparticles. *Phys. Rev. Lett.* **2019**, *123* (15), 158003/1-6.

(47) Capadona, J. R.; Shanmuganathan, K.; Tyler, D. J.; Rowan, S. J.; Weder, C. Stimuli-Responsive Polymer Nanocomposites Inspired by the Sea Cucumber Dermis. *Science (80-.).* **2008**, *319*, 1370–1375.

(48) Gupta, S.; Zhang, Q.; Emrick, T.; Balazs, A. C.; Russell, T. P. Entropy-Driven Segregation of Nanoparticles to Cracks in Multilayered Composite Polymer Structures. *Nat. Mater.* **2006**, *5* (3), 229–233.

(49) Böker, A.; He, J.; Emrick, T.; Russell, T. P. Self-Assembly of Nanoparticles at Interfaces. *Soft Matter* **2007**, *3* (10), 1231–1248.

(50) Rittigstein, P.; Priestley, R. D.; Broadbelt, L. J.; Torkelson, J. M. Model Polymer Nanocomposites Provide an Understanding of Confinement Effects in Real Nanocomposites. *Nat. Mater.* **2007**, *6* (4), 278–282.

(51) Liu, R.; Guo, Y.; Odusote, G.; Qu, F.; Priestley, R. D. Core-Shell Fe3O4 Polydopamine Nanoparticles Serve Multipurpose as Drug Carrier, Catalyst Support and Carbon Adsorbent. *ACS Appl. Mater. Interfaces* **2013**, *5* (18), 9167–9171.

(52) Mora-Huertas, C. E.; Fessi, H.; Elaissari, A. Polymer-Based Nanocapsules for Drug Delivery. *Int. J. Pharm.* **2010**, *385* (1–2), 113–142.

(53) Kalwarczyk, T.; Tabaka, M.; Holyst, R. Biologistics-Diffusion Coefficients for Complete Proteome of Escherichia Coli. *Bioinformatics* **2012**, *28* (22), 2971–2978.

(54) Robertson, C. G.; Roland, C. M. Glass Transition and Interfacial Segmental Dynamics in

Polymer-Particle Composites. *Rubber Chem. Technol.* **2011**, *81* (3), 506–522.

(55) Bailey, E. J.; Griffin, P. J.; Tyagi, M.; Winey, K. I. Segmental Diffusion in Attractive Polymer Nanocomposites: A Quasi-Elastic Neutron Scattering Study. *Macromolecules* **2019**, *52* (2), 669–678.

(56) Schawe, J. E. K. A Comparison of Different Evaluation Methods in Modulated Temperature DSC. *Thermochim. Acta* **1995**, *260* (C), 1–16.

(57) Kremer, F.; Schönhals, A. *Broadband Dielectric Spectroscopy*; Springer-Verlag: Berlin, 2002.

(58) Carroll, B.; Cheng, S.; Sokolov, A. P. Analyzing the Interfacial Layer Properties in Polymer Nanocomposites by Broadband Dielectric Spectroscopy. *Macromolecules* **2017**, *50* (16), 6149–6163.

(59) Springer, T. *Quasielastic Neutron Scattering for the Investigation of Diffusive Motions in Solids and Liquids*; Springer-Verlag: Berlin, 1972.

(60) Dieter Richter, Michael Monkenbusch, and D. S. Neutron Scattering. In *Polymer Science: A Comprehensive Reference*; Matyjaszewski, K., Möller, M., Eds.; Elsevier B.V., 2012; pp 331–360.

(61) Saalwächter, K.; Spiess, H. Solid-State NMR of Polymers. In *Polymer Science: A Comprehensive Reference*; Matyjaszewski, K., Möller, M., Eds.; Elsevier B.V., 2012; pp 185–218.

(62) Papon, A.; Saalwächter, K.; Schäler, K.; Guy, L.; Lequeux, F.; Montes, H. Low-Field NMR Investigations of Nanocomposites: Polymer Dynamics and Network Effects. *Macromolecules* **2011**, *44* (4), 913–922.

(63) Kremer, K.; Grest, G. S. Dynamics of Entangled Linear Polymer Melts: A Molecular-Dynamics Simulation. *J. Chem. Phys.* **1990**, *92* (8), 5057–5086.

(64) Moll, J.; Kumar, S. K. Glass Transitions in Highly Attractive Highly Filled Polymer

Nanocomposites. *Macromolecules* **2012**, *45* (2), 1131–1135.

(65) Holt, A. P.; Griffin, P. J.; Bocharova, V.; Agapov, A. L.; Imel, A. E.; Dadmun, M. D.; Sangoro, J. R.; Sokolov, A. P. Dynamics at the Polymer/Nanoparticle Interface in Poly(2-Vinylpyridine)/ Silica Nanocomposites. *Macromolecules* **2014**, *47* (5), 1837–1843.

(66) Gong, S.; Chen, Q.; Moll, J. F.; Kumar, S. K.; Colby, R. H. Segmental Dynamics of Polymer Melts with Spherical Nanoparticles. *ACS Macro Lett.* **2014**, *3* (8), 773–777.

(67) Baeza, G. P.; Dessi, C.; Costanzo, S.; Zhao, D.; Gong, S.; Alegria, A.; Colby, R. H.; Rubinstein, M.; Vlassopoulos, D.; Kumar, S. K. Network Dynamics in Nanofilled Polymers. *Nat. Commun.* **2016**, *7*, 1–6.

(68) Harton, S. E.; Kumar, S. K.; Yang, H.; Koga, T.; Hicks, K.; Lee, H.; Mijovic, J.; Liu, M.; Vallery, R. S.; Gidley, D. W. Immobilized Polymer Layers on Spherical Nanoparticles. *Macromolecules* **2010**, *43* (7), 3415–3421.

(69) Voylov, D. N.; Holt, A. P.; Doughty, B.; Bocharova, V.; Meyer, H. M.; Cheng, S.; Martin, H.; Dadmun, M.; Kisliuk, A.; Sokolov, A. P. Unraveling the Molecular Weight Dependence of Interfacial Interactions in Poly(2-Vinylpyridine)/Silica Nanocomposites. *ACS Macro Lett.* **2017**, *6* (2), 68–72.

(70) Oh, S. M.; Abbasi, M.; Shin, T. J.; Saalwächter, K.; Kim, S. Y. Initial Solvent-Driven Nonequilibrium Effect on Structure, Properties, and Dynamics of Polymer Nanocomposites. *Phys. Rev. Lett.* **2019**, *123* (16), 167801/1-6.

(71) Papon, A.; Montes, H.; Lequeux, F.; Oberdisse, J.; Saalwächter, K.; Guy, L. Solid Particles in an Elastomer Matrix: Impact of Colloid Dispersion and Polymer Mobility Modification on the Mechanical Properties. *Soft Matter* **2012**, *8* (15), 4090–4096.

(72) Füllbrandt, M.; Purohit, P. J.; Schönhals, A. Combined FTIR and Dielectric Investigation of Poly(Vinyl Acetate) Adsorbed on Silica Particles. *Macromolecules* **2013**, *46* (11), 4626–4632.

(73) Cheng, S.; Holt, A. P.; Wang, H.; Fan, F.; Bocharova, V.; Martin, H.; Etampawala, T.; White, B. T.; Saito, T.; Kang, N. G.; et al. Unexpected Molecular Weight Effect in Polymer Nanocomposites. *Phys. Rev. Lett.* **2016**, *116* (3), 038302/1-5.

(74) Cheng, S.; Carroll, B.; Lu, W.; Fan, F.; Carrillo, J. M. Y.; Martin, H.; Holt, A. P.; Kang, N. G.; Bocharova, V.; Mays, J. W.; et al. Interfacial Properties of Polymer Nanocomposites: Role of Chain Rigidity and Dynamic Heterogeneity Length Scale. *Macromolecules* **2017**, *50* (6), 2397–2406.

(75) Coleman, N. J.; Craig, D. Q. M. Modulated Temperature Differential Scanning Calorimetry: A Novel Approach to Pharmaceutical Thermal Analysis. *Int. J. Pharm.* **1996**, *135* (1–2), 13–29.

(76) Ye, C.; Wiener, C. G.; Tyagi, M.; Uhrig, D.; Orski, S. V.; Soles, C. L.; Vogt, B. D.; Simmons, D. S. Understanding the Decreased Segmental Dynamics of Supported Thin Polymer Films Reported by Incoherent Neutron Scattering. *Macromolecules* **2015**, *48* (3), 801–808.

(77) Glomann, T.; Schneider, G. J.; Allgaier, J.; Radulescu, A.; Lohstroh, W.; Farago, B.; Richter, D. Microscopic Dynamics of Polyethylene Glycol Chains Interacting with Silica Nanoparticles. *Phys. Rev. Lett.* **2013**, *110* (17), 178001/1-5.

(78) Bansal, A.; Yang, H.; Li, C.; Cho, K.; Benicewicz, B. C.; Kumar, S. K.; Schadler, L. S. Quantitative Equivalence between Polymer Nanocomposites and Thin Polymer Films. *Nat. Mater.* **2005**, *4* (9), 693–698.

(79) Starr, F. W.; Schrøder, T. B.; Glotzer, S. C. Molecular Dynamics Simulation of a Polymer Melt with a Nanoscopic Particle. *Macromolecules* **2002**, *35* (11), 4481–4492.

(80) Zhang, W.; Emamy, H.; Pazmiño Betancourt, B. A.; Vargas-Lara, F.; Starr, F. W.; Douglas, J. F. The Interfacial Zone in Thin Polymer Films and around Nanoparticles in Polymer Nanocomposites. *J. Chem. Phys.* **2019**, *151* (12), 124705/1-9.

(81) Franz, C.; Lange, F.; Golitsyn, Y.; Hartmann-Azanza, B.; Steinhart, M.; Krutyeva, M.; Saalwächter, K. Chain Dynamics and Segmental Orientation in Polymer Melts Confined to Nanochannels. *Macromolecules* **2016**, *49* (1), 244–256.

(82) Krutyeva, M.; Wischnewski, A.; Monkenbusch, M.; Willner, L.; Maiz, J.; Mijangos, C.; Arbe, A.; Colmenero, J.; Radulescu, A.; Holderer, O.; et al. Effect of Nanoconfinement on Polymer Dynamics: Surface Layers and Interphases. *Phys. Rev. Lett.* **2013**, *110* (10), 108303/1-5.

(83) Krutyeva, M.; Pasini, S.; Monkenbusch, M.; Allgaier, J.; Maiz, J.; Mijangos, C.; Hartmann-Azanza, B.; Steinhart, M.; Jalarvo, N.; Richter, D. Polymer Dynamics under Cylindrical Confinement Featuring a Locally Repulsive Surface: A Quasielastic Neutron Scattering Study. *J. Chem. Phys.* **2017**, *146* (20), 203306/1-11.

(84) Vo, L. T.; Anastasiadis, S. H.; Giannelis, E. P. Dielectric Study of Poly(Styrene-Co-Butadiene) Composites with Carbon Black, Silica, and Nanoclay. *Macromolecules* **2011**, *44* (15), 6162–6171.

(85) Hanakata, P. Z.; Douglas, J. F.; Starr, F. W. Interfacial Mobility Scale Determines the Scale of Collective Motion and Relaxation Rate in Polymer Films. *Nat. Commun.* **2014**, *5* (May), 1–8.

(86) Roth, C. B.; Dutcher, J. R. Glass Transition and Chain Mobility in Thin Polymer Films. *J. Electroanal. Chem.* **2005**, *584* (1), 13–22.

(87) Priestley, R. D.; Ellison, C. J.; Broadbelt, L. J. Structural Relaxation of Polymer Glasses at Surfaces , Interfaces , and In Between. *Science (80-.).* **2005**, *309* (2005), 456–460.

(88) Holt, A. P.; Bocharova, V.; Cheng, S.; Kisliuk, A. M.; White, B. T.; Saito, T.; Uhrig, D.; Mahalik, J. P.; Kumar, R.; Imel, A. E.; et al. Controlling Interfacial Dynamics: Covalent Bonding versus Physical Adsorption in Polymer Nanocomposites. *ACS Nano* **2016**, *10* (7), 6843–6852.

(89) Kim, S. Y.; Meyer, H. W.; Saalwächter, K.; Zukoski, C. F. Polymer Dynamics in PEG-Silica Nanocomposites: Effects of Polymer Molecular Weight, Temperature and Solvent Dilution. *Macromolecules* **2012**, *45* (10), 4225–4237.

(90) Askar, S.; Li, L.; Torkelson, J. M. Polystyrene-Grafted Silica Nanoparticles: Investigating the Molecular Weight Dependence of Glass Transition and Fragility Behavior. *Macromolecules* **2017**, *50* (4), 1589–1598.

(91) Klonos, P. A.; Goncharuk, O. V.; Pakhlov, E. M.; Sternik, D.; Derylo-Marczewska, A.; Kyritsis, A.; Gun'Ko, V. M.; Pissis, P. Morphology, Molecular Dynamics, and Interfacial Phenomena in Systems Based on Silica Modified by Grafting Polydimethylsiloxane Chains and Physically Adsorbed Polydimethylsiloxane. *Macromolecules* **2019**, *52*, 2863–2877.

(92) Mark, C.; Holderer, O.; Allgaier, J.; Hübner, E.; Pyckhout-Hintzen, W.; Zamponi, M.; Radulescu, A.; Feoktystov, A.; Monkenbusch, M.; Jalarvo, N.; et al. Polymer Chain Conformation and Dynamical Confinement in a Model One-Component Nanocomposite. *Phys. Rev. Lett.* **2017**, *119* (4), 047801/1-5.

(93) Carrillo, J. M. Y.; Cheng, S.; Kumar, R.; Goswami, M.; Sokolov, A. P.; Sumpter, B. G. Untangling the Effects of Chain Rigidity on the Structure and Dynamics of Strongly Adsorbed Polymer Melts. *Macromolecules* **2015**, *48* (12), 4207–4219.

(94) Klonos, P.; Kyritsis, A.; Bokobza, L.; Gun'ko, V. M.; Pissis, P. Interfacial Effects in PDMS/Titania Nanocomposites Studied by Thermal and Dielectric Techniques. *Colloids Surfaces A Physicochem. Eng. Asp.* **2017**, *519*, 212–222.

(95) Akcora, P.; Kumar, S. K.; García Sakai, V.; Li, Y.; Benicewicz, B. C.; Schadler, L. S. Segmental Dynamics in PMMA-Grafted Nanoparticle Composites. *Macromolecules* **2010**, *43* (19), 8275–8281.

(96) Wu, S. Phase Structure and Adhesion in Polymer Blends: A Criterion for Rubber Toughening. *Polymer (Guildf).* **1985**, *26* (12), 1855–1863.

(97) Hall, L. M.; Jayaraman, A.; Schweizer, K. S. Molecular Theories of Polymer Nanocomposites. *Curr. Opin. Solid State Mater. Sci.* **2010**, *14* (2), 38–48.

(98) Hall, L. M.; Anderson, B. J.; Zukoski, C. F.; Schweizer, K. S. Concentration Fluctuations, Local Order, and the Collective Structure of Polymer Nanocomposites. *Macromolecules* **2009**, *42* (21), 8435–8442.

(99) Emamy, H.; Kumar, S. K.; Starr, F. W. Diminishing Interfacial Effects with Decreasing Nanoparticle Size in Polymer-Nanoparticle Composites. *Phys. Rev. Lett.* **2018**, *121*, 207801/1-5.

(100) Swenson, J.; Smalley, M. V.; Hatharasinghe, H. L. M. Mechanism and Strength of Polymer Bridging Flocculation. *Phys. Rev. Lett.* **1998**, *81* (26), 5840–5843.

(101) Allegra, G.; Raos, G.; Vacatello, M. Theories and Simulations of Polymer-Based Nanocomposites: From Chain Statistics to Reinforcement. *Prog. Polym. Sci.* **2008**, *33* (7), 683–731.

(102) Srivastava, S.; Kotov, N. A. Composite Layer-by-Layer (LBL) Assembly with Inorganic Nanoparticles and Nanowires. *Acc. Chem. Res.* **2008**, *41* (12), 1831–1841.

(103) Huang, Y. R.; Jiang, Y.; Hor, J. L.; Gupta, R.; Zhang, L.; Stebe, K. J.; Feng, G.; Turner, K. T.; Lee, D. Polymer Nanocomposite Films with Extremely High Nanoparticle Loadings via Capillary Rise Infiltration (CaRI). *Nanoscale* **2015**, *7* (2), 798–805.

(104) Hor, J. L.; Wang, H.; Fakhraai, Z.; Lee, D. Effect of Physical Nanoconfinement on the Viscosity of Unentangled Polymers during Capillary Rise Infiltration. *Macromolecules* **2018**, *51* (14), 5069–5078.

(105) Wang, H.; Hor, J. L.; Zhang, Y.; Liu, T.; Lee, D.; Fakhraai, Z. Dramatic Increase in Polymer Glass Transition Temperature under Extreme Nanoconfinement in Weakly Interacting Nanoparticle Films. *ACS Nano* **2018**, *12* (6), 5580–5587.

(106) Holt, A. P.; Roland, C. M. Segmental and Secondary Dynamics of Nanoparticle-Grafted

Oligomers. *Soft Matter* **2018**, *14* (42), 8604–8611.

(107) Roh, J. H.; Tyagi, M.; Hogan, T. E.; Roland, C. M. Space-Dependent Dynamics in 1,4-Polybutadiene Nanocomposite. *Macromolecules* **2013**, *46* (16), 6667–6669.

(108) Cheng, S.; Xie, S. J.; Carrillo, J. M. Y.; Carroll, B.; Martin, H.; Cao, P. F.; Dadmun, M. D.; Sumpter, B. G.; Novikov, V. N.; Schweizer, K. S.; et al. Big Effect of Small Nanoparticles: A Shift in Paradigm for Polymer Nanocomposites. *ACS Nano* **2017**, *11* (1), 752–759.

(109) Bailey, E. J.; Griffin, P. J.; Composto, R. J.; Winey, K. I. Multiscale Dynamics of Small, Attractive Nanoparticles and Entangled Polymers in Polymer Nanocomposites. *Macromolecules* **2019**, *52* (5), 2181–2188.

(110) Karatrantos, A.; Clarke, N.; Kröger, M. Modeling of Polymer Structure and Conformations in Polymer Nanocomposites from Atomistic to Mesoscale: A Review. *Polym. Rev.* **2016**, *56* (3), 385–428.

(111) Lin, Y.; Liu, L.; Xu, G.; Zhang, D.; Guan, A.; Wu, G. Interfacial Interactions and Segmental Dynamics of Poly(Vinyl Acetate)/Silica Nanocomposites. *J. Phys. Chem. C* **2015**, *119* (23), 12956–12966.

(112) Klonos, P.; Bolbukh, Y.; Koutsiara, C. S.; Zafeiris, K.; Kalogeri, O. D.; Sternik, D.; Deryło-Marczewska, A.; Tertykh, V.; Pissis, P. Morphology and Molecular Dynamics Investigation of Low Molecular Weight PDMS Adsorbed onto Stöber, Fumed, and Sol-Gel Silica Nanoparticles. *Polymer (Guildf).* **2018**, *148*, 1–13.

(113) Kirst, K. U.; Kremer, F.; Litvinov, V. M. Broad-Band Dielectric Spectroscopy on the Molecular Dynamics of Bulk and Adsorbed Poly(Dimethylsiloxane). *Macromolecules* **1993**, *26* (5), 975–980.

(114) Klonos, P.; Kyritsis, A.; Pissis, P. Effects of Surface Modification and Thermal Annealing on the Interfacial Dynamics in Core-Shell Nanocomposites Based on Silica and Adsorbed PDMS. *Eur. Polym. J.* **2015**, *70*, 342–359.

(115) Litvinov, V. M.; Spies, H. W. 2H NMR Study of Molecular Motions in Polydimethylsiloxane and Its Mixtures with Aerosils. *Die Makromol. Chem.* **1991**, *192*, 3005–3019.

(116) Holt, A. P.; Sangoro, J. R.; Wang, Y.; Agapov, A. L.; Sokolov, A. P. Chain and Segmental Dynamics of Poly(2-Vinylpyridine) Nanocomposites. *Macromolecules* **2013**, *46* (10), 4168–4173.

(117) Tsagaropoulos, G.; Eisenberg, A. Dynamic Mechanical Study of the Factors Affecting the Two Glass Transition Behavior of Filled Polymers. Similarities and Differences with Random Ionomers. *Macromolecules* **1995**, *28* (18), 6067–6077.

(118) Natarajan, B.; Li, Y.; Deng, H.; Brinson, L. C.; Schadler, L. S. Effect of Interfacial Energetics on Dispersion and Glass Transition Temperature in Polymer Nanocomposites. *Macromolecules* **2013**, *46* (7), 2833–2841.

(119) Starr, F. W.; Douglas, J. F.; Meng, D.; Kumar, S. K. Bound Layers "Cloak" Nanoparticles in Strongly Interacting Polymer Nanocomposites. *ACS Nano* **2016**, *10* (12), 10960–10965.

(120) Starr, F. W.; Schrøder, T. B.; Glotzer, S. C. Effects of a Nanoscopic Filler on the Structure and Dynamics of a Simulated Polymer Melt and the Relationship to Ultrathin Films. *Phys. Rev. E* **2001**, *64* (2), 021802/1-6.

(121) Starr, F. W.; Douglas, J. F. Modifying Fragility and Collective Motion in Polymer Melts with Nanoparticles. *Phys. Rev. Lett.* **2011**, *106* (11), 115702/1-4.

(122) Pazmiño Betancourt, B. A.; Douglas, J. F.; Starr, F. W. Fragility and Cooperative Motion in a Glass-Forming Polymer-Nanoparticle Composite. *Soft Matter* **2013**, *9* (1), 241–254.

(123) Cheng, S.; Mirigian, S.; Carrillo, J. M. Y.; Bocharova, V.; Sumpter, B. G.; Schweizer, K. S.; Sokolov, A. P. Revealing Spatially Heterogeneous Relaxation in a Model Nanocomposite. *J. Chem. Phys.* **2015**, *143* (19), 194704.

(124) Patti, A. Molecular Dynamics of Spherical Nanoparticles in Dense Polymer Melts. *J. Phys.*

Chem. B **2014**, *118* (13), 3731–3742.

(125) Berriot, J.; Lequeux, F.; Monnerie, L.; Montes, H.; Long, D.; Sotta, P. Filler–Elastomer Interaction in Model Filled Rubbers, a 1H NMR Study. *J. Non. Cryst. Solids* **2002**, *307–310*, 719–724.

(126) Golitsyn, Y.; Schneider, G. J.; Saalwächter, K. Reduced-Mobility Layers with High Internal Mobility in Poly(Ethylene Oxide)-Silica Nanocomposites. *J. Chem. Phys.* **2017**, *146* (20), 203303/1-8.

(127) Holt, A. P.; Bocharova, V.; Cheng, S.; Kisliuk, A. M.; Ehlers, G.; Mamontov, E.; Novikov, V. N.; Sokolov, A. P. Interplay between Local Dynamics and Mechanical Reinforcement in Glassy Polymer Nanocomposites. *Phys. Rev. Mater.* **2017**, *1* (6), 062601/1-6.

(128) Kim, S. A.; Mangal, R.; Archer, L. A. Relaxation Dynamics of Nanoparticle-Tethered Polymer Chains. *Macromolecules* **2015**, *48* (17), 6280–6293.

(129) Rishi, K.; Beaucage, G.; Kuppa, V.; Mulderig, A.; Narayanan, V.; McGlasson, A.; Rackaitis, M.; Ilavsky, J. Impact of an Emergent Hierarchical Filler Network on Nanocomposite Dynamics. *Macromolecules* **2018**, *51* (20), 7893–7904.

(130) Yang, J.; Melton, M.; Sun, R.; Yang, W.; Cheng, S. Decoupling the Polymer Dynamics and the Nanoparticle Network Dynamics of Polymer Nanocomposites through Dielectric Spectroscopy and Rheology. *Macromolecules* **2020**, *53* (1), 302–311.

(131) Senses, E.; Ansar, S. M.; Kitchens, C. L.; Mao, Y.; Narayanan, S.; Natarajan, B.; Faraone, A. Small Particle Driven Chain Disentanglements in Polymer Nanocomposites. *Phys. Rev. Lett.* **2017**, *118* (14), 147801/1-5.

(132) Kröger, M. Shortest Multiple Disconnected Path for the Analysis of Entanglements in Two- and Three-Dimensional Polymeric Systems. *Comput. Phys. Commun.* **2005**, *168* (3), 209–232.

(133) Shanbhag, S.; Kröger, M. Primitive Path Networks Generated by Annealing and

Geometrical Methods: Insights into Differences. *Macromolecules* **2007**, *40* (8), 2897–2903.

(134) Karayiannis, N. C.; Kröger, M. Combined Molecular Algorithms for the Generation, Equilibration and Topological Analysis of Entangled Polymers: Methodology and Performance. *Int. J. Mol. Sci.* **2009**, *10* (11), 5054–5089.

(135) Fragiadakis, D.; Pissis, P. Glass Transition and Segmental Dynamics in Poly(Dimethylsiloxane)/Silica Nanocomposites Studied by Various Techniques. *J. Non. Cryst. Solids* **2007**, *353* (47–51), 4344–4352.

(136) Yves Termonia. Chain Confinement in Polymer Nanocomposites and Its Effect on Polymer Bulk Properties. *J. Polym. Sci. Part B Polym. Phys.* **2010**, *48*, 687–692.

(137) Zhang, Q.; Archer, L. A. Poly(Ethylene Oxide)/Silica Nanocomposites: Structure and Rheology. *Langmuir* **2002**, *18* (26), 10435–10442.

(138) Nusser, K.; Schneider, G. J.; Richter, D. Microscopic Origin of the Terminal Relaxation Time in Polymer Nanocomposites: An Experimental Precedent. *Soft Matter* **2011**, *7* (18), 7988–7991.

(139) Mangal, R.; Srivastava, S.; Archer, L. A. Phase Stability and Dynamics of Entangled Polymer-Nanoparticle Composites. *Nat. Commun.* **2015**, *6*, 1–9.

(140) Tuteja, A.; Mackay, M. E.; Hawker, C. J.; Van Horn, B. Effect of Ideal, Organic Nanoparticles on the Flow Properties of Linear Polymers: Non-Einstein-like Behavior. *Macromolecules* **2005**, *38* (19), 8000–8011.

(141) Senses, E.; Faraone, A.; Akcora, P. Microscopic Chain Motion in Polymer Nanocomposites with Dynamically Asymmetric Interphases. *Sci. Rep.* **2016**, *6* (April), 1–11.

(142) Bogoslovov, R. B.; Roland, C. M.; Ellis, A. R.; Randall, A. M.; Robertson, C. G. Effect of Silica Nanoparticles on the Local Segmental Dynamics in Polyvinylacetate. *Macromolecules* **2008**, *41*, 1289–1296.

(143) Song, Y.; Zheng, Q. Size-Dependent Linear Rheology of Silica Filled Poly(2-

Vinylpyridine). *Polymer (Guildf).* **2017**, *130*, 74–78.

(144) Casalini, R.; Roland, C. M. Local and Global Dynamics in Polypropylene Glycol/Silica Composites. *Macromolecules* **2016**, *49* (10), 3919–3924.

(145) Mackay, M. E.; Dao, T. T.; Tuteja, A.; Ho, D. L.; Van Horn, B.; Kim, H. C.; Hawker, C. J. Nanoscale Effects Leading to Non-Einstein-like Decrease in Viscosity. *Nat. Mater.* **2003**, *2* (11), 762–766.

(146) Batchelor, G. K. The Effect of Brownian Motion on the Bulk Stress in a Suspension of Spherical Particles. *J. Fluid Mech.* **1977**, *83* (1), 97–117.

(147) Kalathi, J. T.; Grest, G. S.; Kumar, S. K. Universal Viscosity Behavior of Polymer Nanocomposites. *Phys. Rev. Lett.* **2012**, *109* (19), 198301/1-5.

(148) Schneider, G. J.; Nusser, K.; Neueder, S.; Brodeck, M.; Willner, L.; Farago, B.; Holderer, O.; Briels, W. J.; Richter, D. Anomalous Chain Diffusion in Unentangled Model Polymer Nanocomposites. *Soft Matter* **2013**, *9* (16), 4336–4348.

(149) Schneider, G. J.; Nusser, K.; Willner, L.; Falus, P.; Richter, D. Dynamics of Entangled Chains in Polymer Nanocomposites. *Macromolecules* **2011**, *44* (15), 5857–5860.

(150) Wei, Y.; Xu, Y.; Faraone, A.; Hore, M. J. A. Local Structure and Relaxation Dynamics in the Brush of Polymer-Grafted Silica Nanoparticles. *ACS Macro Lett.* **2018**, *7* (6), 699–704.

(151) Senses, E.; Tyagi, M.; Pasco, M.; Faraone, A. Dynamics of Architecturally Engineered All-Polymer Nanocomposites. *ACS Nano* **2018**, *12* (11), 10807–10816.

(152) Li, Y.; Kröger, M.; Liu, W. K. Nanoparticle Effect on the Dynamics of Polymer Chains and Their Entanglement Network. *Phys. Rev. Lett.* **2012**, *109* (11), 118001/1-5.

(153) Smith, G. D.; Bedrov, D.; Li, L.; Byutner, O. A Molecular Dynamics Simulation Study of the Viscoelastic Properties of Polymer Nanocomposites. *J. Chem. Phys.* **2002**, *117* (20), 9478–9490.

(154) Dionne, P. J.; Ozisik, R.; Picu, C. R. Structure and Dynamics of Polyethylene

Nanocomposites. *Macromolecules* **2005**, *38* (22), 9351–9358.

(155) Kalathi, J. T.; Kumar, S. K.; Rubinstein, M.; Grest, G. S. Rouse Mode Analysis of Chain Relaxation in Polymer Nanocomposites. *Soft Matter* **2015**, *11* (20), 4123–4132.

(156) Picu, R. C.; Rakshit, A. Dynamics of Free Chains in Polymer Nanocomposites. *J. Chem. Phys.* **2007**, *126* (14), 144909.

(157) Nusser, K.; Neueder, S.; Schneider, G. J.; Meyer, M.; Pyckhout-Hintzen, W.; Willner, L.; Radulescu, A.; Richter, D. Conformations of Silica-Poly (Ethylene-Propylene) Nanocomposites. *Macromolecules* **2010**, *43* (23), 9837–9847.

(158) Yamamoto, U.; Schweizer, K. S. Theory of Entanglements and Tube Confinement in Rod-Sphere Nanocomposites. *ACS Macro Lett.* **2013**, *2* (11), 955–959.

(159) Mangal, R.; Srivastava, S.; Narayanan, S.; Archer, L. A. Size-Dependent Particle Dynamics in Entangled Polymer Nanocomposites. *Langmuir* **2016**, *32* (2), 596–603.

(160) Li, Y.; Kröger, M.; Liu, W. K. Nanoparticle Geometrical Effect on Structure, Dynamics and Anisotropic Viscosity of Polyethylene Nanocomposites. *Macromolecules* **2012**, *45* (4), 2099–2112.

(161) Karatrantos, A.; Composto, R. J.; Winey, K. I.; Clarke, N. Primitive Path Network, Structure and Dynamics of SWCNT / Polymer Nanocomposites. *IOP Conf. Ser. Mater. Sci. Eng.* **2012**, *40* (1), 1–6.

(162) Karatrantos, A.; Clarke, N.; Composto, R. J.; Winey, K. I. Entanglements in Polymer Nanocomposites Containing Spherical Nanoparticles. *Soft Matter* **2016**, *12* (9), 2567–2574.

(163) Karatrantos, A.; Composto, R. J.; Winey, K. I.; Kröger, M.; Clarke, N. Entanglements and Dynamics of Polymer Melts near a SWCNT. *Macromolecules* **2012**, *45* (17), 7274–7281.

(164) Karatrantos, A.; Clarke, N.; Composto, R. J.; Winey, K. I. Topological Entanglement Length in Polymer Melts and Nanocomposites by a DPD Polymer Model. *Soft Matter* **2013**, *9* (14), 3877–3884.

(165) Riggleman, R. A.; Toepperwein, G.; Papakonstantopoulos, G. J.; Barrat, J. L.; De Pablo, J. J. Entanglement Network in Nanoparticle Reinforced Polymers. *J. Chem. Phys.* **2009**, *130* (24), 244903.

(166) Karatrantos, A.; Clarke, N.; Composto, R. J.; Winey, K. I. Structure, Entanglements and Dynamics of Polymer Nanocomposites Containing Spherical Nanoparticles. *IOP Conf. Ser. Mater. Sci. Eng.* **2014**, *64* (1), 1–6.

(167) Klonos, P.; Kulyk, K.; Borysenko, M. V.; Gun'ko, V. M.; Kyritsis, A.; Pissis, P. Effects of Molecular Weight below the Entanglement Threshold on Interfacial Nanoparticles/Polymer Dynamics. *Macromolecules* **2016**, *49* (24), 9457–9473.

(168) Meerwall, E. D. von. Self-Diffusion in Polymer Systems, Measured with Field-Gradient Spin Echo NMR Methods. In *Advances in Polymer Science*; Springer, Berlin, Heidelberg, 1984; pp 1–29.

(169) Composto, R. J.; Walters, R. M.; Genzer, J. Application of Ion Scattering Techniques to Characterize Polymer Surfaces and Interfaces. *Mater. Sci. Eng. R Reports* **2002**, *38* (3–4), 107–180.

(170) Gam, S.; Meth, J. S.; Zane, S. G.; Chi, C.; Wood, B. A.; Seitz, M. E.; Winey, K. I.; Clarke, N.; Composto, R. J. Macromolecular Diffusion in a Crowded Polymer Nanocomposite. *Macromolecules* **2011**, *44* (9), 3494–3501.

(171) Whitlow, S. J.; Wool, R. P. Diffusion of Polymers at Interfaces: A Secondary Ion Mass Spectroscopy Study. *Macromolecules* **1991**, *24* (22), 5926–5938.

(172) Segalman, R. A.; Jacobson, A.; Kramer, E. J.; Lustig, S. R. Polymer Diffusion in Semicrystalline Polymers Using Secondary Ion Mass Spectroscopy. *Macromolecules* **2004**, *37* (7), 2613–2617.

(173) T.P.Russell. X-Ray and Neutron Reflectivity for the Investigation of Polymers. *Mater. Sci. Reports* **1990**, *5* (4), 171–271.

(174) Muthukumar, M.; Baumgaertner, A. Effects of Entropic Barriers on Polymer Dynamics. *Macromolecules* **1989**, *22* (4), 1937–1941.

(175) Muthukumar, M.; Baumgaertner, A. Diffusion of a Polymer Chain in Random Media. *Macromolecules* **1989**, *22* (4), 1941–1946.

(176) Huang, X. W.; Peng, Y.; Huang, J. H.; Luo, M. B. A Study on the Diffusivity of Polymers in Crowded Environments with Periodically Distributed Nanoparticles. *Phys. Chem. Chem. Phys.* **2017**, *19* (44), 29975–29983.

(177) Yamamoto, U.; Schweizer, K. S. Theory of Anisotropic Diffusion of Entangled and Unentangled Polymers in Rod-Sphere Mixtures. *ACS Macro Lett.* **2015**, *4* (1), 53–57.

(178) Meth, J. S.; Zane, S. G.; Chi, C.; Londono, J. D.; Wood, B. A.; Cotts, P.; Keating, M.; Guise, W.; Weigand, S. Development of Filler Structure in Colloidal Silica-Polymer Nanocomposites. *Macromolecules* **2011**, *44* (20), 8301–8313.

(179) Maxwell, J. C. *A Treatise on Electricity and Magnetism*; Oxford University Press: London, 1873.

(180) Lin, C. C.; Gam, S.; Meth, J. S.; Clarke, N.; Winey, K. I.; Composto, R. J. Do Attractive Polymer-Nanoparticle Interactions Retard Polymer Diffusion in Nanocomposites? *Macromolecules* **2013**, *46* (11), 4502–4509.

(181) Gam, S.; Meth, J. S.; Zane, S. G.; Chi, C.; Wood, B. A.; Winey, K. I.; Clarke, N.; Composto, R. J. Polymer Diffusion in a Polymer Nanocomposite: Effect of Nanoparticle Size and Polydispersity. *Soft Matter* **2012**, *8* (24), 6512–6520.

(182) Choi, J.; Hore, M. J. A.; Meth, J. S.; Clarke, N.; Winey, K. I.; Composto, R. J. Universal Scaling of Polymer Diffusion in Nanocomposites. *ACS Macro Lett.* **2013**, *2* (6), 485–490.

(183) Choi, J.; Hore, M. J. A.; Clarke, N.; Winey, K. I.; Composto, R. J. Nanoparticle Brush Architecture Controls Polymer Diffusion in Nanocomposites. *Macromolecules* **2014**, *47* (7), 2404–2410.

(184) Meth, J. S.; Gam, S.; Choi, J.; Lin, C. C.; Composto, R. J.; Winey, K. I. Excluded Volume Model for the Reduction of Polymer Diffusion into Nanocomposites. *J. Phys. Chem. B* **2013**, *117* (49), 15675–15683.

(185) Choi, J.; Clarke, N.; Winey, K. I.; Composto, R. J. Polymer Diffusion from Attractive and Athermal Substrates. *Macromolecules* **2017**, *50* (7), 3038–3042.

(186) Sauer, B. B.; Zheng, X.; Rubinstein, M.; Rafailovich, M. H.; Schwarz, S. A.; Sokolov, J.; Strzhemechny, Y. Long-Range Effects on Polymer Diffusion Induced by a Bounding Interface. *Phys. Rev. Lett.* **2002**, *79* (2), 241–244.

(187) Choi, K. I.; Kim, T. H.; Yuan, G.; Satija, S. K.; Koo, J. Dynamics of Entangled Polymers Confined between Graphene Oxide Sheets as Studied by Neutron Reflectivity. *ACS Macro Lett.* **2017**, *6* (8), 819–823.

(188) Tung, W. S.; Griffin, P. J.; Meth, J. S.; Clarke, N.; Composto, R. J.; Winey, K. I. Temperature-Dependent Suppression of Polymer Diffusion in Polymer Nanocomposites. *ACS Macro Lett.* **2016**, *5* (6), 735–739.

(189) Ozisik, R.; Zheng, J.; Dionne, P. J.; Picu, C. R.; Von Meerwall, E. D. NMR Relaxation and Pulsed-Gradient Diffusion Study of Polyethylene Nanocomposites. *J. Chem. Phys.* **2005**, *123* (13), 134901.

(190) Miller, B.; Imel, A. E.; Holley, W.; Baskaran, D.; Mays, J. W.; Dadmun, M. D. The Role of Nanoparticle Rigidity on the Diffusion of Linear Polystyrene in a Polymer Nanocomposite. *Macromolecules* **2015**, *48* (22), 8369–8375.

(191) Martin, H. J.; White, B. T.; Yuan, G.; Saito, T.; Dadmun, M. D. Relative Size of the Polymer and Nanoparticle Controls Polymer Diffusion in All-Polymer Nanocomposites. *Macromolecules* **2019**, *52*, 2843−2852.

(192) Desai, T.; Keblinski, P.; Kumar, S. K. Molecular Dynamics Simulations of Polymer Transport in Nanocomposites. *J. Chem. Phys.* **2005**, *122* (13), 134910.

(193) Sorichetti, V.; Hugouvieux, V.; Kob, W. Structure and Dynamics of a Polymer-Nanoparticle Composite: Effect of Nanoparticle Size and Volume Fraction. *Macromolecules* **2018**, *51* (14), 5375–5391.

(194) Zhang, H.; Sun, D. D.; Peng, Y.; Huang, J. H.; Luo, M. B. Diffusivity and Glass Transition of Polymer Chains in Polymer Nanocomposites. *Phys. Chem. Chem. Phys.* **2019**, *21* (41), 23209–23216.

(195) Karatrantos, A.; Composto, R. J.; Winey, K. I.; Clarke, N. Polymer and Spherical Nanoparticle Diffusion in Nanocomposites. *J. Chem. Phys.* **2017**, *146* (20), 203331.

(196) Mu, M.; Clarke, N.; Composto, R. J.; Winey, K. I. Polymer Diffusion Exhibits a Minimum with Increasing Single-Walled Carbon Nanotube Concentration. *Macromolecules* **2009**, *42* (18), 7091–7097.

(197) Mu, M.; Composto, R. J.; Clarke, N.; Winey, K. I. Minimum in Diffusion Coefficient with Increasing MWCNT Concentration Requires Tracer Molecules to Be Larger than Nanotubes. *Macromolecules* **2009**, *42* (21), 8365–8369.

(198) Tung, W. S.; Clarke, N.; Composto, R. J.; Winey, K. I. Temperature Dependence of Polymer Diffusion in MWCNT/PS Nanocomposites. *Macromolecules* **2013**, *46* (6), 2317–2322.

(199) Lin, C. C.; Ohno, K.; Clarke, N.; Winey, K. I.; Composto, R. J. Macromolecular Diffusion through a Polymer Matrix with Polymer-Grafted Chained Nanoparticles. *Macromolecules* **2014**, *47* (15), 5357–5364.

(200) Lin, C. C.; Cargnello, M.; Murray, C. B.; Clarke, N.; Winey, K. I.; Riggleman, R. A.; Composto, R. J. Nanorod Mobility Influences Polymer Diffusion in Polymer Nanocomposites. *ACS Macro Lett.* **2017**, *6* (8), 869–874.

(201) Choi, J.; Clarke, N.; Winey, K. I.; Composto, R. J. Fast Polymer Diffusion through Nanocomposites with Anisotropic Particles. *ACS Macro Lett.* **2014**, *3* (9), 886–891.

(202) Karatrantos, A.; Clarke, N. A Theoretical Model for the Prediction of Diffusion in Polymer/SWCNT Nanocomposites. *Soft Matter* **2011**, *7* (16), 7334–7341.

(203) Choi, J.; Cargnello, M.; Murray, C. B.; Clarke, N.; Winey, K. I.; Composto, R. J. Fast Nanorod Diffusion through Entangled Polymer Melts. *ACS Macro Lett.* **2015**, *4* (9), 952–956.

(204) Lin, E. K.; Kolb, R.; Satija, S. K.; Wu, W. L. Reduced Polymer Mobility near the Polymer/Solid Interface as Measured by Neutron Reflectivity. *Macromolecules* **1999**, *32* (11), 3753–3757.

(205) Zheng, X.; Sauer, B. B.; Alsten, J. G. Van; Schwarz, S. A.; Rafailovich, M. H.; Sokolov, J.; Rubinstein, M. Reptation Dynamics of a Polymer Melt near an Attractive Solid Interface. *Phys. Rev. Lett.* **1995**, *74* (3), 407–410.

(206) Jimenez, A. M.; Zhao, D.; Misquitta, K.; Jestin, J.; Kumar, S. K. Exchange Lifetimes of the Bound Polymer Layer on Silica Nanoparticles. *ACS Macro Lett.* **2019**, *8* (2), 166–171.

(207) Bailey, E. J.; Griffin, P. J.; Composto, R. J.; Winey, K. I. Characterizing the Areal Density and Desorption Kinetics of Physically Adsorbed Polymer in Polymer Nanocomposite Melts. *Macromolecules* **2020**.

(208) Griffin, P. J.; Bocharova, V.; Middleton, L. R.; Composto, R. J.; Clarke, N.; Schweizer, K. S.; Winey, K. I. Influence of the Bound Polymer Layer on Nanoparticle Diffusion in Polymer Melts. *ACS Macro Lett.* **2016**, *5* (10), 1141–1145.

(209) Jouault, N.; Crawford, M. K.; Chi, C.; Smalley, R. J.; Wood, B.; Jestin, J.; Melnichenko, Y. B.; He, L.; Guise, W. E.; Kumar, S. K. Polymer Chain Behavior in Polymer Nanocomposites with Attractive Interactions. *ACS Macro Lett.* **2016**, *5* (4), 523–527.

(210) Jouault, N.; Moll, J. F.; Meng, D.; Windsor, K.; Ramcharan, S.; Kearney, C.; Kumar, S. K. Bound Polymer Layer in Nanocomposites. *ACS Macro Lett.* **2013**, *2* (5), 371–374.

(211) Cai, L. H.; Panyukov, S.; Rubinstein, M. Mobility of Nonsticky Nanoparticles in Polymer

Liquids. *Macromolecules* **2011**, *44* (19), 7853–7863.

(212) Cai, L. H.; Panyukov, S.; Rubinstein, M. Hopping Diffusion of Nanoparticles in Polymer Matrices. *Macromolecules* **2015**, *48* (3), 847–862.

(213) Dell, Z. E.; Schweizer, K. S. Theory of Localization and Activated Hopping of Nanoparticles in Cross-Linked Networks and Entangled Polymer Melts. *Macromolecules* **2014**, *47* (1), 405–414.

(214) Yamamoto, U.; Carrillo, J. M. Y.; Bocharova, V.; Sokolov, A. P.; Sumpter, B. G.; Schweizer, K. S. Theory and Simulation of Attractive Nanoparticle Transport in Polymer Melts. *Macromolecules* **2018**, *51* (6), 2258–2267.

(215) Yamamoto, U.; Schweizer, K. S. Theory of Nanoparticle Diffusion in Unentangled and Entangled Polymer Melts. *J. Chem. Phys.* **2011**, *135* (22), 224902.

(216) Yamamoto, U.; Schweizer, K. S. Microscopic Theory of the Long-Time Diffusivity and Intermediate-Time Anomalous Transport of a Nanoparticle in Polymer Melts. *Macromolecules* **2015**, *48* (1), 152–163.

(217) Yamamoto, U.; Schweizer, K. S. Spatially Dependent Relative Diffusion of Nanoparticles in Polymer Melts. *J. Chem. Phys.* **2013**, *139* (6), 064907.

(218) Ganesan, V.; Pryamitsyn, V.; Surve, M.; Narayanan, B. Noncontinuum Effects in Nanoparticle Dynamics in Polymers. *J. Chem. Phys.* **2006**, *124* (22), 221102.

(219) Egorov, S. A. Anomalous Nanoparticle Diffusion in Polymer Solutions and Melts: A Mode-Coupling Theory Study. *J. Chem. Phys.* **2011**, *134* (8), 084903.

(220) Wöll, D. Fluorescence Correlation Spectroscopy in Polymer Science. *RSC Adv.* **2014**, *4* (5), 2447–2465.

(221) Grabowski, C. A.; Mukhopadhyay, A. Size Effect of Nanoparticle Diffusion in a Polymer Melt. *Macromolecules* **2014**, *47* (20), 7238–7242.

(222) Nath, P.; Mangal, R.; Kohle, F.; Choudhury, S.; Narayanan, S.; Wiesner, U.; Archer, L. A.

Dynamics of Nanoparticles in Entangled Polymer Solutions. *Langmuir* **2018**, *34* (1), 241–249.

(223) Parrish, E.; Seeger, S. C.; Composto, R. J. Temperature-Dependent Nanoparticle Dynamics in Poly(N-Isopropylacrylamide) Gels. *Macromolecules* **2018**, *51* (10), 3597–3607.

(224) Manzo, C.; Garcia-Parajo, M. F. A Review of Progress in Single Particle Tracking: From Methods to Biophysical Insights. *Reports Prog. Phys.* **2015**, *78*, 124601/1-29.

(225) Park, J.; Bailey, E. J.; Composto, R. J.; Winey, K. I. Single Particle Tracking of Non-Sticky and Sticky Nanoparticles in Polymer Melts. *Under_Review* **2020**.

(226) Xue, C.; Zheng, X.; Chen, K.; Tian, Y.; Hu, G. Probing Non-Gaussianity in Confined Diffusion of Nanoparticles. *J. Phys. Chem. Lett.* **2016**, *7* (3), 514–519.

(227) Lungova, M.; Krutyeva, M.; Pyckhout-Hintzen, W.; Wischnewski, A.; Monkenbusch, M.; Allgaier, J.; Ohl, M.; Sharp, M.; Richter, D. Nanoscale Motion of Soft Nanoparticles in Unentangled and Entangled Polymer Matrices. *Phys. Rev. Lett.* **2016**, *117* (14), 147803/1-5.

(228) Kalathi, J. T.; Yamamoto, U.; Schweizer, K. S.; Grest, G. S.; Kumar, S. K. Nanoparticle Diffusion in Polymer Nanocomposites. *Phys. Rev. Lett.* **2014**, *112* (10), 108301/1-5.

(229) Liu, J.; Cao, D.; Zhang, L. Molecular Dynamics Study on Nanoparticle Diffusion in Polymer Melts: A Test of the Stokes-Einstein Law. *J. Phys. Chem. C* **2008**, *112* (17), 6653–6661.

(230) Ge, T.; Kalathi, J. T.; Halverson, J. D.; Grest, G. S.; Rubinstein, M. Nanoparticle Motion in Entangled Melts of Linear and Nonconcatenated Ring Polymers. *Macromolecules* **2017**, *50* (4), 1749–1754.

(231) Medidhi, K. R.; Padmanabhan, V. Diffusion of Polymer-Grafted Nanoparticles in a Homopolymer Matrix. *J. Chem. Phys.* **2019**, *150* (4), 044905.

(232) Chen, T.; Qian, H. J.; Lu, Z. Y. Diffusion Dynamics of Nanoparticle and Its Coupling with

Polymers in Polymer Nanocomposites. *Chem. Phys. Lett.* **2017**, *687*, 96–100.

(233) Karatrantos, A.; Composto, R. J.; Winey, K. I.; Clarke, N. Nanorod Diffusion in Polymer Nanocomposites by Molecular Dynamics Simulations. *Macromolecules* **2019**, *52*, 2513−2520.

(234) Tuteja, A.; Mackay, M. E.; Narayanan, S.; Asokan, S.; Wong, M. S. Breakdown of the Continuum Stokes-Einstein Relation for Nanoparticle Diffusion. *Nano Lett.* **2007**, *7* (5), 1276–1281.

(235) Grabowski, C. A.; Adhikary, B.; Mukhopadhyay, A. Dynamics of Gold Nanoparticles in a Polymer Melt. *Appl. Phys. Lett.* **2009**, *94* (2), 1–4.

(236) Lin, C. C.; Griffin, P. J.; Chao, H.; Hore, M. J. A.; Ohno, K.; Clarke, N.; Riggleman, R. A.; Winey, K. I.; Composto, R. J. Grafted Polymer Chains Suppress Nanoparticle Diffusion in Athermal Polymer Melts. *J. Chem. Phys.* **2017**, *146* (20), 203332/1-8.

(237) Kim, M. J.; Cho, H. W.; Kim, J.; Kim, H.; Sung, B. J. Translational and Rotational Diffusion of a Single Nanorod in Unentangled Polymer Melts. *Phys. Rev. E - Stat. Nonlinear, Soft Matter Phys.* **2015**, *92* (4), 042601/1-8.

(238) Alam, S.; Mukhopadhyay, A. Translational and Rotational Diffusions of Nanorods within Semidilute and Entangled Polymer Solutions. *Macromolecules* **2014**, *47* (19), 6919–6924.

(239) Riseman, J.; Kirkwood, J. G. The Intrinsic Viscosity, Translational and Rotatory Diffusion Constants of Rod-like Macromolecules in Solution. *J. Chem. Phys.* **1950**, *18* (4), 512–516.

(240) Tsay, J. M.; Doose, S.; Weiss, S. Rotational and Translational Diffusion of Peptide-Coated CdSe/CdS/ZnS Nanorods Studied by Fluorescence Correlation Spectroscopy. *J. Am. Chem. Soc.* **2006**, *128* (5), 1639–1647.

(241) Poling-Skutvik, R.; Mongcopa, K. I. S.; Faraone, A.; Narayanan, S.; Conrad, J. C.; Krishnamoorti, R. Structure and Dynamics of Interacting Nanoparticles in Semidilute Polymer Solutions. *Macromolecules* **2016**, *49* (17), 6568–6577.

(242) Poling-Skutvik, R.; Krishnamoorti, R.; Conrad, J. C. Size-Dependent Dynamics of Nanoparticles in Unentangled Polyelectrolyte Solutions. *ACS Macro Lett.* **2015**, *4* (10), 1169–1173.

(243) Poling-Skutvik, R.; Slim, A. H.; Narayanan, S.; Conrad, J. C.; Krishnamoorti, R. Soft Interactions Modify the Diffusive Dynamics of Polymer-Grafted Nanoparticles in Solutions of Free Polymer. *ACS Macro Lett.* **2019**, *8*, 917−922.

(244) Senanayake, K. K.; Fakhrabadi, E. A.; Liberatore, M. W.; Mukhopadhyay, A. Diffusion of Nanoparticles in Entangled Poly(Vinyl Alcohol) Solutions and Gels. *Macromolecules* **2019**, *52* (3), 787–795.

(245) Senanayake, K. K.; Mukhopadhyay, A. Nanoparticle Diffusion within Dilute and Semidilute Xanthan Solutions. *Langmuir* **2019**, *35* (24), 7978–7984.

(246) Carroll, B.; Bocharova, V.; Carrillo, J. M. Y.; Kisliuk, A.; Cheng, S.; Yamamoto, U.; Schweizer, K. S.; Sumpter, B. G.; Sokolov, A. P. Diffusion of Sticky Nanoparticles in a Polymer Melt: Crossover from Suppressed to Enhanced Transport. *Macromolecules* **2018**, *51* (6), 2268–2275.

(247) Ren, K. X.; Jia, X. M.; Jiao, G. S.; Chen, T.; Qian, H. J.; Lu, Z. Y. Interfacial Properties and Hopping Diffusion of Small Nanoparticle in Polymer/Nanoparticle Composite with Attractive Interaction on Side Group. *Polymers (Basel).* **2018**, *10* (6), 598/1-18.

(248) Volgin, I. V.; Larin, S. V.; Abad, E.; Lyulin, S. V. Molecular Dynamics Simulations of Fullerene Diffusion in Polymer Melts. *Macromolecules* **2017**, *50* (5), 2207–2218.

(249) Volgin, I. V.; Larin, S. V.; Lyulin, A. V.; Lyulin, S. V. Coarse-Grained Molecular-Dynamics Simulations of Nanoparticle Diffusion in Polymer Nanocomposites. *Polymer (Guildf).* **2018**, *145*, 80–87.

(250) Cao, X. Z.; Merlitz, H.; Wu, C. X. Tuning Adsorption Duration to Control the Diffusion of a Nanoparticle in Adsorbing Polymers. *J. Phys. Chem. Lett.* **2017**, *8* (12), 2629–2633.

(251) Karatrantos, A.; Koutsawa, Y.; Dubois, P.; Clarke, N.; Kröger, M. Miscibility and Nanoparticle Diffusion in Ionic Nanocomposites. *Polymers (Basel).* **2018**, *10* (9), 1010/1-16.

(252) Srivastava, S.; Kandar, A. K.; Basu, J. K.; Mukhopadhyay, M. K.; Lurio, L. B.; Narayanan, S.; Sinha, S. K. Complex Dynamics in Polymer Nanocomposites. *Phys. Rev. E - Stat. Nonlinear, Soft Matter Phys.* **2009**, *79* (2), 021408/1-7.

(253) Hoshino, T.; Murakami, D.; Tanaka, Y.; Takata, M.; Jinnai, H.; Takahara, A. Dynamical Crossover between Hyperdiffusion and Subdiffusion of Polymer-Grafted Nanoparticles in a Polymer Matrix. *Phys. Rev. E* **2013**, *88* (3), 032602/1-7.

(254) Ranka, M.; Varkey, N.; Ramakrishnan, S.; Zukoski, C. F. Impact of Small Changes in Particle Surface Chemistry for Unentangled Polymer Nanocomposites. *Soft Matter* **2015**, *11* (8), 1634–1645.

(255) Senses, E.; Narayanan, S.; Mao, Y.; Faraone, A. Nanoscale Particle Motion in Attractive Polymer Nanocomposites. *Phys. Rev. Lett.* **2017**, *119*, 237801/1-5.

(256) Srivastava, S.; Agarwal, P.; Mangal, R.; Koch, D. L.; Narayanan, S.; Archer, L. A. Hyperdiffusive Dynamics in Newtonian Nanoparticle Fluids. *ACS Macro Lett.* **2015**, *4* (10), 1149–1153.

(257) Liu, S.; Senses, E.; Jiao, Y.; Narayanan, S.; Akcora, P. Structure and Entanglement Factors on Dynamics of Polymer-Grafted Nanoparticles. *ACS Macro Lett.* **2016**, *5* (5), 569–573.

(258) Song, J. J.; Bhattacharya, R.; Kim, H.; Chang, J.; Tang, T. Y.; Guo, H.; Ghosh, S. K.; Yang, Y.; Jiang, Z.; Kim, H.; et al. One-Dimensional Anomalous Diffusion of Gold Nanoparticles in a Polymer Melt. *Phys. Rev. Lett.* **2019**, *122* (10), 107802/1-6.

(259) Guo, H.; Bourret, G.; Corbierre, M. K.; Rucareanu, S.; Lennox, R. B.; Laaziri, K.; Piche, L.; Sutton, M.; Harden, J. L.; Leheny, R. L. Nanoparticle Motion within Glassy Polymer Melts. *Phys. Rev. Lett.* **2009**, *102* (7), 075702/1-4.

(260) Senses, E.; Tyagi, M.; Natarajan, B.; Narayanan, S.; Faraone, A. Chain Dynamics and Nanoparticle Motion in Attractive Polymer Nanocomposites Subjected to Large Deformations. *Soft Matter* **2017**, *13* (43), 7922–7929.

(261) Jang, W. S.; Koo, P.; Bryson, K.; Narayanan, S.; Sandy, A.; Russell, T. P.; Mochrie, S. G. Dynamics of Cadmium Sulfide Nanoparticles within Polystyrene Melts. *Macromolecules* **2014**, *47* (18), 6483–6490.

(262) Srivastava, S.; Archer, L. A.; Narayanan, S. Structure and Transport Anomalies in Soft Colloids. *Phys. Rev. Lett.* **2013**, *110* (14), 148302/1-5.

(263) Narayanan, R. A.; Thiyagarajan, P.; Lewis, S.; Bansal, A.; Schadler, L. S.; Lurio, L. B. Dynamics and Internal Stress at the Nanoscale Related to Unique Thermomechanical Behavior in Polymer Nanocomposites. *Phys. Rev. Lett.* **2006**, *97* (7), 075505/1-4.

(264) Kim, D.; Srivastava, S.; Narayanan, S.; Archer, L. A. Polymer Nanocomposites: Polymer and Particle Dynamics. *Soft Matter* **2012**, *8* (42), 10813–10818.

(265) Yang, S.; Liu, S.; Narayanan, S.; Zhang, C.; Akcora, P. Chemical Heterogeneity in Interfacial Layers of Polymer Nanocomposites. *Soft Matter* **2018**, *14* (23), 4784–4791.

(266) Senses, E.; Narayanan, S.; Faraone, A. Nanoscale Particle Motion Reveals Polymer Mobility Gradient in Nanocomposites. *ACS Macro Lett.* **2019**, *8*, 558–562.

(267) Kandar, A. K.; Srivastava, S.; Basu, J. K.; Mukhopadhyay, M. K.; Seifert, S.; Narayanan, S. Unusual Dynamical Arrest in Polymer Grafted Nanoparticles. *J. Chem. Phys.* **2009**, *130* (12), 1–6.

(268) Dierker, S. B.; Pindak, R.; Fleming, R. M.; Robinson, I. K.; Berman, L. X-Ray Photon Correlation Spectroscopy Study of Brownian Motion of Gold Colloids in Glycerol. *Phys. Rev. Lett.* **1995**, *75* (3), 449–452.

(269) Leheny, R. L. XPCS: Nanoscale Motion and Rheology. *Curr. Opin. Colloid Interface Sci.* **2012**, *17* (1), 3–12.

(270) Genix, A. C.; Oberdisse, J. Structure and Dynamics of Polymer Nanocomposites Studied by X-Ray and Neutron Scattering Techniques. *Curr. Opin. Colloid Interface Sci.* **2015**, *20* (4), 293–303.

(271) Bras, W.; Stanley, H. Unexpected Effects in Non Crystalline Materials Exposed to X-Ray Radiation. *J. Non. Cryst. Solids* **2016**, *451*, 153–160.

(272) Lin, C.; Gam, S.; Meth, S.; Clarke, N.; Winey, K. I.; Composto, R. J. Do Attractive Polymer − Nanoparticle Interactions Retard Polymer Diffusion in Nanocomposites? *Macromolecules* **2013**, *46*, 4502–4509.

(273) Mu, M.; Seitz, M. E.; Clarke, N.; Composto, R. J.; Winey, K. I. Polymer Tracer Diffusion Exhibits a Minimum in Nanocomposites Containing Spherical Nanoparticles. *Macromolecules* **2011**, *44* (2), 191–193.

(274) Schneider, G. J. Dynamics of Nanocomposites. *Curr. Opin. Chem. Eng.* **2017**, *16*, 65–77.

(275) Triolo, A.; Lo Celso, F.; Negroni, F.; Arrighi, V.; Qian, H.; Lechner, R. E.; Desmedt, A.; Pieper, J.; Frick, B.; Triolo, R. QENS Investigation of Filled Rubbers. *Appl. Phys. A Mater. Sci. Process.* **2002**, *74*, 490–492.

(276) Chrissopoulou, K.; Anastasiadis, S. H.; Giannelis, E. P.; Frick, B. Quasielastic Neutron Scattering of Poly(Methyl Phenyl Siloxane) in the Bulk and under Severe Confinement. *J. Chem. Phys.* **2007**, *127* (14).

(277) Kropka, J. M.; Garcia Sakai, V.; Green, P. F. Local Polymer Dynamics in Polymer− C60 Mixtures. *Nano Lett.* **2008**, *8* (4), 1061–1065.

(278) Arrighi, V.; Higgins, J. S.; Burgess, A. N.; Floudas, G. Local Dynamics of Poly(Dimethyl Siloxane) in the Presence of Reinforcing Filler Particles. *Polymer.* **1998**, *39* (25), 6369–6376.

(279) Kamiya, H.; Suzuki, H.; Kato, D.; Jimbo, G. Densification of Alkoxide-Derived Fine Silica Powder Compact by Ultra-High-Pressure Cold Isostatic Pressing. *J. Am. Ceram. Soc.* **1993**,

76 (1), 54–64.

(280) Iijima, M.; Kamiya, H. Layer-by-Layer Surface Modification of Functional Nanoparticles for Dispersion in Organic Solvents. *Langmuir* **2010**, *26* (23), 17943–17948.

(281) Sears, V. F. Neutron Scattering Lengths and Cross Sections. *Neutron News* **1992**, *3* (3), 26–37.

(282) Ryong-Joon, R. *Methods of X-Ray and Neutron Scattering in Polymer Science*; Oxford University Press: New York, 2000.

(283) Meyer, A.; Dimeo, R. M.; Gehring, P. M.; Neumann, D. A. The High-Flux Backscattering Spectrometer at the NIST Center for Neutron Research. *Rev. Sci. Instrum.* **2003**, *74* (5), 2759–2777.

(284) Azuah, R. T.; Kneller, L. R.; Qiu, Y.; Tregenna-Piggott, P. L. W.; Brown, C. M.; Copley, J. R. D.; Dimeo, R. M. DAVE: A Comprehensive Software Suite for the Reduction, Visualization, and Analysis of Low Energy Neutron Spectroscopic Data. *J. Res. Natl. Inst. Stand. Technol.* **2009**, *114* (6), 341.

(285) Elmaci, A.; Hacaloglu, J. Thermal Degradation of Poly(Vinylpyridine)S. *Polym. Degrad. Stab.* **2009**, *94* (4), 738–743.

(286) Inoue, R.; Kanaya, T.; Nishida, K.; Tsukushi, I.; Telling, M. T. F.; Gabrys, B. J.; Tyagi, M.; Soles, C.; Wu, W. L. Glass Transition and Molecular Mobility in Polymer Thin Films. *Phys. Rev. E - Stat. Nonlinear, Soft Matter Phys.* **2009**, *80* (3), 1–4.

(287) Soles, C. L.; Douglas, J. F.; Wu, W. L.; Dimeo, R. M. Incoherent Neutron Scattering as a Probe of the Dynamics in Molecularly Thin Polymer Films. *Macromolecules* **2003**, *36* (2), 373–379.

(288) Tonelli, A. E. Conformational Characteristics of Poly(2-Vinylpyridine). *Macromolecules* **1985**, *18* (12), 2579–2583.

(289) Papadopoulos, P.; Peristeraki, D.; Floudas, G.; Koutalas, G.; Hadjichristidis, N. Origin of

Glass Transition of Poly(2-Vinylpyridine). A Temperature- and Pressure-Dependent Dielectric Spectroscopy Study. *Macromolecules* **2004**, *37* (21), 8116–8122.

(290) Holt, A. P.; Sangoro, J. R.; Wang, Y.; Agapov, A. L.; Sokolov, A. P. Chain and Segmental Dynamics of Poly (2-Vinylpyridine) Nanocomposites. *Macromolecules* **2013**, *46* (10), 4168–4173.

(291) Mueller, R.; Kammler, H. K.; Wegner, K.; Pratsinis, S. E. OH Surface Density of SiO2 and TiO2 by Thermogravimetric Analysis. *Langmuir* **2003**, *19* (1), 160–165.

(292) Jouault, N.; Zhao, D.; Kumar, S. K. Role of Casting Solvent on Nanoparticle Dispersion in Polymer Nanocomposites. *Macromolecules* **2014**, *47* (15), 5246–5255.

(293) Wolf, C. M.; Kanekal, K. H.; Yimer, Y. Y.; Tyagi, M.; Omar-Diallo, S.; Pakhnyuk, V.; Luscombe, C. K.; Pfaendtner, J.; Pozzo, L. D. Assessment of Molecular Dynamics Simulations for Amorphous Poly(3-Hexylthiophene) Using Neutron and X-Ray Scattering Experiments. *Soft Matter* **2019**, *15* (25), 5067–5083.

(294) Tyagi, M.; Alegría, A.; Colmenero, J. Heterogeneous Dynamics of Poly(Vinyl Acetate) Far above T g: A Combined Study by Dielectric Spectroscopy and Quasielastic Neutron Scattering. *J. Chem. Phys.* **2005**, *122* (24), 244909/1-13.

(295) Mackay, M. E.; Tuteja, A.; Duxbury, P. M.; Hawker, C. J.; Van Horn, B.; Guan, Z.; Chen, G.; Krishnan, R. S. General Strategies for Nanoparticle Dispersion. *Science (80-.).* **2006**, *311* (5768), 1740–1743.

(296) Crawford, M. K.; Smalley, R. J.; Cohen, G.; Hogan, B.; Wood, B.; Kumar, S. K.; Melnichenko, Y. B.; He, L.; Guise, W.; Hammouda, B. Chain Conformation in Polymer Nanocomposites with Uniformly Dispersed Nanoparticles. *Phys. Rev. Lett.* **2013**, *110* (19), 1–5.

(297) Jouault, N.; Kumar, S. K.; Smalley, R. J.; Chi, C.; Moneta, R.; Wood, B.; Salerno, H.; Melnichenko, Y. B.; He, L.; Guise, W. E.; et al. Do Very Small POSS Nanoparticles Perturb

S-PMMA Chain Conformations? *Macromolecules* **2018**, *51*, acs.macromol.8b00432.

(298) Ndoro, T. V. M.; Voyiatzis, E.; Ghanbari, A.; Theodorou, D. N.; Böhm, M. C.; Müller-Plathe, F. Interface of Grafted and Ungrafted Silica Nanoparticles with a Polystyrene Matrix: Atomistic Molecular Dynamics Simulations. *Macromolecules* **2011**, *44* (7), 2316–2327.

(299) Liu, J.; Wu, Y.; Shen, J.; Gao, Y.; Zhang, L.; Cao, D. Polymer–Nanoparticle Interfacial Behavior Revisited: A Molecular Dynamics Study. *Phys. Chem. Chem. Phys.* **2011**, *13* (28), 13058.

(300) Goswami, M.; Sumpter, B. G. Anomalous Chain Diffusion in Polymer Nanocomposites for Varying Polymer-Filler Interaction Strengths. *Phys. Rev. E - Stat. Nonlinear, Soft Matter Phys.* **2010**, *81* (4), 1–8.

(301) Starr, F. W.; Schrøder, T. B.; Glotzer, S. C. Effects of a Nanoscopic Filler on the Structure and Dynamics of a Simulated Polymer Melt and the Relationship to Ultrathin Films. *Phys. Rev. E. Stat. Nonlin. Soft Matter Phys.* **2001**, *64* (2 Pt 1), 021802.

(302) Huang, J.; Mao, Z.; Qian, C. Dynamic Monte Carlo Study on the Polymer Chain in Random Media Filled with Nanoparticles. *Polymer (Guildf).* **2006**, *47* (8), 2928–2932.

(303) Kutvonen, A.; Rossi, G.; Ala-Nissila, T. Correlations between Mechanical, Structural, and Dynamical Properties of Polymer Nanocomposites. *Phys. Rev. E* **2012**, *85* (4), 041803.

(304) Karatrantos, A.; Clarke, N.; Composto, R. J.; Winey, K. I. Polymer Conformations in Polymer Nanocomposites Containing Spherical Nanoparticles. *Soft Matter* **2015**, *11* (2), 382–388.

(305) Karatrantos, A.; Clarke, N.; Composto, R. J.; Winey, K. I. Polymer and Spherical Nanoparticle Diffusion in Nanocomposites ‡. **2016**, *203331*, 2–7.

(306) Kremer, K.; Grest, G. S. Dynamics of Entangled Linear Polymer Melts : A Moleculardynamics Simulation Dynamics of Entangled Linear Polymer Melts : A

Molecular-Dynamics Simulation. *J. Chem. Phys.* **1990**, *92* (8), 5057.

(307) Plimpton, S. Fast Parallel Algorithms for Short-Range Molecular Dynamics. *Journal of Computational Physics*. 1995, pp 1–19.

(308) Tung, W. S.; Composto, R. J.; Riggleman, R. A.; Winey, K. I. Local Polymer Dynamics and Diffusion in Cylindrical Nanoconfinement. *Macromolecules* **2015**, *48* (7), 2324–2332.

(309) Pressly, J. F.; Riggleman, R. A.; Winey, K. I. Increased Polymer Diffusivity in Thin-Film Confinement. *Macromolecules* **2019**, *52* (16), 6116–6125.

(310) Pressly, J. F.; Riggleman, R. A.; Winey, K. I. Polymer Diffusion Is Fastest at Intermediate Levels of Cylindrical Confinement. *Macromolecules* **2018**, *51* (23), 9789–9797.

(311) Lepcio, P.; Ondreas, F.; Zarybnicka, K.; Zboncak, M.; Caha, O.; Jancar, J. Bulk Polymer Nanocomposites with Preparation Protocol Governed Nanostructure : The Origin and Properties of Aggregates and Polymer Bound Clusters. *Soft Matter* **2018**, *14*, 2094–2103.

(312) Jouault, N.; Lee, D.; Zhao, D.; Kumar, S. K. Block-Copolymer-Mediated Nanoparticle Dispersion and Assembly in Polymer Nanocomposites. *Adv. Mater.* **2014**, *26* (24), 4031–4036.

(313) Fleer, G. J.; Cohen Stuart, M. A.; Scheutjens, J. M. H. .; Cosgrove, T.; Vincent, B. *Polymers at the Interface*, 1st ed.; Chapman and Hall: London, 1993.

(314) Senses, E.; Akcora, P. Tuning Mechanical Properties of Nanocomposites with Bimodal Polymer Bound Layers. *RSC Adv.* **2014**, No. 4, 49628–49634.

(315) Starr, F. W.; Douglas, J. F.; Meng, D.; Kumar, S. K. Bound Layers “Cloak” Nanoparticles in Strongly Interacting Polymer Nanocomposites. *ACS Nano* **2016**, *10* (12), 10960–10965.

(316) Gin, P.; Jiang, N.; Liang, C.; Taniguchi, T.; Akgun, B.; Satija, S. K.; Endoh, M. K.; Koga, T. Revealed Architectures of Adsorbed Polymer Chains at Solid-Polymer Melt Interfaces. *Phys. Rev. Lett.* **2012**, *109* (26), 265501/1-5.

(317) Jiang, N.; Cheung, J.; Guo, Y.; Endoh, M. K.; Koga, T.; Yuan, G.; Satija, S. K. Stability of

Adsorbed Polystyrene Nanolayers on Silicon Substrates. *Macromol. Chem. Phys.* **2018**, *219* (3), 1–10.

(318) Jiang, N.; Endoh, M. K.; Koga, T.; Masui, T.; Kishimoto, H.; Nagao, M.; Satija, S. K.; Taniguchi, T. Nanostructures and Dynamics of Macromolecules Bound to Attractive Filler Surfaces. *ACS Macro Lett.* **2015**, *4* (8), 838–842.

(319) Napolitano, S.; Wübbenhorst, M. The Lifetime of the Deviations from Bulk Behaviour in Polymers Confined at the Nanoscale. *Nat. Commun.* **2011**, *2* (1).

(320) Kramer, E. J.; Green, P.; Palmstrem, C. J. Interdiffusion and Marker Movements in Concentrated Polymer-Polymer Diffusion Couples Couples. *Polymer (Guildf).* **1984**, *25*, 473–480.

(321) Green, P. F.; Kramer, E. J. Matrix Effects on the Diffusion of Long Polymer Chains. *Macromolecules* **1986**, *19* (4), 1108–1114.

(322) Agapov, A. L.; Novikov, V. N.; Hong, T.; Fan, F.; Sokolov, A. P. Surprising Temperature Scaling of Viscoelastic Properties in Polymers. *Macromolecules* **2018**, *51* (13), 4874–4881.

(323) LaVan, D. A.; McGuire, T.; Langer, R. Small-Scale Systems for in Vivo Drug Delivery. *Nat. Biotechnol.* **2003**, *21* (10), 1184–1191.

(324) Ayandele, E.; Sarkar, B.; Alexandridis, P. Polyhedral Oligomeric Silsesquioxane (POSS)-Containing Polymer Nanocomposites. *Nanomaterials* **2012**, *2* (4), 445–475.

(325) Crank, J. *The Mathematics of Diffusion*; Clarendon Press: Oxford, 1979.

(326) Nambiar, R. R.; Blum, F. D. Segmental Dynamics of Bulk Poly(Vinyl Acetate)-D3 by Solid-State 2H NMR: Effect of Small Molecule Plasticizer. **2008**, *41*, 9837–9845.

(327) Lodge, T. Reconciliation of the Molecular Weight Dependence of Diffusion and Viscosity in Entangled Polymers. *Phys. Rev. Lett.* **1999**, *83* (16), 3218–3221.

(328) Genix, A. C.; Bocharova, V.; Carroll, B.; Lehmann, M.; Saito, T.; Krueger, S.; He, L.; Dieudonné-George, P.; Sokolov, A. P.; Oberdisse, J. Understanding the Static Interfacial

Polymer Layer by Exploring the Dispersion States of Nanocomposites. *ACS Appl. Mater. Interfaces* **2019**, *11*, 17863−17872.